University of Delhi

Doctoral Thesis

A new look at triple-GEM detector and Dark Matter search at Large Hadron Collider

Ph.D. Student
Mohit Gola

Ph.D. Supervisor
Dr. Ashok Kumar

A thesis submitted in fulfilment of the requirements for the degree of Doctor of Philosophy

at the

Department of Physics & Astrophysics

January, 2021

Declaration

This thesis describes work done by the candidate during his tenure as Ph.D. student at the Department of Physics and Astrophysics, University of Delhi, Delhi, India under the supervision of Dr. Ashok Kumar. The work reported in this thesis is original and it has not been submitted earlier for any degree to any university.

Candidate ....

Mohit Gola

Supervisor ....

Dr. Ashok Kumar

Head of Department ....

Prof. Brajesh C. Choudhary

Department of Physics and Astrophysics

University of Delhi

Delhi-110007, India

Date: ....

Certificate of Originality

The research work reported in this thesis entitled "**A new look at triple-GEM detector and Dark Matter search at Large Hadron Collider**" has been carried out by me at the **Department of Physics and Astrophysics**, University of Delhi, Delhi, India. The manuscript has been subjected to plagiarism check by **Urkund** software. The work submitted for consideration of award of Ph.D. is original.

....

Mohit Gola

Name and Signature of the Candidate

Student Approval Form

Name of the Author	**Mohit Gola**
Department	Department of Physics and Astrophysics
Degree	Doctor of Philosophy
University	University of Delhi
Guide	Dr. Ashok Kumar
Thesis Title	A new look at triple-GEM detector and Dark Matter search at Large Hadron Collider
Year of Award	2020 (expected)

Agreement

1. I hereby certify that if appropriate, I have obtained and attached here to a written permission/statement from the owner(s) of each third party copyrighted matter to be included in my thesis/dissertation, allowing distribution as specified below.

2. I hereby grant to the university and its agents the non-exclusive license to archive and make accessible, under the conditions specified below, my thesis/dissertation, in whole or in part in all forms of media, now or hereafter known. I retain all other ownership rights to the copyright of the thesis/dissertation. I also retain the right to use in future works (such as articles or books) all or part of this thesis, dissertation, or project report.

Conditions:

1. Release the entire work for access worldwide	No
2. Release the entire work for 'My University'only for: 1 Year 2 Year 3 Year and after this time release the work for access worldwide.	 3 Year
3. Release the entire work for 'My University'only while at the same time releasing the following parts of the work (e.g. because other parts relate to publications) for worldwide access: a) Bibliographic details and Synopsis only b) Bibliographic details, synopsis and the following chapters only c) Preview/Table of Contents/24 page only	No
4. View Only (No Downloads) (worldwide)	No

....

Signature of the Scholar Signature and seal of the Guide

Place: ....

Date: ....

Publications

Journal Publications

1. **M. Gola**, S. Malhotra, A. Kumar, Md. Naimuddin, "Stability test performed on the triple GEM detector built using commercially manufactured GEM foils in India", JINST 14 P08004 (2019).

2. **M. Gola**, A. Shah, A. Ahmad, S. Malhotra, A. Kumar, Md. Naimuddin, "Performance of the triple GEM detector built using commercially manufactured GEM foils in India", NIM A 951 (2019).

3. A. Shah, **M. Gola**, A. Ahmad, R. Sharma, S. Malhotra, A. Kumar, Md. Naimuddin, P. Menon, K. Srinivasan, "Development, Characterization and Qualification of first GEM foils produced in India", NIM A 892 (2018).

4. D. Abbaneo, Ashok Kumar, **M. Gola**, et al., "Layout and assembly technique of the GEM chambers for the upgrade of the CMS first muon endcap station", NIM A 918 (2019).

5. A. Ahmed, **M. Gola**, A. Kumar, Md. Naimuddin, "Development and qualification of triple-GEM detector built with large size single mask foils produced in India", JINST 15 P02003 (2020).

6. C. Chen, **M. Gola**, A. Kumar et al., "Search for Dark Matter candidate in Higgs to bb + Missing Transverse Energy (Mono-H) final state", CMS AN-15-209, JHEP 10 (2017).

7. D. Abbaneo, Ashok Kumar, **M. Gola**, et al., "Performance of GE1/1 Chambers for the CMS Muon Endcap Upgrade", NIM A 972 (2020).

Scientific notes

1. **Detector Note**, "Layout and assembly techniques of the GEM chambers for the upgrade of the CMS first Muon End- cap Station", CMS DN-15-020.

2. **Detector Note**, "Performance of GE1/1 Chambers for the CMS Muon Endcap Upgrade", CMS DN-16-016.

3. **Internal Note**, "The GE1/1 Chamber Layout for the CMS Forward Muon Upgrade and its Assembly Technique", CMS IN-2019/006.

Award

1. Awarded with the **CMS Detector Award 2019** for demonstrating high standards of excellence and contribution to the Muon project in CMS. Mainly for major contributions to the GE1/1 GEM chamber assembly and quality control, including the development of procedures to characterize chamber performance.

Conference proceedings

1. **M. Gola**, "CMS Phase-II upgrade using GEM detectors" at MPGD 2019, La Rochelle, France; J. Phys.: Conf. Ser. 1498 (2020) 012054.

2. **M. Gola**, "Muon Chamber End-cap Upgrade of the CMS Experiment with Gas Electron Multiplier (GEM) Detectors and their Performance", Springer Proc. in Phy. 203 (2018) 591.

3. A. Shah, A. Kumar, **M. Gola** et al., A Novel Assembly Procedure of GE1/1 Detectors for CMS High Luminosity Phase of the LHC, Spring. Proc. in Phy., 203 (2018) 775.

4. S. Malhotra, **Mohit Gola**, et al., Various Studies with Gas Electron Multiplier (GEM) Detectors, Springer Proc.Phys. 203 (2018) 105.

5. R. Rizwan, **Mohit Gola**, et al., "Design and Development of Gas Leakage Station for Gas Electron Multiplier (GEM) Chamber", Springer Proc.Phys. 203 (2018) 889.

Conference/Workshop attended

1. Presented a talk on "Delhi University GE2/1 production site readiness"; 24th CMS GEM workshop at CERN, Geneva from 30th September to 4th October 2019.

2. Presented a talk on "Stability test performed on commercially manufactured GEM foils in India" at IPRD2019, Italy, Siena from 14th-17th October 2019.

3. Presented a talk on "CMS Phase-II upgrade using GEM detectors" at MPGD 2019, La Rochelle, France from 5th-10th May, 2019.

4. Presented a poster on "Characterization of first GEM foils and triple- GEM detector developed in India", at MPGD 2019, La Rochelle, France from 5th-10th May, 2019.

5. Presented a talk on "Update on QCs performed on GEM Foils produced in India"; 22nd CMS GEM workshop at CERN, Geneva, from 18th-22nd June 2018.

6. Presented a talk on "Muon Chamber End-cap Upgrade of the CMS Experiment with Gas Electron Multiplier (GEM) Detectors and their Performance" at XXII DAE-BRNS HEP Symposium held at University of Delhi, India from 12th-16th December, 2016.

7. Attended XIV GEM Upgrade Workshop, held at CERN, Geneva from 18th-22nd July, 2016.

8. Attended X SERC School on Experimental High Energy Physics, held at University of Delhi from 19th April to 9th May, 2016.

9. Attended "Using the Physics Analysis Toolkit (PAT) in your Analysis", International School held at CERN, Geneva from 29th June to 3rd July, 2015.

The Compact Muon Solenoid Collaboration

confers on

Mohit Gola

University of Delhi

a

CMS 2019 Detector Award

for

major contributions to the GE11 GEM chamber assembly and quality control, including the development of procedures to characterize chamber performance

The Collaboration Board Chairperson
(Harrison B. Prosper)

The Experiment Spokesperson
(Roberto Carlin)

February 3rd, 2020

For

My Loving Parents

&

My Brother

Acknowledgments

This Ph.D. thesis represents not only my work else it is the accumulated knowledge, wisdom, and experience which I have gained over the years. This thesis would not have been that simple without the help and support of a few people whom I would like to thank and acknowledge that without whom I would not have been able to complete this.

Firstly, I'd like to express my deepest gratitude to my supportive boss Dr. Ashok Kumar, for being the most friendly supervisor. Your support, guidance, and overall insights in this field have made this an inspiring experience for me. I whole-heartedly appreciate your persistent help, long hour discussion, and your incredible amount of faith in my ability that became a benchmark of my Ph.D. Without your practical suggestions, helpful advice, and constructive criticism: - the goal of this project could have been not fulfilled.

I'm deeply indebted to Dr. Md. Naimuddin, the professor of our research group who is an astonishing person from numerous points of view. I still remember my first interaction with you when I started learning about the gaseous detectors, and from that point, you have played a crucial role in being my mentor. I am fortunate that I have got an opportunity to work under your supervision. The long and meaningful discussion we had over numerous topics were vital in inspiring me to think out of the box. You have always been a source of energy ever since we have started having discussions (at DU or CERN) during my Ph.d. and it has shaped me well into a great physicist. I also wish to express my deepest gratitude to other professors in our research group: - Prof. Brajesh Choudhary, Prof. Kirti Ranjan, and Dr. Ashutosh Bhardwaj. I whole-heartedly appreciate your great advice which proved monumental towards the success of this thesis.

The work reported in this thesis has been carried out partially at CERN as well as at DU, which was not possible without the India-CMS collaboration, which provided me an amazing platform for demonstrating my research, and I am deeply thankful for that. I would like to pay my special regards to funding agencies like DAE-DST and UGC, which helped me monetarily throughout my Ph.D. without their support and funding, I could not have reached my goal.

I am thankful to Dr. Archana Sharma, and I incredibly value the support she has offered me during my Ph.D. I praise the enormous amount of her help in arranging the things I needed for my research.

I would like to extend my deepest gratitude to Dr. Shivali Malhotra, now at Texas A&M University (TAMU), for the work which we have done together at DU lab. It has been an extremely incredible experience to work with you. Also, thanks for the sparkling and extraordinary memories which we have shared, and I appreciate the honest and insightful feedback which you have offered me from time to time.

From the bottom of my heart, I would like to thank my colleagues for their support at the University of Delhi: - Dr. Ajay Kumar, Dr. Daljeet Kaur, Dr. Varun Sharma, Dr. Rocky Bala Garg, Aman Phogat, Asar Ahmed, Priyanka Phogat, Arjun Chettri, Prajesh Sharma, Mohd. Rafiq, Rizwan, and Hemant. Likewise, my thanks to colleagues at CERN- Dr. Michele Bianco, Dr. Jeremie Merlin, Marek Gruchala, Aamir Irshad, Mohsin Abbas. I would like to recognize Dr. Aashaq Shah, Mahesh, Bhumika & Israr for the proof-reading of my thesis and their significant input. I must say thanks to the lab staff Md. Younus, Aamir Hussain, and Pradhan Ali for their help.

A huge amount of gratitude also goes to my flat mates: - Hasib, Mehar, Tahir, Aamir & Bilal. The time which we spent together at CERN was the experience of a lifetime. Your affirmation through this period is beyond any words, and your friendship is irreplaceable.

A special thanks to my elder brother Nitin Kumar Gola, who is an amazing person in too many ways. He has always helped me in clearing the doubts regarding the electronics. His consolidated support, backing, and appreciation always helped me to remain focused on my work. You have been always like a brother cum friend for me. I would also like to thank my sisters Sheetal and Neha for their love and affection. I also express profound gratitude to Ragni Singh for all the help and support.

I don't know how to express my gratitude for my parents without whom it wasn't possible to achieve this goal. Their love and support have always been unconditional to me. Thank you for teaching me good things in life and shaping me into a person

whatever I am today. Your patience and sacrifice will consistently be an inspiration for my whole life.

Date:

Place: Delhi   Mohit Gola

Abstract

The research in this thesis is mainly based on the physics analysis and the upgrade of the muon system of Compact Muon Solenoid (CMS) experiment at the Large Hadron Collider (LHC). In physics analysis, it consists of the associated production of the dark matter with Higgs boson decaying to pair of bottom quarks. On the detector contribution, it includes the production and testing of Gas Electron Multiplier (GEM) detectors for the CMS upgrade. In addition to this, it includes the extensive R&D on the India made GEM foils and advanced tests performed on these foils.

There is a necessity of evolution in detectors to progress in Elementary Particle Physics. Starting from the Multiwire Proportional Counter (MWPC) invented by G. Charpak in 1968 which consists of thin anode wire sandwiched between the two cathodes. Despite their long term use in nuclear and particle experiments, it has some limitations, mainly shows the reduction in gain for the incoming flux of $\sim 10^4$ mm^{-2}. To get rid of this limitation in rate handling capacity, in 1968 the Micro Strip Gas Chamber (MSGC) is developed by A. Oed, consists of adjacent cathode and anode strips. It gives two orders of magnitude better rate handling capacity with respect to MWPCs but it faces the destructive discharges which is leading to the irreversible damages. To overcome this issue a concept of multi-level amplification was introduced by F. Sauli, in which the amplification layers are operated at the gain far below the discharge limit. Using the same concept, a Gas Electron Multiplier (GEM), consists of polymer ($\sim 50\ \mu m$) coated both sides with metallic surface ($\sim 5\ \mu$m) has been invented.

The LHC is the most powerful and world's largest particle accelerator to date having four collision points, out of which, CMS is one of the general-purpose detectors. To extract the new physics at the LHC, it requires the upgrade of the detector elements to cope up with the harsh radiation environment. The LHC will be upgraded in several phases that will allow significant expansion of its physics program. The

final luminosity of the accelerator is expected to exceed $5 \times 10^{34}\mathrm{cm}^{-2}\mathrm{s}^{-1}$, five times more than the original design value. The forward region of the CMS muon system consists of Cathode Strip Chambers (CSCs) and the degradation in the performance of these chambers with time will ruin the Level-1 (L1) trigger efficiency. To cope with the corresponding increase in background rates and trigger requirements, the installation of additional sets of muon detectors based on GEM technology, referred to as GE1/1, GE2/1 and ME0, has been planned. The installation and commissioning of the GE1/1 chambers is ongoing, while the GE2/1 and ME0 detectors are expected to be installed between the years 2022 and 2024. Before the installation of these chambers, a detailed quality controls (QCs) procedure has been set up and described in great detail in this thesis. Also, the description of the GE2/1 and ME0 upgrade is included for the sake of completeness.

Out of several QCs designed to validate the detector for CMS muon chamber upgrade, gain uniformity of the detector is one of the major tests since it is an important parameter of any gaseous detector. To overcome the limitation of doing gain uniformity sector-by-sector, a new readout system is designed by RD51 known as a Scalable Readout System (SRS), and later opted by CMS GEM collaboration for the quality assurance of the GEM detectors. Which consists of APV25 front-end chip with 128 readout channels connected to the readout board of the detector. It is important to quantify the non-uniformity present in the channels of ASIC in order to disentangle with the non-uniformity of the detector. Also, due to big size ($\sim$1 m) and no spacers present in the middle of the detector, there is a finite probability of the bending in the readout PCB which may results in the non-uniformity in the induction gap[1]. A novel technique has been developed to observe the possible bending in the readout board/induction gap.

Furthermore, the increasing demand for GEM foils has been driven by their application in many current and proposed High Energy Physics (HEP) experiments. Keeping in mind the demanding GEM foil production process, the commercialization of GEM foils has been realized and established for the first time in India by Micropack Pvt. Ltd., a Bengaluru based company. However, it's a long and laborious effort to validate the foils delivered by these companies to claim that the GEM detectors made from them are compatible with high scientific standards. An extensive

[1]It is important to check the flatness of the induction gap because the signal formation particularly takes place in this region.

R&D has been performed on the different set of foils including single and double mask samples produced by the company.

An important part of the Ph.D. work includes the search for the dark matter candidate at LHC. The search was based on the assumption that if non-gravitational interaction occurs between dark matter and standard model particle, the search of dark matter like a candidate is feasible at the LHC energy scale. Such topologies are known as mono-X searches, where X (=g, q, γ, Z, W, or Higgs boson) is the standard model particle. The production of standard model particle is either due to Initial State Radiation (ISR) or due to new vertex couplings. For Higgs boson, ISR is highly suppressed hence the mono-h channel is only due to the direct coupling of dark matter with standard model particle. The data collected using proton-proton collisions at center of mass energy ($\sqrt{s}$) of 13 TeV in the year 2015, corresponds to an integrated luminosity of 2.3 fb^{-1}. The Higgs boson decaying to a pair of bottom quarks with missing transverse energy in the final state has been studied. Finally, the results were interpreted using two-Higgs Doublet Model (2HDM).

Contents

List of Figures

1

Thesis layout

> *"Nothing in life is to be feared, it is only to be understood. Now is the time to understand more, so that we may fear less."*
>
> – Marie Curie

The CMS detector has produced many excellent particle physics results which include the discovery of the Higgs particle. The discovery of Higgs leads to the properties measurement of this unique particle, the existence of the dark matter, and supersymmetric particles. and their detection probability at LHC. During my Ph.D. we tried to search for the associated production of dark matter with a Higgs boson decaying to a pair of bottom quarks. Starting from the generator level studies for the measurement of branching ratio and cross-section using the MadGraph generated data. The data from proton-proton collisions at center of mass energy ($\sqrt{s}$) of 13 TeV, collected in 2015 with the CMS detector at the LHC, correspond to an integrated luminosity of 2.3 fb^{-1} was used and results are interpreted in the context of a Z'-two-Higgs-doublet model.

The LHC requires time-to-time upgrades to explore the hidden sector of fundamental physics. This results in the harsh environment on the detectors mainly in the forward region and hence impose the necessity of the detector upgrades, the muon chamber upgrade of the CMS experiment is one of the major upgrades. The CMS GEM community will be installing trapezoidal shape triple-GEM detectors in the forward region of the muon station. In the decades of past years, it has been demonstrated that these detectors can be used in the high rate environment without any loss in the performance. After the extensive R&D of several years, these detectors are going to be installed at the different courses of time to increase the reconstruction efficiency of the Muons.

Nowadays, the GEM technology has been used by many nuclear and particle experiments and their upgrades, due to the excellent spatial resolution, high rate capabilities, etc. Till now CERN was the only distributor of the GEM foils, but with the technology of transfer, few other industries across the globe have started manufacturing these foils employing the same photo-lithographic technique.

Chapter 1 is a prologue that provides a general overview and thesis layout.

Chapter 2 gives an overview of the evolution of the gaseous detectors which describes the advantages and disadvantages of the technology. Along with this, it explains in detail the geometric parameters of the GEM. It also describes the properties of the GEM detectors and their use in the CMS muon chamber upgrade.

Chapter 3 explains the optimized design of the full-size GE1/1 detectors for the upgrade of the CMS muon end-caps. A precise Quality Controls (QCs) procedure has been established in order to validate these detectors before installing them in CMS cavern. The first half of this chapter explains the assembly and QCs procedure and their setups. In total 144 chambers are going to be installed during the Long-Shutdown 2 (LS2) out of which 16 chambers were tested and delivered by Delhi University (DU). We will show the facility built at DU and the total number of detectors assembled ans their results. The second half of this chapter deals with an overview of future upgrades of CMS muon spectrometer. We present the detailed description of GE2/1 and ME0 upgrades expected to be installed in 2022 and 2024 in terms of design, pre-production chambers, mechanics, installation services, etc.

Chapter 4 describes the necessity of local production of GEM foils in India. GEM has been utilized for various applications and CERN has been the sole supplier of the GEM foils until recently when few private companies started manufacturing GEM foils under the transfer of technology (TOT) from CERN. However, it's a long process to validate the foils delivered by these companies to claim that the GEM detectors made from them are compatible with high scientific standards. An India based company Micropack Pvt. Ltd. began fabricating both double and single mask GEM foils. This chapter describes in detail the production and testing of double mask foil as well as single mask technique requirements. Starting from a 10 cm $\times$ 10 cm GEM foil manufactured with double mask etching technique has been tested for optical inspection and all the QCs along with the advanced studies. The double mask etching technique limits the maximum size of the GEM hence requires a new etching procedure known as a single mask technique. Micropack produced the first batch of 30 cm $\times$ 30 cm single mask foils in a joint effort with DU. A triple-GEM detector was constructed using these foils to test for the fundamental quality controls and for a few advanced studies.

Chapter 5 is proposing and exploring the use of multichannel readout electronics, already used in quality assurance for gain uniformity studies of GE1/1 detectors, to measure the uniformity of the induction gap in GEM based detectors. The measurement will furthermore provide a qualification of the readout electrodes in terms of disconnected or shorted channels. The proposed method rely on the indirect measurement of the capacitance between the readout strips and the bottom of the last GEM foil. The measurement is obtained pulsing the bottom of the GEM foil and measuring the amplitude of the signal in the readout electrodes. In this work, the signals are read with the analog APV25 front-end chip and the RD51 SRS. A detailed description of installation and commissioning of SRS has been discussed. Also, the studies on small and large area triple GEM detector, relative variations under mechanical stress and in presence of standard electrical fields, defects in readout electrodes will be presented in this chapter.

Chapter 6 this chapter dedicated to a search for dark matter which is performed looking for events with large missing transverse momentum and a Higgs boson decaying either to a pair of bottom quarks or to a pair of photons. Results are interpreted in the context of a Z'-two-Higgs-doublet model, where the gauge symmetry of the standard model is extended by a $\mathrm{U}(1)_{Z'}$ group, with a new massive Z' gauge boson, and the Higgs sector is extended with four additional Higgs bosons. In this model, a high-mass resonance Z' decays into a pseudoscalar boson A and a light SM-like scalar Higgs boson, and the A decays to a pair of dark matter particles. No significant excesses are observed over the background prediction. Combining results from the two decay channels yields exclusion limits in the signal cross-section in the $m_{Z'} - m_A$ phase space. For example, the observed data exclude the Z' mass range from 600 to 1860 GeV, for Z' coupling strength $g_{Z'} = 0.8$, the coupling of A with dark matter particles $g_\chi = 1$, the ratio of the vacuum expectation values $\tan\beta = 1$, and $m_\mathrm{A} = 300$ GeV. The results of this analysis are valid for any dark matter particle mass below 100 GeV.

Chapter 7 is an epilogue that summarizes the contributions of this Ph.D. project to the CMS muon upgrade. It also sums up the results of R&D and the outcome of physics analysis performed throughout the tenure of this work.

2

Introduction to gaseous detectors

"Your imagination is your preview of life's coming attractions."

– Albert Einstein

This chapter deals with the basic phenomena of interaction of charged and neutral particles with the matter. In the past, many gaseous detectors have been invented using such technique. A history of gaseous detectors starting from the wire chambers has been discussed. Finally, the properties and parameters of the Gas Electron Multiplier (GEM) is well explained.

2.1 Interaction of radiation with matter

Radiation contains two types of particles; charged particles (e.g. electron, proton, muon, alpha particle, and other heavy charged ions) and neutral particles (e.g. photons, neutrons, etc). This section describes the interaction of both charged and neutral particles with matter [**1**, **2**].

2.1.1 Interaction of charged particles with matter

Charged particles interact with matter primarily through coulomb forces. They interact directly with the orbital electrons of the absorber atom. There can be an interaction of the incoming charged particles with the nucleus of the absorber atom as well. All these interactions with the charged particle lead to either excitation (raises the electron to a higher-lying shell within the absorber atom) or ionization (remove completely the electron from the atom) of the atoms of active medium in the detector.

When an energetic charged particle traverse the active volume, a number of ionizing interactions take place along its path, resulting in the creation of primary electron-ion pairs. The electron ejected from the shell of interacting atom or molecule have enough energy to surpass the ionization potentials of the elements present in the gas mixture, thus creating more electron-ion pairs. The electron-ion pairs thus created by the electrons ejected from the interacting atom produce the secondary ionization [**3**].

Charged particle lose their energy in a large number of discrete interactions with the detection medium [**4**]. For charged particles, the linear stopping power $S(E) = -\frac{dE}{dx}$ is defined as the loss of energy E per unit length "dx" due to excitation and ionization. The average differential energy loss per unit length is described by Bethe-Bloch formula

$$-\frac{dE}{dx} = \frac{4\pi e^4 z^2}{m_0 v^2} NZ[ln\left(\frac{2m_0 v^2}{I}\right) - ln(1-\beta^2) - \beta^2] \tag{2.1}$$

where e, m_0 are electron charge and electron rest mass respectively. Also, β is defined as $\beta = \frac{v}{c}$ where c is the speed of light. The incoming charged particle has a velocity v, charge ze. The absorbing atoms have an atomic number Z and number density N. I is the mean excitation ionization potential of the absorber and is determined empirically.

2.1.2 Interaction of photons with matter

Depending upon the energy numerous interaction mechanisms are possible for photon interactions, primarily three processes play an important role in radiation detection which are photoelectric absorption, Compton scattering, and pair production. All these processes lead to either complete or partial transfer of photon energy.

1. **Photoelectric absorption:**

   In this process, a photon interacts with an absorber atom in which the photon completely disappears and releases a photoelectron from one of the inner bound shell of the absorber atom, as shown in the Figure 2.1. This interaction is with the atom as a whole and can not take place with the free electrons. The most probable origin of the photoelectron is the most tightly bound K shell of the atom. If a photon with an energy of $h\nu_0$ interacts with an atom then the energy carried by the emitted photoelectron is derived as

$$E_{e-} = h\nu_0 - E_b \tag{2.2}$$

where E_b represents the binding energy of the photoelectron in its shell. This equation also sets a limitation on the energy of incoming photon i.e. $h\nu_0$ must be greater than the binding energy of the electron in the shell.

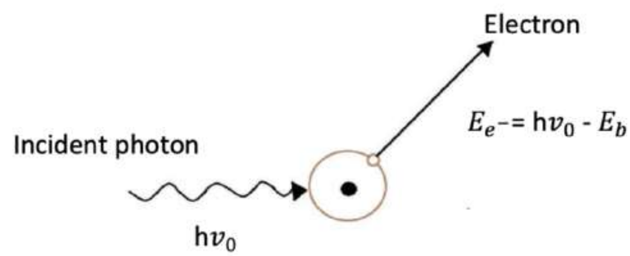

Figure 2.1: Shows the photoelectric absorption process.

For gamma or X-rays of relatively low energy interact mainly through the photoelectric process. A material with high atomic number Z makes this process more enhanced. The probability of photoelectric absorption per atom depends upon the photon energy and the atomic number Z of the absorber and is roughly have proportionality relation as

$$\tau \propto \frac{Z^n}{E_\gamma^{3.5}} \tag{2.3}$$

where the exponent for the gamma-ray energy region of interest can take a value between 4 and 5.

2. **Compton scattering:**

   In this process, the incoming gamma-ray photon interacts with the electron in the absorbing medium. A photon transfers partial energy to the electron, and hence the photon as well as electron scattered with different angles respect to its original direction. The energy transfer to the electron depends upon the angle of the scattering of the photon which can vary from zero to a large value. The equation which relates the energy transfer of the photon to the electron is simply obtained by the energy and momentum conservation according to the image shown in the Figure 2.2.

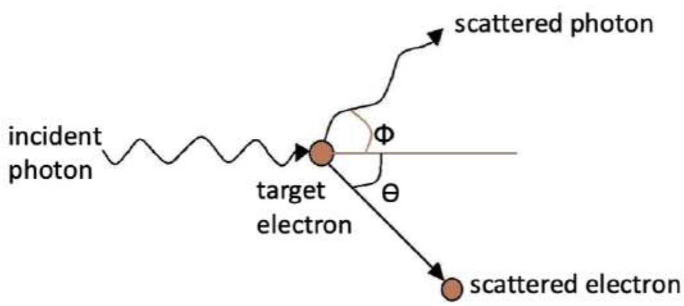

Figure 2.2: Shows the Compton scattering process.

Consider an incident photon of energy $h\nu$ interacts with an electron having rest mass m_0. The photon scatters at an angle ϕ with respect to the original direction with the transfer of a portion of its energy to the electron. The electron recoils through an angle θ with respect to the direction of the incoming photon. The equation of the energy of a scattered photon is given by

$$h\nu^{'} = \frac{h\nu}{1 + \frac{h\nu}{m_0 c^2}(1 - cos\phi)} \tag{2.4}$$

where c is speed of light. The energy transferred to the electron is given by

$$E_{e-} = h\nu^{'} - h\nu. \tag{2.5}$$

The maximum energy is transferred by a photon to the electron when it scatters at an angle of 180°, and no energy is transferred when it passes without interaction i.e. at 0° angle. The probability of Compton scattering increase linearly with Z i.e. the number of electrons available at the scattering target. The Klein-Nishina formula for the differential cross-section $\frac{d\sigma}{d\Omega}$ describes the angular distribution of scattered gamma-ray photons as

$$\frac{d\sigma}{d\Omega} = Zr_0^2 \left(\frac{1}{1 + \alpha(1 - cos\phi)}\right)^2 \left(\frac{1 + cos^2\phi}{2}\right) \left(1 + \frac{\alpha^2(1 - cos\phi)^2}{(1 + cos^2\phi)(1 + \alpha(1 - cos\phi))}\right) \tag{2.6}$$

where $\alpha = \frac{h\nu}{m_0 c^2}$ and r_0 is the classical electron radius.

3. **Pair production:**

   The process of production of electron and positron pair from a gamma-ray photon in the vicinity of the nucleus is called pair production. This reaction is only energetically possible when the energy of the gamma-ray photon is at least twice the rest mass energy of the electron (1.022 MeV). All the excess energy carried by the photon above the 1.022 MeV converts into kinetic energy shared by the positron and electron. Normally two annihilated photons produced in the slowing down process of the positron as a secondary product of their interaction as shown in the Figure 2.3.

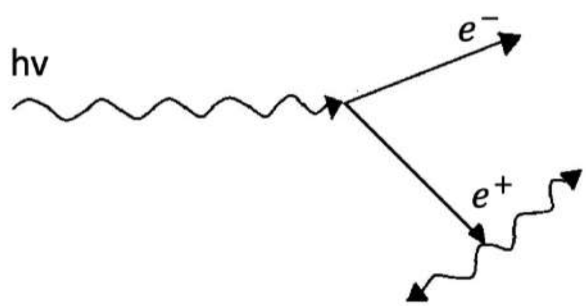

Figure 2.3: Shows the pair production process.

   The probability of pair production increases with the increase in the incoming energy of the incident gamma-ray photon as well as varies approximately as the square of the atomic number of the absorber.

The variation of the probability of all the three processes with different energies of photons and atomic number of absorber atoms is shown in the Figure 2.4.

2.2 History of gaseous detectors

Most of the earlier and widely used gaseous detectors work on the principle of detection of charge produced in the gas medium when radiation passes through it. In all types of gas detectors generally three process predominantly takes place:

- Ionization of gas medium.

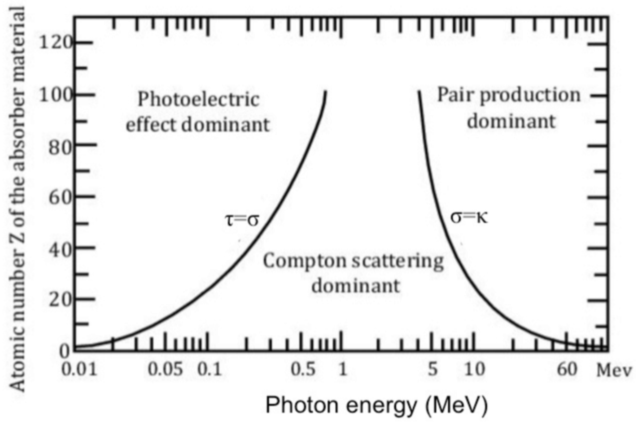

Figure 2.4: Shows the probability of different processes of photons with varying energy [**1**].

- Gas multiplication.
- Collection of the charge particles across anode and cathode.

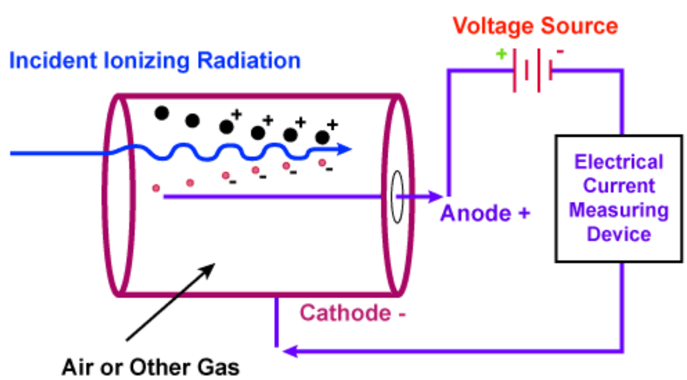

Figure 2.5: Shows the example of gas detector [**1**].

Figure 2.5 shows a single wire proportional counter consists of a cylindrical cathode and a few order of micrometer thin anode wire mounted along the axis of the cylindrical geometry. Cathode and anode are enclosed in a gas-tight volume filled with the counting gas. The electric field in the detector tube is given as

$$E(r) = \frac{V}{rln(\frac{b}{a})} \tag{2.7}$$

Where V is the voltage applied between anode and cathode, a is the anode wire radius, and b is the cathode inner radius. Gas multiplication requires a sufficient amount of electric field. For an anode radius a = 0.005 cm, cathode inner radius b

= 1.0 cm and applied voltage V = 1000 V; one can get an electric field 3.03 V/m; which is enough to get multiplication in the gas for the desired amplification gain.

2.2.1 Multiwire Proportional Counters (MWPCs)

MWPC [**5**, **6**] extends the principle of single wire proportional counter. It consists of a series of equally spaced anode wires sandwiched between two cathode plates as shown in the Figure 2.6. Typical wire spacing is 2 mm with an anode-cathode gap that varies between 7 mm to 8 mm. MWPC provides better spatial resolution as it contains more number of anode wires in the same region as compare to single wire proportional counter.

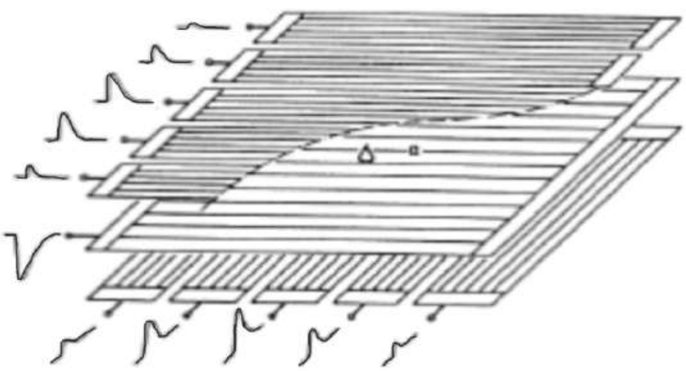

Figure 2.6: Shows the image of a multiwire proportional counter [**1**].

A plot of the electric field lines created by a grid of anode wires (running perpendicular to the plane of the paper) that are placed equidistant between two parallel cathode plates at the top and bottom as shown in the Figure 2.7. The field is uniform away from the grid and a high field region is created in the immediate vicinity of each grid wire. Near the anode wire field varies as $\frac{1}{r}$ i.e. the distance from the wire.

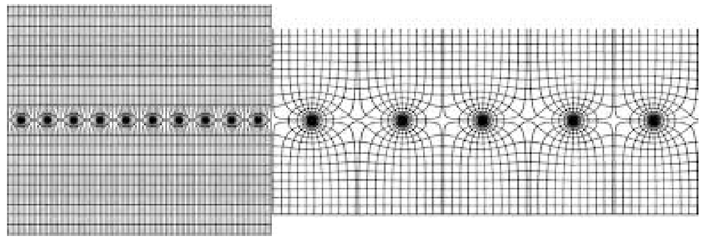

Figure 2.7: Shows the electric field lines in MWPC [**1**].

Upon reaching the high field region, the electrons created in the medium by radiation quickly get accelerated to form an avalanche. An interaction near to the anode induces a signal on the nearest wire helps in attaining the good spatial resolution. MWPC is also used for measuring the trajectory of the incoming particle, known as MWPC telescope shown in the Figure 2.8. Reading the positions of the signal wires allows better track reconstruction. An additional capability of MWPC is multi-track resolution [**7**]. Since each wire work as a separate detector, two or more hits could be detected per track. The MWPC is a relatively fast detector and can be used for the timing applications. The timing resolution for a typical 2 mm wire spacing is found to be about 25-30 ns.

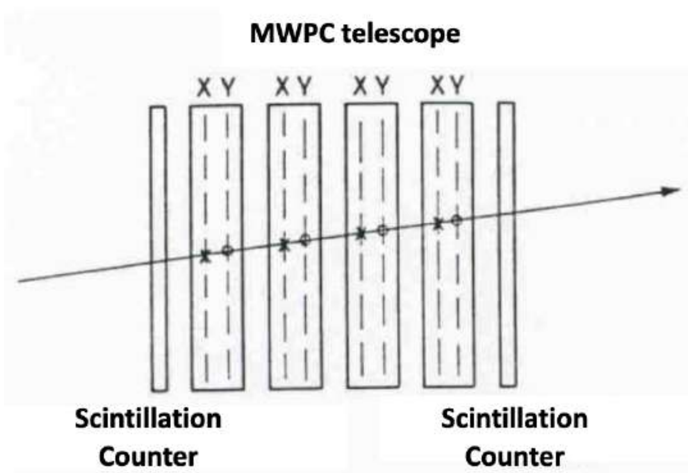

Figure 2.8: Shows the MWPC telescope for particle tracking. Each MWPC contains an X and Y wire plane [**7**].

MWPC works on a constant applied voltage however it is difficult to maintain a constant voltage across the wires. The wires should be tight enough, and any kind of wave or distortion in the wire alters the electric field between them and as a consequence it affects the gain of the detector. A high voltage always runs across the wire due to which it is very difficult to place in very close proximities. The wires should be placed far enough to avoid the sparks between them and hence it limits the spatial resolution in MWPCs. For a 2 mm diameter wire gap detector, the maximum attained spatial resolution is about 0.5 mm. Another disadvantage of MWPC is the formation of charge cloud in the active volume of the detector. As the drift velocity of positive ions is much less than the electrons, positive ions start making a cloud in the gas region which reduces the electric field on anode wires and affects the multiplication process.

2.2.2 Micro Pattern Gas Detectors (MPGDs)

In the early 1990s, techniques such as photolithography, selective etching, and laser machining began to apply in designing more sophisticated gas-filled devices classified under the category micropattern gas detectors [**8**]. They have fine-scale detail in their structure and at the readout stage that help in achieving a spatial resolution of the order of few micrometers which is very useful in particle tracking or radiation imaging applications. There are many types of detectors which comes under the class of MPGDs, some of them are discussed here.

2.2.2.1 Micro Strip Gas Chamber (MSGC)

To reduce some limitations of MWPCs a multi anode gas-filled detector was first proposed by Anton Oed in 1988. MSGC [**9**, **10**] contains an insulating substrate on which metallic electrodes are formed by etching techniques. An example of a resulting pattern of anode strip (also called as micro gap) is shown in the Figure 2.9. In MSGCs the anode strips are placed close to each other (few microns) so that high electric field can be generated, very much similar to the anode wires in the case of MWPCs. Comparable to the standard proportional counters the avalanche formation occurs near to the anode strips in the MSGCs as well. The region between the drift plane and the anodes is filled with the multiplication gas, and the ionization due to the incoming radiation occurs in this volume.

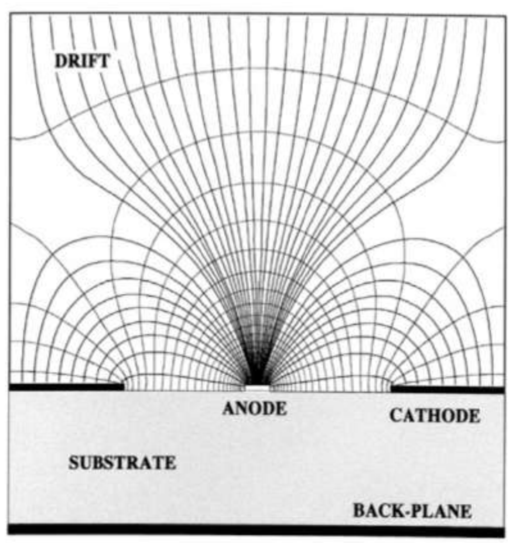

Figure 2.9: Shows the pattern of anode for MSGC [**10**].

Etched metallic strips provide an advantage over wires as it helps in achieving a better spatial resolution compared to the MWPCs. Another advantage of MSGCs is that most of the positive ions generated in the process of avalanche quickly mitigates to the cathode instead of drifting to higher distances towards the cathode as in MWPCs as shown in the Figure 2.10.

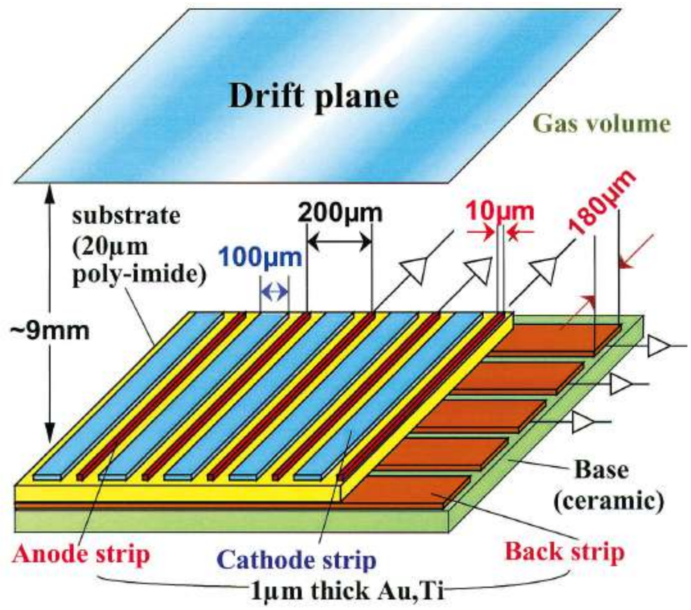

Figure 2.10: Shows the image of MSGC [**1**].

In MSGC alternating anode and cathode strips are supported on an insulating substrate which also collects some positive charge formed near the surface which leads to a possible buildup of surface charges. This buildup of charges causes voltage instabilities and distortion of the electric field. Another disadvantage is the lower gain of the detector which is limited by the maximum voltage that can be applied. Applying a higher field between cathode and anode strips results in the occasional but irreversible discharges that could physically damage the structure of the electrodes and may cause permanent damage to the detector.

2.2.2.2 Gas Electron Multiplier (GEM)

To detect the low ionization events the detector has to be exposed with high fields and that makes MSGCs operation difficult due to fragile electrodes operated at high voltages. The major limitation of the earlier detectors was to achieve the high gains for which one need to operate the detector at very high voltage that may lead to the discharges.

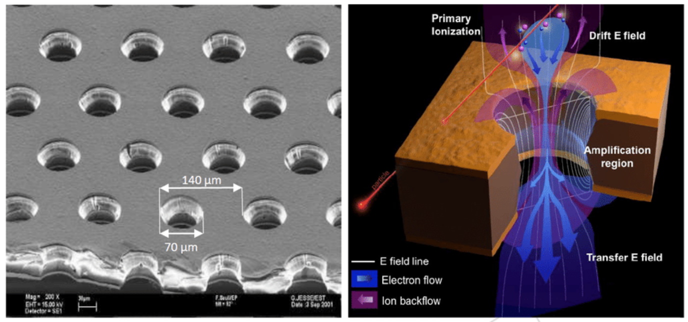

Figure 2.11: Shows the cross-sectional view of the GEM [**11**].

To overcome these difficulties a multi-stage amplification, each working on a gain far below the discharges has been designed. Using the same concept, GEM detector [**11**, **12**] was introduced, having a similar principle for the detection of radiation but working on fields not enough to provoke the discharges. GEM is a thin PCB like sheet (typically 50 micron) of insulating material (Kapton) with both surfaces coated with the thin layer of conducting electrode ($\sim$ 5 micron). A regular pattern of holes on the GEM foil are produced through chemical etching or other micro-fabrication processes. The size of the holes is nearly 70 μm with a pitch of 140 μm as shown in the Figure 2.11.

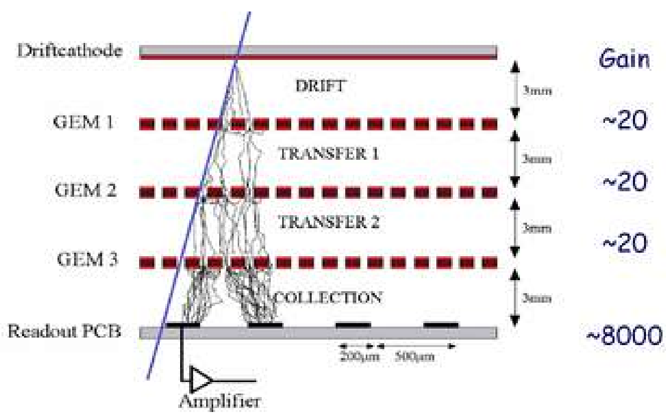

Figure 2.12: Shows the pictorial representation of triple-GEM detector [**11**].

The GEM detectors can reach up to a gain of 10^4 by cascading the GEM foils and each of them working at a potential difference of less than 500 V. A schematic diagram of the triple GEM detector is shown in the Figure 2.12. The GEM detectors have an excellent rate capability of $\sim$ MHz/mm^2, having a spatial resolution of $\sim$ 150 μm, and timing resolution of less than 10 ns, respectively. Also, it has no substrate material present as compared to MSGC, hence no bulk damage has been observed in the GEM detectors.

2.2.2.3 Micromegas

Micromegas or micro-mesh [**13**, **14**] gaseous structure is a modified version of a parallel plate avalanche chamber. The space between anode and cathode is divided into two volumes by a porous micromesh structure as shown in the Figure 2.13. The incident radiation creates electron-ion pairs in the volume between cathode and micromesh, then these electrons are forced to drift towards the mesh in the presence of an electric field for the multiplication. The gas volume region is around few millimeters, sufficient to create enough ion pairs for an incoming minimum ionizing particle making it detectable. Mesh is produced by micro-fabrication techniques and has a high transparency for these ionizing particles.

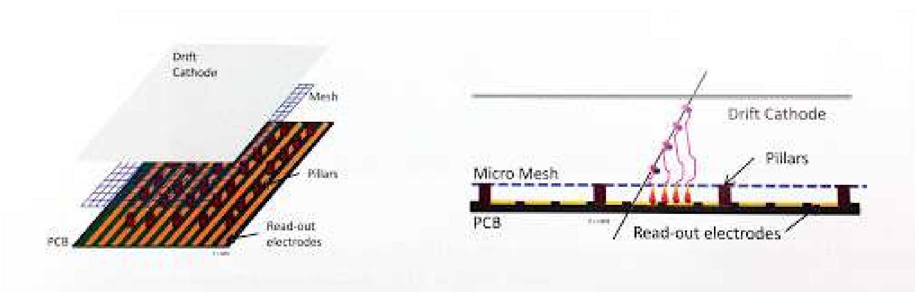

Figure 2.13: Shows the principle of a micromegas detector [**14**].

The region between mesh and anode is kept very small ($\mathcal{O}(100\ \mu m)$) so that reasonable applied voltage can produce a high electric field, which provides a gain between 10^3 and 10^4. This small gap between mesh and anode also helps in the formation of fast output pulse ($\mathcal{O}(ns)$). This small gap is normally accomplished by the use of insulating pillars or other support between the mesh and anode plane. If anode consists of position-sensitive strips or pixels, then the centroid of the avalanches that are formed can be spatially recorded. Under the favourable conditions a spatial resolution achieved varies between 10 to 15 μm.

2.3 CMS muon system

After discussing the history of gaseous detectors in great details this section is dedicated to the gaseous detector technology used in the muon system of the Compact Muon Solenoid (CMS) experiment at Large Hadron Collider (LHC) [**15**]. Figure 2.14 shows the accelerator system overview and CERN experiment along with the detectors subsystem of CMS experiment as shown in the Figure 2.15.

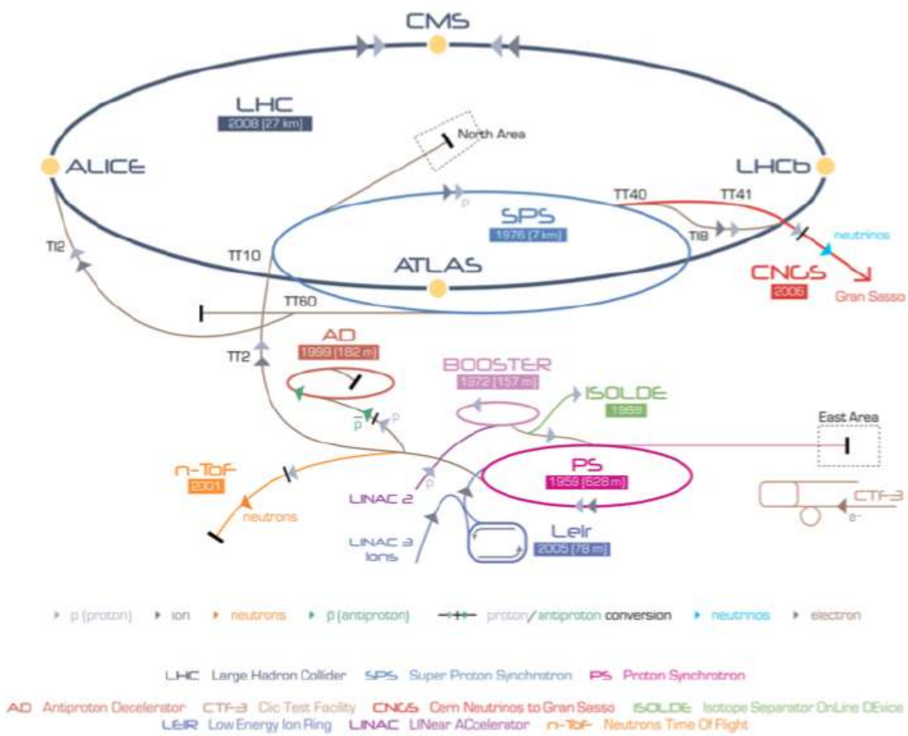

Figure 2.14: Shows the overview of the Large hadron Collider (LHC) [**17**].

It comprises of three different types of gaseous detectors namely Resistive Plate Chambers (RPCs), Drift Tubes (DTs), and Cathode Strip Chambers (CSCs) [**16**, **17**], all based on the principle of ionization produced in the gas volume due to incoming charge particle. Figure 2.16 shows the position of these detectors in the CMS muon system, and they are used for the particle triggering and tracking. The CMS muon system is divided into two parts: one is the barrel i.e. the cylindrical part and another is the end-cap or forward region i.e. the disk part.

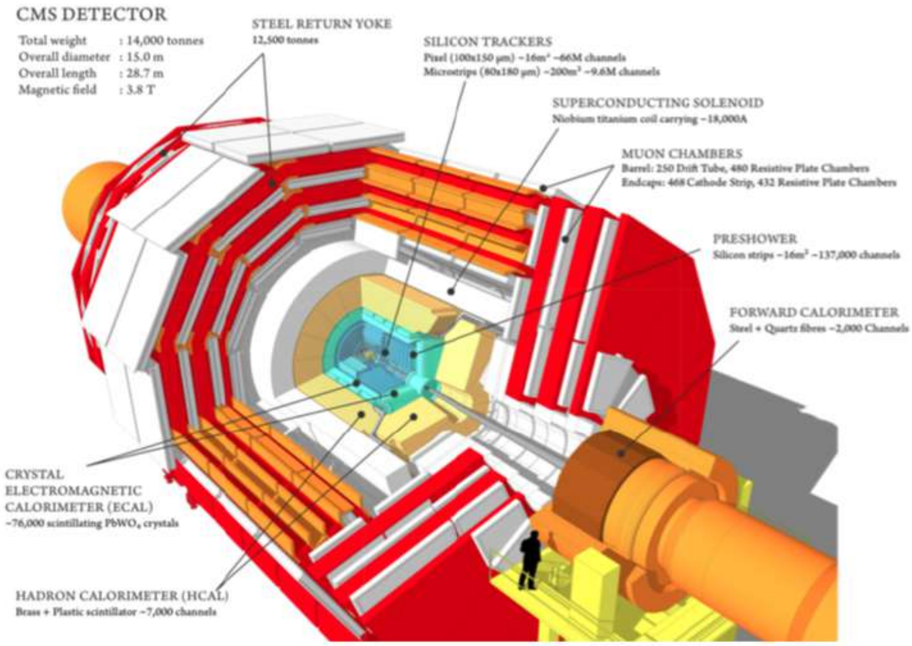

Figure 2.15: Shows the overview of the CMS experiment and its detector subsystem [**17**].

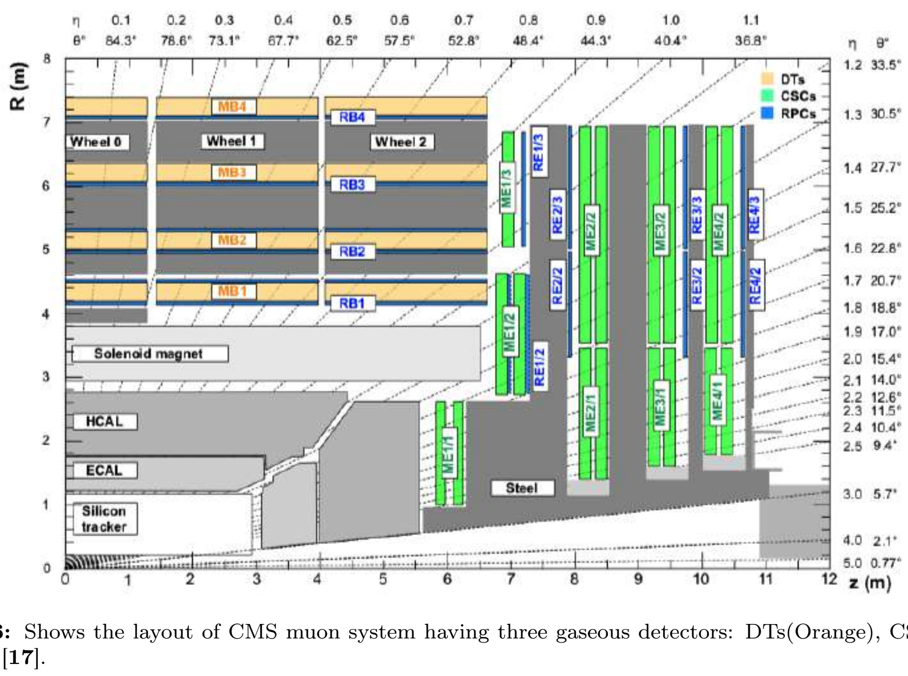

Figure 2.16: Shows the layout of CMS muon system having three gaseous detectors: DTs(Orange), CSCs(Green), RPCs(Blue) [**17**].

2.3.1 Drift Tubes (DTs)

The DTs [**18**] comes in an array of cells each having a dimension of 2.4 m long and 42 mm wide. Each cell contains an anode wire at the centre that stretched over the length, the traversing particle produces the clusters along its path. An image of the single DT cell is shown in the Figure 2.17.

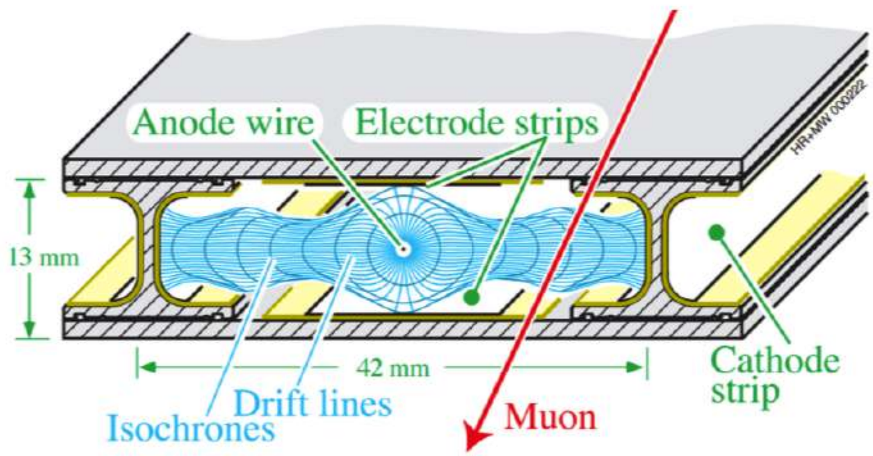

Figure 2.17: Shows the image of a DT cell highlighting the field lines along the anode wire [**17**].

A DT cell is filled with a gas mixture of Ar/CO_2 in a ratio of 85%/15% with an expected flux of 2 Hz/cm^2. The CMS muon system has in total 130 DT cells which corresponds to 172,000 active anode wires each with a diameter of 250 μm. The DTs are used for the muon tracking in the barrel region of the CMS muon system because these cells are grouped together in a staggered geometry to give a spatial resolution of the order of 100 μm.

2.3.2 Cathode Strip Chambers (CSCs)

The CSCs [**19**] having six gas gaps of trapezoidal shape with anode wires stretched radially, and perpendicular to cathode strips over the anode wires. The active area of the largest CSC is 3.4 $\times$ 1.5 m^2 and has an excellent rate capability. Due to this these chambers have been used in the forward region (end-cap disks) of the CMS muon system. The principle of CSC is to measure the co-ordinate when the traversing muon triggers the avalanche near the anode wires in the presence of the very high field as shown in the Figure 2.18. The CMS muon system have in total of 1000 CSC anode wires in three different rings of the disks. The spatial resolution of each CSC is varied between 100 μm to 200 μm and timing resolution of about $\sim$ 10 ns. They have good spatial resolution and hence used for a muon tracking in the forward region of CMS.

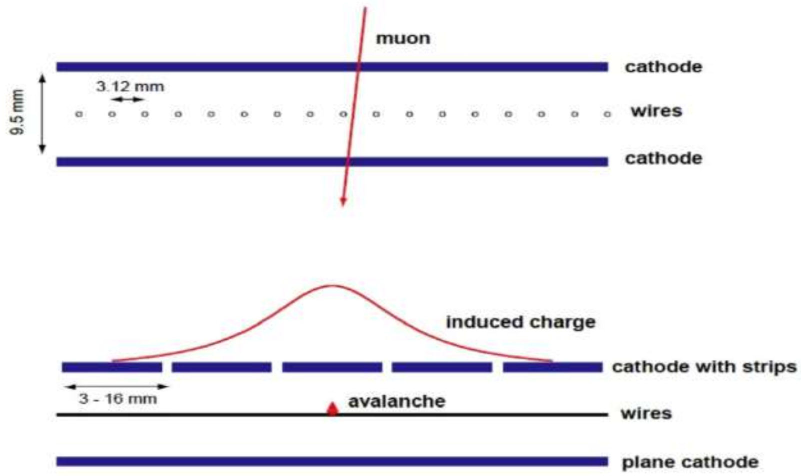

Figure 2.18: Shows the principle of CSC for plane cathode (top) and strip cathode (bottom) [**17**].

2.3.3 Resistive Plate Chambers (RPCs)

RPCs [**20**] are the only gaseous detector used for particle triggering in the CMS muon system so far, it contains a parallel plate structure filled with a gas mixture of 95.2% $C_2H_2F_4$, 4.5% $i - C_4H_{10}$, and 0.3% SF_6. They have excellent timing resolution of about 1 ns and reduced spatial resolution is of the order of mm, hence this detector technology is used for particle triggering in both barrel and end-caps region. Figure 2.19 shows the CMS RPC having two gas gaps covered with a readout with one dimension strips enclosed in the faraday cage.

Figure 2.19: Shows the layout of double gas gap RPC [**17**].

The RPCs can handle a rate of $\sim$1 kHz/cm^2 with a dimension of 2.455 m long and width vary between 1.5 m and 2.08 m. The CMS muon system have a total 1232 RPCs out of which 480 are in barrel and 756 in end-caps.

2.3.4 CMS high eta GEM upgrade

The LHC is heading towards a high luminosity [**21**] upgrade which will increase the instantaneous luminosity to about 5 times as compared to the present value. As a consequence, the particle flux will increase in the forward region of the CMS muon system up to several kHz/cm^2. Currently, the CMS muon system is only equipped with the CSCs in the end-cap region and hence becomes less efficient for the muon tracking and identification due to the increase in particle flux [**22**].

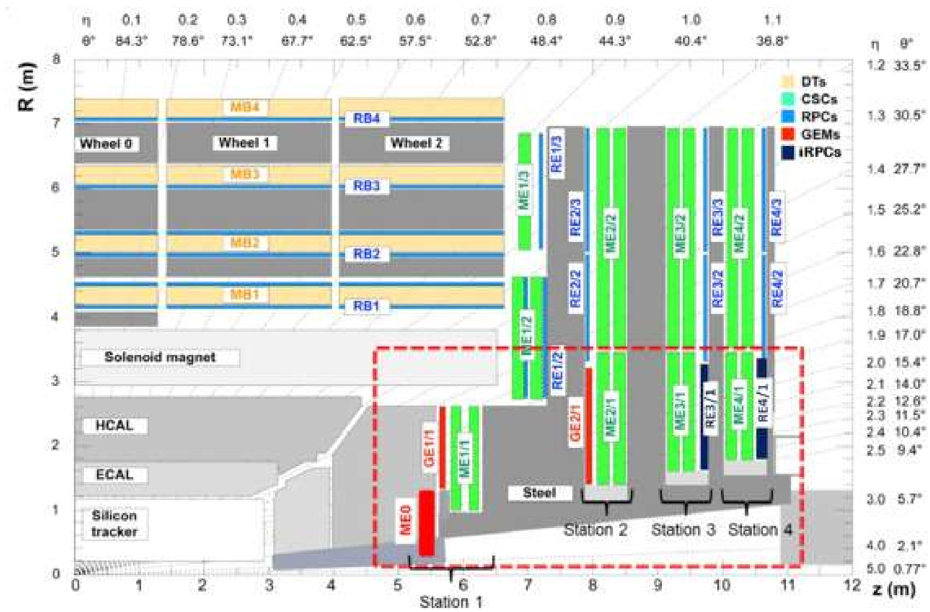

Figure 2.20: Shows the different upgrades of CMS muon system with GEM detectors [**17**].

Also, the RPCs present in the forward region for the muon triggering is limited to the rate handling capacity. To efficiently reconstruct the muons in the forward region a new layer of detector system will be required. The CMS muon collaboration has decided to install a new gaseous detector which will work both for triggering as well as tracking of the muons. The CMS muon collaboration has decided to install the GEM based detector in front of the CSC to increase the number of hits in the forward region of the CMS. Figure 2.20 shows the upgrades of the CMS muon system with GEM detector and chapter 3 gives a detailed description of these upgrades.

2.4 Parameters and properties of GEM

This section is dedicated to understand the influence of different parameters and few important properties of GEM foil as well as the detector. This thesis is based on the new look at the triple-GEM detector [**23**] and it is important to understand the effect of each parameter relevant for its performance such as the gap between the planes and the GEM foils, the field between and across the foils, collection and extraction efficiency of the foil, etc. Also, it is important to study the influence of these parameters on the overall working of the detector in the appropriate gas mixture.

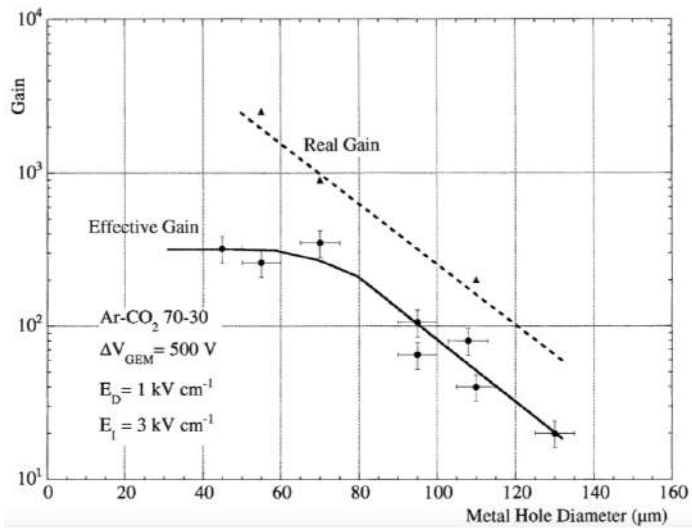

Figure 2.21: Shows the dependency of GEM foil gain on the hole diameter [**24**].

2.4.1 Influence of hole

It has been observed in the past that the hole diameter and shape has a direct impact on the gain of the GEM foil. A photolithographic technique has been used to produce these holes and a standard GEM foil is defined as the one having an outer diameter of 70 μm and an inner diameter of 50 μm. The earlier measurement of GEM foils shows that the hole diameter equal to the thickness of the foil results in the maximum gain. Making holes narrower compared to the thickness of the foil creates the higher field across it for a particular applied voltage. This impose the field lines to end-up on the bottom of the foil and results in the loss of electrons and hence the decrease in gain.

Figure 2.21 shows that a sort of plateau has been obtained for the hole diameter of 70 μm [**12**].

2.4.2 Influence of gap

In this thesis, a triple-GEM detector having a gap configuration of 3 mm / 1 mm / 2 mm / 1 mm for the Drift / Transfer1 / Transfer2 / Induction gap has been used. This gap configuration was first used by the Large Hadron Collider beauty (LHCb) experiment and then opted by the CMS experiment at the LHC to get the best timing resolution ($<$ 10 ns). To produce a sufficient amount of primary ionization a 3 mm of drift gap has been chosen. A higher transfer1 gap can ruin the timing resolution due to the bi-GEM effect and hence set to the 1 mm. Because the ionization produced in this gap will be multiplied by the subsequent two more GEM foils and can produce a signal in time before the signal coming from the drift region. A transfer2 gap has been set to 2 mm to maximize the transfer of charge on the top of the third GEM foil. An induction region where the signal formation takes place is set to 1 mm which is big enough to produce significant integrated charge without any discharges.

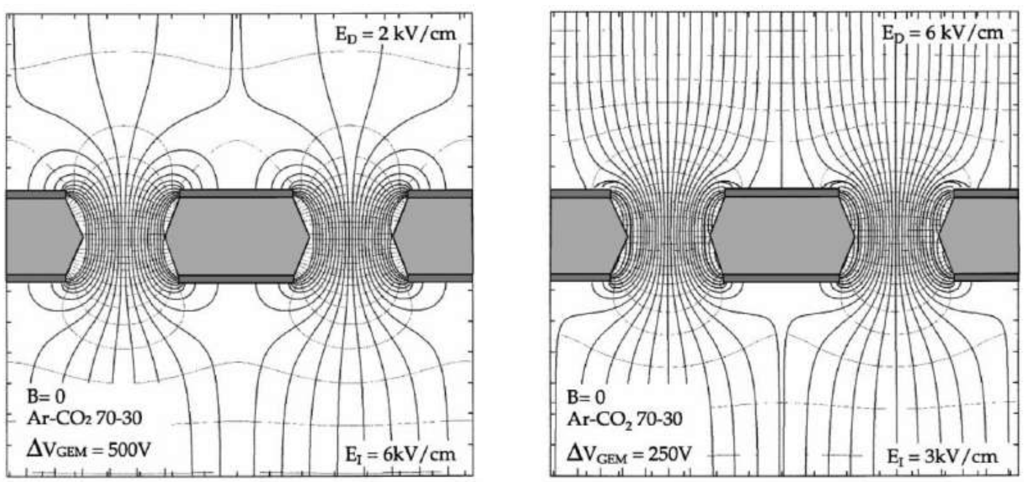

(a) (b)

Figure 2.22: Shows the influence of (a) lower, and (b) higher drift field [**24**].

2.4.3 Influence of field

A sufficiently large electric field is applied across and between the GEM foils to get a detectable electronic signal. A high voltage is applied using a resistive network, so that all the foils and gaps could be power up simultaneously. First, is the drift region (a gap between cathode and the first GEM foil) where the primary ionization takes place and number of charged particle created in this region move under the influence of this drift field. A weak field (< 0.5 kV/cm) in the drift region is overcome by the recombination of the primary charge, further increasing the field results the maximum transfer of particle inside the hole of first GEM foil, and drift field above ∼3.5 kV/cm causes the charges to fall on the copper of the first GEM foil instead of holes as shown in the Figure 2.22.

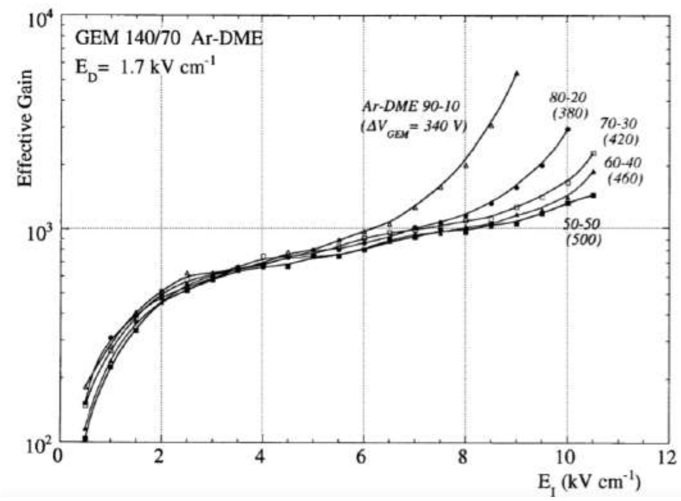

Figure 2.23: Shows the influence of induction field on the gain of the detector [**24**].

Second is the transfer region (a gap between the GEM foils), the role of this field is to transfer the charge successfully to the next amplification stage. The last gap is known as the induction region (a gap between the bottom of last GEM and anode), it has a direct impact on the gain of the detector. The effective gain increases linearly with the induction field up to ∼3 kV/cm, further increase in the field could provoke the propagation of discharges to the anode and the total current is overcome by ions instead of an electron which can be clearly seen by the ion tail in the Figure 2.23 [**24**].

2.4.4 Collection and extraction efficiencies of GEM

The number of electrons entered in the GEM with respect to the electrons created above GEM is known as the collection efficiency of the GEM. It depends upon the field above the GEM foil, the collection efficiency decreases as the field above the GEM increases as shown in the Figure 2.24 (a) to (c). On the other hand, the extraction efficiency for a GEM is defined as the number of electrons extracted from the GEM with respect to the electrons present in the hole [**25**]. The extraction efficiency depends upon the field below the GEM foil, and it increases when the field below GEM increases as shown in the Figure 2.24 (d) to (f).

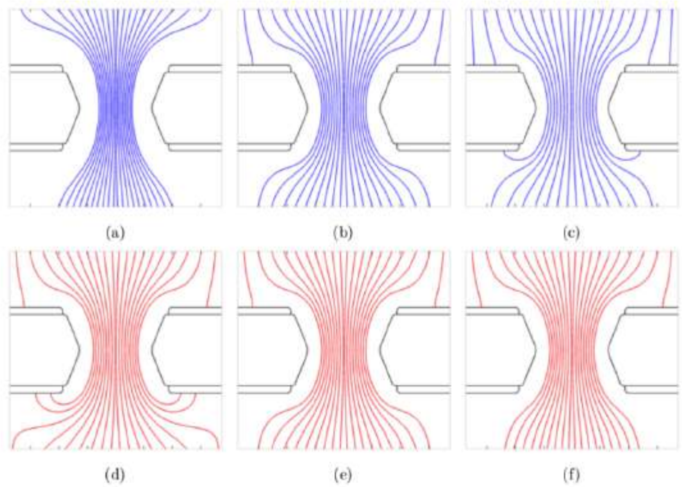

Figure 2.24: From (a) to (c) shows the variation of field above the GEM, and (d) to (f) shows the variation of field below the GEM [**25**].

2.4.5 Gas mixture

A usage of noble gases is suitable for the counting purposes due to their low attachment coefficient but the operation of a gaseous detector in pure noble gases limits the gain hence a quencher is required for a proper operation (due to their molecular structure). The use of noble gases helps in detecting the low energy particle as well as, they get ionize easily under the low electric field[1]. To find a suitable gas mixture for a detector few parameters are needed to optimize [**26**, **27**], such as;

- **Drift and diffusion:** The electron drifts in the presence of an electric field along its direction (known as drift velocity) and it highly depends upon the pressure, temperature, pollutants (mainly water, oxygen etc.). The motion of electron under the influence of electric field causes the scattering of the particle due to collision with the gas atoms. For the application of tracking and triggering detectors a gas mixture having high drift velocity and low diffusion is required.

[1]Because of the low ionization potential for the noble gases

- **Penning effect:** When an excited atom of gas molecule transfers its energy to another neutral atom before coming to the ground state, known as penning effect. For a suitable gas mixture, the collision time of excited and neutral atom should be less than the de-excitation of the excited atom.

- **Lorentz angle:** In the presence of perpendicular magnetic field an angle made by the drifting electron swarm with the electric field is known as the Lorentz angle. It can affect the drift velocity of a particle moving in the presence of electric and magnetic field hence it should be low enough to avoid its effect for a particular chosen gas mixture.

2.4.6 Gain

The real gain of the detector is defined as the ratio of the number of electrons below and above GEM, however, due to loss of electrons on the kapton and copper of the GEM foil only a fraction of charges reach to the anode as shown in the Figure 2.25. Hence experimentally we only measure the so-called "effective gain" defined as the ratio of output current over input current.

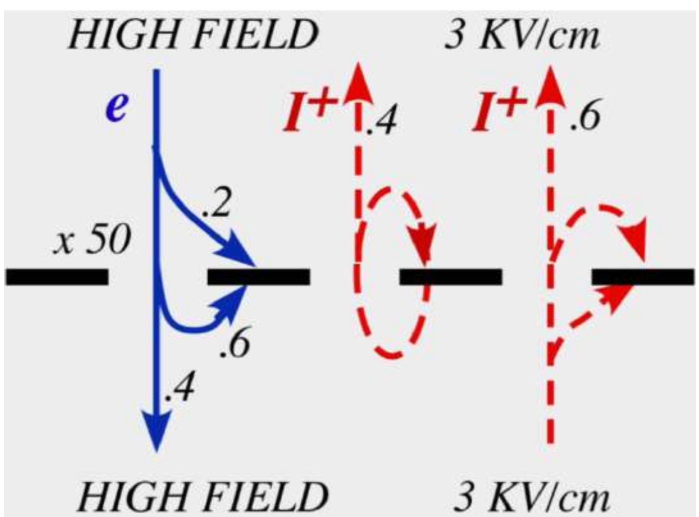

Figure 2.25: Shows the fraction of charge transfer for electron and ion for high drift and induction field.

2.4.7 Timing resolution

A particle crossing the drift gap produces the number of primary particles and each primary gives rise to a cluster at the anode. The rising edge of the cluster corresponding to each primary electron crossing the discriminator gives the time track of the passing event. The first cluster produced due to the primary electron nearest to the first GEM foil has the shortest arrival time and gives the intrinsic timing resolution of the detector. It is defined as the product of an average number of clusters produced times the electron drift velocity.

2.4.8 Spatial resolution

The spread of the electron cloud occurs while drifting under the electric field and consequently affects the spatial resolution of the detector [**28**]. Mainly the transverse dispersion of the electron cluster produces an enormous impact on the spatial resolution. Supposing the cluster cloud is spread according to Gaussian distribution and it spreads over the single strip, the spatial resolution is defined as the ration of pitch[2] over the variance of the uniform distribution i.e. $\sqrt{12}$.

$$\sigma_{Res} = \frac{Pitch}{\sqrt{12}} \tag{2.8}$$

[2]The distance between the two consecutive strips

3

CMS muon upgrade using GEMs

"Work gives you meaning and purpose, and life is empty without it."

– Stephen Hawking

The LHC is the most powerful particle accelerator, till date, built by the European Organization for Nuclear Research (CERN), Geneva. It has four collision points out of which one of the collision point experiment capable of studying different aspects of the proton-proton collisions is called as CMS experiment. A discovery potential could be increased by upgrading the LHC and its detectors, and the upgrade in LHC will increase the center of mass energy up to 14 TeV and luminosity to $5 - 7 \times 10^{34}$ cm^{-2} s^{-1}. Due to an increase in the collision rate the detection environment in the CMS will also get affected, hence, requires an upgrade in the detector system to increase overall detection capabilities. One of the major upgrades of the CMS experiment is to install a new gaseous detector in the end-cap region to cope-up the abrupt increase in the rate [**21**]. Due to excellent rate handling capacity CMS GEM collaboration decided to install a GEM based gaseous detector layer in the end-cap region of CMS muon station. It will cover the pseudo-rapidity range of $1.55 < |\eta| < 2.18$.

3.1 GE1/1 upgrade

A triple-GEM technology based upgrade known as GE1/1 has been approved by the CMS collaboration in 2015 to ensure the good performance and longevity of these detectors. Along the same line, a "slice test" was also approved under which 10

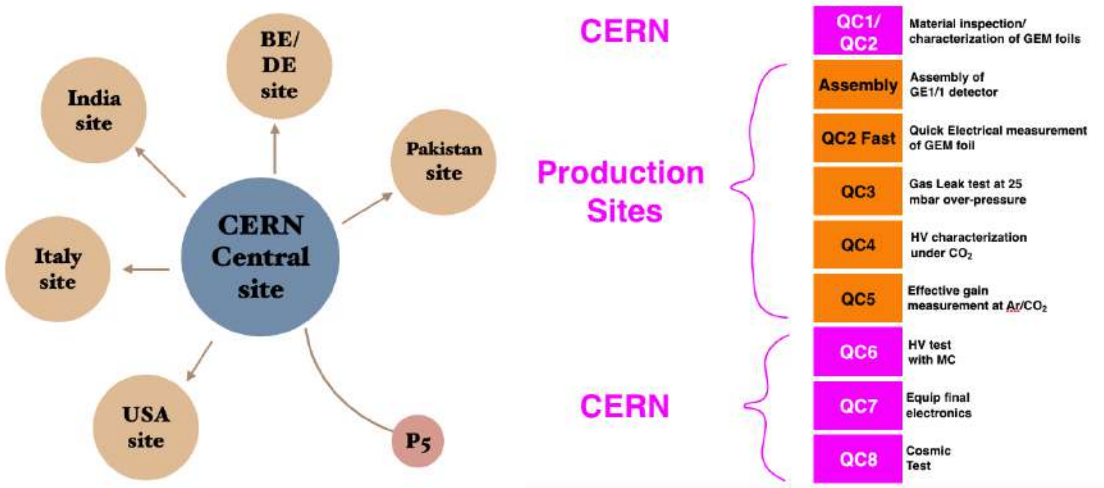

(a) (b)

Figure 3.1: Shows the schematic of (a) sites involved in production of GE1/1 detectors for CMS muon upgrade, and (b) QC procedure for production sites.

detectors were installed in YE1/1 region of CMS to demonstrate the capability of this technology. Due to available space, the CMS GEM collaboration decided to install 144 trapezoidal shape GEM detectors, the assembly and testing of these chambers has been divided into several production sites as shown in the Figure 3.1 (a). Before the installation of these detectors in the CMS the key factors that play major role for their best performance are Quality Control (QC) and Quality Assurance (QA). For this purpose a precise QC procedure has been established as shown in the Figure 3.1 (b).

3.2 Quality controls

A controlled environment has been required to do all the operations and measurements. In other words clean room for the assembly, sophisticated gas mixture for the measurements, and temperature and humidity controlled ambient conditions.

A precise Quality Controls (QCs) procedure has been set up in order to build a triple-GEM detector as shown in the Figure 3.1 (b), which needs to follow in a particular order both at CERN as well as at the production sites [**17**]. First, the material required to produce these detectors is manufactured by private companies and requires a set of QA tests before shipping them to the various production sites. These QA has been performed at CERN which includes the flatness of the readout (RO) and drift PCBs, connectivity of RO board connectors, thin coating of the internal

(a) readout board.

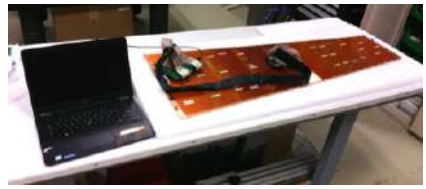

(b) test of readout board connectivity.

(c) measurement of external frame groove.

(d) measurement of O-ring thickness.

Figure 3.2: Shows the list of components required to build the GE1/1 detector and their quality assurance.

and external frames, groove measurement of the external frame, the thickness of the O-ring as shown in the Figure 3.2. The next step is to check the quality of GEM foils i.e. a quick optical inspection shall be performed in order to look for the possible damages like any scratches, defects, etc. in the cleanroom. And perform QC2 fast and long (described in the next section) to ensure the quality and the stability of GEM foils before shipping them to the production sites as shown in the Figure 3.3.

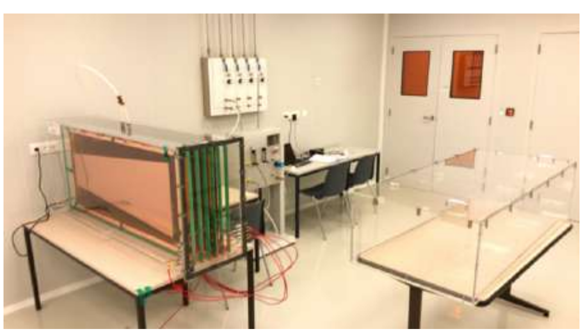

(a)

(b)

Figure 3.3: Shows the (a) QC2 long station for testing GEM foils, and (b) shipment box with necessary raw material is ready for the shipment to the production sites.

3.2.1 Leakage current measurement (QC2)

When a voltage is applied across the GEM foil a current flows from top to bottom of the foil which is mainly driven by the surface conductivity of the foil (also called leakage current). The applied voltage across the GEM foil is very high as compared to the actual operating voltage which may help in cleaning the foil. This current highly depends upon the defects and contamination in the foil. By measuring the leakage current quality of the foil can actually be determined. From the experiments, it is found that a 10 cm $\times$ 10 cm active area foil has leakage current less than 1 nA. This test must be performed when foils are placed inside the sealed vessel and flushed with the Nitrogen gas in order to control the surface conductivity of the foil. For a quick check, it can also be tested in a cleanroom having controlled ambient conditions using an insulation meter (i.e. Megger). Figure 3.4 shows the leakage current measurements of the GEM foils used for the slice test GE1/1 detectors.

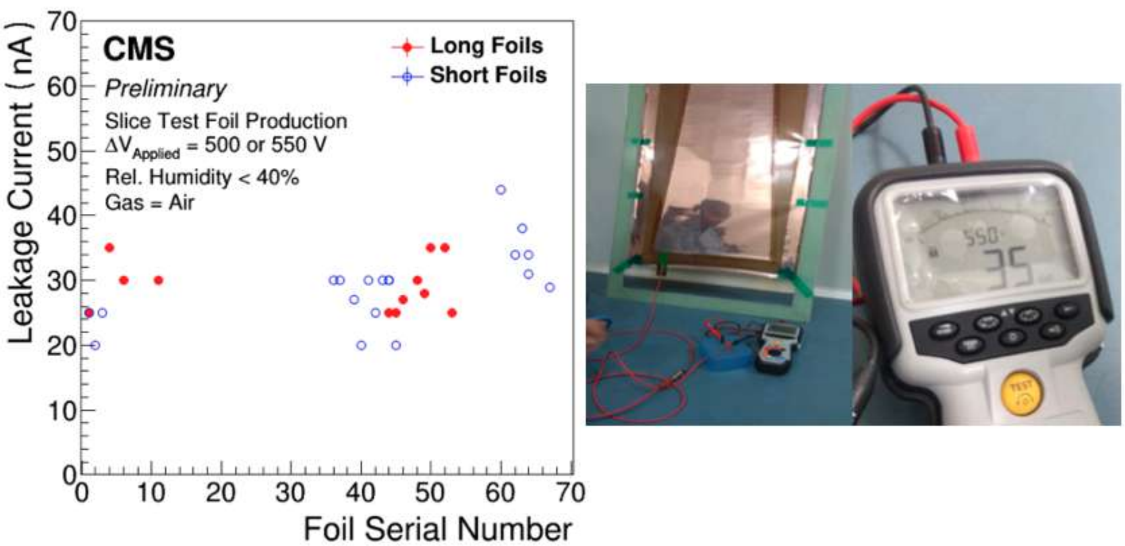

(a) (b)

Figure 3.4: Shows the (a) leakage current of GEM foils used in slice test GE1/1 detectors, and (b) measurement of leakage current.

3.2.2 Assembly of GE1/1 detector

There is a minimum requirement for a particular production site to assemble and test the GE1/1 detector in terms of hardware as well as manpower. Also to have the uniform measurements with the minimal systematics errors all the production sites shall be equipped with similar types of equipment. After receiving the shipment box from CERN, the GE1/1 detector has been assembled in a cleanroom, rated at least class 1000. The assembly of the GE1/1 detector has been divided into two parts; the pre-assembly performed outside the cleanroom and the assembly of the detector performed inside the cleanroom [**29**, **30**].

1. **Preparation of the RO board:**

   The preparation of the RO board includes placement of the brass inserts in the dedicated housing over the flanges from the strip side. On the connector side perform 3 mm threading in the dedicated hole for the gas inlet and outlet of the detector as shown in the Figure 3.5.

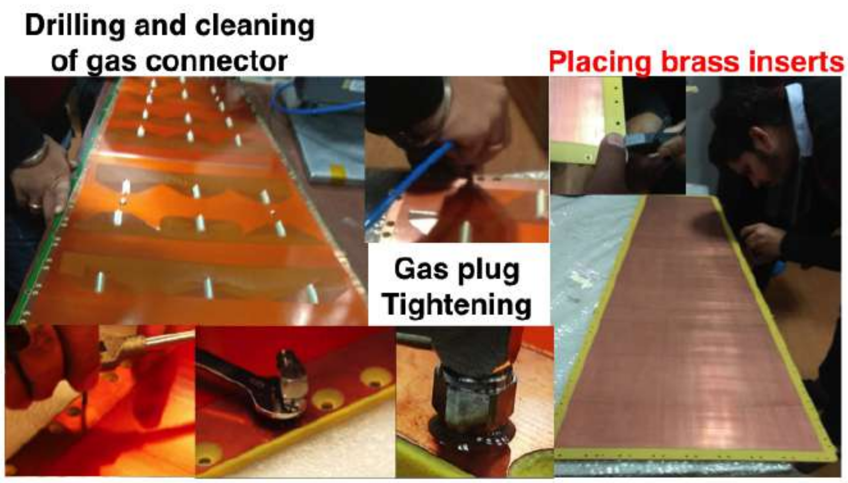

Figure 3.5: Shows the preparation of the RO board.

2. **Preparation of the drift board:**

   The preparation of the drift board includes the mounting of the pull-outs in the dedicated holes, dedicated soldering of the high voltage pins for powering up the GEM foils and another dedicated soldering of the SMD devices as shown in the Figure 3.6.

3. **Preparation of internal and external frames:**

   Preparation of frames for GE1/1 detector includes the insertion of brass inserts in the internal frame of thickness 3 mm and placing the O-ring on the grooving of the external frame as shown in the Figure 3.7.

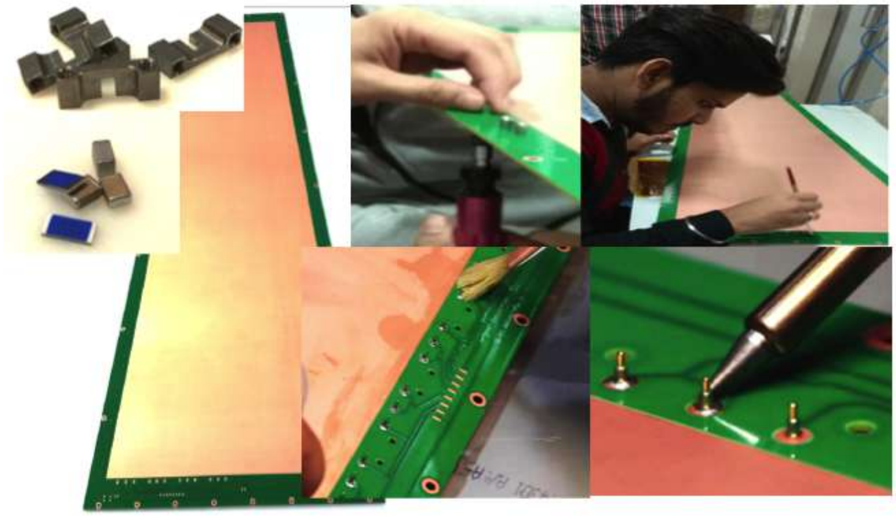

Figure 3.6: Shows the preparation of the drift board.

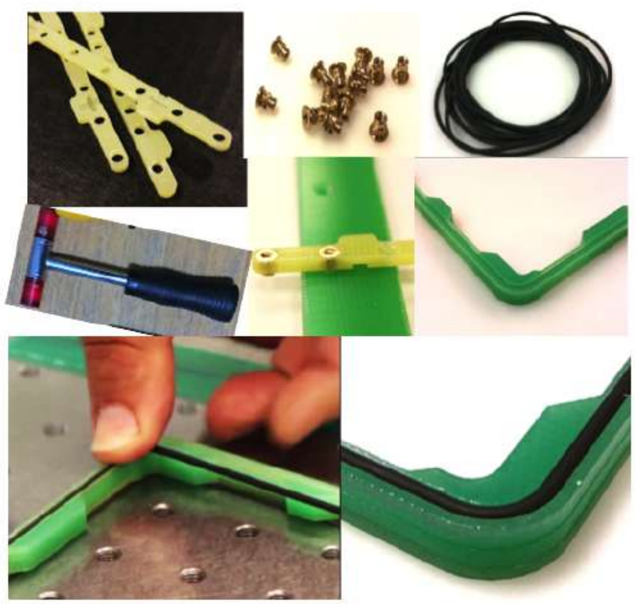

Figure 3.7: shows the preparation of the internal and external frames.

4. **Detector Assembly:**

   The GE1/1 is a three-GEM foils stack within the trapezoidal shape external frame sandwiched between RO and drift PCBs. It forms four gaps namely drift/transfer1/transfer2/induction gap at a fixed distances of 3 mm/1 mm/2 mm/1 mm respectively. Thanks to the new mechanical stretching technique known as NS2 ("No stretch No stress") technique which helps in providing the tension to foils as shown in the Figure 3.8.

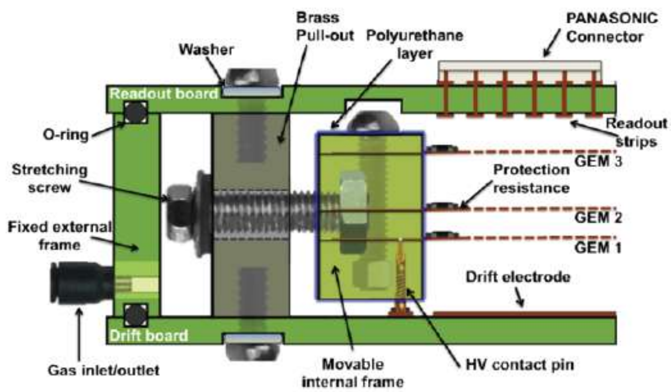

Figure 3.8: Shows the NS2 stretching technique.

   The assembly of a big size triple-GEM detector is a very crucial part as it starts with the base plexiglass having dedicated holes in a shape of the trapezoid to place the alignment pins in order to align the whole stack throughout the assembly. The FR4 frames have been used to make the gaps. Only 3 mm spacers use the brass inserts to hold the complete stack of three GEM foils from top to bottom. The stack has been prepared by placing the internal frames and GEM foils at a particular distance followed by the regular measurement of leakage current to ensure the clean and perfect foils. Finally, cover the stack with the RO board to complete the assembly. The flow chart of the assembly procedure with main steps shown in the Figure 3.9. Appendix A describes the detailed step by step procedure to assemble a big size triple-GEM detector.

3.2.3 Gas leak test (QC3)

The assembly of the GE1/1 detectors includes several hundreds of screws in the drift and RO PCBs so it is important to measure the tightness of the gas. Any possible

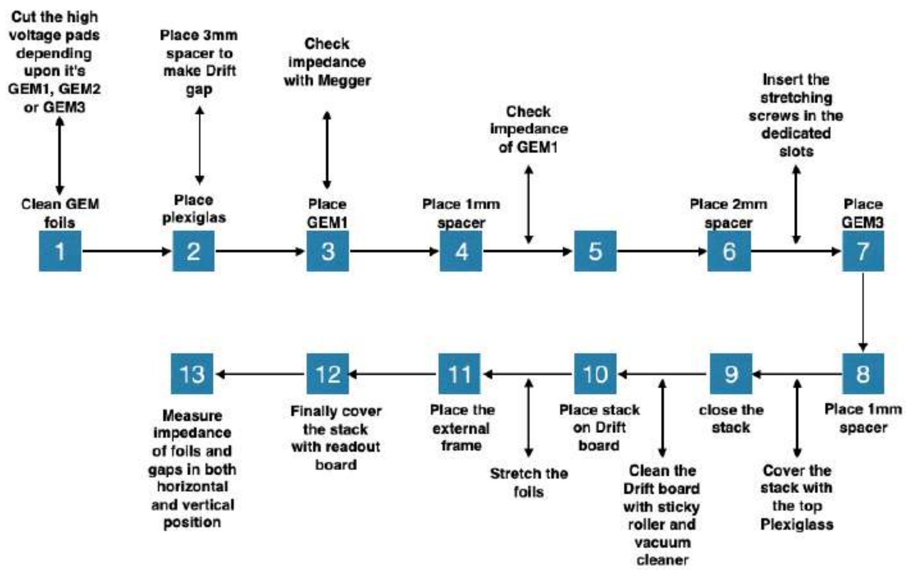

Figure 3.9: Shows the flow chart of the assembly procedure highlighting the main steps.

leakage in the detector is the wastage of the gas as well as it can be the source of the contamination such as air, water and unknown species which can degrade the detector performance. An accurate technique has been developed to measure the possible leakage in the detector. The detector should be over-pressured with a safe limit of 25 mbar with any choice of a gas mixture, and then stop the flow by closing the inlet and outlet valve of the gas panel as shown in the Figure 3.10.

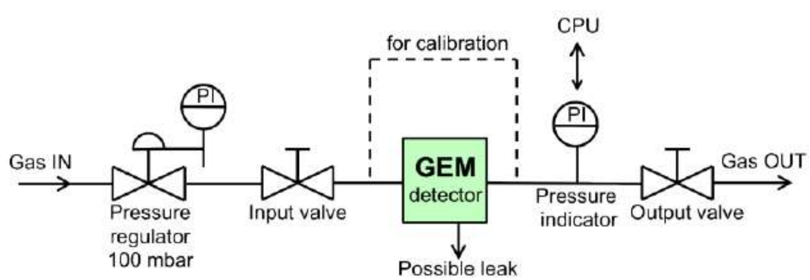

Figure 3.10: Shows the setup for measuring the gas leak.

A pressure drop is measured across the detector using pressure transducer which is well controlled by an Arduino based microcontroller. The time required to drop the pressure to zero scale is defined as the leak rate of the detector. During the measurement of pressure across the detector, the atmospheric pressure and temperature are well recorded using the same system with the dedicated sensors [**31**]. Also, it is important to locate the place of leakage for the detectors having leak rate more than the accepted value (i.e. 7 mbar/hr with initial over-pressure of 25 mbar) and equally important to immediately fix it. The possible reasons for the leakage and remedies thereafter are listed below:

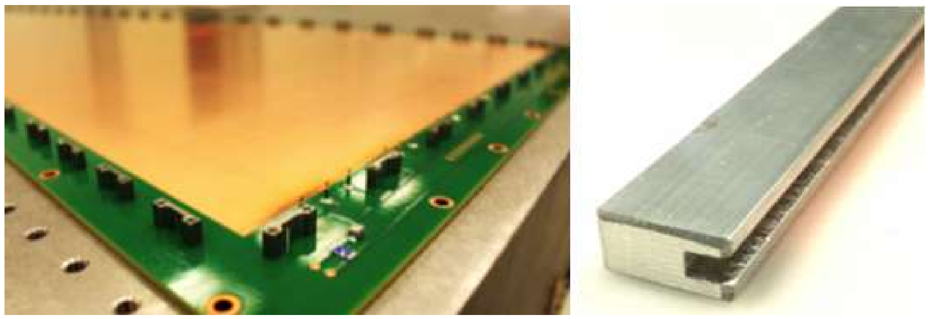

Figure 3.11: QC3 tips and trick first step.

1. It is important to align the pull-outs on the drift board manually using the guiding rail. And check the compatibility of the O-ring with the grooving of the external frame as shown in the Figure 3.11.

2. While inserting the O-ring in the external frame groove, press it vertically after 2-3 cm to uniformly distribute the material, pushing with your finger along the frame cause the accumulation of material at the end. In case of the wavy structure that cannot be removed by the finger, a soft hammer can be used as shown in the Figure 3.12.

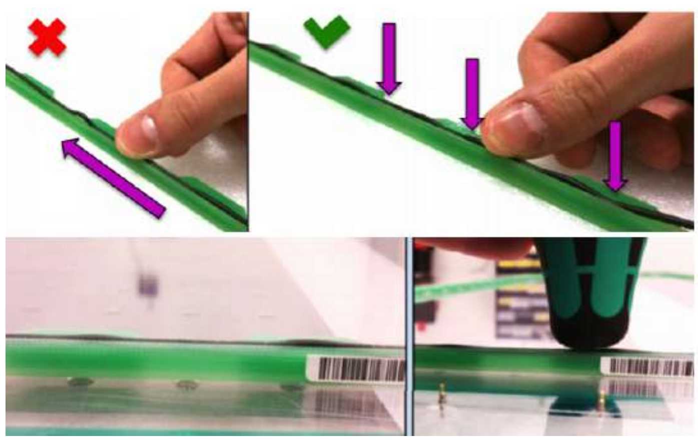

Figure 3.12: QC3 tips and trick second step.

3. Check the flatness of O-ring in external frame groove and make sure it's not sticking out, inspect multiple times with eyes and fingers from both sides of the frame as shown in the Figure 3.13.

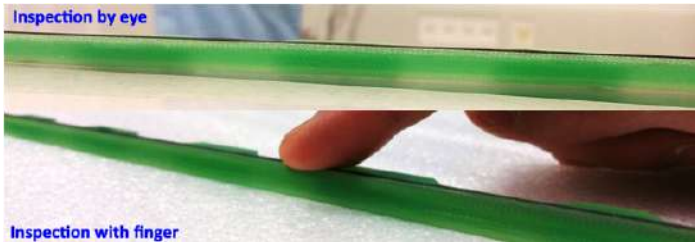

Figure 3.13: QC3 tips and trick third step.

4. The last stage of internal frames 1 mm thickness for the induction gap has chamfers on one side to accommodate the head of the M2 screws. This chamfer should face up i.e. RO side. If they are not inserted properly the screw head will stick out and create a large difference between the RO PCB and the stack as shown in the Figure 3.14.

Figure 3.14: QC3 tips and trick fourth step.

5. Apply the green tapes on the screws of RO and drift board all around the trapezoid to look for the possible leak points. Make the tape flat all around the screws because the detector is over-pressured with 25 mbar, it is possible to see a bubble around the leaky hole as shown in the Figure 3.15.

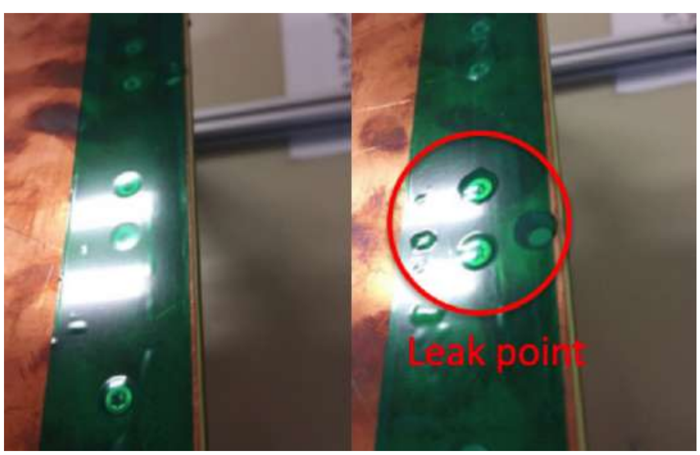

Figure 3.15: QC3 tips and trick fifth step.

6. In the case of the leak, screws can be tightened with 1.3 Nm torque.

Figure 3.16: QC3 tips and trick sixth step.

This is the best way to press the O-ring between the PCBs to stop the leakage as shown in the Figure 3.16.

3.2.4 High voltage test (QC4)

The high voltage distribution of GE1/1 detectors uses the resistive divider to power up the GEM foils. The test is performed under the flushing of CO_2 gas because we operate the detector at very high voltage i.e. 4.9 kV.

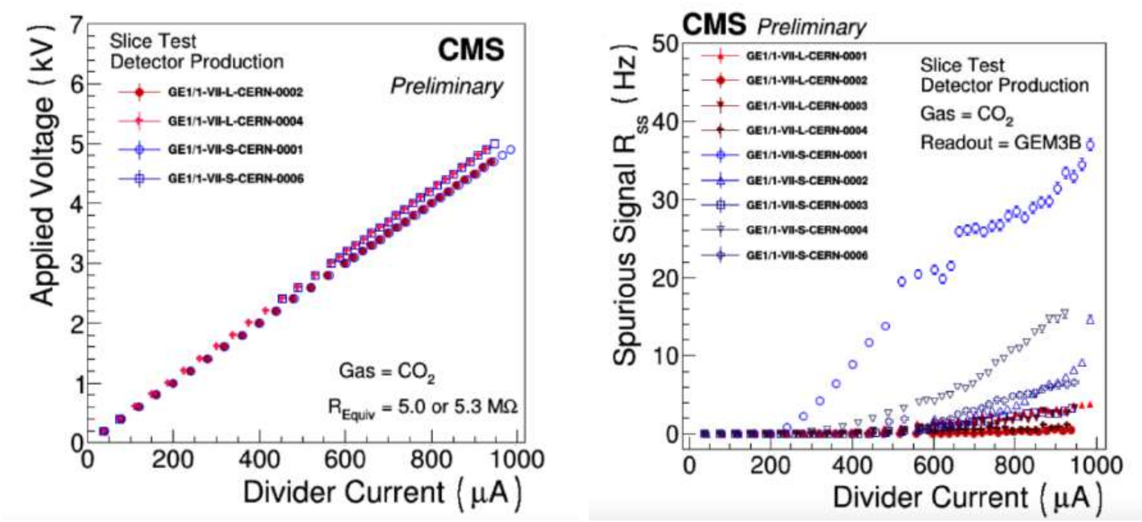

(a) (b)

Figure 3.17: Shows the (a) I-V measurement, and (b) measurement of spurious signal for the slice test GE1/1 detectors.

Simultaneously the rate of the spurious signal was measured, spurious signals could be induced on the bottom of the last GEM foil, above the anode strip. Figure 3.17

shows the current-voltage (I-V) and spurious signal measurements for the slice test detectors.

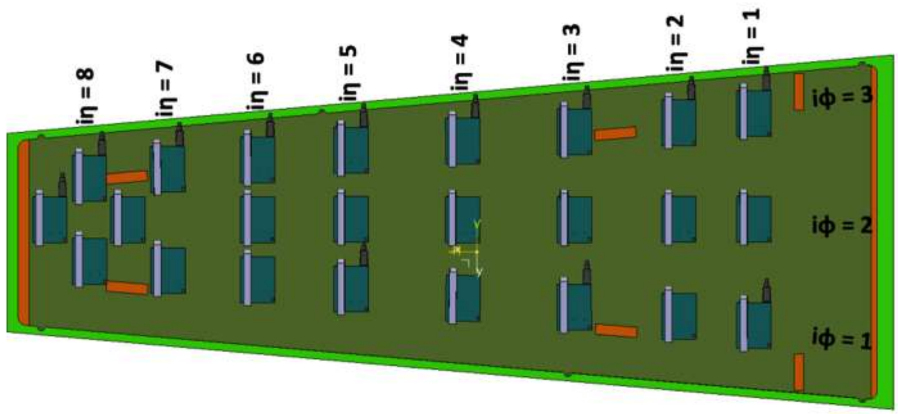

Figure 3.18: Shows the nomenclature for GE1/1 RO board.

3.2.5 Effective gain and uniformity measurement (QC5)

For any gaseous detector the important parameter is the gain and necessary to check its behaviour with respect to the input voltage. By measuring the gain an operating point of detector can be fixed. The effective gain is defined as the ratio of output current divided by input current.

$$G = \frac{I_{RO}}{n_p \times R_s \times e} \tag{3.1}$$

Where; I_{RO} is the current collected on the RO, R_S is the interaction rate, n_p is the average number of primary electrons and e is the charge of the electron. The effective gain was measured in the particular sector of the RO $(i\eta, i\phi)$ = (4,2), according to the nomenclature shown in the Figure 3.18.

The GE1/1 detector has total 24 sectors, 3 sectors in ϕ direction and 8 sectors in η direction. For the slice test two different geometries of GE1/1 detectors was built namely GE1/1-long and GE1/1-short with the dimensions 120.6 cm × 23.1 cm × 44.6 cm and 106.1 cm × 23.1 cm × 42.0 cm. Figure 3.19 shows the measurement of effective gain with respect to the input voltage for both types of GE1/1 detectors.

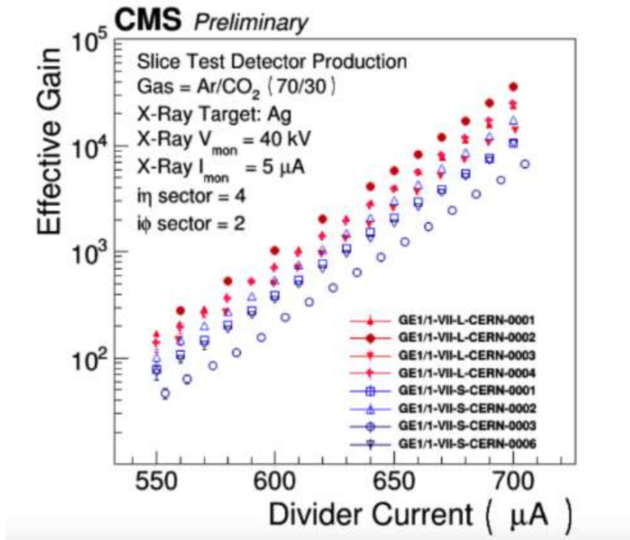

Figure 3.19: Shows the effective gain measurement for the slice test GE1/1 detectors.

The observed difference in effective gain curves may be due to the bending of the RO and drift board PCBs, which contains the anode strips and the cathode. Due to the bending of the PCBs, the detector volume gets close and modifies the fields [**32**]. Due to the large size of the GE1/1 detectors and no spacer present in the middle of the detector, it is important to measure the uniformity of gain over the active area. This is the crucial step to validate the detector to proceed for the next quality control and also helps in finding the possible dead regions present in the detector as well as in the RO board. A Scalable Readout System (SRS) based data acquisition is used to measure the uniformity of the detector which utilizes the multichannel APV25 front-end chip developed by CERN RD51 group. The details about the SRS system are illustrated in Chapter 5.

The detector iη sectors are partitioned into slices where each slice covers an area equivalent to the four anode strips. Figure 3.20 (a) shows the ADC spectrum obtained using a silver target X-ray source in a particular slice.

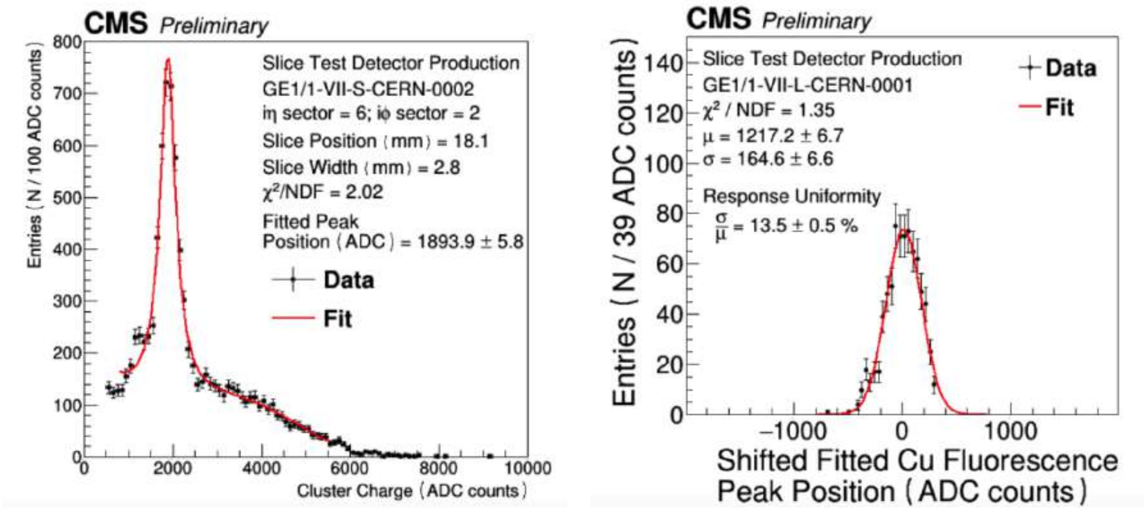

(a) (b)

Figure 3.20: Shows the (a) ADC spectrum for one slice, and (b) bulk response uniformity plot for slice test GE1/1 detectors.

The distribution is fitted with the gaussian function to extract the mean of the main peak. GE1/1 detector contains in total of 3072 strips distributed over 768 slices. The mean of fitted peak position from 768 slices has been plotted together to calculate the response uniformity of the detector. The distribution obtained hence fitted with the gaussian function whose mean and sigma are used to calculate the bulk gain uniformity of the detector as shown in the Figure 3.20 (b).

3.3 GE1/1 production at Delhi University

The aim of CMS GEM collaboration is to install 144 trapezoidal shape triple-GEM detectors in the CMS muon chamber during LS2. To speed up the production rate; the assembly and testing is divided into several production sites all over the world. Mainly the whole production is divided into three major parts; first is the reception of material from companies at CERN and their quality assurance, second is the assembly and testing of the detector at production sites (as mentioned in the Section 3.2), and last assembly and commissioning of the super-chamber at CERN. Each production site has to demonstrate the capability of assembling and testing the GE1/1 size detector for which a QC jamboree has been setup. It includes the production of one detector and their testing (from QC2 to QC5). DU is one of the approved production site and in total 16 GE1/1 detectors were delivered by India, out of which 8 detectors were assembled and tested (QC2 to QC5) at DU and 8 detectors were assembled and tested partially (only for two quality controls QC3 and QC4) at Panjab University (PU). Due to the only one X-ray and SRS system facility working in India, the 8 detectors built at PU were tested for QC5 at DU only. Here are the facilities and results of the detector built at DU along with the QC5 results of PU detectors:

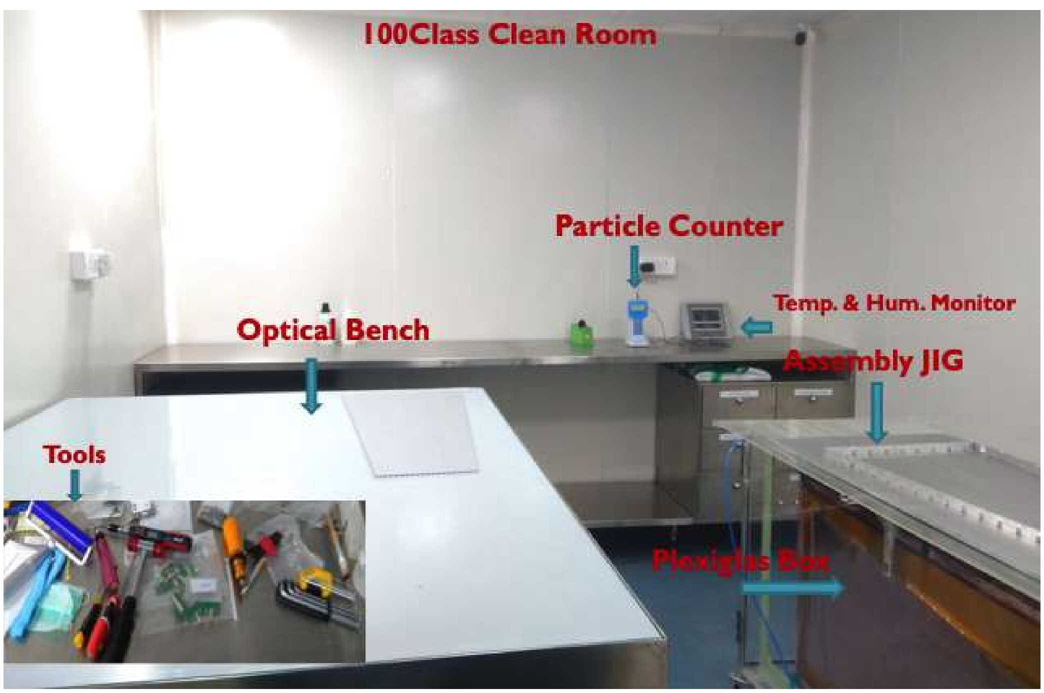

Figure 3.21: Shows the fully equipped class 100 clean room at DU.

3.3.1 Assembly facility

We have a clean room of class 100, an order of magnitude lower compare to the minimum requirement to assemble a triple-GEM detector (i.e. class 1000). It is equipped with two large benches in order to perform the assembly of the stack and further closing of the chamber. An auxiliary bench with multiple drawers for the tooling along with a dust particle counter for, measuring the cleanliness of the room is also placed inside. A big size storage (to store GE1/1 size GEM foils) box with the facility to flush the nitrogen gas, for cleaning the GEM foils as shown in the Figure 3.21.

Figure 3.22: Shows the gas leak setup at DU.

3.3.2 QC3 measurement

A gas leak test setup to measure the leak rate of the detectors is also arranged and is made using local industry, having a gauge pressure sensor controlled by an Arduino based system. Using the same board the atmospheric temperature and pressure can also be recorded during the measurement. The calculation of leak rate is done with the same principle as mentioned in the section 3.2.3, This test is performed with the flushing of CO_2. Figure 3.22 shows the image of the setup at DU. Figure 3.23 shows the QC3 test results for 8 GE1/1 detectors assembled at DU.

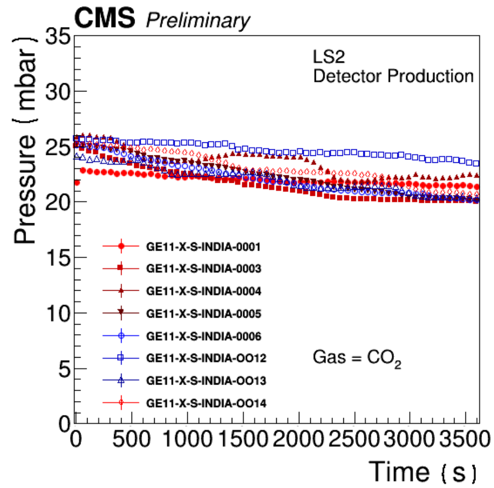

Figure 3.23: Shows the results of QC3 tests for the GE1/1 detector tested at DU.

3.3.3 QC4 measurement

A dedicated setup for the measurement of the high voltage distribution circuit of GE1/1 detector is developed. For this measurement detector is connected to the QC3 stand and flushed with CO_2 for 5 hours at the rate of 5 ℓ/hr prior to start the measurement.

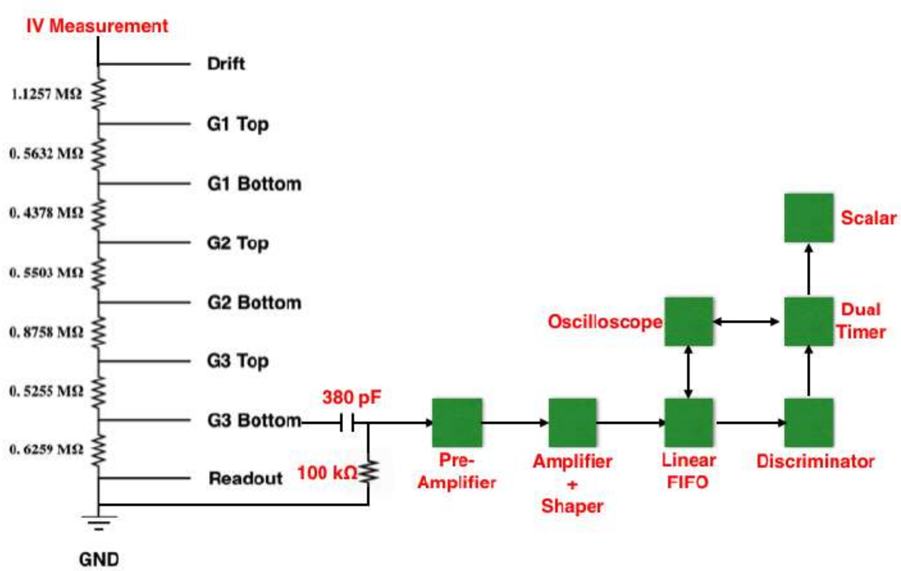

Figure 3.24: Shows the schematic for the DAQ for QC4 spurious signal measurement.

A schematic of data acquisition setup (DAQ) for QC4 measurement is shown in the Figure 3.24. The negative programmable power supply was used and can deliver a current up to 1 mA with a resolution of 1 μA. The total resistance of the circuit measured with the multimeter is 5 MΩ. Figure 3.25 (a) and (b) shows the result of I-V characteristics and spurious signal measurement for GE1/1 detectors tested at DU.

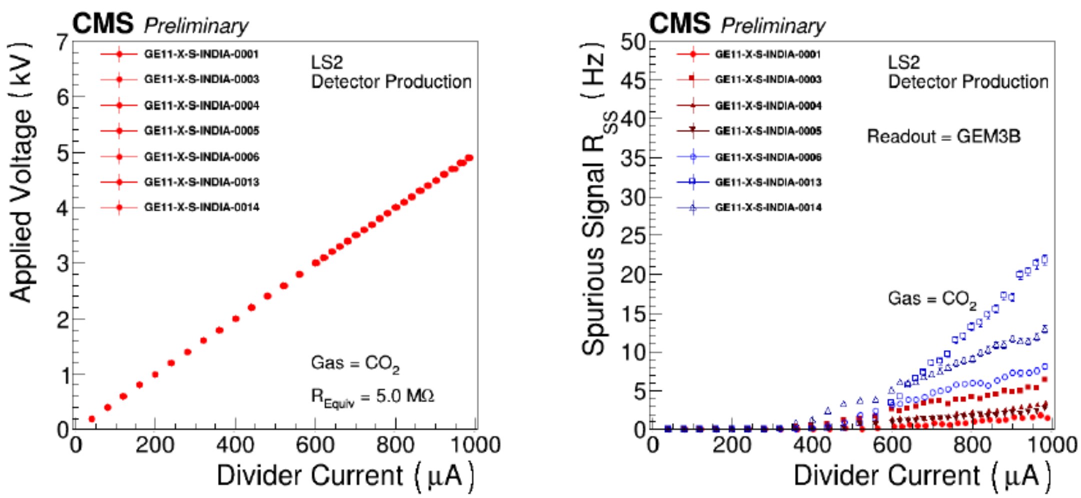

(a) (b)

Figure 3.25: Shows the (a) IV measurement, and (b) spurious signal measurement for the GE1/1 detector tested at DU.

3.3.4 QC5 measurement

The QC5 test is mainly divided into two parts; one is measurement of the effective gain with respect to the divider current of the detector and second is the measurement of the gain uniformity of the detector. Both the tests are performed under the irradiation of the X-ray with the flow of Ar/CO_2 gas mixture in a ratio of 70%/30% inside the detector. We have X-ray facility inside a thick copper box (act as a shielding) to measure the effective gain and gain uniformity of the detector along with the dedicated DAQ system to read and process the signal from GEM detectors as shown in the Figure 3.26.

At DU we have tested the effective gain and uniformity of 16 GE1/1 detectors because of the only working X-ray facility in India. Figure 3.27 shows the effective gain measurement and response uniformity for the India made GE1/1 detectors. All of them are validated in terms of quality to make the super-chamber and further commissioning at CERN while some of them are already installed in the CMS cavern.

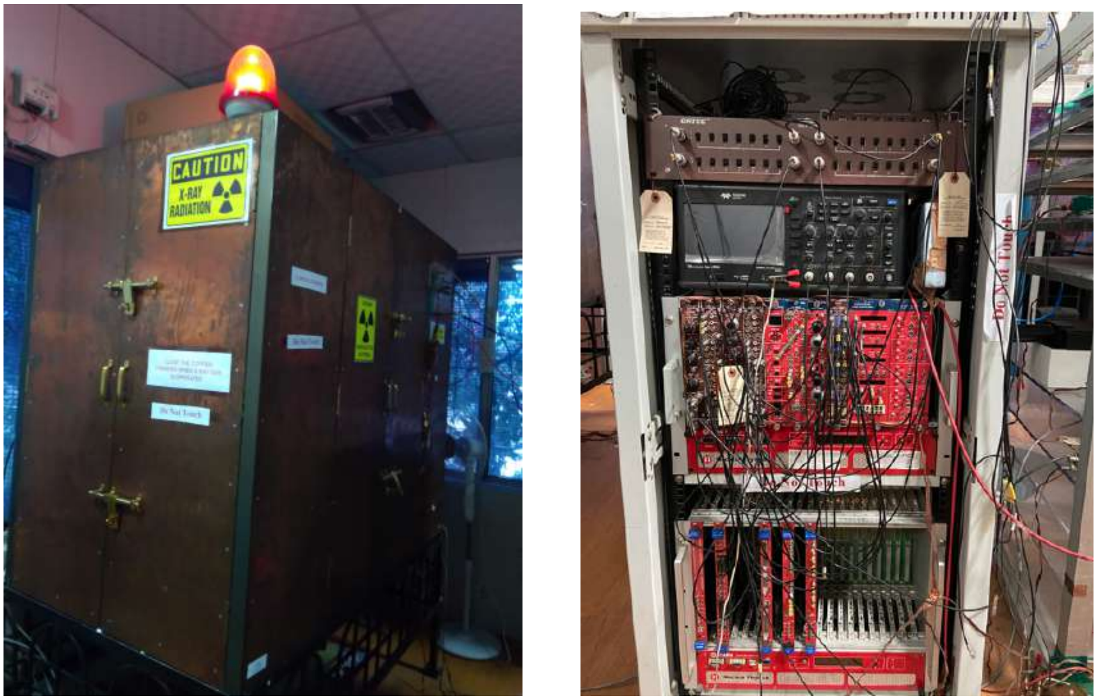

(a) (b)

Figure 3.26: Shows the (a) X-ray irradiation facility, and (b) dedicated DAQ system for signal processing at DU.

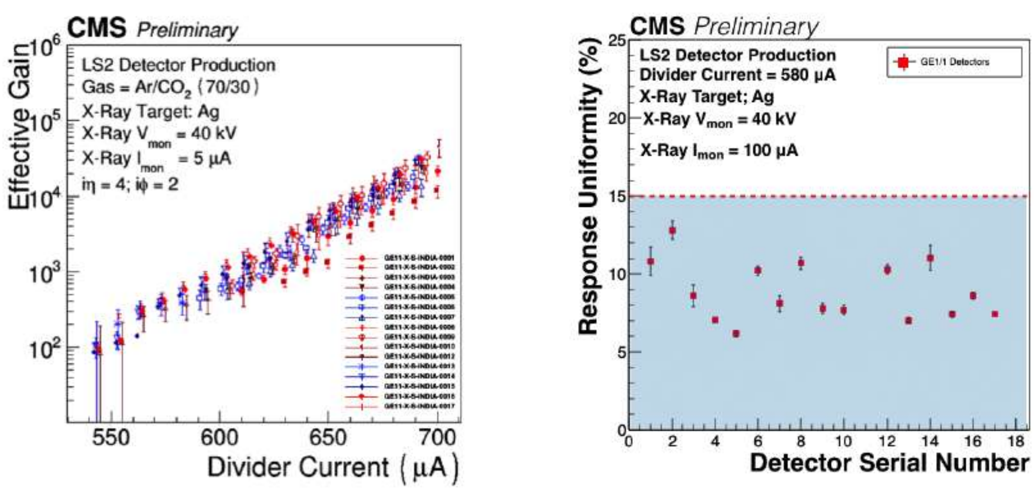

(a) (b)

Figure 3.27: Shows the (a) superimposed effective gain curve, and (b) gain uniformity of the GE1/1 detectors tested at DU.

3.4 GE2/1 upgrade

A major upgrade of the LHC, High Luminosity LHC (HL-LHC) has been decided to increase the extent for the new physics searches. As a consequence the integrated luminosity will increase ten times with respect to the designed LHC value. The projected evolution of instantaneous and integrated luminosities [**33**, **34**] is shown in the Figure 3.28.

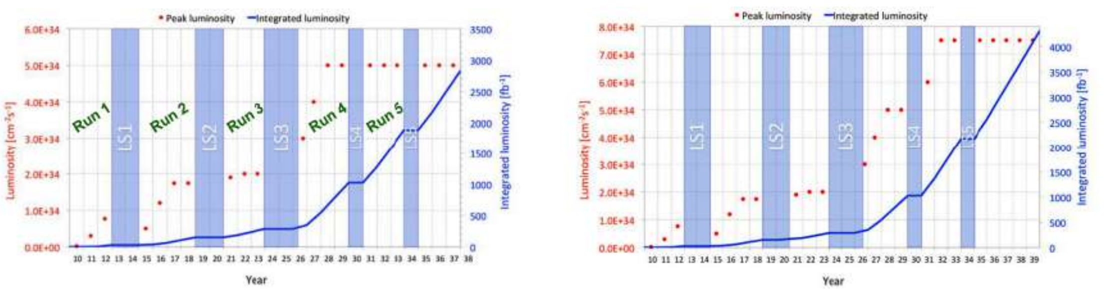

(a) (b)

Figure 3.28: Shows the (a) LHC schedule and designed values for instantaneous and integrated luminosity, and (b) ultimate values for instantaneous and integrated luminosity [**34**].

The proton-proton collision centre of mass energy ($\sqrt{s}$) is expected to increase from 13 TeV to 14 TeV. After finishing the data taking with the Phase-I CMS detector in the year 2023, a long shutdown for HL-LHC upgrade will be followed till the year 2026. The high luminosity data taking period with the upgraded Phase-II CMS detector is expected to end in year 2038. The upgrade program helps in exploiting the physics potential of the LHC and will allow to improve the sensitivity of the physics channels limited in statistics.

The muon detectors play a central role in CMS. The most sensitive signatures of the production of new particles often include one or more muons. Therefore, CMS was built with several complementary sub-detectors to identify muons, already at trigger level, and to measure their momentum and charge over a broad range of energies. To cope with the increase in background rates and trigger requirements, the GE2/1 and ME0 [**35**] GEM detectors will be installed in the CMS muon spectrometer.

Many particle physics experiments like COMPASS [**36**], TOTEM [**37**] and LHCb [**38**] are using the GEM technology and it has operated reliably at hit rates of the order of a few MHz/cm^2. No aging and deterioration in the performance have been reported so far.

The GE2/1 detector consists of 20-degree trapezoidal shape triple-GEM chambers

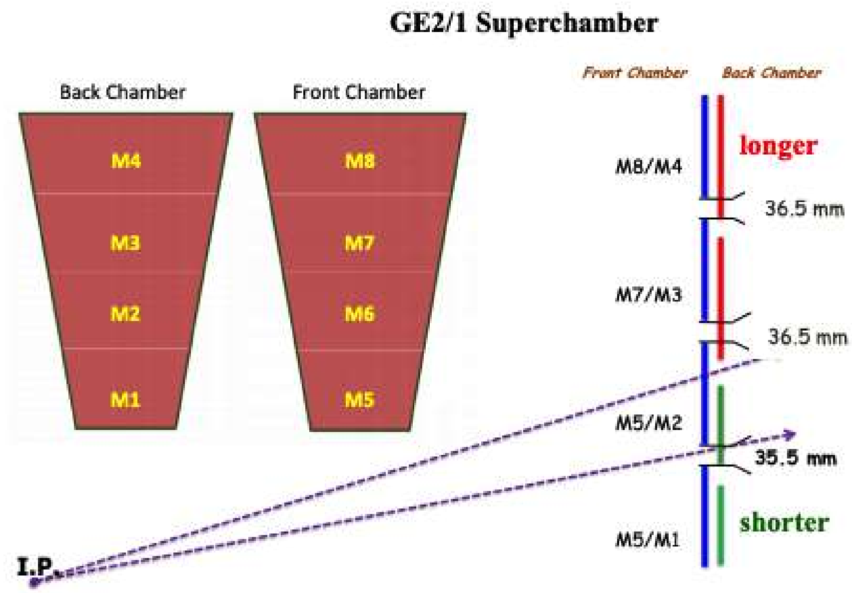

Figure 3.29: Shows the GE2/1 module numbering and overlap of active area between front and back layer [**35**].

arranged in two layers in each of the CMS end-caps. The GE2/1 system provides a second ring of the GEM muon detectors in the end-cap region next to the ME2/1 chambers. The GE2/1 detectors will cover the pseudo-rapidity (η) range of 1.62 $< |\eta| <$ 2.43 having total active readout area of 1.45 m^2. The eta range of GE2/1 partially overlaps with that of GE1/1 and extends coverage to the range 2.1 $< |\eta| <$ 2.43. The two layers of the GE2/1 system consist of front chambers, closer to the interaction point, and back layers. For convenience, a pair of GE2/1 chambers covering the same eta (η) and phi (ϕ) region is referred to as a super-chamber although each chamber is completely independent of the other. Each GE2/1 chamber consists of four modules M1-M4, each being a single CMS triple-GEM detector. The full system consists of 72 GE2/1 chambers (36 per end-cap) which corresponds to 288 basic GE2/1 modules. Each module is assembled from a drift and a RO PCB, external and internal frames, and set of GEM foils specific for each module. The assembly and qualification of the modules can be done independently from the other chamber components. Each single module is segmented into four partitions along the η-direction and 1,536 strips along the ϕ-direction. Strips that belong to the same η-partition are routed to the RO connectors in groups of 128 strips to match the granularity of the front-end electronics. The modules differ from each other only with respect to their dimensions, number and type of components are very similar for all the eight module types. The unavoidable non-active gap between two adjacent modules in one GE2/1 chamber is 35.5 mm wide in this design. To avoid an overlap between the gaps of two chamber layers within the super-chamber, the front and back chambers are staggered by making them of different sizes as shown in the Figure 3.29.

3.4.1 GE2/1 pre-production modules

Eight GE2/1 modules have been assembled and tested at the CERN 904 lab facility. After the assembly of the modules basic quality controls tests QC2-QC5 have been performed.

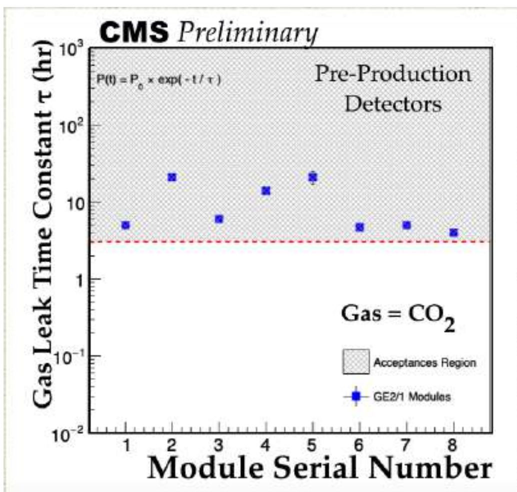

(a)

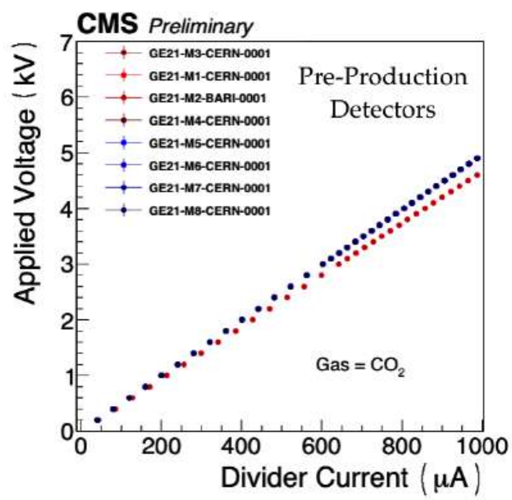

(b)

Figure 3.30: Shows the (a) gas leak test, and (b) high voltage test for GE2/1 modules.

Initially, the gas leak test has been performed on these modules according to the procedure mentioned in the section 3.2.3, result is shown in the Figure 3.30 (a). Then an HV test (QC4) is performed to check the behaviour of the high voltage distribution circuit of the detector as shown in the Figure 3.30 (b). Since no strange behaviour observed during the I-V measurement, hence the detector has been sent for the next QC i.e. effective gain measurement and results are shown in the Figure 3.31 (a). The gain uniformity of the modules is shown in the Figure 3.31 (b) which gives the mild variation in gain over the active area of the detector.

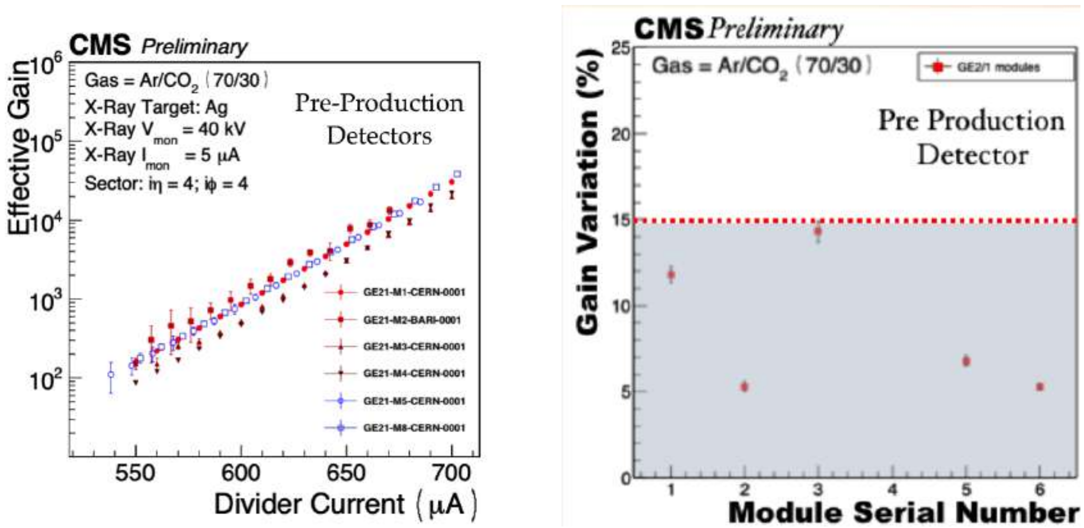

(a) (b)

Figure 3.31: Shows the (a) effective gain measurement, and (b) gain uniformity test for GE2/1 modules.

3.4.2 GE2/1 electronics, integration and commissioning

The main components used to readout a single GE2/1 chamber are shown in the Figure 3.32 (a). The front-end readout chips (VFAT3) for each module are mounted on a GEM Electronics Board (GEB). Communication to the off-detector electronics is provided by Opto-Hybrid (OH) boards one for each module. The VFAT3 chips designed for GE1/1 will also be used for the GE2/1. Each detector will require 48 VFAT3 chips [**39**].

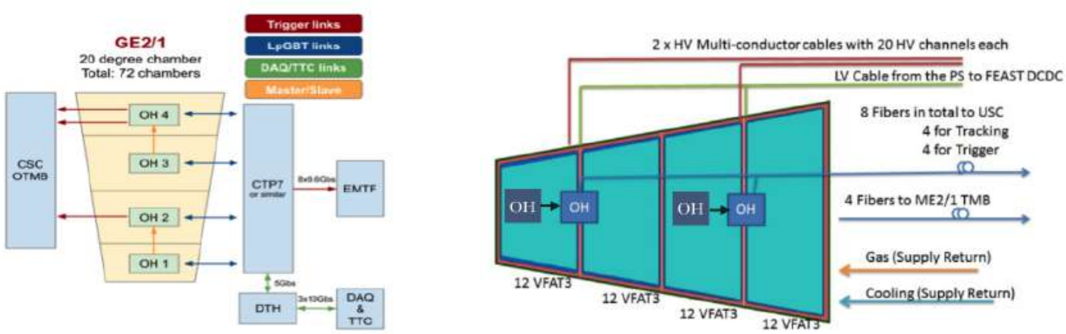

(a) (b)

Figure 3.32: Shows the (a) diagram of the GE2/1 electronics readout system for CMS, and (b) overview of the GE2/1 detector services [**35**].

The GE2/1 chambers will be installed after LS2, during End-Year Technical Stops (EYTS). The chambers for one end-cap will be installed in EYTS 2021-2022 and those for the other end-cap in EYTS 2022-2023. The services needed for a single GE2/1 detector are shown in the Figure 3.32 (b). There are pipes for gas and cooling, four low-voltage cables for the electronics, four HV cables for the detector, and eight optical fibers for readout and control. Four fibers run from the OH to the service cavern (USC55) and four fibers run from the OH to the ME2/1 Optical Trigger Mother Board (OTMB).

3.5 ME0 upgrade

The ME0 system will cover $2.03 < |\eta| < 2.8$ using six layers of triple-GEM detectors as shown in the Figure 3.33 (a). The six layers provide good pattern recognition and background rejection. The ME0 system provides unique coverage in the range of 2.4 $< |\eta| < 2.8$ and extends the coverage provided by the CSCs, RPCs and GE2/1 in the range $2.03 < |\eta| < 2.4$. Based on the simulation the muon identification efficiency is estimated to be approximately 95% for transverse momentum as low as 3 GeV.

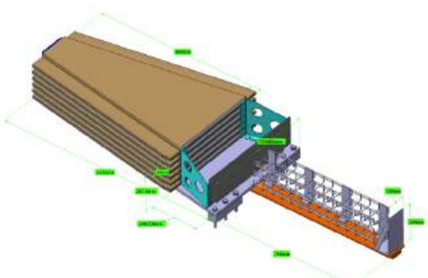

(a)

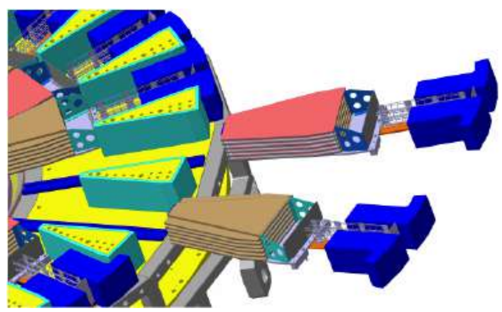

(b)

Figure 3.33: Shows the (a) layout of ME0 stack with six triple-GEM layers including cable trays, and (b) 3D drawing of the insertion of two adjacent stacks of six ME0 modules into the end-cap nose [**35**].

The ME0 system is composed of 18 super-chambers per end-cap. Each super-chamber is mounted on a 15 mm thick Aluminum plate to give mechanical strength as shown in the Figure 3.33 (b). Each detector layer is 33.4 mm thick and the 6-layer super chamber is 224.4 mm thick, including shielding. The area of ME0 chamber is similar as the GE1/1 detector. The readout segmentation of an individual chamber layer is 8 sectors in η and 3 sectors in ϕ; each sector ϕ contains 128 radial strips.

3.5.1 ME0 electronics, integration and commissioning

The electronics architecture is the same for all the three upgrades, also the DAQ layout will be similar to GE2/1. Each module uses a single GEB PCB board. The signal is readout by the VFAT3 chips and in total 24 chips are placed on a single GEB board per module. Finally the signal is routed to the single OH board as shown in the Figure 3.34 (a).

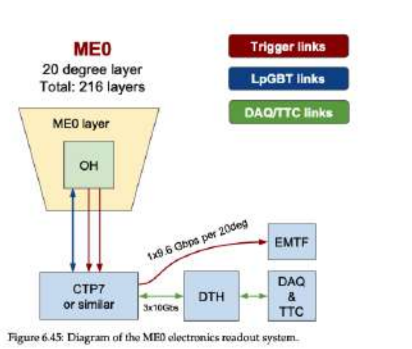

(a)

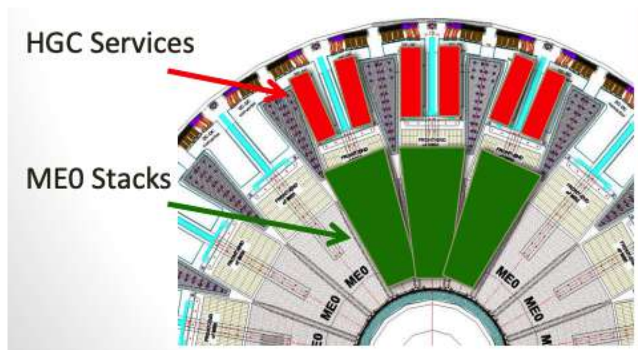

(b)

Figure 3.34: Shows the (a) diagram of the ME0 electronics readout system, and (b) ME0 insertion in the CMS experiment [**35**].

ME0 installation schedule has been designed to avoid conflict with the HGC installation schedule, in particular with the High Granularity Calorimeter (HGC) services installation as shown in the Figure 3.34 (b). ME0 installation will proceed in bursts of 3 stacks (60 deg) at a time, with HGC following right behind ME0 installation and covering ME0 with HGC services. Three low voltage (LV) cables with two LV channels per cable are required to power and run the single ME0 stack. Three high voltage (HV) cables are required to power the six triple-GEM detector along with pipes for the gas in addition to cooling supply and return lines.

4

R&D on Indian GEM foils

"I was taught that the way of progress was neither swift nor easy."

– Marie Curie

The GEM is the new age detector for nuclear and particle physics experiments. It is comprised of an excellent insulator (Kapton/Apical) having a thickness of 50 μm which is covered with 5 μm copper layer on both sides and pierced with a regular array of holes. From its invention, CERN has been the sole supplier of the GEM foils until recently when few private companies started manufacturing GEM foils under the transfer of technology (TOT) from CERN. However, it's a long process to validate the foils delivered by these companies for claiming that the GEM detectors made from them are compatible with the high scientific standards. Along these lines, an India based company Micropack Pvt. Ltd. began fabricating both double and single mask GEM foils. This chapter is broadly divided into two parts first part is about the double mask foils production and testing and second half about the single mask requirements, production and testing. At first The Micropack Pvt. Ltd has produced first few 10 cm $\times$ 10 cm double mask GEM foils, which were then distributed to few collaborating partners for testing reliability and performance of foils before they can be accepted by the scientific community. Characterization of three such foils have already been performed by studying their optical properties using a CCD scanner. Using these foils a triple-GEM detector has been built and various performance characteristics have been measured. We specifically discuss measurements on gain, resolution and gain uniformity, by utilizing local quality control setups particularly build at DU. It is important to study various long and short term effects on these foils due to the applied voltage as well as the flux of the incident particles. We also report the effect on gain stability of triple-GEM detectors due to the polarising field induced by X-rays on the polyimide foils. A measurements of variations in the effective gain at very high particle flux of the order of MHz/mm^2 has been presented. Because of the double mask technique, the size of the GEM foil was constantly constrained so to overcome this issue single mask technique was developed in year 2010. Micropack produced the first batch of 30 cm $\times$ 30 cm single mask foils in a joint effort with DU. A triple-GEM detector was constructed using these foils to test the fundamental quality controls, which include effective gain measurement, energy spectrum, and gain uniformity. Along with this, few advance studies which include discharge probability, rate capability, and charging up for this detector and foils have been discussed.

4.1 Double mask GEM foils

The GEM, first proposed by Fabio Sauli in 1997 [**11**, **12**, **40**], is a composite grid consisting of two conducting surfaces separated by a thin insulator (i.e. Kapton/Apical) etched with a regular matrix of open channels. Detectors built using these foils prove to be one of the most promising particle detectors in various scientific fields such as nuclear and particle physics, astronomy as well as medical diagnostics [**41**, **42**]. This is due to their excellent position resolution [**43**], good timing resolution [**44**], high rate detection capabilities [**45**], low ion backflow [**46**], design flexibility and large area coverage [**47**]. An increase in beam energy and luminosity in various accelerator facilities generated a lot of interest to use GEM detectors for future experiments or upgrades of existing experiments [**21**].

Initially, Micropack has started manufacturing GEM foils using CERN's patented double-mask (or bi-conical) [**48**] etching processes. A detailed description of the fabrication process can be found in Ref. [**49**]. To start with, 10 cm $\times$ 10 cm GEM foils having $\sim$600,000 holes with an inner hole diameter of 50 μm, outer hole diameter of 70 μm and pitch (i.e. the distance between the center of two neighbouring holes) of 140 μm have been manufactured.

4.1.1 Foil production

Several Indian Institutions, including the University of Delhi, are part of the muon detector upgrade project of the CMS experiment at the LHC. Indian groups are planning to contribute approximately one fifth of the total GEM detectors required for the CMS GE1/1 upgrade and future GE2/1 upgrade. As a result, an intensive R&D program on GEM detectors has been initiated at these institutions. Micropack Pvt. Ltd. in Collaboration with Indian Institutions have embarked upon the development of GEM foils in India.

In the later part of 2013, Micropack signed a TOT agreement with CERN for the development of GEM foils in India. After continuous efforts, refining of processes and repeated trials, Micropack has been successful in realizing 10 cm × 10 cm double mask GEM foils, meeting the standard dimensional requirements. The double-mask GEM foils were produced by Micropack in a similar fashion as produced at the CERN PCB workshop [**50**], using photo-lithographic techniques in which hole patterns are transferred to the copper-clad polyimide substrate using microscopic masks placed on the top and bottom of the substrate. A 15 μm thick photo-resistive layer is applied on both sides of the substrate and the mask is placed on top of the base material and engraved on the photo-resist by UV-light exposure. The foil used was a 50 μm PI (Apical Type NP) film with 5 μm copper foil on either side. Several solvents and acid baths are used to etch copper layer to form the copper holes. The polyimide is then dissolved by chemical etching using the copper layer as a mask.

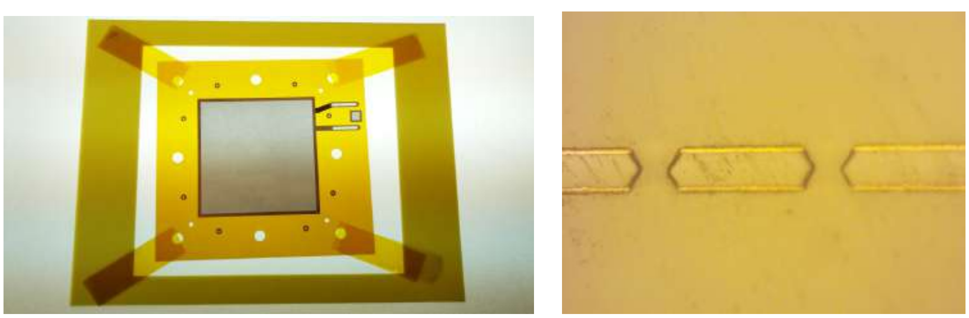

(a) (b)

Figure 4.1: Shows the (a) 10 cm × 10 cm GEM foil encapsulated in a frame, and (b) Cross-sectional view of the foil showing the double cone structure of the engraved holes.

Figure 4.1 (a) shows the newly produced 10 cm × 10 cm GEM foil. Figure 4.1 (b) shows the cross-sectional view of the foil showing the double cone structure of the engraved holes. The realization of the foils has been achieved primarily through accurate lithographic and controlled chemical processes with a double cone hole structure to enhance the end gain. In order to qualify these GEM foils as commercially and scientifically reliable, a number of quality control tests needed to be performed. Therefore, we have characterized the foils by studying their optical to render them usable for further applications.

4.1.2 Optical assessment

The GEM foil performance depends heavily upon the hole geometry and their pattern. A GEM foil with a 140 μm pitch using a hexagonal hole pattern contains approximately 600,000 holes. Any irregularity or defect in the hole pattern and its geometry can profoundly affect their performance. It becomes therefore very important to study the hole geometry structure of the foil and to locate every glitch and piece of debris which could lead to foil failure. Though the qualitative estimate of hole density and diameters can manually be studied using optical microscope but such a technique can become labor intensive especially when there are large number of holes to be analyzed. To overcome this problem, various techniques have been developed to study the optical properties [**51**, **52**], where geometrical properties of the foils have been measured using an automated 2D CCD scanner. However, in our study we have used a slightly different approach to explore the geometrical properties of the GEM foils. Each of the foils were scanned using Micro lensing technique with an AF-S Micro Nikon 40 mm 1:2.8G lens where multiple images of micrometer resolution per pixel were captured. A soft box (1 m $\times$ 1 m) light source has been used to provide uniform illumination to the GEM foils. A sketch of the optical measurement setup is shown in the Figure 4.2.

The quantities that have been optically measured are the inner and outer hole diameters. The various kinds of possible imperfections that have been observed are un-etched areas, under-size hole, oversize holes, without hole areas, excess etching and burnt holes. All these imperfections are shown in the Figure 4.3. Also, the scan with the front light ON and the back light OFF has been performed as to make the scan sensitive to the outer holes. For the inner holes of the foil, the scan has been performed with the front light OFF and back light ON.

To assess the entire area of the foil, each of the foil were divided into several sub-sectors. While capturing inner holes, the foil was divided into 54 (9$\times$6) sub-sectors, whereas to capture outer holes the foil was divided into 56 (8$\times$7) sub-sectors. Images

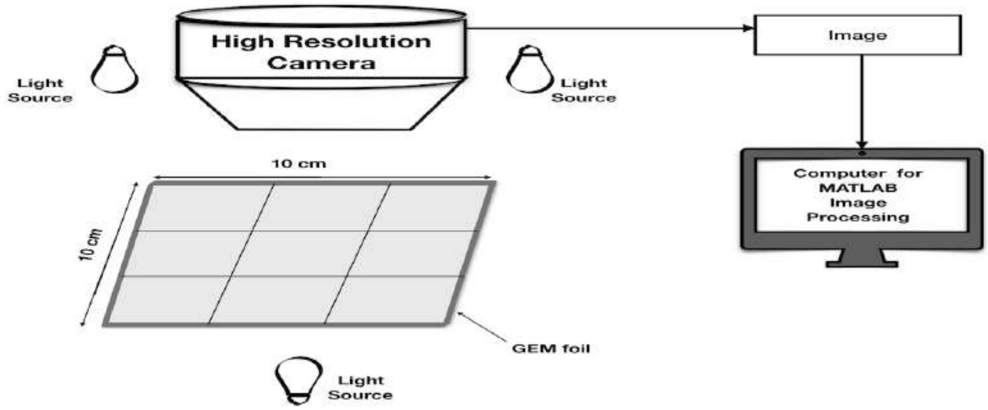

Figure 4.2: Shows the sketch of the setup used for the optical measurements.

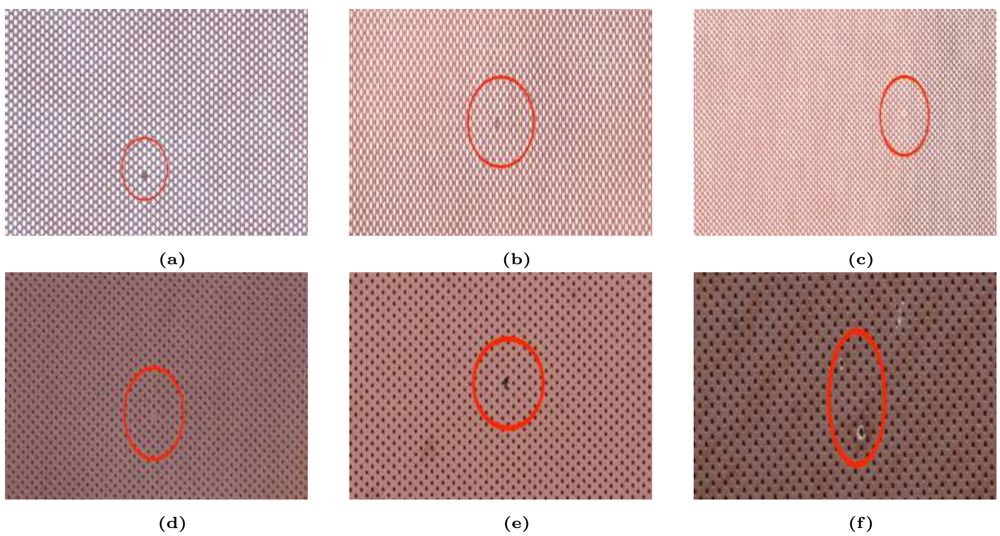

Figure 4.3: Shows the observed imperfections in the foils: (a) un-etched area, (b) under-size hole, (c) over-size hole, (d) missing hole, (e) excess etching, and (f) burnt area.

were captured in such a way that each image corresponds to a sub-sector. Each captured image has been then processed using an Image Processing Toolkit within MATLAB [**53**], which contains built-in algorithm specifically designed to convert the pixel information obtained from images into numerical measurements. Therefore, the toolkit has been used to convert the primary image acquired by the camera into gray-scale image as shown in the Figure 4.4 (a). In order to obtain the binary threshold to separate the holes from background, the gray scale image was converted into intensity histogram as shown in the Figure 4.4 (b). The left peak in the figure represents the light reflected back from the edges of holes and screen behind the foil while the right peak represents the light from the copper surface. Each of the holes were labeled for

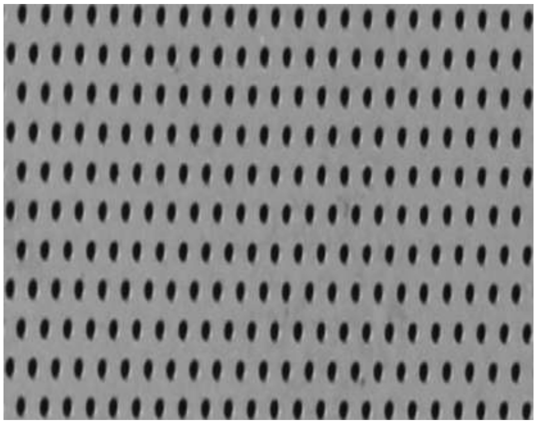

(a)

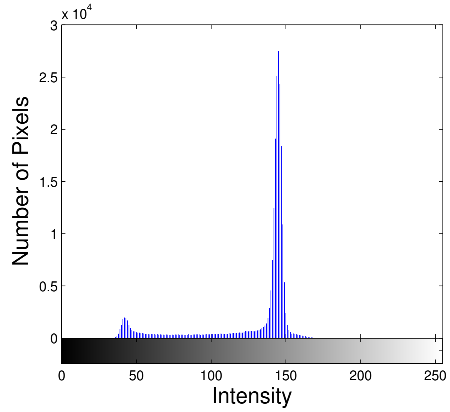

(b)

Figure 4.4: Shows the (a) image formed in gray-scale, and (b) histogram of gray-scale image for the calculation of gray threshold.

each sub-sector. The hole diameter in pixels were calculated for each side of the GEM foils.

The data generated from MATLAB has been processed further using ROOT [**54**] to estimate the mean diameter in pixels of inner and outer holes for each sub-sector and finally for the entire foil. The diameter values in pixels were converted into micrometers using the image resolution of inner and outer holes as 5.6 μm/pixel and 7.2 μm/pixel, respectively. An example of the hole size distribution of inner and outer holes are shown for one of the sub-sectors in the Figure 4.5.

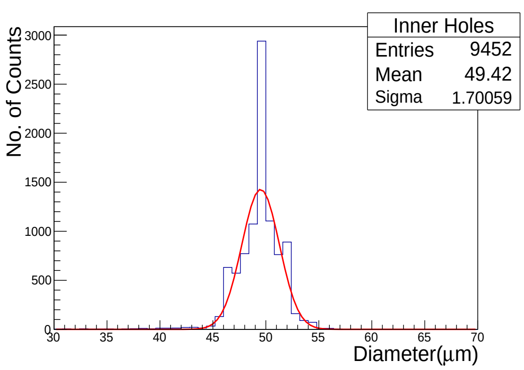

(a)

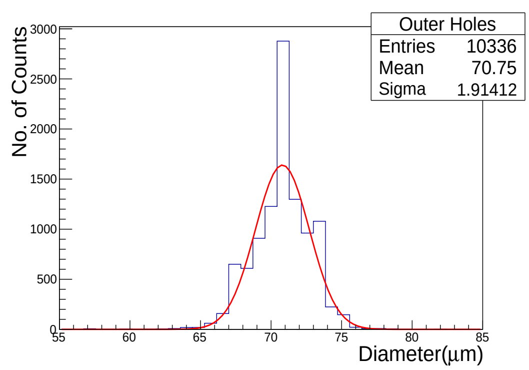

(b)

Figure 4.5: Shows the hole size distribution of (a) inner, and (b) outer holes for one sector.

From the fit to the distribution of holes diameter for each sub-sector, we obtained the mean diameter and standard deviation values for all the sub-sectors. As a result, we obtained 54 values of mean and sigma corresponding to 54 sub-sector for inner holes and 56 values of mean and sigma corresponding to 56 sub-sectors for the outer holes. We then statistically combine these individual means and sigmas of each sub-sector to estimate the mean diameter and standard deviation for inner and outer holes for the entire GEM foil.

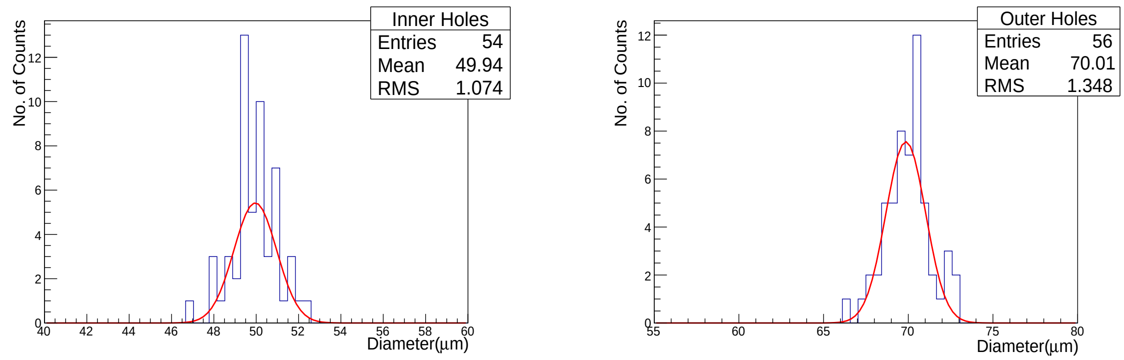

(a) **(b)**

Figure 4.6: Shows the mean diameter of (a) inner holes of all the sectors, and (b) outer holes of all the sectors. The hole distributions were fitted with Gaussian functions to extract values for mean and standard deviation as shown in the Figure 4.7.

The distribution of mean diameters of all the sub-sectors for inner and outer holes of one GEM foil is shown in the Figure 4.6. The mean hole diameter for the entire foils estimated from Gaussian fit of this distribution gives a value of 49.94 μm and 70.01 μm for inner and outer holes respectively. The standard deviation obtained from each sub-sector has been statistically combined to extract the value over the entire foil and was found to be 1.60 μm and 2.02 μm for inner and outer holes respectively. The pitch obtained from the optical measurement is 140.0 $\pm$ 2.4 μm. The mean diameter of inner and outer holes for all the three foils are shown in the Figure 4.7.

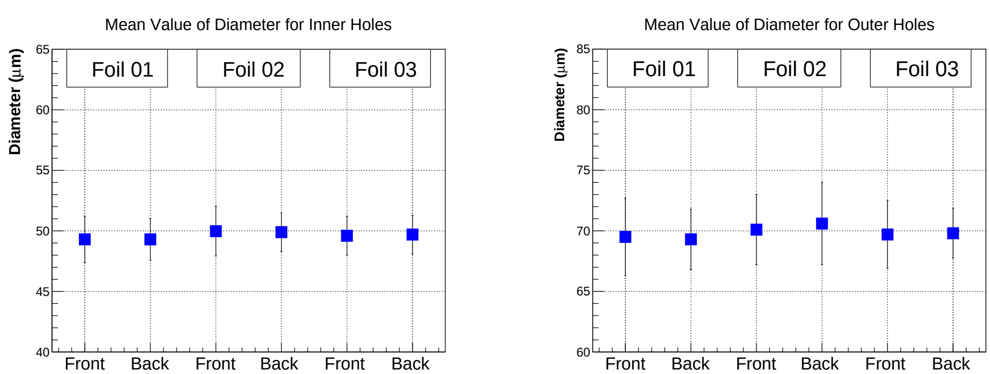

(a) **(b)**

Figure 4.7: Shows the mean diameter for (a) Inner, and (b) outer holes for each side of GEM foils. The error bars represent the 1 standard deviation error obtained from statistical combination of the standard deviations of hole diameter distributions of each sub-sector.

The error bars on the mean diameters shows the value of standard deviation. The findings are consistent with the double mask GEM foils produced else where and in use [**52**, **55**]. Further, in the Figure 4.8 (a), scanning electron microscope (SEM) images of one of the GEM foil are shown, and Figure 4.8 (b) shows the average inner and outer hole diameters of 49.51 μm and 72.55 μm, respectively with an average pitch of 140.44 μm. This measurement of hole diameters from SEM measurement is in fair agreement with the values obtained from optical assessment.

The number of each type of defect in Apical Type NP or in Copper has been estimated and are shown in the Figure 4.9 (a) and (b). There were a total of 785 number of defects including Copper and Apical Type NP out of approximately 600,000 holes in one of the 10 cm $\times$ 10 cm GEM foils which correspond to 0.13% of defects.

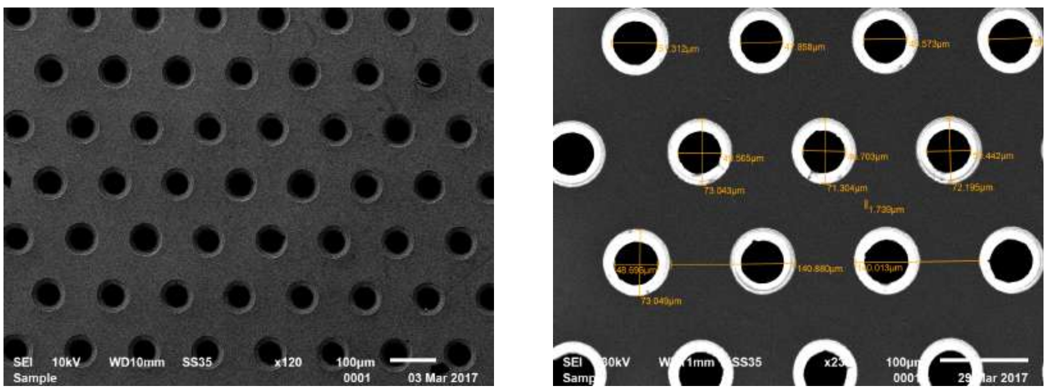

(a) (b)

Figure 4.8: Shows the (a) SEM image at μm level resolution showing the overall uniformity of the foil sample, and (b) hole diameters and the pitch under SEM at μm level resolution.

Similar number of defects were also observed in other two foils. Earlier optical studies on CERN foils have revealed similar defects. More recently, ALICE collaboration has also started an effort to optically characterize all the foils that they are planning to use for Time Projection Chamber (TPC) detector [**56**, **57**].

4.1.3 Performance of triple-GEM detector

Normally, a triple-GEM gaseous detector is built using a drift cathode, three GEM foils and one of them shown in the Figure 4.10 (a), and Printed Circuit Board (PCB) anode or readout board is shown in the Figure 4.10 (b), mounted as a stack inside a closed epoxy frame [**58**]. This frame is used for gas tightness having openings located at two diagonal corners, one for the gas inlet and another one for the gas

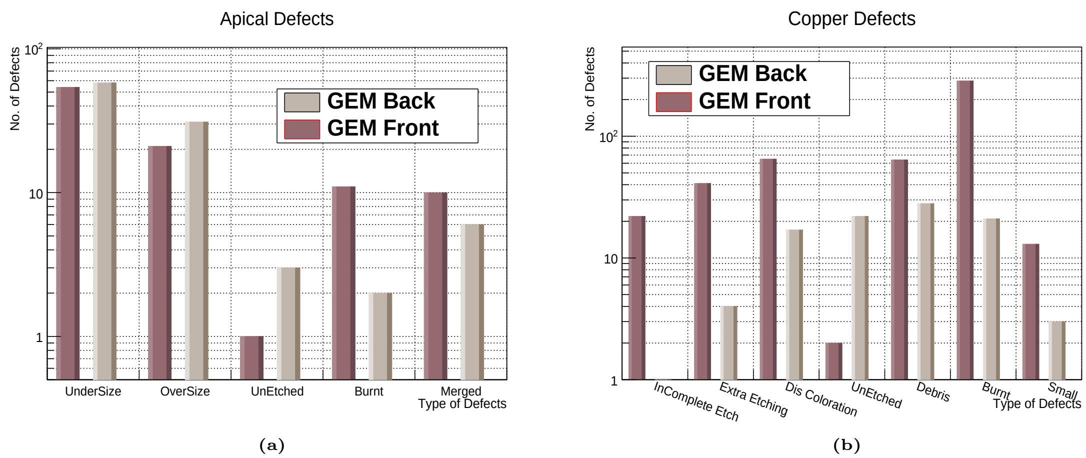

Figure 4.9: Shows the number of defects seen in (a) Insulator (Apical Type NP), and (b) Copper for one of the 10 cm $\times$ 10 cm foil.

outlet. Usually, GEM detector works in a gas medium in which gas ionisation takes place due to the electron acceleration under the influence of electric field. Since, working under purely noble gas medium can cause the avalanche creation beyond the limits which leads to sparks and cause a permanent damage to the detector, we also require lower proportion of a quenching gas in the medium. Many studies have been performed on the selection of gas mixture to be used for this detector, details can be found in Ref. [**58**, **59**, **60**, **61**]. We have used the gas mixture with Argon (70%) and CO_2 (30%) for our studies.

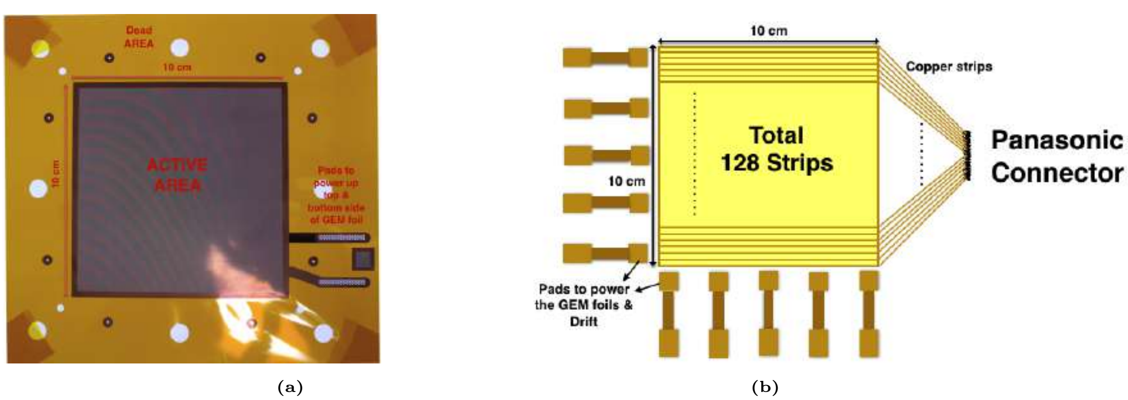

Figure 4.10: Shows the (a) one of the GEM foil manufactured by Micropack Pvt. Ltd. with two HV pads at bottom right, and (b) schematic of readout board used having 128 strips connected to a Panasonic to LEMO connector

A triple-GEM detector prototype [**62**] has been built with a drift gap, two transfer gaps and an induction gap of 3 mm, 1 mm, 2 mm, and 1 mm respectively as shown in the Figure 4.11. This is the same gap configuration which is used in CMS GEM community for muon-endcap GE1/1 upgrade [**21**]. These gaps are created by placing spacers at the edges of the adjacent GEM foils. The drift region is where the primary electrons are generated and due to the field present in this space, the primary charges move towards first GEM foil. This drift field depends on the potential between the cathode and top metal of the first GEM foil. The electric field generated inside the holes is ∼100 times the field present in the drift region where each hole work as an individual proportional counter. Due to the field inside the holes, electrons gain rapid energy which leads to an avalanche creation. The electrons further created are accelerated towards the second GEM foil due to the transfer field present between the bottom of one GEM foil and the top of the next one. This process is repeated for the succeeding foil with asymmetric potential across the foils and gaps. At last, the induction field, which is present between the last GEM foil and the ground anode, is responsible to deposit most of the charges created in the avalanche on the anode plane.

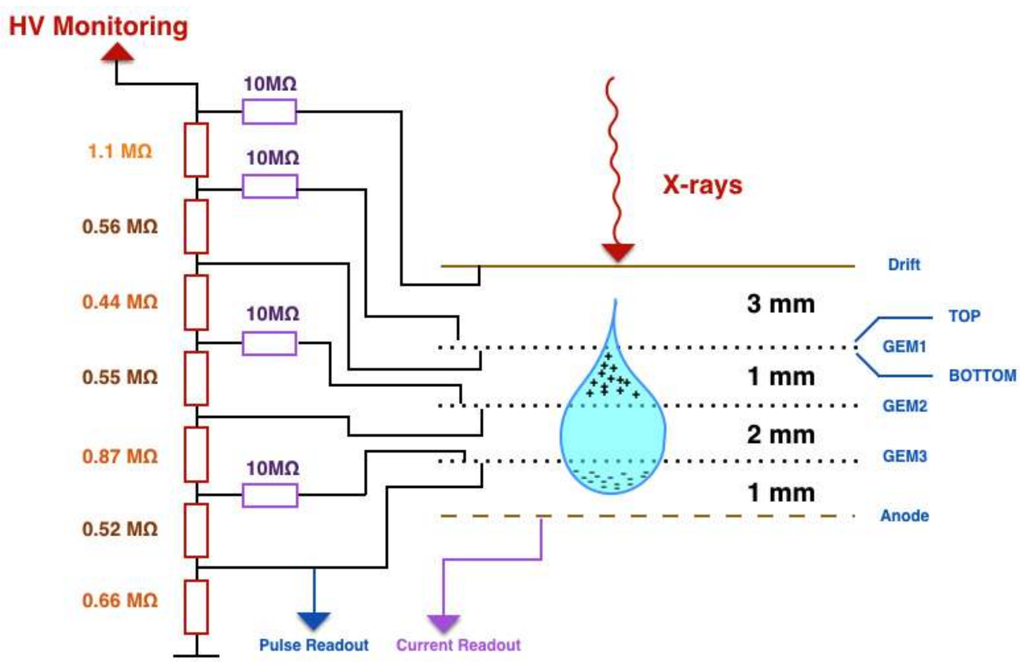

Figure 4.11: Shows the triple-GEM detector prototype with high voltage resistive divider, showing various gap configuration and avalanche formation due to incident X-rays

Each GEM foil is powered using voltage divider network through a single channel (as shown in the Figure 4.11). Additionally, four 10 MΩ resistors (known as protection resistors) are used between the HV divider and drift as well as top of each GEM foil to prevent the excess current flow through the foil in case of discharge. Since each GEM foil is working at nominal gain, the higher effective gain can be reached at lower working voltages. It also lowers the chances of discharge [**63**] inside the active medium. The readout strips detect the charge deposition of the amplified signal and transfer it to the DAQ for further signal processing.

4.1.3.1 Setup

In order to study the characteristics of GEM detector, a setup is shown in the Figure 4.12 has been put in place. The standard gas mixture with 70% Argon and 30% CO_2 is used and flow rate of the gas is kept at 3.0 ℓ/h which is controlled by gas mixing unit with calibrated mass-flow controllers. A readout plane (anode) consisting of 128 strips is used, which is large enough to cover the whole charge cluster. An X-ray source with silver target having characteristic energy of 22.1 keV is used as a generator for the gain measurement.

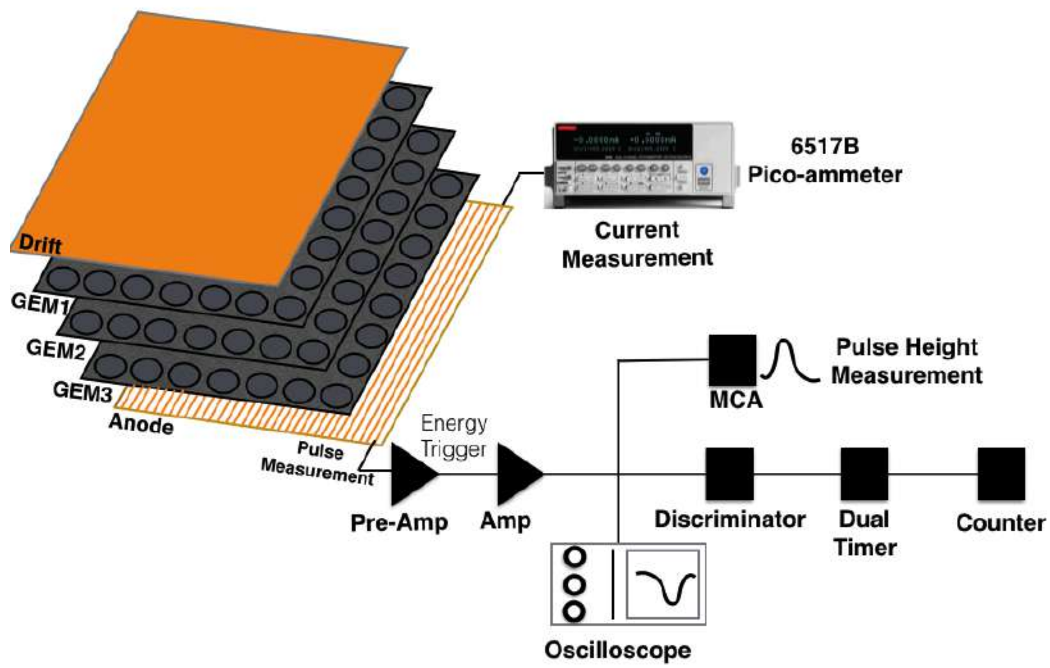

Figure 4.12: Shows the schematic of the setup used for various studies using 10 cm $\times$ 10 cm triple-GEM detector prototype.

The current measurement is performed using the Panasonic to LEMO connector from the readout and fed into Electrometer 6517B [**64**] which is further interfaced using LabView software.

For the pulse measurement, the signal generated at the anode is processed using charge sensitive Pre-amplifier (ORTEC 142IH) and further connected with the Timing Filter Amplifier (ORTEC TFA 474) to amplify and record the signals obtained from the readout strips. The output of the TFA is fed into the Discriminator (ORTEC CFD 935) and rectangular discriminated pulse is sent to the Scalar and Counter for the rate measurement study.

For measurement of energy resolution, multi-channel analyzer (ORTEC MCA 927) is used. Since MCA requires positive pulse hence the polarity of the signal is inverted using TFA. This setup has already been utilized for performing various studies on different prototypes of GEM Detector at DU [**65**].

4.1.3.2 Behaviour under high voltage

After stabilization of the gas mixture inside the detector and reducing the electronic noise, the performance of the triple-GEM detector has been studied. The detector is powered using the HV divider that provides an appropriate voltage for safe and stable operation. The behaviour of the detector is studied by varying the high voltage which results in variation of an electric field across the GEM foils as well as between the four gaps within the detector.

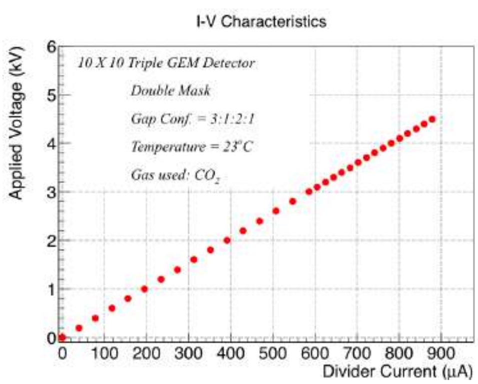

(a)

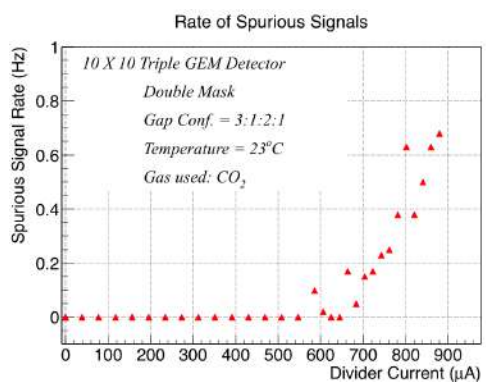

(b)

Figure 4.13: Shows the (a) I-V characteristics of the detector with an equivalent resistance of 5.12 MΩ, and (b) variation of spurious signal rate obtained from GEM3 bottom as a function of the divider current.

In order to avoid any damage to readout electronics as well as detector, it is very important to ascertain the behaviour of the detector under high voltages. Before starting the measurement, a total resistance of the circuit was measured to be 5 MΩ, which includes 4.7 MΩ from HV divider and 0.3 MΩ from HV filter which is placed between the power supply and the detector. According to the standard procedure used by CMS-GEM community [**32**] , GEM detectors having a gap configuration of

3 mm/1 mm/2 mm/1 mm and HV resistive divider as shown in the Figure 4.11 have been operated up to 4.9 kV Volts while flushing non-amplifying gas such as CO_2. Therefore, for this study the detector was flushed with pure CO_2 having a flow rate of 3.0 ℓ/h for 4 hours prior to powering the detector. Using the power supply (CAEN N1470), the voltage across the detector was increased in the steps of 200 V initially upto 3 kV, and after this the voltage was increased in the steps of 100 V and the corresponding current was measured. Simultaneous measurement of signal counts was done for every set of voltage. The rate calculated from these counts is called spurious signal rate which is defined as the rate of signals which are not originated from the ionisation of the gas. The rate of the spurious signal is measured from the bottom of the last GEM foil as a function of the current running through the resistive divider of the HV distribution circuit.

During the operation the detector shows an ohmic behaviour which can be clearly seen in the Figure 4.13 (a). Thus, plotting I-V characteristics shows straight line behaviour and its slope gives us the total effective resistance of the circuit, which comes out to be 5.12 $\pm$ 0.0003 MΩ. As shown in the Figure 4.13 (b), the rate of the spurious signal increases as we increase the voltage/current across the detector and the maximum spurious signal rate observed is 0.7 Hz at a divider current of $\sim$900 μA.

4.1.3.3 Gain measurement

The effective gain is the central parameter of the GEM detector which explains the geometrical as well as the electrical properties together with the gas compositions. Also, in order to localize and detect particle efficiently, a stable and homogeneous gain over a long operation period is necessary.

As explained earlier in this chapter, under the influence of the high electric field the electrons are guided into the GEM holes which leads to the multiplication of the charge. But, due to the fact that not all the amplified charge reach the anode, on the basis of which one can differentiate the "*real*" gain with the "*effective*" gain [**66**]. The definition of effective gain is described in Section 2.2.5 and can be calculated experimentally as:

$$G = \frac{\mid I_{with\ source} - I_{without\ source} \mid}{n_{primary}\ e\ R} \tag{4.1}$$

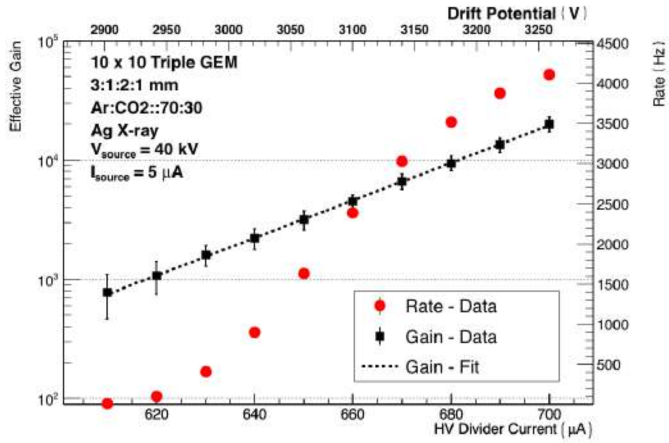

Figure 4.14: Shows the variation of rate and gain of the triple-GEM detector as a function of divider current and drift voltage.

where, $I_{with\ source}$ is the current measured from readout in the presence of X-ray source, $I_{without\ source}$ is the current measured from readout in the absence of any source, $n_{primary}$ are the number of primary electrons created in the drift region which are ∼346 while operating X-rays at a voltage of 40 kV and current of 5 μA, e is the electronic charge and R is the real interaction rate in the drift volume. In order to start the gain measurement we also ramped up the detector to 700 μA. Then, the rate and the corresponding current are recorded both with and without the X-ray source. After this, we decrease the current across the detector in the step of 10 μA and again measure the readout current and the rate for both the settings of X-rays. This procedure is iterated until the rate with and without source becomes equal. As we observe in the Figure 4.14, the effective gain of the GEM detector exponentially increases with an increase in the detector voltage. The maximum measured rate is ∼4 kHz; with a corresponding measured gain of $\sim 2 \times 10^4$ at divider current of 700 μA. For the GE1/1 GEM detector prototype, a gain of more than 10^4 is measured at detector current of 700 μA [**32**].

4.1.3.4 Energy resolution

Energy resolution is ability of a detector to precisely determine the energy of the incoming radiations.

Energy resolution (E_{res}) of GEM detector for incoming X-ray source is defined as the percentage of Full Width Half Maximum (FWHM) to the height of the resulting

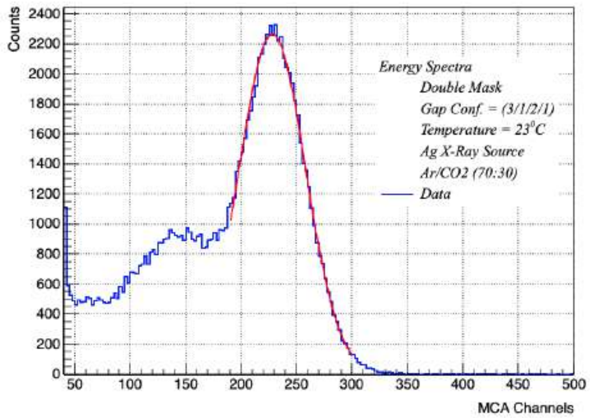

Figure 4.15: Shows the energy Spectrum obtained with X-rays (Ag-target) operated at 40 kV and 5 μA at divider current of 700 μA.

Gaussian peak, and given as:

$$E_{res} = \frac{FWHM}{Peak\ value} = \frac{2.35 \times \sigma}{Peak\ value} \tag{4.2}$$

Figure 4.15 shows a typical energy spectrum [**62**] acquired with the silver target X-ray source. E_{res} as calculated from the peak is $\sim$30% at the divider current of 700 μA across the detector.

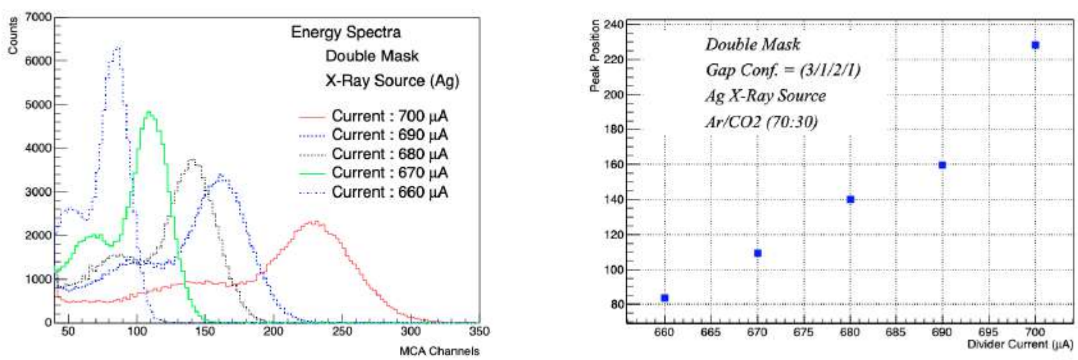

(a) (b)

Figure 4.16: Shows the (a) pulse height spectra for various GEM voltages, and (b) variation of MCA peak position as a function of divider current across the detector.

As in the case of gain measurement of the detector, we again decrease the value of the divider current in the steps of 10 μA and we plot the corresponding energy spectra as shown in the Figure 4.16 (a). As we decrease the current across the detector, the peak position of MCA shifts towards the left which explains that the avalanche electrons decreases with the decrease in the voltage across the GEM detector [**67**]. Figure 4.16 (b) shows the peak position of all the spectra with respect to the divider current which shows an exponential behaviour as expected.

4.1.3.5 Gain uniformity

There are several factors responsible for non-uniformity of gain over the whole surface of the GEM detectors. These includes a variation of gas gaps due to inaccurate stretching, quality of GEM foils, non-uniformity or defects in holes over the foil area, etc. Thus, the gain uniformity test is quite significant for checking the detector response over the entire surface area. For this, we have divided the active region of the detector i.e. 100 cm^2 into 5 $\times$ 5 sectors of equal area. The X-ray source with a collimator was then placed at the centre of each sector and at a particular value of the divider current the gain at each sector was measured.

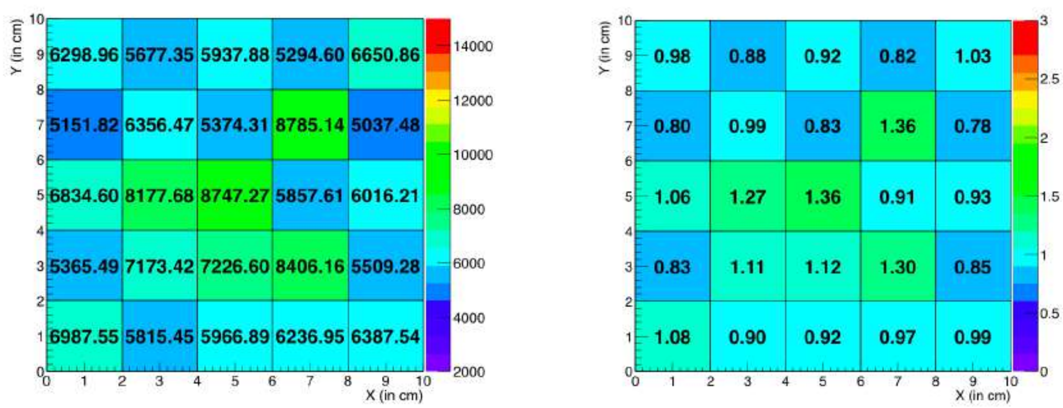

(a) (b)

Figure 4.17: Shows the (a) uniformity of gain for 5 $\times$ 5 equal sectors of 10 cm $\times$ 10 cm triple-GEM detector, and (b) normalized gain uniformity with respect to the average value of gain.

Figure 4.17 (a) shows the effective gain value for each sector of the GEM detector at the divider current of 650 μA. As we can see, the effective gain is higher in the central region of the detector and lower at the corners. This can be accounted as the effect of non-planarity in the foils due to gluing of the frames [**17**]. Figure 4.17 (b) shows the normalized plot of the gain uniformity in which gain value in each sector is divided by the average gain over the entire surface of the detector. This figure also shows the same behaviour i.e. higher values at centre and lower at the edges.

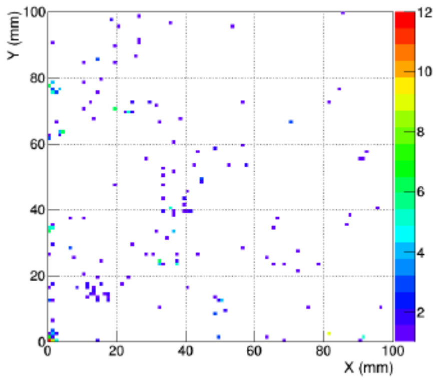

(a)

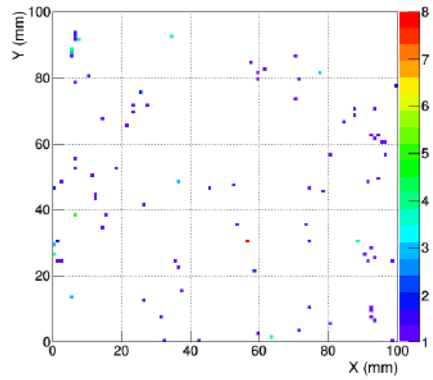

(b)

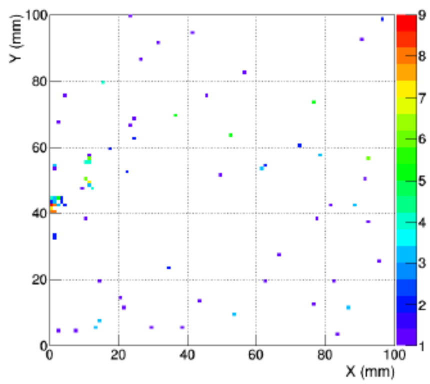

(c)

Figure 4.18: Shows the position of all types of defects present in (a) first GEM foil, (b) second GEM foil, and (c) third GEM foil used in the assembly of the GEM detector.

4.1.3.6 Correlation between foil defects and uniformity

The operational characteristics of a GEM foil can vary with local variation in the size or the shape of the holes. Thus, the distribution and size of the holes over a GEM foil should be uniform to achieve uniform functionality of the detector over the active surface. The process of manufacturing GEM foils can introduce occasional defects which may affect the performance of a GEM detector. During the optical scanning of these commercially manufactured GEM foils, different types of defects were observed like over-etched, under-etched, unetched, burnt, merged holes etc., which were mainly due to the etching process [**68**]. These are broadly divided into two types: insulator defects and copper defects. Since the gain of the detector also depends on the geometry of the foils and the defects present on it [**69**], we have prepared a defect map for each foil showing the position of the various defects. This

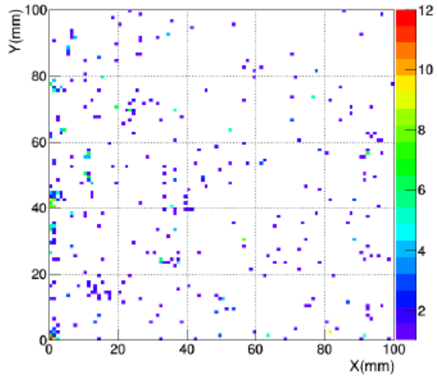

Figure 4.19: Shows the total defects after stacking the three foils inside the detector.

is performed by dividing the foil into 5 $\times$ 5 sectors of equal area so that we can see one to one correspondence of the defects with the results of uniformity. Each sector was further divided and enlarged so that the defects were easily seen through the naked eye.

Since the defects present in the foils are of the order of μm so to make them visible in the figure each defective hole is enlarged 20 times ($\sim$1 mm in the figure). Also, each figure includes the defects from both the sides of the GEM foil as well as both types of defects (i.e insulator and copper defects). Figure 4.18 shows the position of all the defects of those three foils which were used to build the detector. We have also prepared a defect map, as shown in the Figure 4.19, summarizing total defects of these foils according to the stack orientation of the foils inside the detector.

As seen from the figure, the defects due to all three foils were distributed over the entire area of the detector. In order to estimate the effect of defects, we need to compare the Figure 4.19 with the uniformity shown in the Figure 4.17. Even though the defects are distributed over the entire foil(s), if we look closely then some sectors of the foil(s) have more defects than others. For example, the total defects in (x, y) (0-20 mm, 0-20 mm) sector are comparatively more but the same sector in the Figure 4.17 does not show any reduction in gain. The gain in other sectors also does not show any direct correlation with the defect map. This may be due to the fact that the actual number of defective holes are quite small compared to good holes (i.e. 785 defective holes in 600,000 holes which corresponds to 0.13% of defects) and hence it does not affect the performance of the foil(s).

4.1.4 Stability measurements

The active area of the GEM foil used for these studies is 10 cm × 10 cm; they have been manufactured with the double-mask etching technique to have 70 μm (50 μm) outer (inner) hole diameter with a pitch of 140 μm. The triple-GEM detector was built with 3 mm/1 mm/2 mm/1 mm for Drift/Transfer1/Transfer2/Induction gap configuration and all the foils were powered up using a high voltage (HV) resistive divider whose schematics is shown in the Figure 4.20 (a).

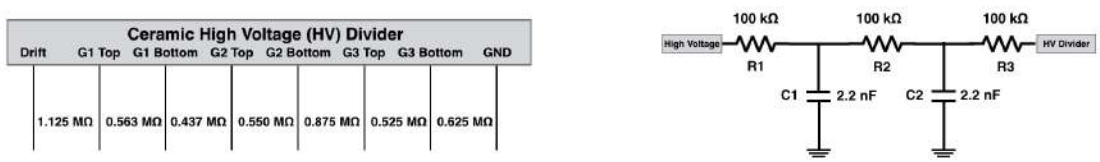

(a) (b)

Figure 4.20: Shows the schematic of (a) high voltage resistive ceramic divider, and (b) high voltage filter used for triple-GEM detector prototype

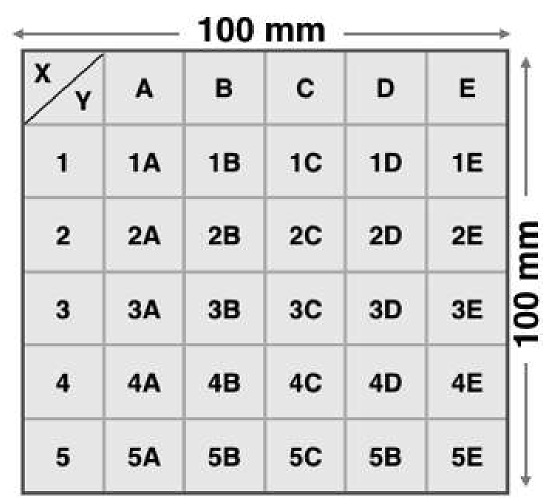

Figure 4.21: Shows the schematic of nomenclature used for 5 by 5 grid.

The measurements with the GEM detector are mainly affected due to the noise, which has been controlled with a ground shielding placed on the top of the readout board to shield the detector from the background noise. A high voltage low pass filter (Shown in the Figure 4.20 (b)) was placed between the power supply and detector to reduce the electronics noise so that a stable voltage can be provided to the electrodes.

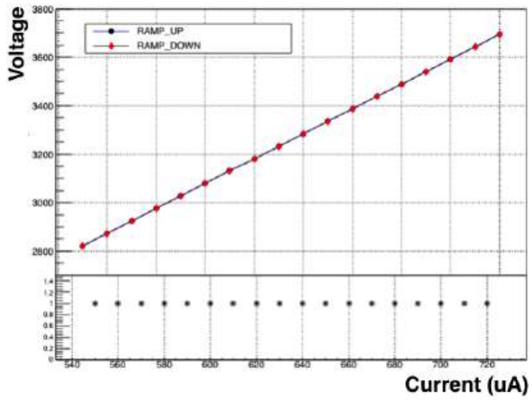

Figure 4.22: Shows the I-V Characteristics of the detector showing ohmic behaviour while ramping up (black circles) and ramping down (red diamonds) at different operating voltages.

The active area of the GEM detector was divided into 5 $\times$ 5 equal sectors each covering an area of 20 mm $\times$ 20 mm and their nomenclature was fixed as shown in the Figure 4.21. A 1 mm collimator was placed in the front of the X-ray and it was placed perpendicular to the detector touching the drift volume. Therefore, while exposing the particular sector with X-rays, our setup ensured that no other neighbouring sectors got exposed to the beam.

For the studies reported here, a mixture of Argon (Ar) and Carbon dioxide (CO_2) in the ratio of 70% and 30% respectively have been used [**60**]. The main advantage of this mixture is that these gases are non-flammable, eco-friendly and that they are easily available and relatively cheap [**61**, **62**]. A gas mixing unit is used for supplying the fixed mixture and the flow rate was controlled by the mass flow controllers which has been set to 5 ℓ/h for all the measurements. The same setup i.e. shown in the Figure 4.12 has been used for the current and pulse measurements.

4.1.4.1 Gain stability

The effective gain of a detector is a unique parameter used to relate the general properties which include the electrical and geometrical properties together with the gas composition. The gain stability is very important for gaseous detectors because any unwanted variation in gain causes a change in efficiency.

As mentioned high voltage divider is used to power up the GEM foils and using it a current-voltage (I-V) curve is obtained when the voltage is first ramped up and then ramped down across the divider. The measured current shows same slope for ramping up and ramping down and hence no hysteresis in I-V has been observed [**70**].

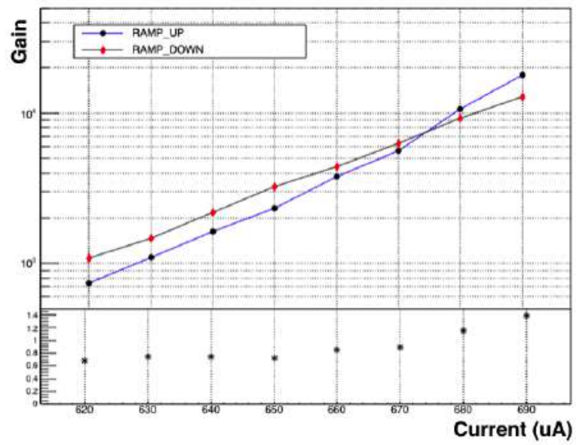

Figure 4.23: Shows the effective gain of the detector as a function of current across the detector while ramping up (black circles) and ramping down (red diamonds).

Figure 4.22 shows an ohmic behaviour at a given range of divider current across the detector with a total resistance of the circuit as 5 MΩ (which includes the resistance of HV filter as 0.3 MΩ and HV divider as 4.7 MΩ).

In order to understand the hysteresis as a function of other parameters of the GEM detector, a measurement of effective gain has been performed. The measurement has been done while ramping up and then ramping down the divider current across the detector. The outcome of this exercise is shown in the Figure 4.23. The measurements were taken by varying the current in steps of 10 μA from 620 μA to 690 μA by setting the corresponding voltage and then in the reverse direction with waiting time of 2 minutes between each measurement. As expected, the gain varies exponentially with respect to the current. However, looking at the variation in the log scale, the slope of the gain has been found to be different while ramping up and ramping down. This is a manifestation of hysteresis effect in gain [**71**] of the detector which is due to the charging up or polarisation effects in the foils.

The gain stability of a triple-GEM detector is affected mainly by two effects: the charging up and the polarisation effects. The charging up effect occurs due to the multiplication of the charge near the surface of the foil which results in the trapping of the charge in the hole [**72**] . The polarisation effect, on the other hand, is due to the movement of the charges inside the polyimide layer after applying the voltage across the foil. It is independent of the charge deposited by the particle but depends upon the geometrical and electrical properties of the foil. The polarisation effect can be explained with the help of a trapping model, as described in [**73**] for Kapton-H film. Due to the absorption of the photon by polyimide during the irradiation of X-rays, electron excitation in the polyimide occurs. The presence of an electric field across the foil makes these electrons move in its direction unless they get captured by some trapping center in the foil. This process results in an increase of the anode current which in turn increases the gain. However, when the dynamic equilibrium is reached the gain starts to saturate.

To estimate the gain stability in time and variations in the gain due to polarisation effect, a series of measurements of gain of the detector was carried out for several hours. The anode current was recorded while irradiating a sector of the detector with Amptek Mini-X X-ray [**74**] source for 30 seconds. This process was repeated at an interval of 5 minutes for the same sector until a stable gain value had been achieved. These measurements were performed at various values of gain of the detector to estimate the dependency of divider current (or gain) on polarisation effect. During the measurement ambient temperature was continuously monitored using an ARDUINO based system.

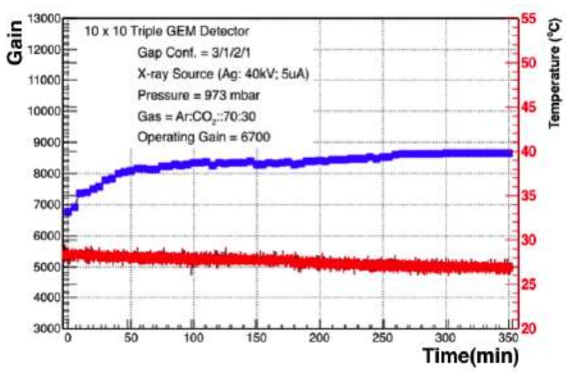

Figure 4.24: Shows the variation of effective gain (blue squares) of the detector as a function of time having initial gain of 6.8k for triple-GEM detector and variation of temperature was also recorded every second and plotted (red continuous line).

Figure 4.24 shows the value of gain with respect to time. The measurement started with a gain of 6.8k and the plateau was observed after 6 hours showing a difference of ∼29% in gain. During the measurement, the ambient temperature was monitored continuously. From the measurement it is visible that the percentage difference of change in gain and the time taken to reach the stable gain depends upon the initial value of the gain of the detector. For an initial gain of 11k and 15k, the time to reach the gain plateau is 5 hours and 2.5 hours as shown in the Figure 4.25 (a) and (b) respectively. From this measurement, we conclude that the gain variation due to the polarisation can be mitigated by switching ON the detector for several hours prior to the start of precise measurements of timing and efficiency of the detector.

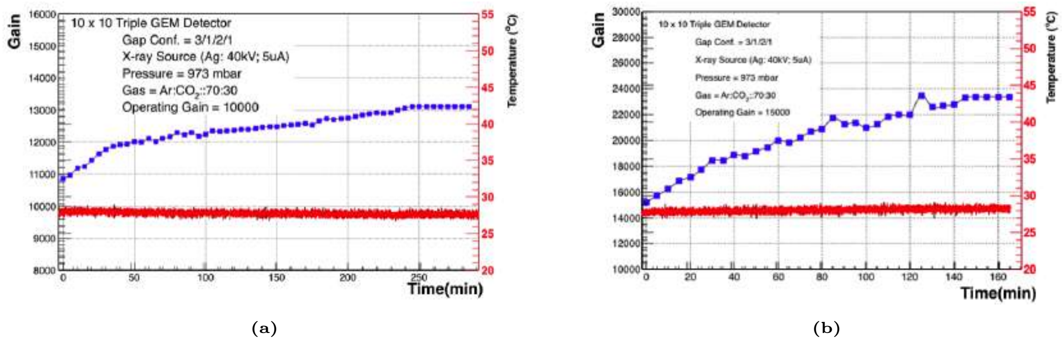

Figure 4.25: Shows the variation of effective gain (blue squares) of the detector as a function of time having initial gain of (a) 10k, and (b) 15k for triple-GEM detector and variation of temperature was also recorded every second and plotted (red continuous line).

Since the polarisation effect is a global phenomena, a gain scan was performed before and after the test to disentangle the local and global fluctuations. A comparison of gain at different positions before and after the polarisation effect is shown in the Figure 4.26.

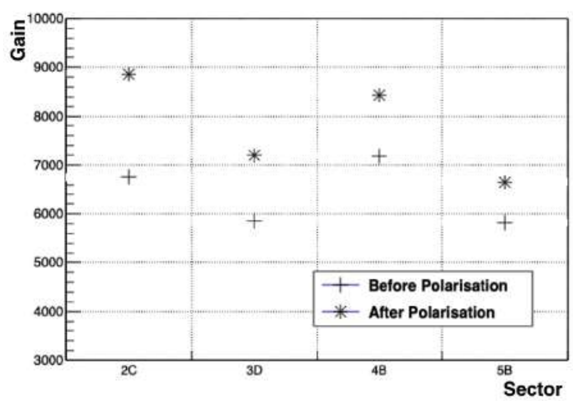

Figure 4.26: Shows the comparison between the initial and final gain scans for the polarisation measurement of the triple-GEM detector. The detector was irradiated at position 2C by X-ray source with an initial gain of 6.7k.

Initially, the X-ray source was placed at sector 2C according to the nomenclature shown in the Figure 4.21 for ∼6 hours. The gain at the position (3D, 4B,and 5B) which were not irradiated is increased by a few tens percent with respect to the initial gain value. And this increase in gain is due to the polarisation which is a global phenomena.

4.1.4.2 Rate capability

The MPGD technologies were mainly introduced in response to the limited rate capability of the Multiwire Proportional Counters (MWPC) to handle fluxes higher than several kHz/mm^2. Reducing the amplifying structure to the microscopic scale helps quickly mitigate the effect of space charge which results in higher gains even for the high incoming particle flux [**25**].

GEM detectors are known for their stable operation even at very high particle flux. In the particular case of the triple-GEM technology, we can distinguish three different regions depending on the incoming flux of particles. The detector shows stable gain when the incoming flux is of the order of a few tens of kHz/mm^2 (horizontal region), at a particular value of divider current (or gain) across the detector. As the flux increases to few MHz/mm^2 (upward region) the gain increases as well. Further increase in the value of flux results in the decrease of the gain (downward region).

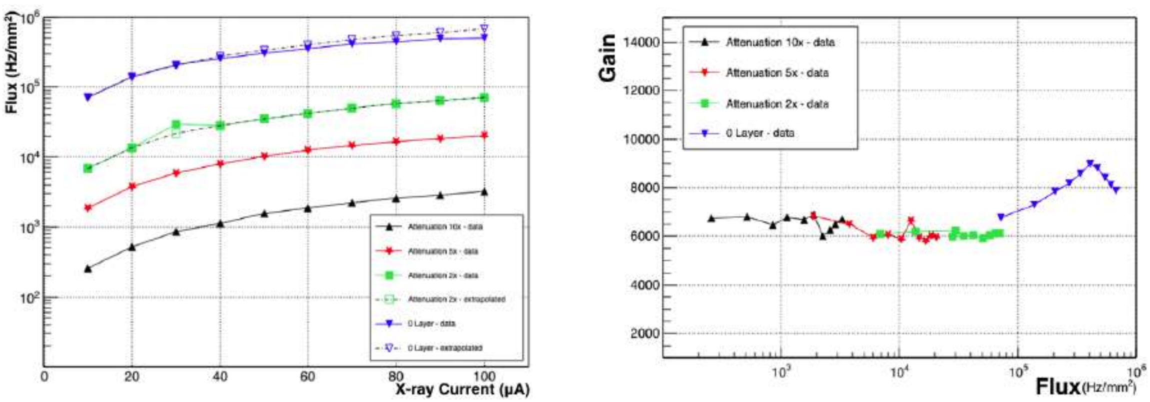

(a) (b)

Figure 4.27: Shows the (a) flux provided by the X-ray source using different layers of Copper attenuators vs. the X-ray source supply current, and (b) rate capability for triple-GEM detector operated at a nominal effective gain of approximately 6.5k.

To check the dependency of the effective gain with the X-ray flux, known as rate capability, a collimated beam of 22.1 KeV X-rays of about 1 mm beam diameter from a Silver X-ray generator has been used to produce the primary ionisation in the conversion volume.

To estimate the effective gain as a function of the particle flux, the X-ray was placed on a particular sector to measure the amplified detector current. The X-ray flux was adjusted by changing the X-ray tube power or by attenuators. The flux delivered to the detector was calculated by taking into account the X-ray rate measured by the discriminator and the known diameter of the collimator. Since, for the higher rate, discriminator starts to saturate due to pile up, the interaction rate on the detector was measured using the copper attenuators. Once the attenuation factor is known, the interaction rate can be extrapolated to obtain the rate without attenuator. Figure 4.27 (a) shows the estimated flux for different power of the X-ray source. Figure 4.27 (b) shows the measurement of rate capability at the initial detector gain of 6.5k. The detector gain is stable from lowest flux used up to about 50 kHz/mm^2. For higher fluxes, up to approximately 0.4 MHz/mm^2, the effective gain increases as a function of flux. Further increasing the flux results in a decrease of the effective gain.

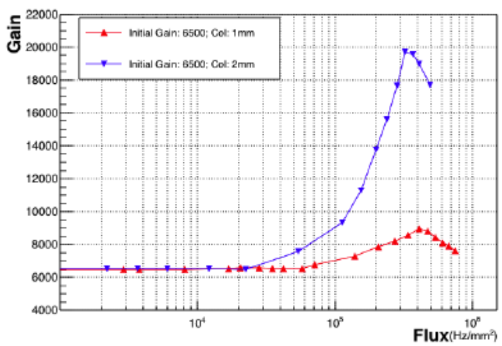

(a)

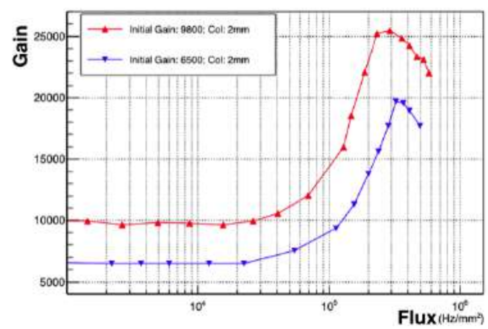

(b)

Figure 4.28: Shows the dependence of effective gain as a function of flux (a) having same initial gain but different collimator, and (b) different initial gain but same collimator for triple-GEM detector.

The rate capability studies were further extended by using two different collimators in front of the X-ray source, and the result is shown in the Figure 4.28 (a) with an initial detector gain of 6.5k for both collimators. By changing the collimator from 1 mm to 2 mm, the area of the sector under irradiation increases 4 times which causes a steeper increase in the effective gain. The rate capability measurement was performed for initial gains of 6.5k and 9.8k with 2 mm collimator, as shown in the Figure 4.28 (b). The observed change for different initial gain is related to the charge density in the detector. And higher nominal gain leads to the appearance of the observed effects at lower particle fluxes with the increase being steeper while a decreased gain will shift the effect towards higher fluxes. This is due to the fact that the field distortion depends upon the number of ions generated and accumulated in the detector. For a higher nominal effective gain of 9.8k, the number of ions in the detector volume is larger than compared to a detector operated at a gain of 6.5k.

4.2 Single mask GEM foils

In the double mask etching technique, it is essential to keep the mask alignment between top and bottom layers within 5-10 μm, due to which the size of GEM foil is limited to few tens of cm^2 of area. To overcome this restriction a new etching technique was developed by CERN in 2010, known as single mask etching technique. Employing single mask technique the foils with asymmetric holes with lesser hole asymmetry has been produced having wide hole opening of 85 μm on one side and narrow hole opening of 70 μm on the other side. The impact of these hole asymmetry has been understood very well in the past [**75**]. Micropack Pvt. Ltd. has produced the first batch of 30 cm $\times$ 30 cm single mask GEM foils. Using these foils a triple-GEM detector has been built and various fundamental characteristics were measured to test the validity of these foils.

In this work, all the measurements were carried out on the triple-GEM detector built using the 30 cm $\times$ 30 cm single mask GEM foils. The detector have been assembled using a self-stretching technique known as "No Stretch, No Stress (NS2)" technique [**29**, **76**] to stretch the GEM foils. The three GEMs were sandwiched between the drift and readout board surrounded by the gas frame made of epoxy for the gas tightness. The readout board having an active area equal to the GEM foils and having six Panasonic connectors, with 128 strips each, to readout the induced signal have been used. For the present detector the drift gap, transfer gaps, and induction gap were kept at 3 mm, 1 mm, 2 mm, and 1 mm respectively. The GEM detector was powered up using the 8-pin integrated resistors high voltage divider with the first pin connected to the drift board, second to the seventh pin connected to the top and bottom of the three GEMs and the last pin connected to the ground as shown in the Figure 4.20 (a). The measurements for single mask GEM foils have been performed with the same gas mixture of Ar/CO_2 in a ratio of 70%/30%. A similar setup (shown in the Figure 4.12) has been used for pulse and current measurement.

4.2.1 Effective gain, gain uniformity and energy spectrum

One of the important characteristics of any gaseous detector is their gain [**66**, **77**]. It is important to evaluate the gain for each input voltage to check any non-linearity in the performance of the detector. By measuring the current of the signal produced by the GEM detector and the rate of the primary ionization, the effective gain of the detector is estimated according to the formula mentioned in the Section 4.1.3.3.

The detector was then irradiated with Amptek Mini-X X-ray source from the drift side and the rate of the X-ray was estimated by counting the signal using the schematic shown in the Figure 4.12 and the output current was measured directly using the Keithley 6517B pico-ammeter according to the same schematic. The Figure 4.29 (a) shows the measurement of effective gain along with the rate with respect to the divider current. It shows the exponential behaviour of effective gain with rate plateau. The maximum gain at 700 μA is 15.4k [**32**].

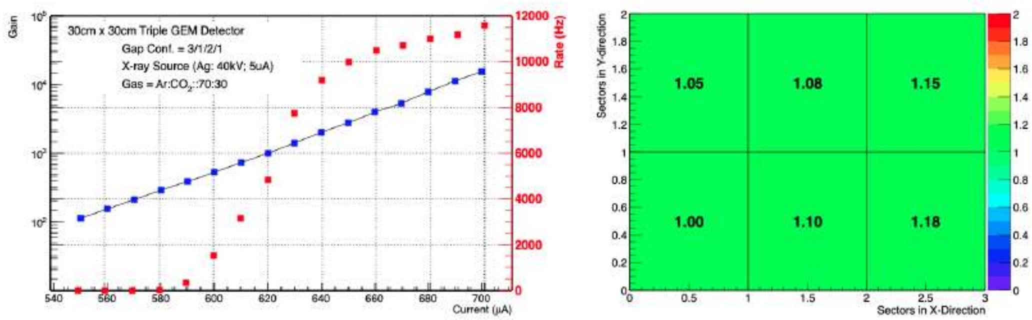

(a) (b)

Figure 4.29: Shows the (a) effective gain (Blue) and rate (Red) of the detector as a function of divider current, and (b) gain uniformity over the surface of the GEM foil.

The variation of gain over the large area GEM foils is an important factor of the triple-GEM detector. This have been estimated with X-ray exposing the whole detector. Uniformity of the gain is very important feature because most of the characteristics like rate capability, discharge probability, etc. are dependent upon the gain. The readout board contains six identical sectors each having 128 strips and the gain has been measured in all the sectors. Figure 4.29 (b) shows the measurement of effective gain for each sector. The maximum variation of gain has been measured to be $\pm 8.2\%$ with respect to the mean value of gain. This is well within the allowed variations [**21**].

The energy spectrum of the detector was obtained with two different sources Amptek Mini-X X-ray and ^{109}Cd source. From this spectrum, energy resolution can be calculated using the main peak. We used a multi channel analyzer (ORTEC MCA 927), which allow us to inspect each individual event in the detector to measure the energy resolution with the ^{109}Cd source. We obtained the energy resolution to be 30%. This is in conformity with the measurement obtained with CERN foils [**67**].

Figure 4.30 (a) and (b) shows the energy spectrum obtained using Mini-X X-ray and ^{109}Cd source respectively. The energy resolution calculated from the main peak of the ^{109}Cd source spectra comes out to be 30%.

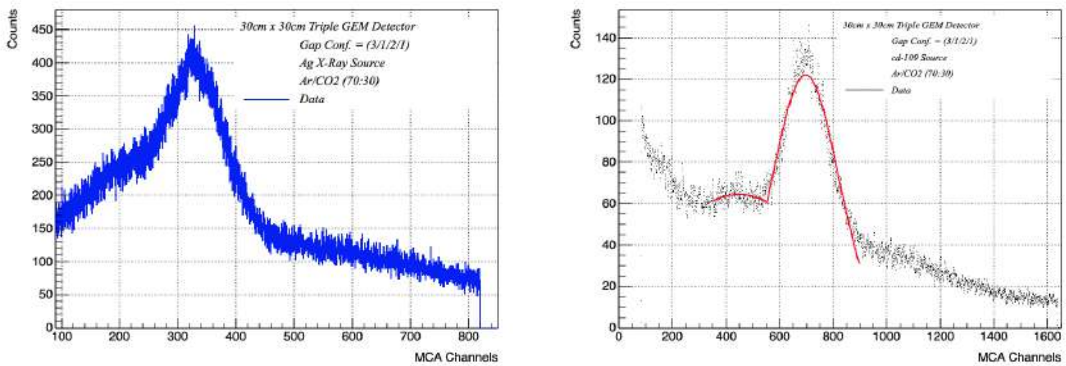

(a) (b)

Figure 4.30: Shows the MCA spectrum obtained using (a) Amptek Mini-X X-ray, and (b) ^{109}Cd Source.

4.2.2 Charging up

The polarization effect occurs due to the movement of the charge inside the polyimide and it is independent from the charge deposited by particles. On the other hand, When the GEM detector is irradiated then due to the deposition of the charge inside the GEM hole the field in the hole gets modified. This is a well understood phenomena of GEM detectors known as charging up [**45**, **78**]. The durability of the gain over time is essential for reaching a stable detector performance. The charging up occurs during the multiplication process inside the GEM holes. Due to the excellent resistivity of the polyimide the free charges get attached to the walls of the holes until the equilibrium condition is reached. The effect mainly depends upon the number of charges crossing the holes per unit time. The amplitude and stabilization time are mainly dependent upon the two things; interaction rate and the effective gain.

The setup described in the Figure 4.12 has been used to measure the charging up effect. The electrodes were powered up for more than 12 hours prior to start of the measurement to avoid the polarisation effect [**79**]. The ^{109}Cd source was attached to the detector and the effective gain and energy spectrum have been obtained in the regular interval of 5 and 2 minutes respectively. For each measurement of energy spectra, the measured pulse height was fitted with the Gaussian distribution to extract the mean position of the peak.

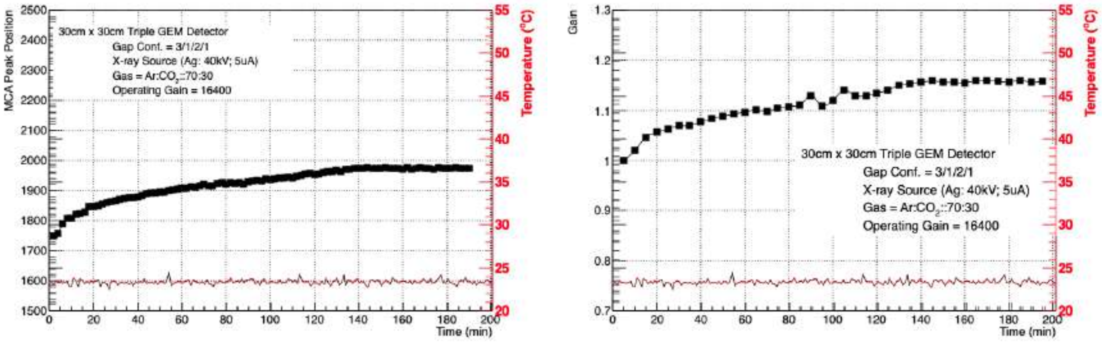

(a) (b)

Figure 4.31: Shows the (a) variation of MCA peak obtained using ^{109}Cd source as a function of time, and (b) variation of effective gain using ^{109}Cd source as a function of time for triple-GEM detector and variation of temperature was also recorded every 30 second and shown by dashed lines above.

The Figure 4.31 (a) and (b) shows the energy spectrum and effective gain obtained at regular interval of time, respectively. The effective gain and energy spectrum measurements reveals that they increased up to 1.15 and 1.13 times respectively with respect to the initial value. The time required to reach the plateau was ~3 hr for both the measurements. This variation mainly depends upon the modified electric field inside the hole. Both the quantities start reaching the sort of plateau because no further deposition of charges takes place on the surface of the polymide due to continuous multiplication of charges [**72**]. The amplitude and time taken to reach the plateau is in well agreement with the measurements done in the past with the CERN foils [**17**].

4.2.3 Rate handling measurement

The Multi-wire proportional chambers are limited in rate handing capacity upto 10^5Hz/mm^2 and crossing this limit causes the decrease in gain due to the space charge effect. The GEM detectors are proven to show a stable gain for the flux higher than 10^5Hz/mm^2. In this study, we have taken measurement at the rate exceeding of 10^5Hz/mm^2 to check the behavior of commercially manufactured single mask GEM foils at higher flux.

Figure 4.32 shows the measurement of the rate capability obtained by varying the flux of the incident X-ray photons [**25**] using Amptek Mini-X X-ray with a characteristic energy of 22.1 keV with 1 mm collimation. Under the irradiation of X-rays, the amplified current at different settings of X-ray were recorded using the pico-ammeter

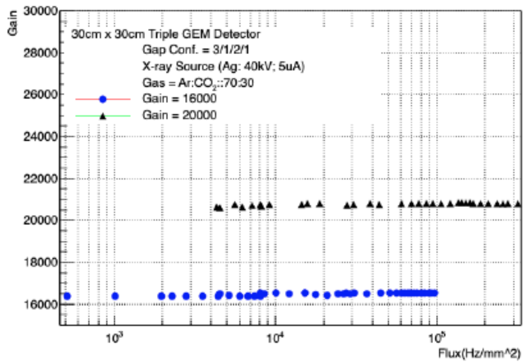

Figure 4.32: Effective gain of the detector as a function of incident flux for two different gain values (a) 16.4k, and (b) 20.5k. No deterioration of gain with increase in the flux have been observed.

connected to the readout of the detector. Copper attenuators have been placed in front of the X-ray beam to vary the flux. An event-by-event signal have been readout using the setup shown in the Figure 4.12.

The rate capability have been measured for the two different values of initial gain i.e. ∼16k and ∼20k. For the initial gain of 16k and 20k, the maximum flux reached were 10^5Hz/mm^2 and 0.3×10^6Hz/mm^2 by pushing the X-ray to the maximum intensity. No decrease in the gain have been observed for either of the gain values [**80**].

4.2.4 Discharge probability

The main limitation of the GEM detectors are the tendency of spark or discharge [**63**] inside the detector. The spark or discharge occurs when the multiplication increases the Raether's limit [**81**, **82**]. The applications of all the MPGD technologies requires that the GEM detectors operate at sufficiently high gain; and in case of any high intense incident beam the spark with finite probability are produce which can damage the detector. The discharge probability is defined as the ratio of the number of discharges produced by the incident beam to the total number of particle crossing the detector. For counting the number of discharges an antenna based system was placed near the high voltage divider to identify the spark with the enhancement of the operating current. The counting of the number of particles crossing the detectors were measured from the readout using the NIM modules with the schematic shown in the Figure 4.12. The gain of the detector have been varied from 20k to 70k, while the detector was irradiated with the ^{241}Am highly ionizing α-particle. The α-particles were chosen as source because it can produce the number of primaries 100 times more than minimum ionizing particle (MIP).

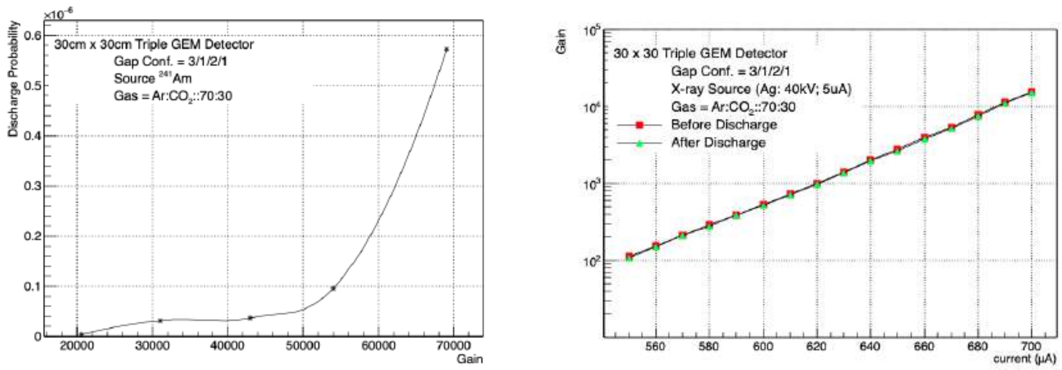

(a) (b)

Figure 4.33: Shows the (a) discharge probability as a function of Gain obtained using ^{241}Am source, and (b) effective gain measurement before and after discharge probability measurement for triple-GEM detector.

The Figure 4.33 (a) shows the discharge probability measurement as a function of different value of the gain. The discharge probability at the nominal gain of 10^4 was calculated to be 3.4×10^{-9}, which shows that roughly one discharge occurs every 10^9 heavily ionizing particle passing through the detector [**83**, **84**]. The lower discharge probability is because of the two reasons; Firstly, the asymmetric distribution of voltage in the three GEM foils and sharing of the gain between the three amplification stages, which is independent of the readout plane which helps in stopping the propagation of the streamer. Secondly, due to the design of the big size GEM foils i.e. the foil is divided into several segments each with an area of 100 cm^2. A 10 MΩ protection resistor is connected to each segment to limit the maximum energy and stop the propagation of the discharge. An effective gain measurement have been performed before and after the discharge probability test to identify any possible degradation of the GEM foil/detector in the area under the irradiation, which is shown in the Figure 4.33 (b). This clearly shows no performance degradation due to the discharges.

5

Gain uniformity and induction gap thickness measurement

> *"You'll never change your life until you change something you do daily. The secret of your success is found in your daily routine."*
>
> – John C. Maxwell

Many existing experiments and their upgrades in High Energy Physics (HEP) are proposing and utilizing Micro Pattern Gas Detectors (MPGDs) to have large area coverage [**47**]. Before using these detectors in an experiment it is important to perform the precise QA/QCs to ensure their performance [**32**]. And this requires continuous improvement in these QA/QC procedures such that it is reliable in terms of measurement, data generated should be reproducible, and provide as much information as possible. Along the same line, a method has been developed to qualify the induction gap in a GEM detector. It is of paramount importance to look for the flatness of the induction gap because the gain of the GEM detector is linearly dependent upon it. Non-uniformity in this gap cause variation of gain over the surface (i.e. the gain uniformity) as a consequence worsen the overall energy resolution of the detector, compromise the compatibility with the dynamic range of the electronics, and stability of the detector. This work propose the use of multichannel analog readout chips, used for gain uniformity measurements, to measure the uniformity of the induction gap [**17**]. This gives the direct comparison between the two measurements, the overall gain of the detector and induction gap, and to see if they are correlated. Using the existing setup to understand the detector more does not have an additional over-load to the QA/QC procedure. The result of this measurement does not only help in QA/QC procedure but also helps in R&D measurements in the validation of the prototypes

5.1 Commissioning of SRS

The installation of the SRS [**85**, **86**] requires the FEC connected to the ADC using a PCIe connector installed in a standard euro-crate to convert an analog signal into digital generated by the ASIC. The connection between the ASIC and the FECs is done using the HDMI cables.

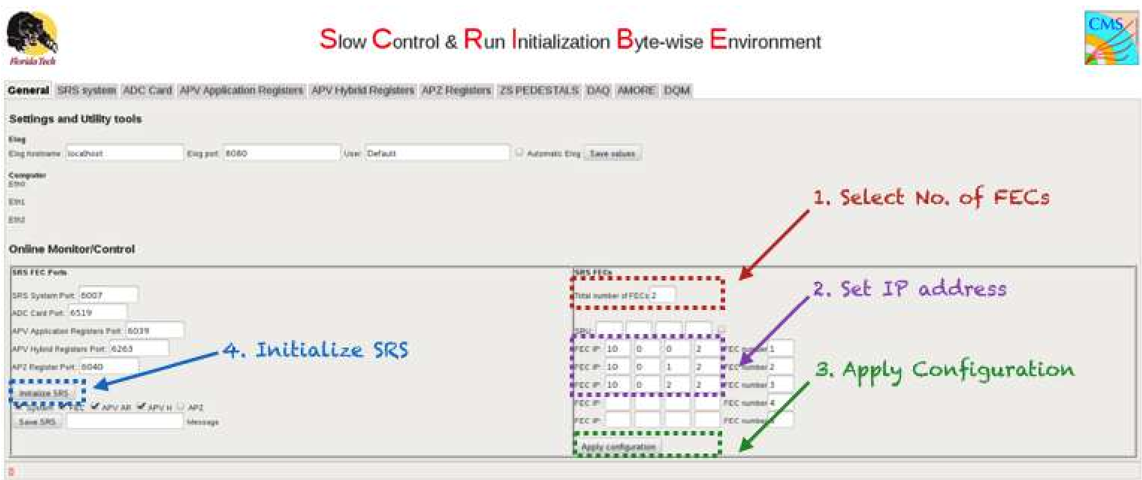

Figure 5.1: Shows the steps to select the number of FECs and Initialize SRS using SCRIBE.

The hardware setup is controlled with computer using an ethernet interface and the settings of the parameters for SRS could be done using the Slow Control and Run Initialization Byte-wise Environment (SCRIBE) software. Finally, the online data-taking is performed using the DATE software-defined by the ALICE group. After installing this DAQ software in the dedicated computer one can start the initialization process of the SRS system.

The very first step after powering ON the FECs is to define the hardware components (FECs, IP, etc.) and initialize them, which could be done using the SCRIBE online software as follows:

1. Select the number of FECs active in the general tab and press "Apply Configuration".

2. Initialize the SRS by pressing the "SRS Initialize" again in general tab.

3. Set the proper registers for the ASIC in the APV application register tab.

as shown in the Figure 5.1.

Ensure that the number of FECs chosen in SCRIBE should match with the quantity of FECs dynamic in the equipment tab of "editDb" as shown in the Figure 5.2 which could be called using the terminal by simply running an alias of editDb. Furthermore, specify the IP addresses for all the active FECs in "allfecs.txt" file present in the "/srsconfig" directory, which are "10.0.0.2" and "10.0.1.2" for the particular case.

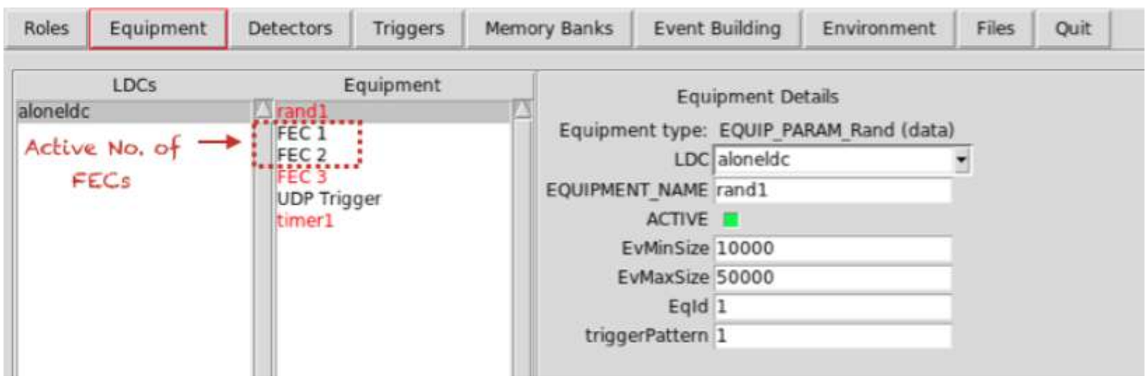

Figure 5.2: Shows the output of editDb command.

After making sure that FECs are initialized the next step is to set the correct phase which depends upon the hardware components in use and needs to find again if any change in hardware occurs. To set the correct phase at least one APV [**87**] pair (master and slave) must be connected and call a routine that loops over the HDMI slots of ADC card and look for the APV(s) connected. This can be done simply using a script "./zs_config PLL" present in the "/var/www/cgi-bin" directory. This will create a ROOT file named with the timestamp and contains phases for all the APVs connected. The correct phase is defined as the one where the initial header reaches the value below 1300 and the reset signal in between each time bin also taking reading between 3000-1300, as shown in the Figure 5.3.

After finding the correct phase it is equally important to load this phase in the appropriate file, which is "zs.txt" present in the "/srsconfig" directory, in this file edit the first line. Also, edit the last line of the "fec_phase.txt" file present in the same directory i.e. "/srsconfig".

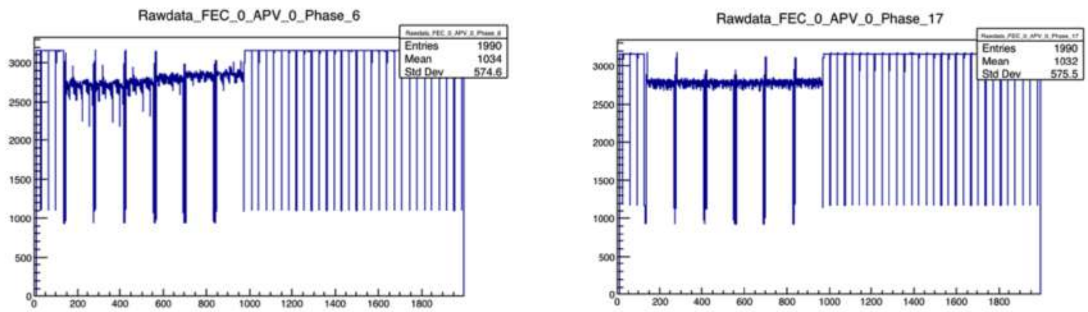

(a) (b)

Figure 5.3: Shows the (a) incorrect phase , and (b) correct phase for an APV25 ASIC.

The next step is to set the correct FEC masking, the "ZS button" in the DAQ tab of SCRIBE provides automatic configuration of the number of APV chips connected to the HDMI slots of the ADC. The system should know in advance number of APV chips connected and their respective slots in a particular FEC, for this, a zero suppression (ZS) script must be initiated which first runs a loop over all HDMI slots and then, once it knows the number of APVs and their respective HDMI slot, a second loop configures only for those APV(s). Configuring an HDMI slot where no APV is connected, a warning flag raises and it prevents data-taking to start.

This procedure could be done manually as well instead of running ZS script, for this set the FEC mask in the file "fecmask0" and "fecmask1" located in the directory "/srsconfig" for the FEC1 and FEC2 respectively. Here are an example of some of the hexadecimal values corresponds to the number of chips connected to the ADC:

1. 0000000000000001 means HDMI0 master APV at ADC1
2. 0000000000000010 means HDMI0 slave APV at ADC1
3. 0000000000000011 means HDMI0 master and Slave APV at ADC1
4. 0000000000000100 means HDMI1 master APV at ADC2
5. 0000000000001000 means HDMI1 slave APV at ADC2
6. 0000000000001100 means HDMI1 master and Slave APV at ADC2
7. 1111111111111111 means all HDMI with all master & slave APVs at all ADC ports

The above binary values must be written in hexadecimal number, for instance; 0000000000000011 corresponds to 3 and 1111111111111111 corresponds to ffff.

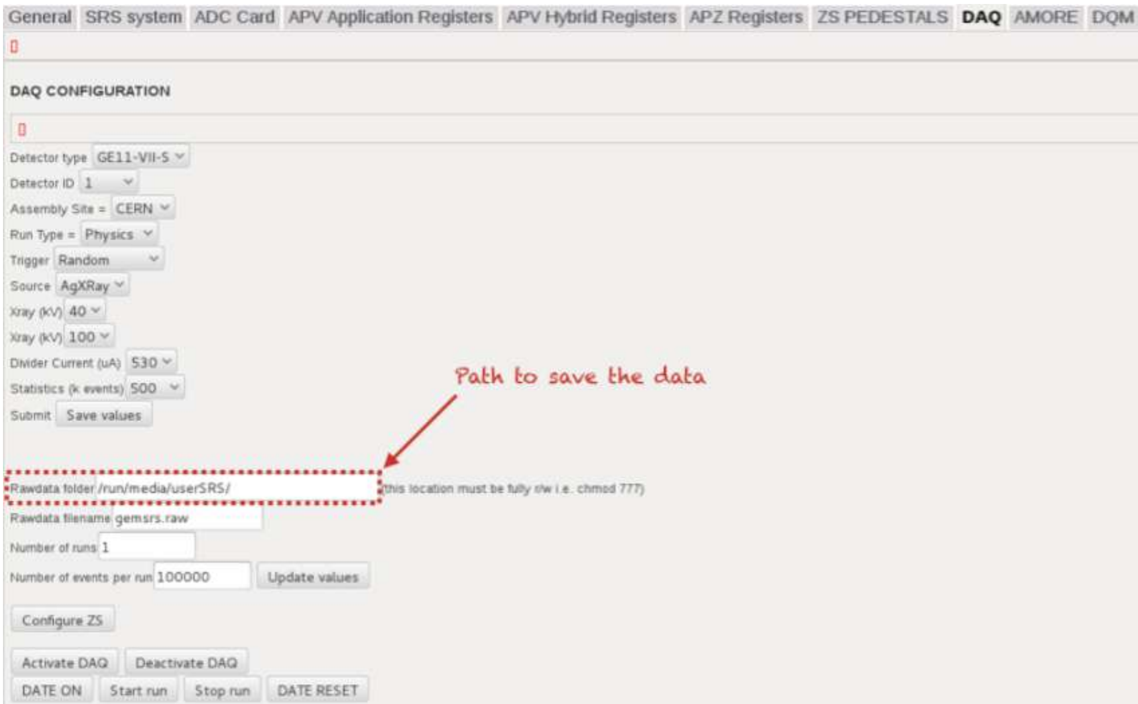

Figure 5.4: Shows the step to set the path in DAQ tab of SCRIBE to save the collecting data.

After the successful initialization and commissioning of the SRS system, the next step is to find the noise present in each channel of the APV connected to the RO board of the detector. For this, the APV chips should be connected to the RO board or left floating and the detector should not be powered ON. This is known as the pedestal run and can be obtained by invoking the routine "./zs_script.sh" located in the directory "/var/www/cgi-bin". This will generate a root file with the name "APZ_sigma_pedestal.root" at the path mentioned in the DAQ tab of the SCRIBE as shown in the Figure 5.4 and every time this routine called it will re-write the same file so it is important to save this file in a different directory or with a different name for later tracking of the APV history.

After collecting the pedestal and sigma make sure no noisy channel(s) present in the APV. It is important to look at the pedestal and sigma because the ZS threshold is calculated using sigma distribution of each APV. To find the threshold the value of sigma for each channel of APV is plotted in a distribution and the mean of that distribution defines the threshold for ZS. Figure 5.5 (a) and (b) shows the example

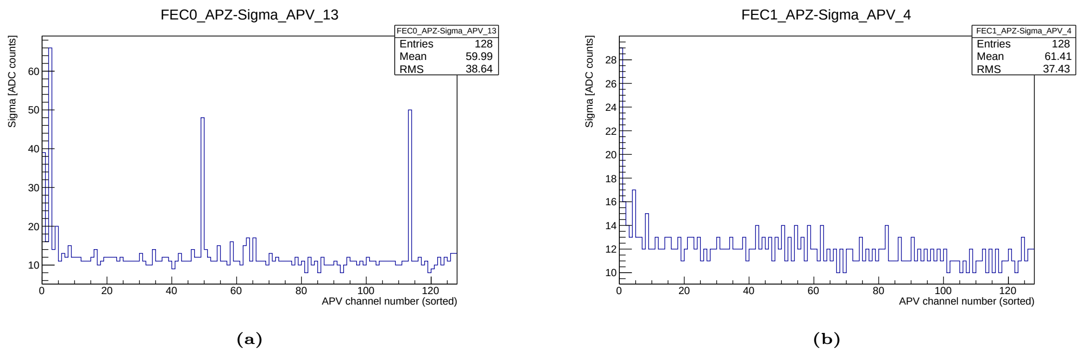

Figure 5.5: Shows the (a) pedestal with noisy strip(s) , and (b) pedestal with no noisy strip for an APV25 ASIC.

of both noisy and good APV respectively. The noise of the APV can be reduced by doing proper grounding (prefer a "star" ground). It was observed during the data-taking that using the APV chip with many noisy channels causes "DATE" software to crash frequently.

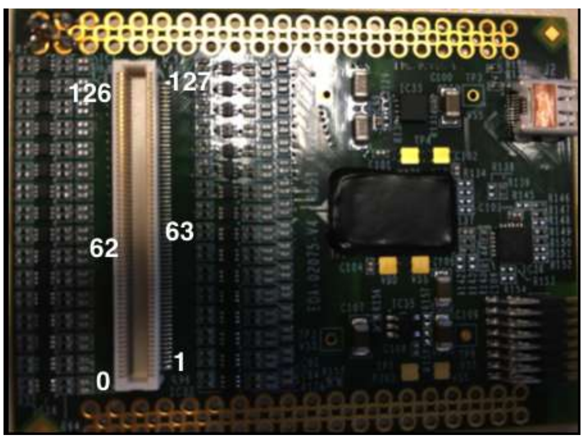

Figure 5.6: Shows the APV25 ASIC/chip.

At the point when pedestal of each APV does not incorporate any noisy strip and no strange behavior observed, configure the zero suppression firmware on the FECs from the terminal by running the following commands in the given sequence;

1. /var/www/cgi-bin/nconf.sh : To initialize the FEC-APV memories to standard
2. /var/www/cgi-bin/zs_config.sh : To calibrate pedestal of APV chip as mentioned in fecmask0 and fecmask1 file
3. /var/www/cgi-bin/nconf.sh : To put all default setting again issue this command.

The data taking using APV is meaningful only when the mapping functions between the APV channels and RO board strips defined correctly which helps in locating the possible defect present either in the RO board strip(s) or APV channel(s).

In GE1/1 generation X detector, three types of mapping functions are used because RO strips and APV channels are not mapped one to one [**17**]. In APV chip pins are characterized as the zeroth pin on the left side of the Panasonic connector and the first pin is on the right side of the Panasonic and so on, as shown in the Figure 5.6. The mapping function mainly depends upon the strips which are below vias or above vias, where vias is used to send the data from the bottom of the RO to the top as shown in the Figure 5.7.

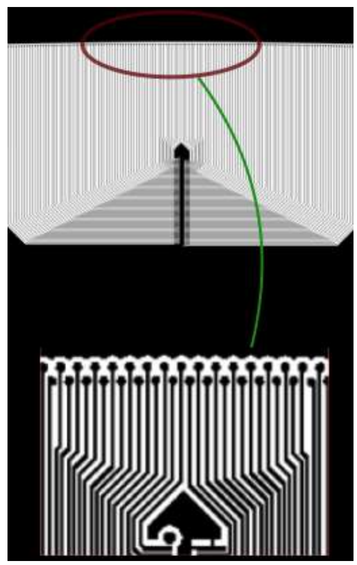

Figure 5.7: Shows the Vias on readout board.

5.2 Convention and definition of mapping functions

It is important to define the convention of the local coordinates of the detector. For this the trapezoidal shape detector should be placed inside X-ray box in a way such that Panasonic connectors are facing the observer standing out of the box, the wide base of the trapezoid is towards the sky and narrow side is towards the earth and all APVs are connected in WEST orientation i.e. when APV chips are fixed on the RO board the HDMI ports should be on the left side, as shown in the Figure 5.8.

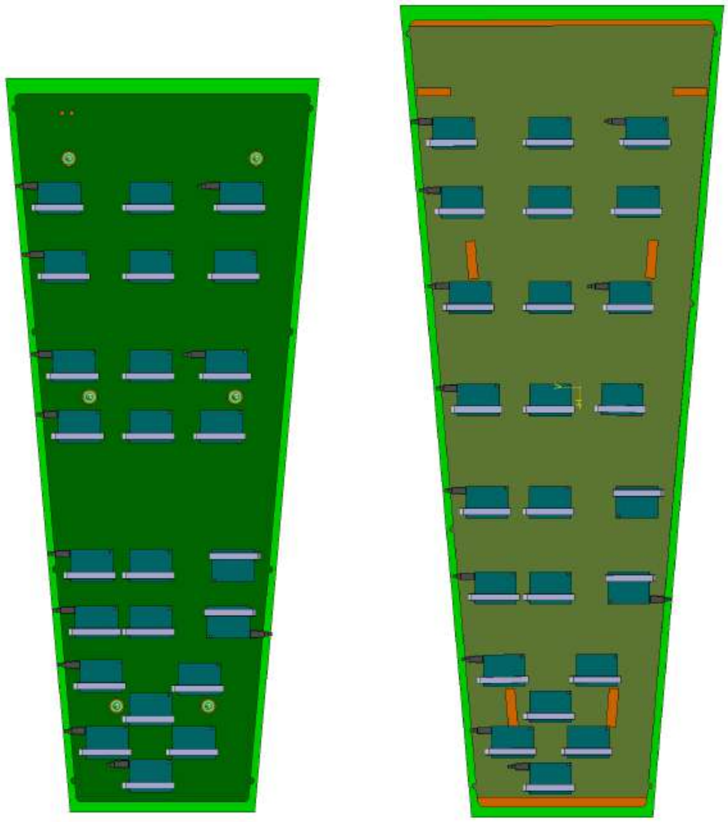

(a) (b)

Figure 5.8: Shows the GE11 hardware convention for (a) short, and (b) long RO board.

Using this configuration of hardware and software, the phi co-ordinate and strips are defined as follows.

1. Phi co-ordinate convention:

   The right most sector is defined as ϕ_1 and the left most as ϕ_3 given 3ϕ sectors in each η segment, which is following to the CMS co-ordinate system.

2. RO board strips convention:

   The right most strip is the zeroth strip and left most is the 383 strip in each iη segment and each (iη , iϕ) sector has in total 128 strips.

After setting the co-ordinate system for the detector, the mapping between the RO strips and APV channels is as follows.

1. Mapping for below vias strips:

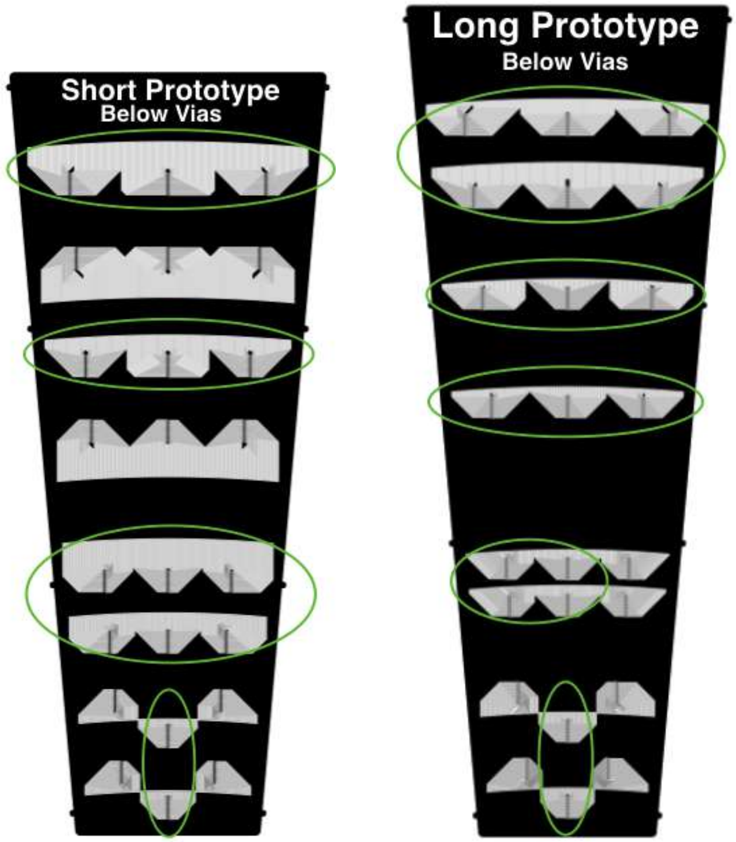

(a) (b)

Figure 5.9: Shows the GE11 RO board top view for (a) short, and (b) long GE11-X prototype having sectors below vias.

As shown in the Figure 5.9 sectors highlighted are below vias for both short and long GE11-X prototype. The mapping is different for odd and even strips on RO board as explained due to schematic of the pin distribution on the APV chip.

(a) For odd RO strips $= (((127 - APVchNo)/2) + 64)$

(b) For even RO strips $= (APVchNo/2)$

This implies APV channel no. 0 is connected to RO strip 0, channel no. 1 is connected to strip 127, channel no. 2 is connected to strip 1, channel no. 3 is connected to strip 126 and so on. And this mapping function will be used in the analysis framework to understand the data collected using SRS.

2. Mapping for above vias strips:

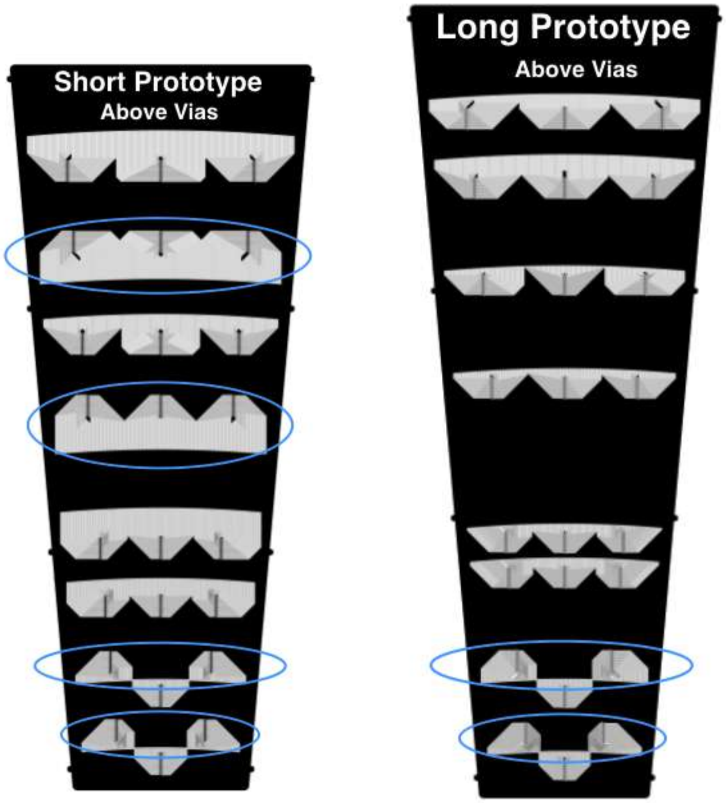

(a) (b)

Figure 5.10: Shows the GE11 RO board top view for (a) short, and (b) long GE11-X prototype having sectors above vias.

As shown in the Figure 5.10, sectors highlighted are above the vias for both short and long prototype. The mapping is different for odd and even strips on RO as explained due to schematic of the pin distribution on the APV chip.

(a) For odd RO strips $= (((APVchNo - 1)/2) + 64)$

(b) For even RO strips $= ((126 - APVchNo)/2)$

This implies APV channel no. 0 is connected to RO strip 63 , channel no. 1 is connected to strip 64, channel no. 2 is connected to strip 62, channel no. 3 is connected to strip 65 and so on .

3. Mapping for sectors (5,1) & (6,1):

Because of the less space present on the narrow side of the GE11-X detectors the HDMI cables must be inverted which change the mapping in like manner for appeared highlighted sectors shown in the Figure 5.11 . The mapping is

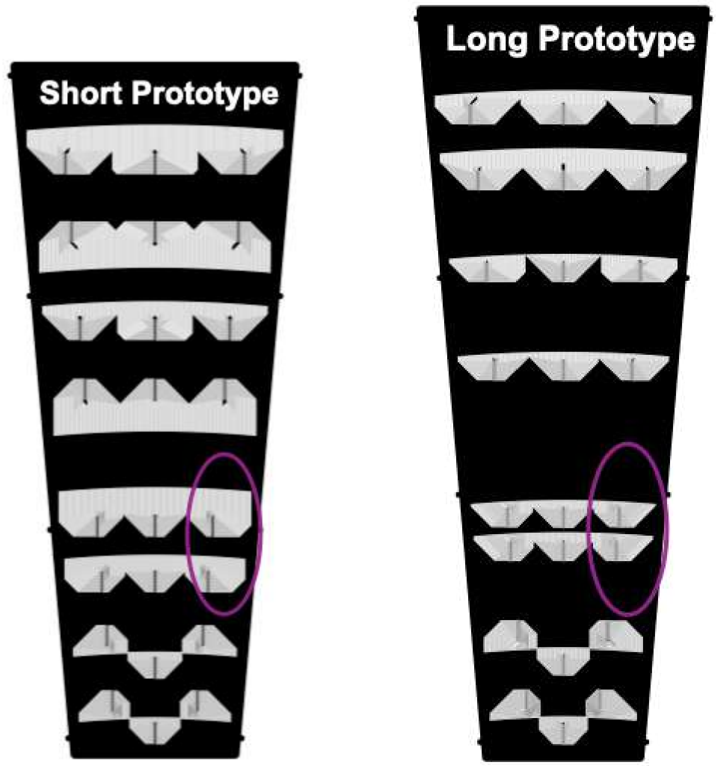

(a) (b)

Figure 5.11: Shows the GE11 RO board top view for (a) short, and (b) long GE11-X prototype for sectors (5,1) & (6,1).

distinctive for odd and even strips on RO as discussed because of schematic of the pin distribution on the APV chip.

(a) For odd RO strips = $(127 - APVchNo)/2$

(b) For even RO strips = $(64 + (APVchNo/2)$

This implies APV channel no. 0 is connected to RO strip 64 , channel no. 1 is connected to strip 63, channel no. 2 is connected to strip 65, channel no. 3 is connected to strip 62 and so on.

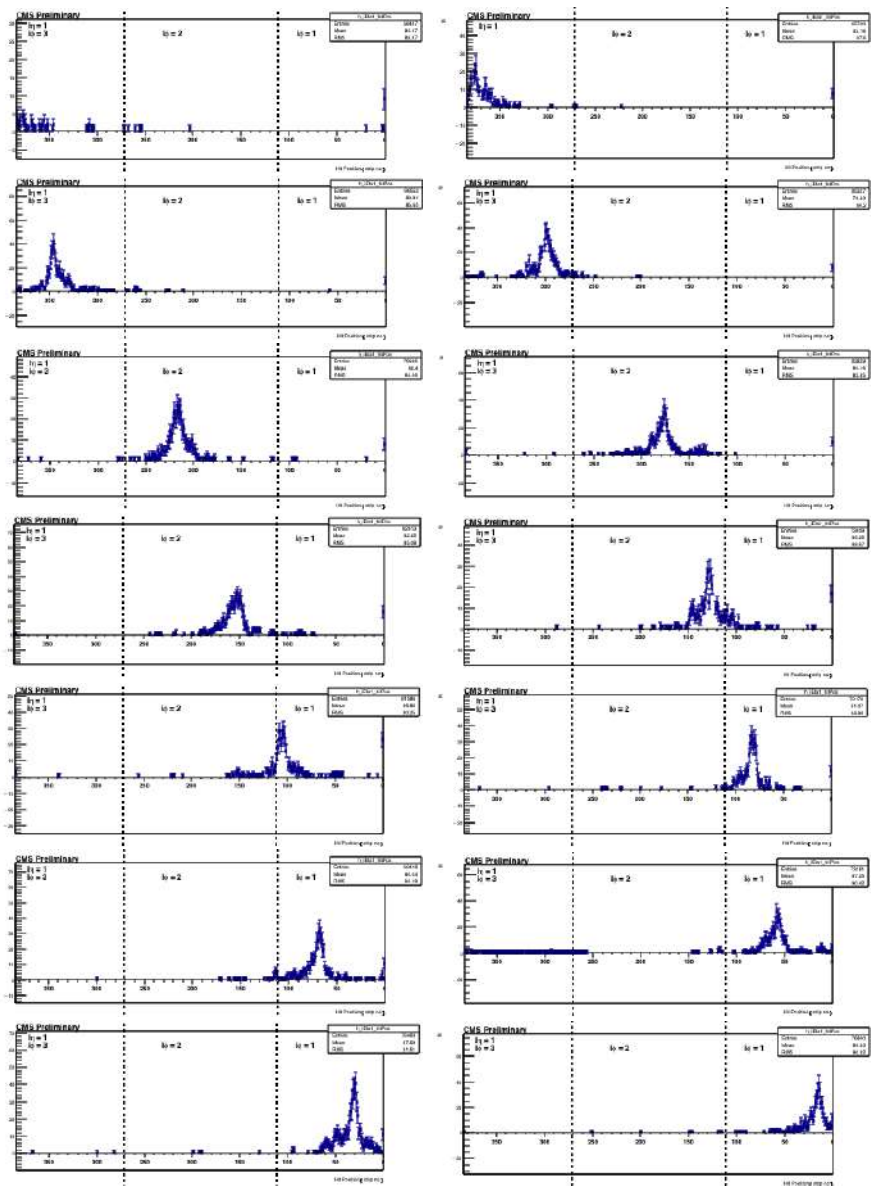

Figure 5.12: Shows the scanning of an eta sector using ^{109}Cd radioactive source.

5.3 Verification of mapping

Before starting the data-taking for the gain uniformity measurement of the triple-GEM detector using SRS, it is important to verify the mapping functions for all the sectors using a calibrated radioactive source, for the particular case we have used ^{109}Cd radioactive source. For this measurement GE11-X-S-CERN-0003 detector was used while operating at the gain of 540. In total 250k events are collected for each position of the source for sufficient statistics. Scanning of an η segment contains three-sectors in (η, ϕ) coordinate system according to the convention mentioned in the Section ?? has been performed, starting from the left side of the detector the source was moved towards the right and looked for the ^{109}Cd peak as shown in the Figure 5.12. The position of the peak during the scanning of the segment shows that the defined mapping is behaving as expected.

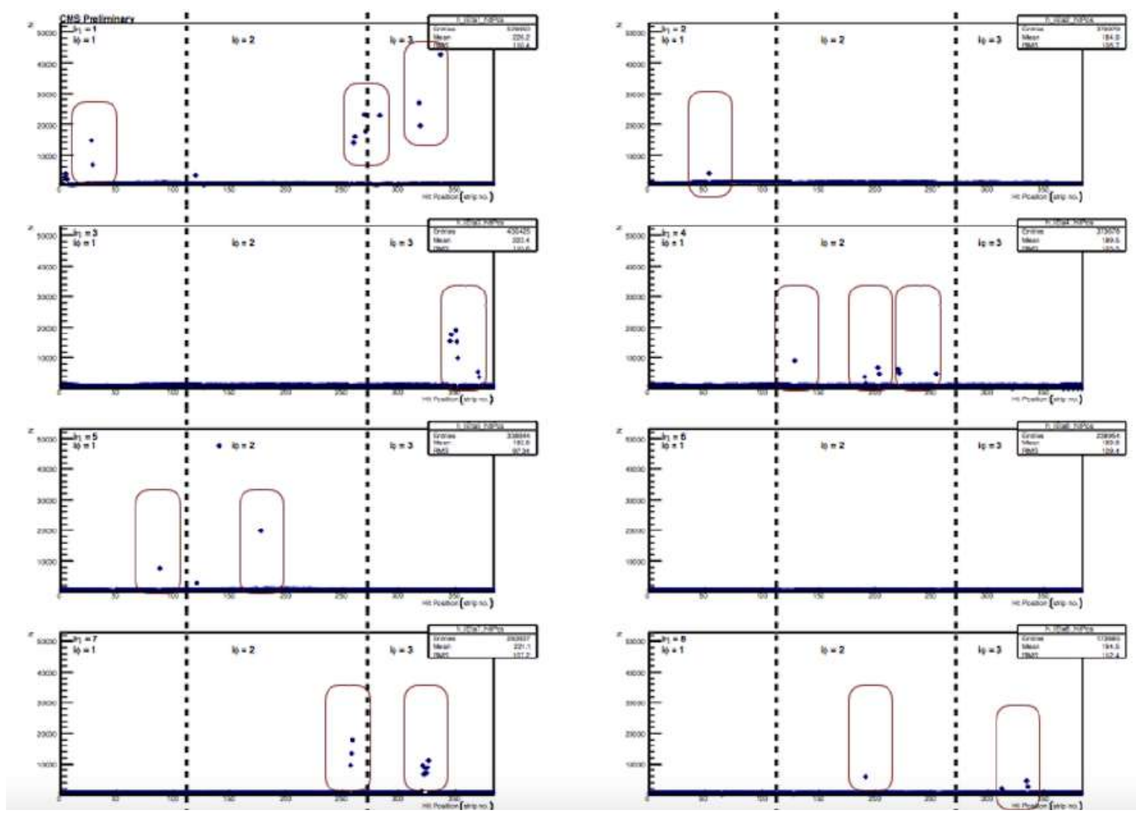

Figure 5.13: Shows the HitADC vs StripNo. with noisy APV channels.

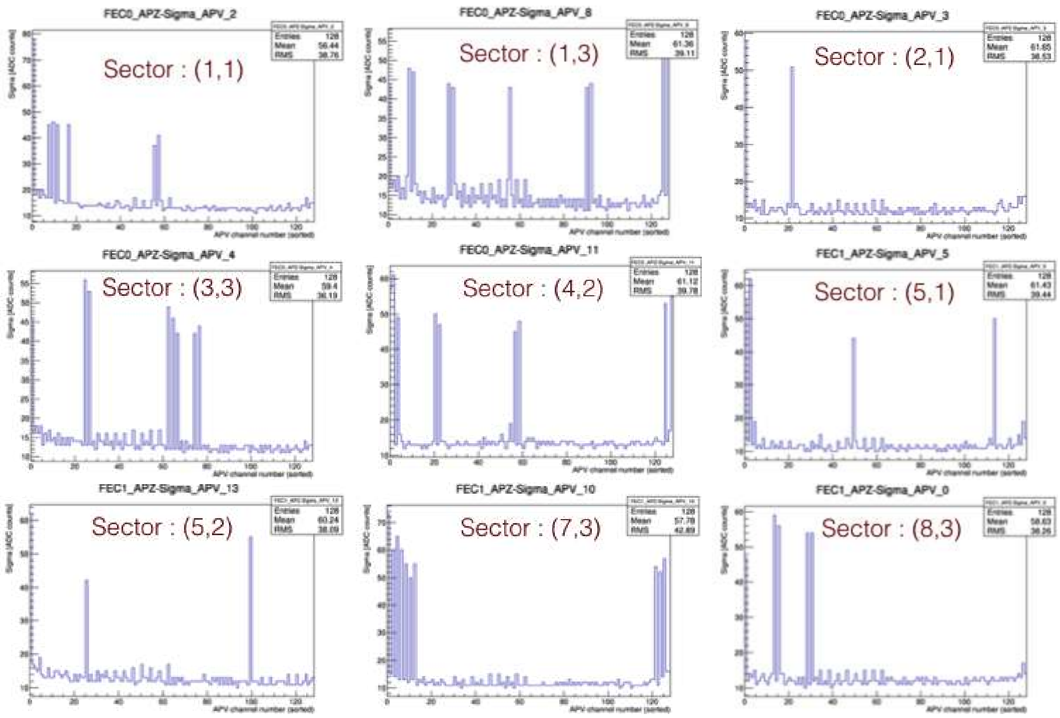

Figure 5.14: Shows the pedestal plot for different sectors in a GE11-X detector.

5.4 Results and interpretation

After setting up the working procedure for the commissioning and initialization of the SRS, also successful testing of the mapping, gain uniformity measurement has been performed. We have collected in total 3 Million events with a triple-GEM detector namely GE11-X-S-CERN-0003 operating at the gain of 540. After analyzing the data we looked at the HitADC vs Strip No., plot as shown in the Figure 5.13.

The highlighted excess in the plot is a direct result of the noisy channels of the APVs, which is confirmed by looking at the pedestal/sigma of the APVs collected using the step mentioned in section 5.1, as shown in the Figure 5.14. The pedestal is collected when APVs are connected to the detector and the detector was not powered ON, to make sure the noise coming from the APV chip only but not originating from the detector. After doing the proper grounding or replacing the noisy APVs and again generating the HitADC vs StripNo. plot does not reflect any excess, as shown in the Figure 5.15.

Now no excess is visible but few dips are present at fixed positions for each sector depending upon they are below or above vias. This could be because of any of the following reason(s): either due to the detector ground or due to the APV ground or due to edge effect. The dips at two end corners are due to the mechanical defect in GE11-X detectors i.e. the GEM foil active area is at 10° and the RO board is at 10.15° both with respect to the beam center. So at the edge near to the strip 0 or strip 383 there are fewer counts (dip) because there is no GEM foil present corresponding to those particular strips.

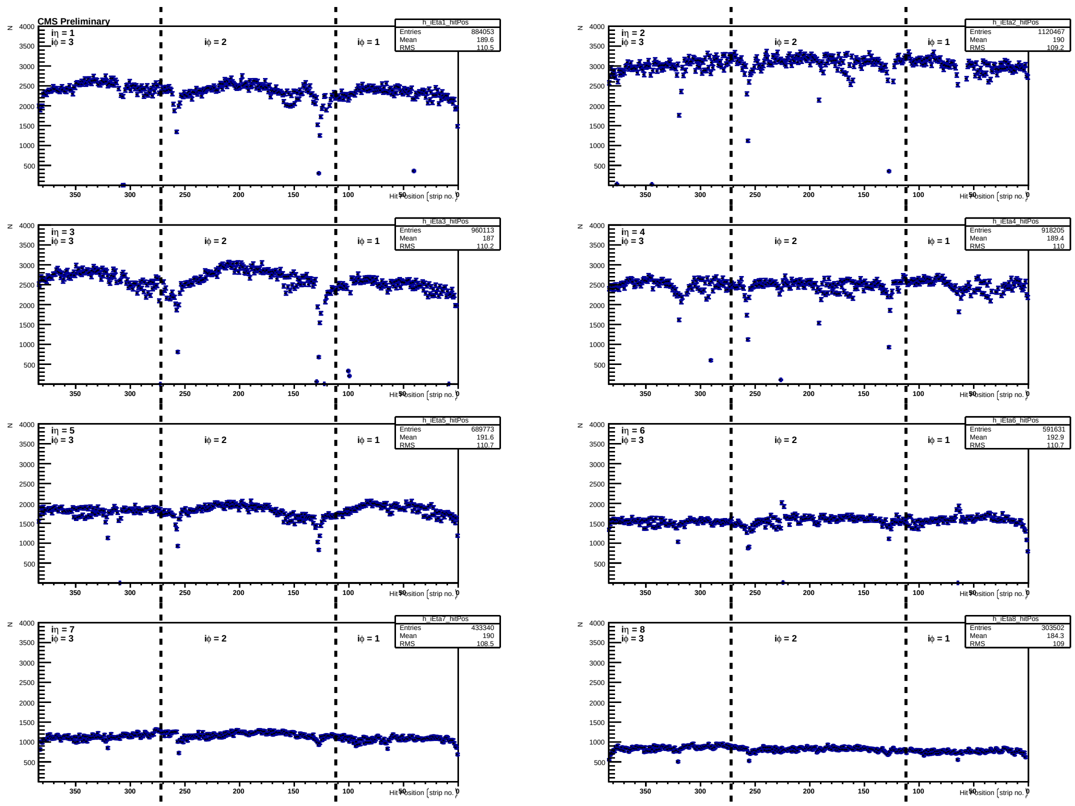

Figure 5.15: Shows the HitADC vs StripNo. without noisy APV channels.

A detailed interpretation of the plots generated using the collected data is as follows:

5.4.1 Hit and cluster position

In an event, if a strip is fired with a charge greater than the threshold of ZS, we call it a "hit". The plot hit position in the Figure 5.16 shows the number of strips fired out of the total number of events collected.

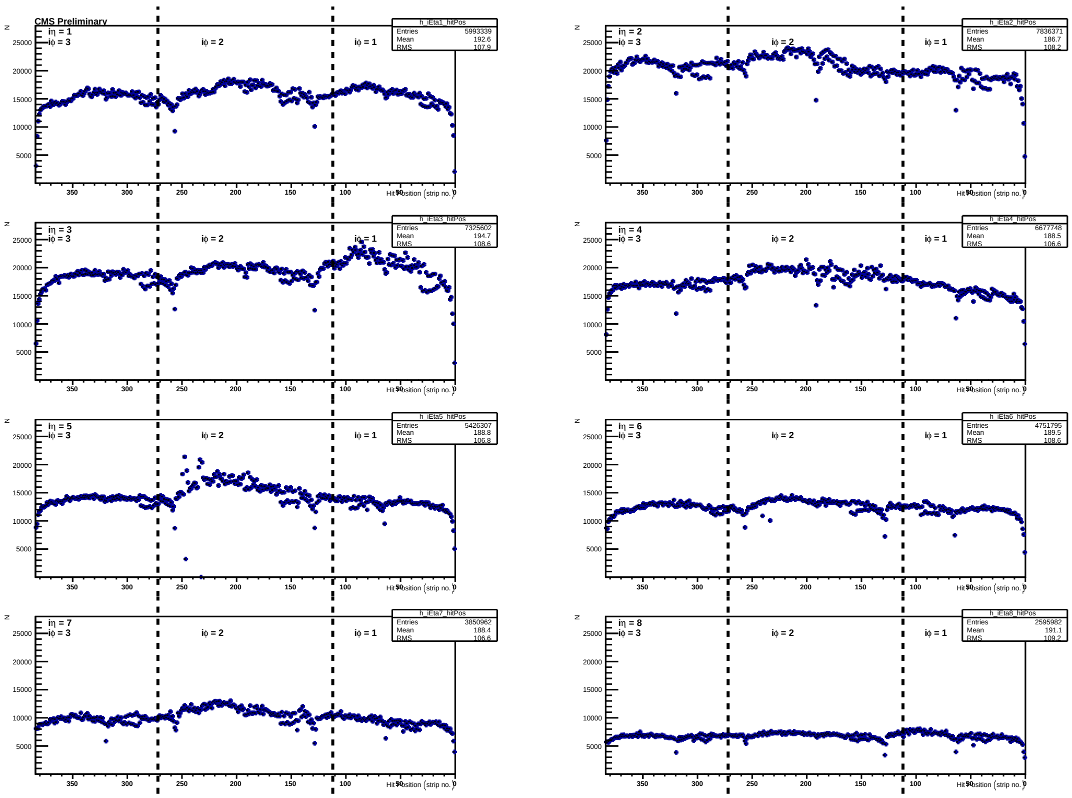

Figure 5.16: Shows the Hit position vs StripNo. plot for GE11-X detector.

In an event, the total number of strips fired with a charge greater than the threshold. Out of these, the strip with maximum charge gives the position of the cluster for that event, as shown in the Figure 5.17.

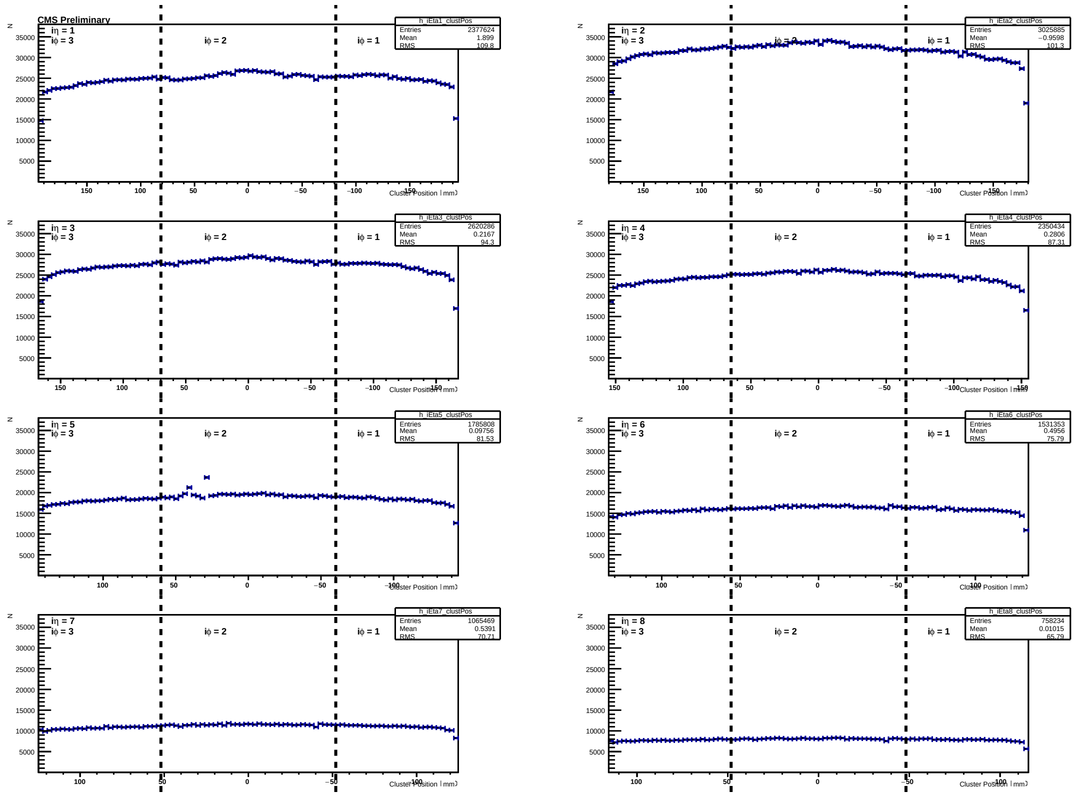

Figure 5.17: Shows the cluster position vs StripNo. plot for the GE11-X detector.

5.4.2 Hit and cluster ADC

The HitADC plot is shown in the Figure 5.18 is used to look at the saturation level of the APV, in this plot we are expecting a peak with a smooth tail but this does not correspond to the photopeak. This can be explained with an example, if in an event four strips were fried because of the charge spread then HitADC plot for that event will be the spectrum obtained using charge collected at each strip and placing it in a single bin, as shown in the Figure 5.19. On the other hand if four strips are fired at a time due to the charge spread then sum of the total charge collected at all these strips and place that value in a single bin gives the cluster ADC plot as shown in the Figure 5.20. The cluster ADC plot as shown in the Figure 5.21 should end up with the copper fluorescence peak. The argon escape peak but usually, this is hard to resolve as it appears mostly as a knee in triple-GEM detectors and generally not resolvable using the SRS, an electron bremsstrahlung continuum background and a small fraction of unconverted silver k_α and k_β lines which again appears like a knee.

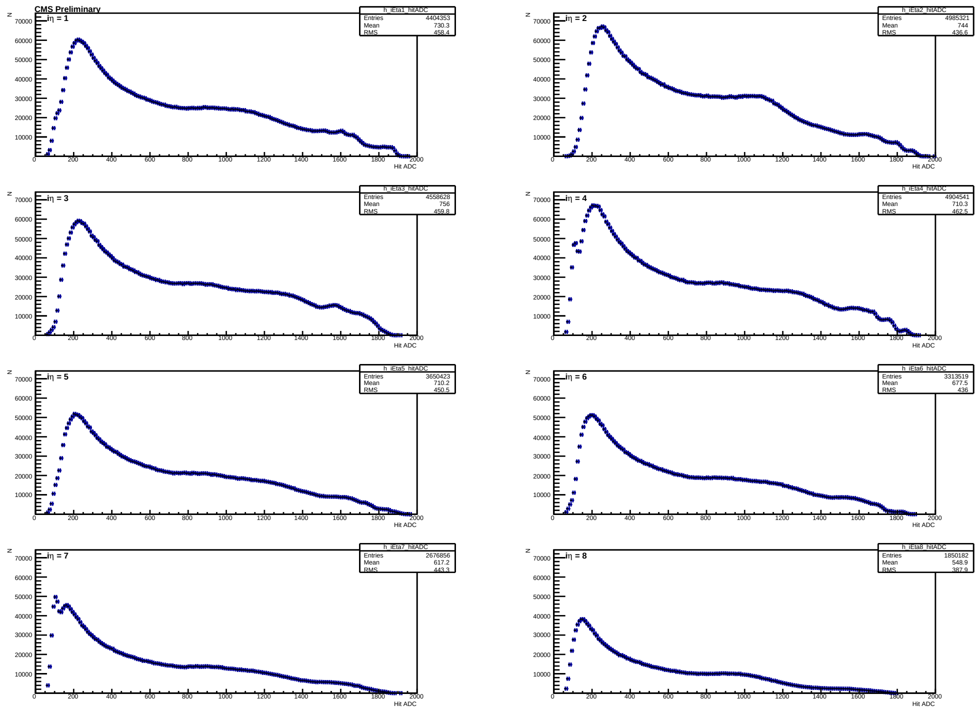

Figure 5.18: Shows the HitADC vs StripNo. plot for GE11-X detector.

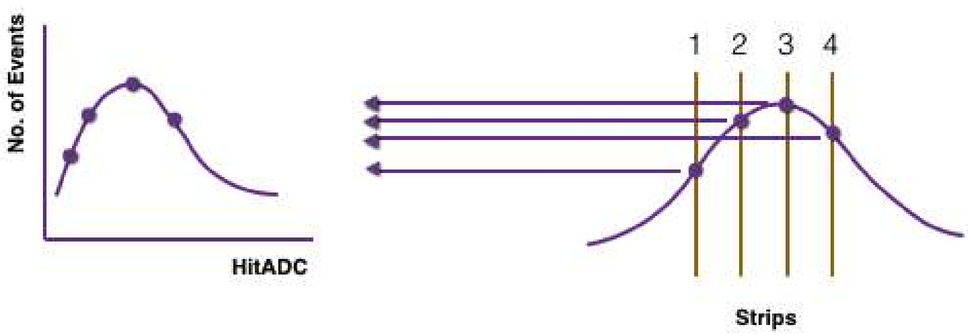

Figure 5.19: Shows the definition for HitADC plot.

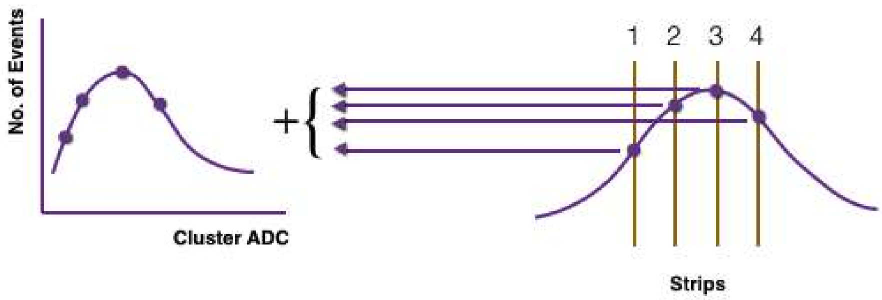

Figure 5.20: Shows the definition for clusterADC plot.

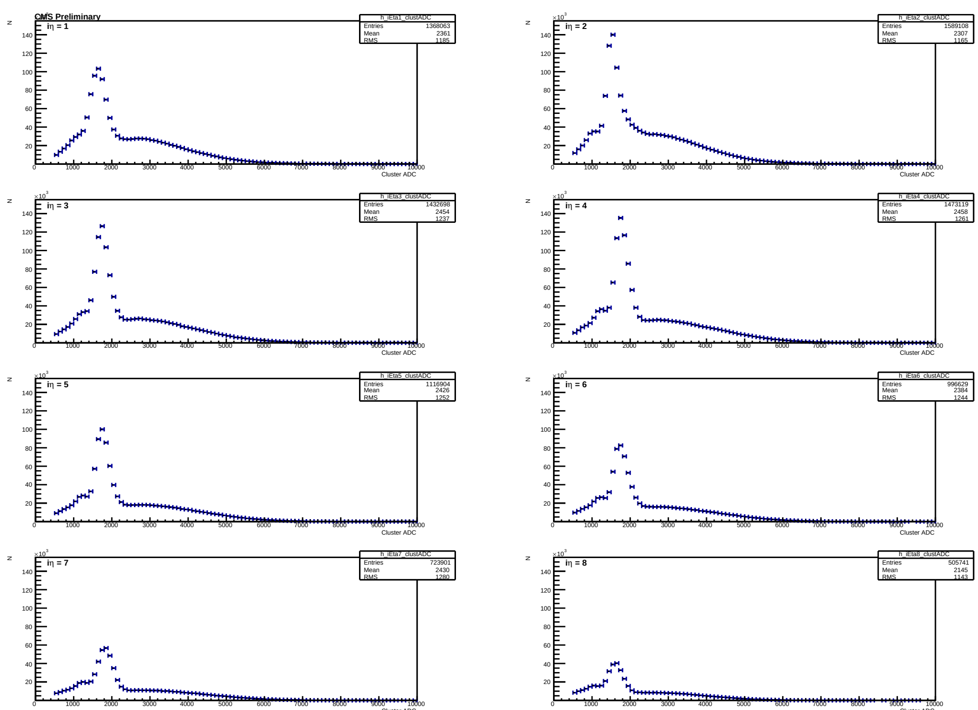

Figure 5.21: Shows the clusterADC vs StripNo. plot for GE11-X detector.

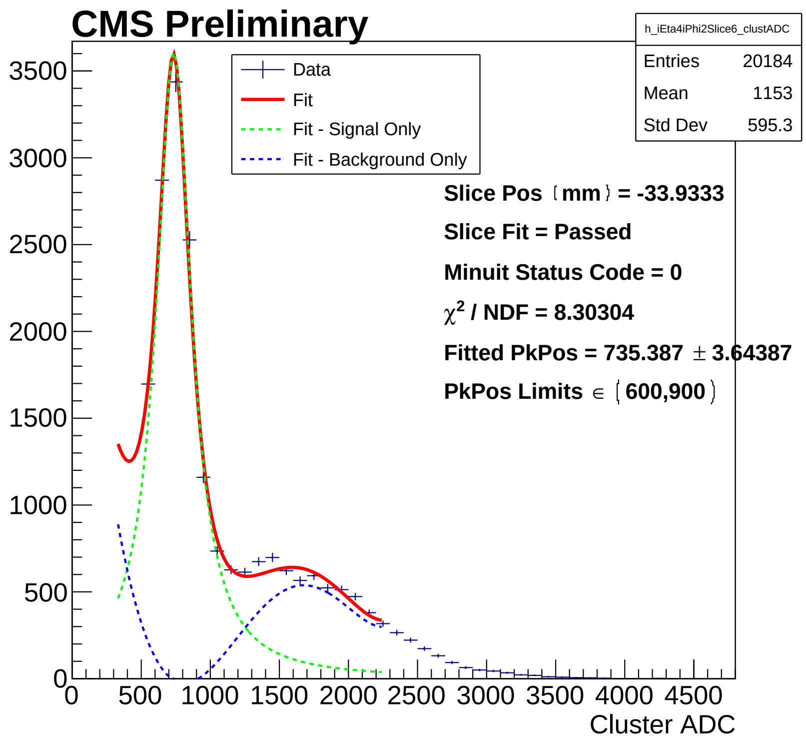

Figure 5.22: Shows the ADC peak position for a slice.

5.4.3 Charge cluster ADC spectrum from slice

The detector in η row partitioned in slices where each slice covers an area of about four anode strips and in total there are 768 slices over the detector. And charge cluster ADC spectrum is obtained from each slice of the detector and fitted with a Cauchy distribution for the photopeak and a 5^{th} order polynomial to model the combination of electron bremsstrahlung continuum background and a small fraction of unconverted silver k_α and k_β. An example from one of the slice for GE11-X detector is shown in the Figure 5.22.

5.4.4 Uniformity map

The photopeak obtained from the charge cluster ADC peak fit from each slice is assigned to the (xSlice, ySlice) co-ordinate point in the detector local coordinate system. The set ADC_{peak} is then normalized to the average peak position of the slices to create the normalized set of fixed positions (ADC_{norm}). Then the ordered triplets of (xSlice, ySlice, ADC_{norm}) are plotted in 3D space as shown in the Figure 5.23. This plot gives a visualization for the uniformity of the GE11-X detector.

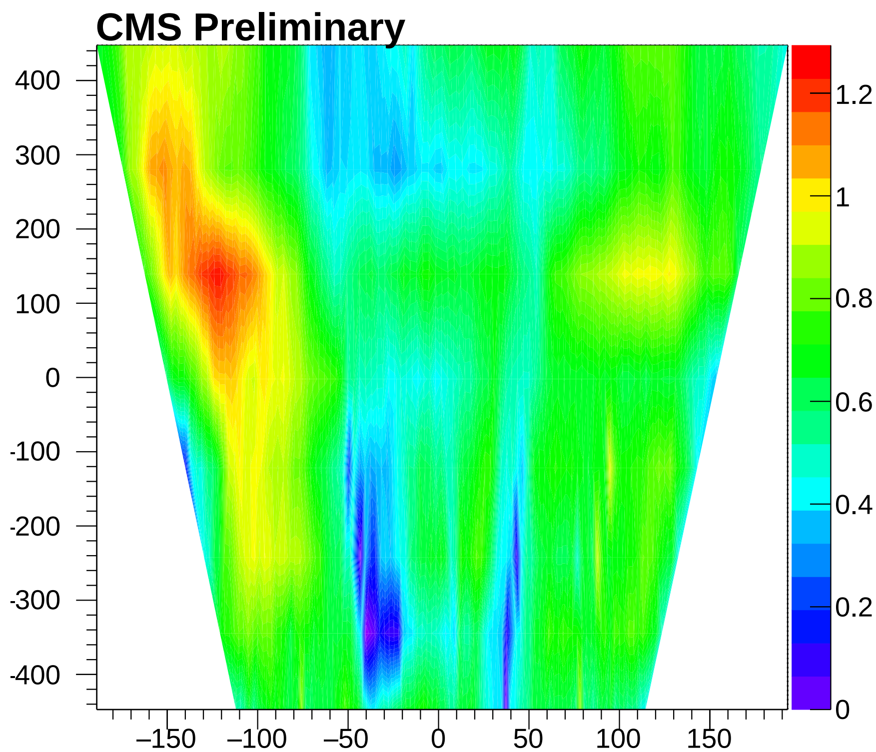

Figure 5.23: Shows the response fir peak position plot for all the slices of GE11-X detector.

5.4.5 Bulk response uniformity

Bulk response uniformity R_U of a GE1/1 detector is a percent error defined as:

$$R_U = \frac{\sigma}{\mu} \times 100\%$$

The set of all ADC peak positions from all the slices are plotted together and the dataset is fitted with the Gaussian distribution to extract the mean (μ) and standard deviation(σ) from the fit. Each value of the ADC peak is shifted by the average value of the set ADC_{peak} to be center around the zero for a better understanding. And bin width is always taken as the one-quarter of the standard deviation of the ADC_{peak} dataset. The bulk response uniformity plot for GE11-X detector is shown in the Figure 5.24.

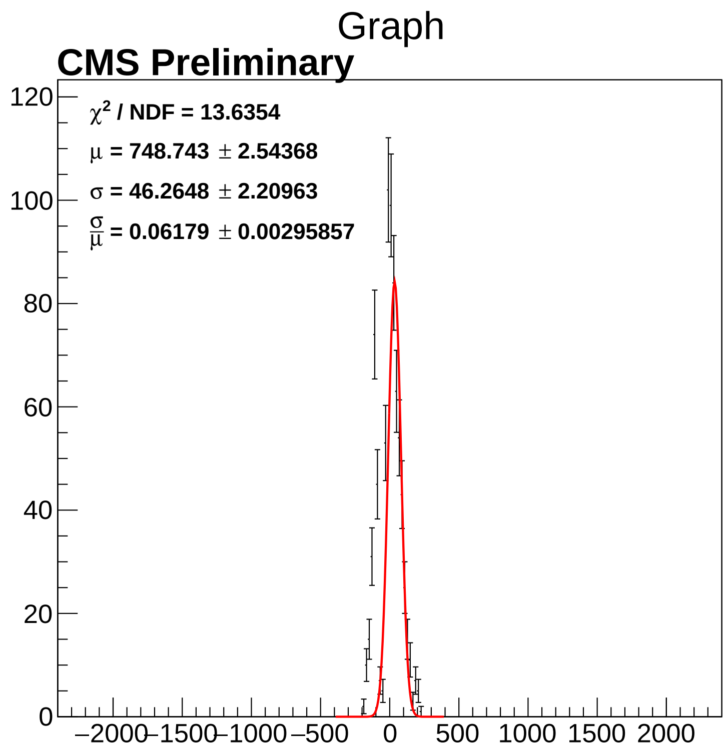

Figure 5.24: Shows the response uniformity plot for GE11-X detector.

5.5 Measurement of induction gap thickness

The method used in this paper relies on the indirect measurement of the gap through the capacitance between readout electronics and bottom GEM. In this method an external trigger must be sent to the bottom of the GEM and information of the gap can be determined using the capacitance of the gap. The measurement can be done with high voltage applied to the detector. This method requires a multichannel analog front-end chip and it should be calibrated to disentangle the non-uniformity of the chip with the detector. The caveats associated with this technique that it is sensitive to all the types of coupling like one we observed due to the fan-out on the readout as shown in the Figure 5.30. This method can be used to qualify readout electrodes. Shorts or missing connections will be identified for instance because of the anomalous electrode capacitance.

5.5.1 Setup

The setup as shown in the Figure 5.25 used for the measurements presented in this paper mainly divided into two parts: one is the charge injection circuity which utilizes a GEM detector, HV decoupled pulsing circuit, etc. and setup of data-taking and processing using the SRS.

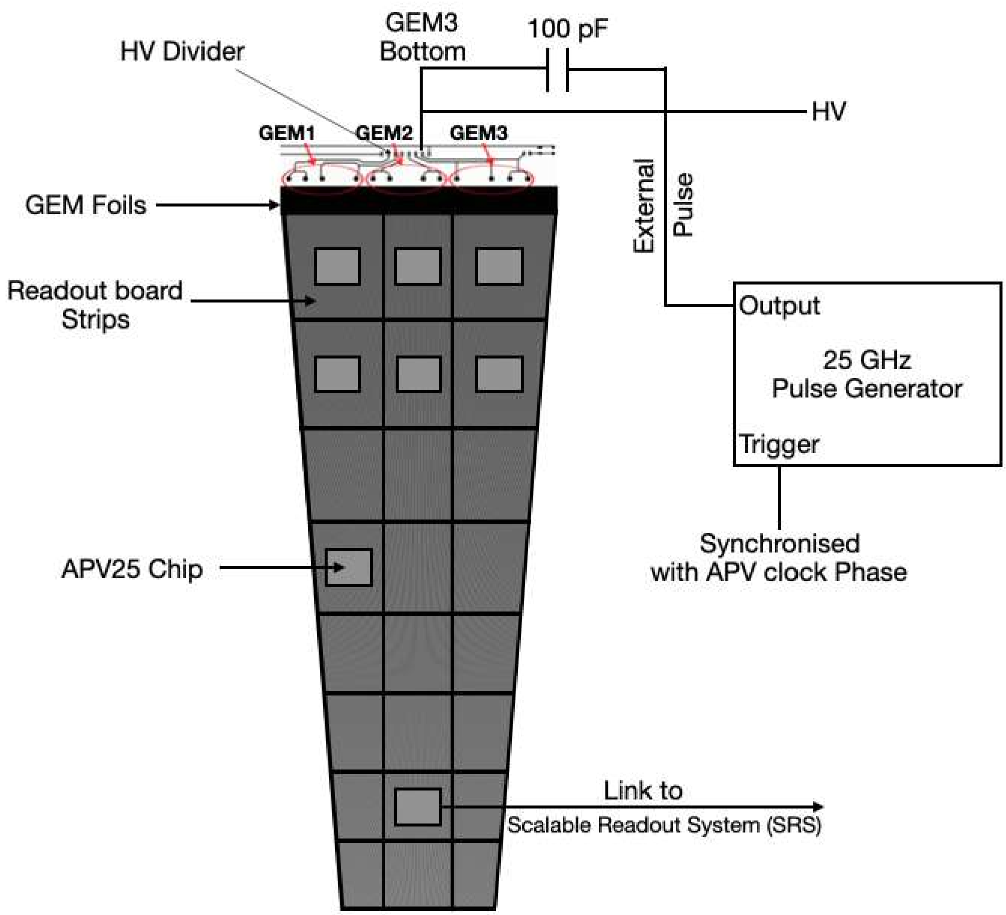

Figure 5.25: Shows the schema for the technique developed using SRS.

The external pulse has been generated using the 25 GHz pulse generator with a definite pulse frequency of 1 kHz, amplitude 1.15 V peak to peak, width 1 μS, and delay of 300 ns. The pulse from the pulse generator fed into the bottom of the GEM foil in series with 100 pF capacitor and a 50 Ω termination. The external pulser has been synchronized with the SRS clock using a synchronous NIM signal produced by the SRS. The NIM output of SRS and pulse generator trigger output has been fed to the oscilloscope.

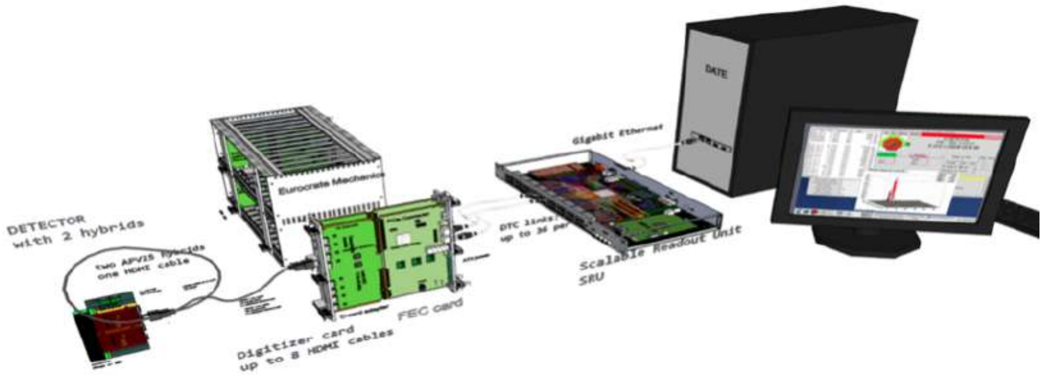

Figure 5.26: Shows the schematic for the data taking using SRS.

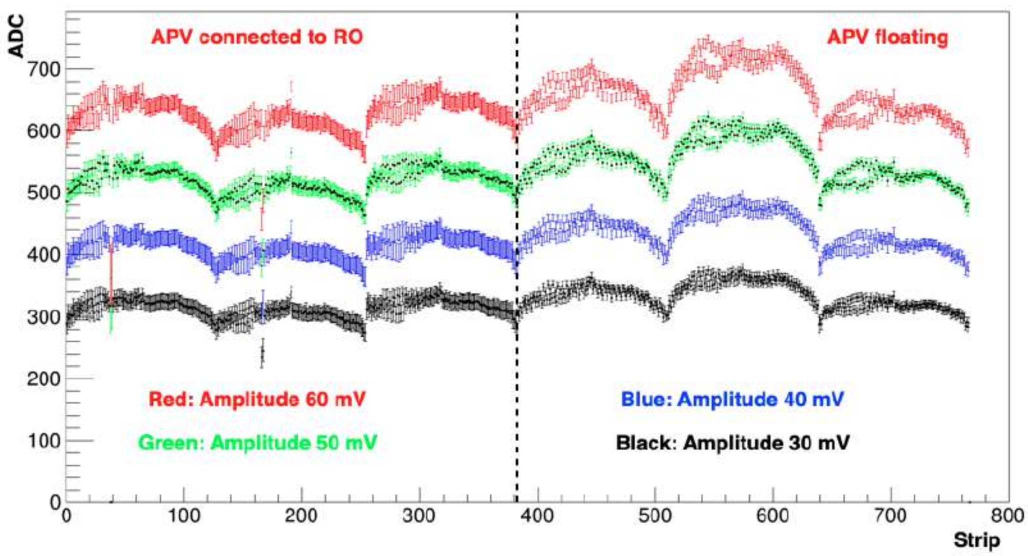

Figure 5.27: Shows the behaviour of APV-pair operated in calibration mode for different amplitude input pulse.

A dedicated computer installed with the LabView software for controlling the SRS system as well as for acquiring the raw data. A SRS based DAQ which is developed by the RD51 collaboration at CERN, used for the quality assurance of the micro pattern gaseous detectors, such as Gas Electron Multiplier (GEM) [**11**, **12**], Micromegas (MM), etc. [**14**]. The SRS is divided into two major parts; first the readout ASIC connected to the readout system (in this particular case we have used APV25), and second is the front-end cards use to interface the chip with rest of the system as shown in the Figure 5.26. Analog front end chip with 128 channels that will be digitized with a sampling clock of 40MHz as shown in the Figure 5.6, the details of the chip can be found elsewhere [**87**]. It is of the paramount importance to establish the presence of any kind of non-uniformity in the input channels of the ASIC. For this, a calibration mode of the ASIC has been used and controlled using a LabView software. The setting of the pulse amplitude and the number of strips fired at a time was also set using the same software. The 16-strips fired at a time and the position of these strips have been varied with the help of the LabView software. Finally, the acquired data was combined to study the commutative effect. Figure 5.27 shows the ADC value recorded for different amplitude of input pulses. For this, three pairs of master and slave APVs has been used, out of which master APVs were connected to the readout board and slave APVs were left floating. A similar pattern has been observed for both the APVs either connected to RO board or left floating hence there is finite non-uniformity present in the channels of the APV chip.

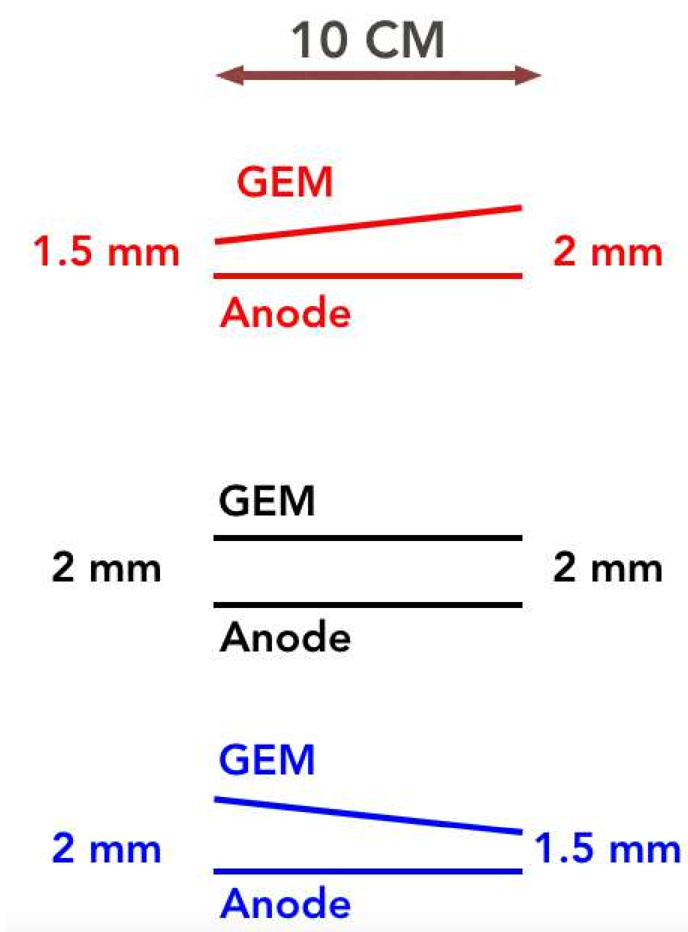

Figure 5.28: Shows the different orientations for GEM and Anode plane.

5.5.2 Measurements and results

A series of measurements have been carried out on the small and large size GEM detectors in order to extract the information regarding the flatness of the induction gap. Also, the application of this technique has been described in terms of deformation of the induction gap, quality assurance of the readout board, etc.

5.5.2.1 Measurement of sensitivity of the induction gap

The aim of this measurement is to check the sensitivity of the signal gap utilising the capacitance of the gap. The experimental setup for this measurement uses the two dimensional readout (RO) board having an active area of 10 cm × 10 cm and consists of 256 strips in X-direction and equal number in Y-direction. A GEM foil having an active area similar to RO board mounted on the top of the RO board [**88**, **89**]. The output of the pulser has been connected to the bottom of the HV trace of GEM foil. Panasonic connectors in X-direction were equipped with the APV25 chip and Y-direction strips were terminated with 0 Ω. Three different gap configurations were tested in order to look for the induction gap sensitivity as shows in the Figure 5.28.

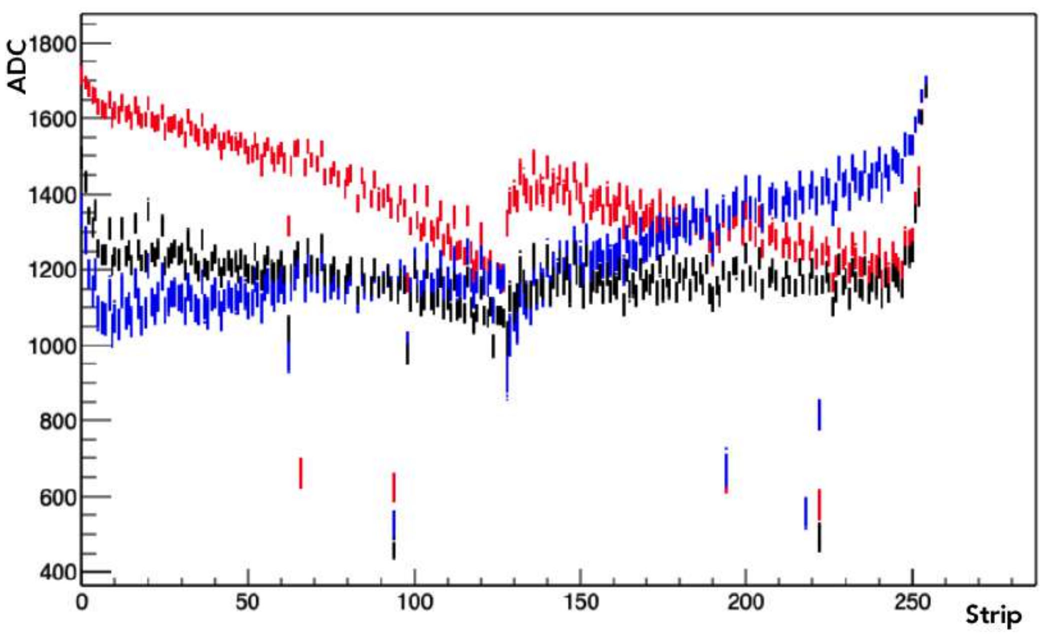

Figure 5.29: Shows the ADC value for each strip for all the three configurations.

Firstly, a gap of 2 mm was maintained between the bottom of the GEM foil and anode then the foil was tilted with the asymmetric gap of 1.5 mm on the left and

2 mm on the right, and vice-versa. Figure 5.29 shows a clear variation in the ADC value with respect to strip for the three different gap configurations.

5.5.2.2 Measurement on large area triple-GEM detector

After testing this technique on 10 cm × 10 cm GEM detector, it has been applied to the big size triple-GEM detector with known non-uniformity in the induction gap. For this measurement a triple-GEM detector having physical dimension of 1 m × 55 cm × 24 cm with a gap configuration of 3 mm/1 mm/2 mm/1 mm for the Drift/Transfer1/Transfer2/induction gap, respectively has been used. The readout board for this detector is 3 mm thick PCB having in total 3072 one-dimensional strips and having known deformation in the detector.

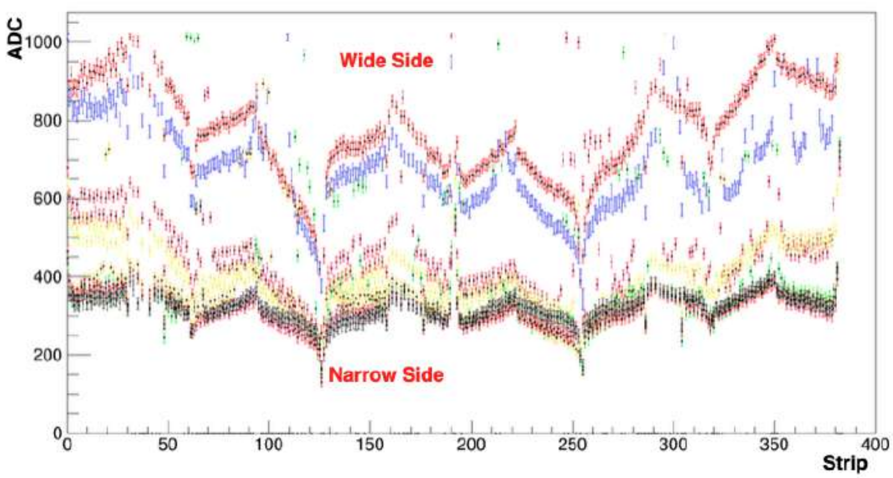

Figure 5.30: Shows the ADC value for each strip and for all the eta segments of GE11 detector.

The RO board is divided into 8 η segment and 3 ϕ partitions such that each (η, ϕ) sector has 128 strips. RO board has different strip lengths for each eta segment as going from the wider side to the narrow side. A high voltage divider has been used to power up the GEM foils and gaps simultaneously. A trigger pulse was sent to the bottom of the third GEM foil in parallel to the divider, and scan of each eta segment has been performed as shown in the Figure 5.30.

It shows that the detector is not completely flat and having a clear manifestation of the bending (outward) in the RO board. Due to different strip lengths in each eta sector, a correction on capacitance has been applied for two particular eta segment with respect to the widest segment as shown in the Figure 5.31.

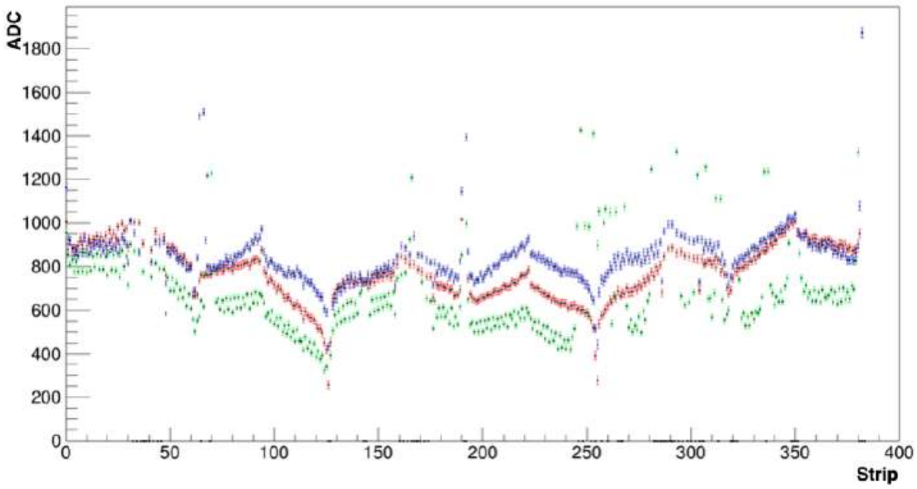

Figure 5.31: Shows the capacitance correction applied on the two particular Eta sectors namely eta3 and eta8 with respect to the eta1.

5.5.2.3 Measurement of induced deformation of the induction gap

The aim of this measurement is to ensure that the technique developed could observe both type of bending either inward or outward. In order to demonstrate this a weight of roughly 5 kg has been placed on one of the eta segment and look for the ADC value with respect to the strip. The two plots i.e. with weight placed on RO and without are plotted together to see the difference as shown in the Figure 5.32. The plot with weight having higher ADC value for the particular area, where the weight was placed, hence shows the bending of the RO board in the opposite direction i.e. inward. The distribution for both the measurements is fitted with a 2^{nd} order polynomial function to visualize the deformation of the RO board.

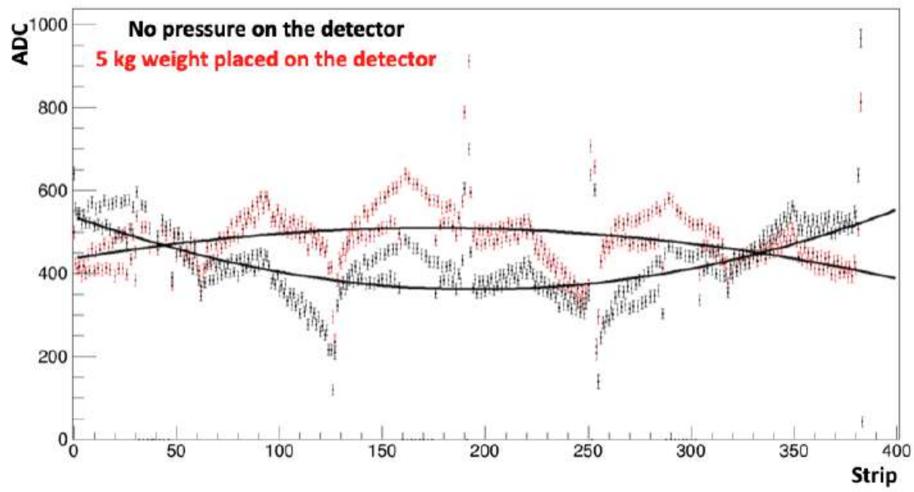

Figure 5.32: Shows the ADC value for each strip for one of the eta segment with and without 5kg weight placed on the RO board.

5.5.2.4 Measurement in presence of the induction field

This method has been tested with the high voltage on to ensure that we are able to do the measurement in the nominal operating conditions because electrostatic forces could induce displacement that depends on the field. To understand this a 700 V has been applied to the bottom of the third GEM foil and at same divider pad an external trigger pulse was also sent.

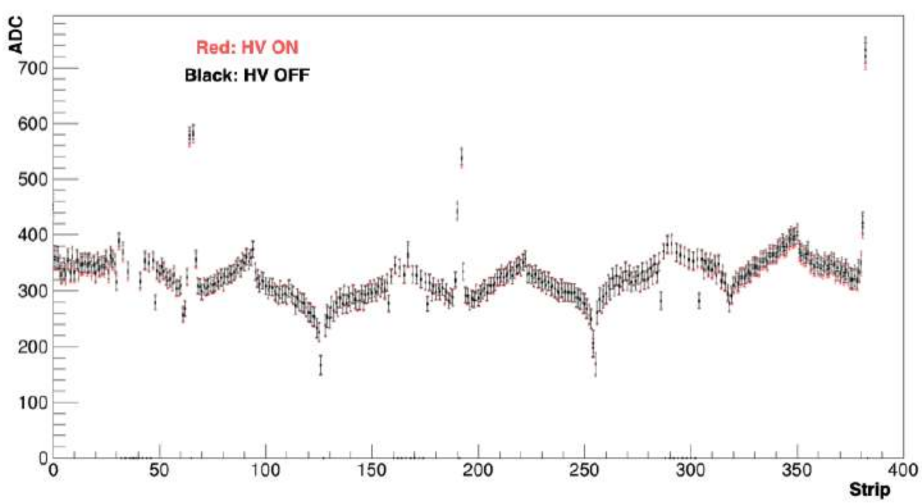

Figure 5.33: Shows the ADC value for each strip for one of the eta segment when HV is ON and OFF.

A measurement has been carried when the high voltage is off as well on and two spectrum were plotted together as shown in the Figure 5.33. No variation in the ADC spectrum with respect to strip observed, hence it shows that this technique works in the presence of high voltage and can be used to monitor if electrostatic force will induce variation in gap. Also, this measurement confirms that the mechanical stretching used to stretch the foils is sufficient to overcome the sag due to running high voltage.

5.5.2.5 Measurement of readout electrodes integrity

The advantage of using a multichannel front-end chip is to locate the defect(s) present in each strip. A measurement has been carried in readout sector where few strips were shorted as well as broken. The ADC spectrum with respect to strip has been plotted as shown in the Figure 5.34 and observed that due to change in capacitance for shorted, broken and damaged strips, a higher value of ADC was observed. Also, the location of the damaged strips highlighted in the plot (5.34) has been compared with the physical location of the bad strips on the RO board for a particular sector. Hence this technique can be used to do the quality assurance of the readout boards well before using them in detector assembly.

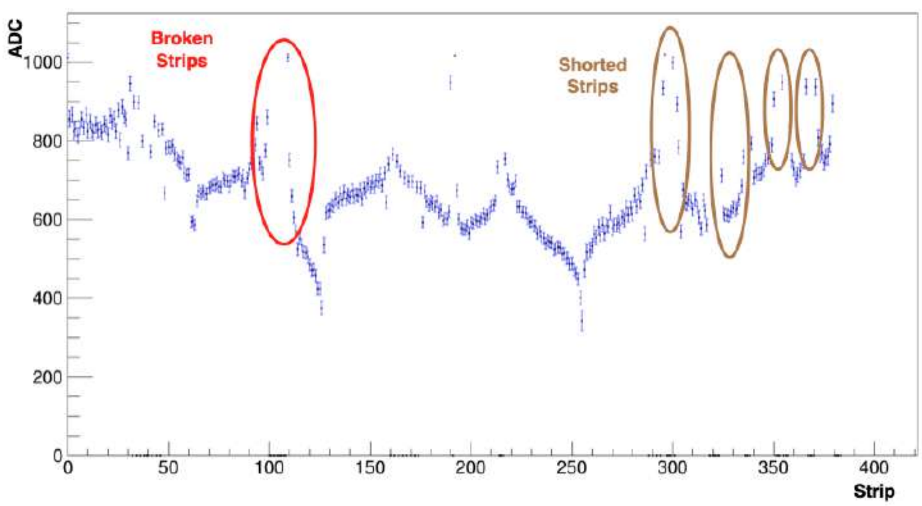

Figure 5.34: Shows the ADC value for each strip for one of the eta segment having defects present in the strips of the RO board PCB.

6

Dark matter search at LHC

"Whatever the mind can conceive and believe, it can achieve."

– Napoleon Hill

Astrophysical observations have provided strong evidence for the existence of dark matter (DM) in the universe [**90**]. However, its underlying nature remains unknown and cannot be accommodated within the standard model (SM). The recent discovery of a Higgs boson with mass of about 125 GeV by the ATLAS and CMS [**91**, **92**, **93**] experiments provides an additional handle to probe the dark sector beyond the SM. In the analyses presented here, it is assumed that there are five physical Higgs bosons, and that the new state corresponds to the light neutral CP-even state h. If DM has origin in particle physics, and if other than gravitational interactions exist between DM and SM particles, DM particles (χ) could be produced at the CERN LHC. One way to observe DM particles would be through their recoil against a SM particle X (X = g, q, γ, Z, W, or h) that is produced in association with the DM. This associated production of DM and SM particles is often referred to as mono-X production. The SM particle X can be emitted directly from a quark or gluon as initial-state radiation, or through a new interaction between DM and SM particles, or as final-state radiation. The Higgs boson radiation from an initial-state quark or gluon is suppressed through Yukawa or loop processes, respectively. A scenario in which the Higgs boson is part of the interaction producing the DM particles gives mono-h searches a uniquely enhanced sensitivity to the structure of couplings between the SM particles and the dark matter [**94**, **95**, **96**]. At the LHC, searches for DM in the mono-h channel have been performed by the ATLAS Collaboration using data corresponding to integrated luminosities of $20fb^{-1}$ at the center of mass energy $\sqrt{s}$ of 8 TeV and $3.2fb^{-1}$ at $\sqrt{s} = 13$TeV, through the decay channels $H \rightarrow b\bar{b}$ [**97**, **98**] and $H \rightarrow \gamma\gamma$ [**99**].

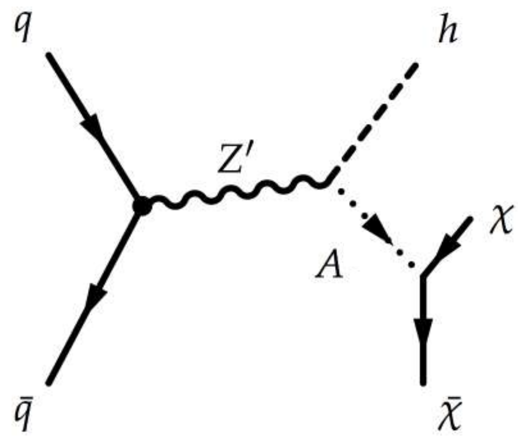

Figure 6.1: Shows the leading order Feynman diagram of the Z'-2HDM "simplified model". A pseudoscalar boson A decaying into invisible dark matter is produced from the decay of an on-shell Z' resonance. This gives rise to a Higgs boson and missing transverse momentum.

6.1 Mono-higgs search

In this chapter, a search for DM is presented in the mono-h channel in which the Higgs boson decays to either a pair of bottom quarks ($b\bar{b}$) or photons ($\gamma\gamma$). The results have been interpreted using a benchmark "simplified model" recommended by the ATLAS-CMS Dark Matter Forum, which is described in Ref. [**100**] Z'-two-Higgs-doublet-model (Z'-2HDM) [**96**], where a heavy Z' vector boson is produced resonantly and decays into a SM-like Higgs boson h and an intermediate heavy pseudoscalar particle A, which in turn decays into a pair of DM particles, as shown in the Figure 6.1.

In the Z'-2HDM model, the gauge symmetry of the SM is extended by a $\mathrm{U}(1)_{Z'}$ group, with a new massive Z' gauge boson. A Type-2 2HDM [**101**, **102**] is used to formulate the extended Higgs sector. A doublet Φ_u couples only to up-type quarks, and a doublet Φ_d couples to down-type quarks and leptons. Only Φ_u and right-handed up-type quarks u_R have an associated charge under the $U(1)_{Z'}$ group, while Φ_d and all other SM fermions are neutral. After electroweak symmetry breaking, the Higgs doublets attain vacuum expectation values v_u and v_d, resulting in five physical Higgs bosons: a light neutral CP-even scalar h, assumed to be the observed 125 GeV Higgs boson, a heavy neutral CP-even scalar H, a neutral CP-odd scalar A, and two charged scalars $H^{\pm}$. The particular analysis is performed in the context of the so-called alignment limit where the h has SM-like couplings to fermions and gauge bosons, and the ratio of the vacuum expectation values $\tan\beta = v_u/v_d > 0.3$, as implied from the perturbativity limit of the Yukawa coupling [**96**, **103**] of the top quark, the h-H mixing angle α is related to β by $\alpha = \beta - \pi/2$.

The benchmark model is parametrized through six quantities: (i) the pseudoscalar mass m_A, (ii) the DM mass m_χ, (iii) the Z' mass $m_{Z'}$, (iv) $\tan\beta$, (v) the Z' coupling strength $g_{Z'}$, and (vi) the coupling constant between the A and DM particles g_χ.

Only the masses m_A and $m_{Z'}$ affect the kinematic distributions of the objects in the final states studied in this analysis. In fact, when A is on-shell, i.e. $\mathrm{m_A} > 2\mathrm{m}_\chi$, the distributions have little dependence on m_χ. The remaining parameters modify the production cross section of Z', branching fraction, and decay widths of the Z' and the A, resulting in only small changes to the final-state kinematic distributions.

This analyses considers a Z' resonance with mass between 600 and 2500 GeV and an A with mass between 300 and 800 GeV, while the mass of DM particles m_χ is less than or equal to 100 GeV. The parameters $\tan\beta$ and g_χ are fixed at unity and two different assumptions on $g_{Z'}$ are evaluated as described in more details later. Values of m_A below 300 GeV are excluded by constraints on flavor changing neutral currents from measurements of $\mathrm{b} \to \mathrm{s}\gamma$ [**102**], and are not considered in this analysis.

The branching fraction for decays of A to DM particles, $\mathcal{B}(\mathrm{A} \to \chi\overline{\chi})$, decreases as m_χ increases; for the range of m_A considered, the relative decrease of $\mathcal{B}(\mathrm{A} \to \chi\overline{\chi})$ is less than 7% as m_χ increases from 0 to 100 GeV. Therefore, although signals with m_χ $=$ 100 GeV are considered in this search, the results are valid for any value of dark matter particle mass below 100 GeV.

The results presented here consider only A decays to DM particles and the final signal cross section $\sigma(\mathrm{Z}' \to \mathrm{Ah} \to \chi\overline{\chi}\mathrm{h})$ includes the value of $\mathcal{B}(\mathrm{A} \to \chi\overline{\chi})$. With the assumed dark matter particle mass, the value of $\mathcal{B}(\mathrm{A} \to \chi\overline{\chi})$ is $\approx$ 100% for m_A= 300 GeV. The branching fraction starts to decrease for m_A greater than twice the mass of the top quark as the decay $\mathrm{A} \to \mathrm{t\bar{t}}$ becomes kinematically accessible. For example, if m_A = 400 (800) GeV, $\mathcal{B}(\mathrm{A} \to \chi\overline{\chi})$ reduces to 54 (42)%. The quantity $\mathrm{P_T^{miss}}$, calculated as the negative vectorial sum of the transverse momentum (p_T) of all objects identified in an event, represents the total momentum carried by the DM particles.

The magnitude of this vector is referred to as $\mathrm{P_T^{miss}}$. For a given value of $m_{Z'}$,

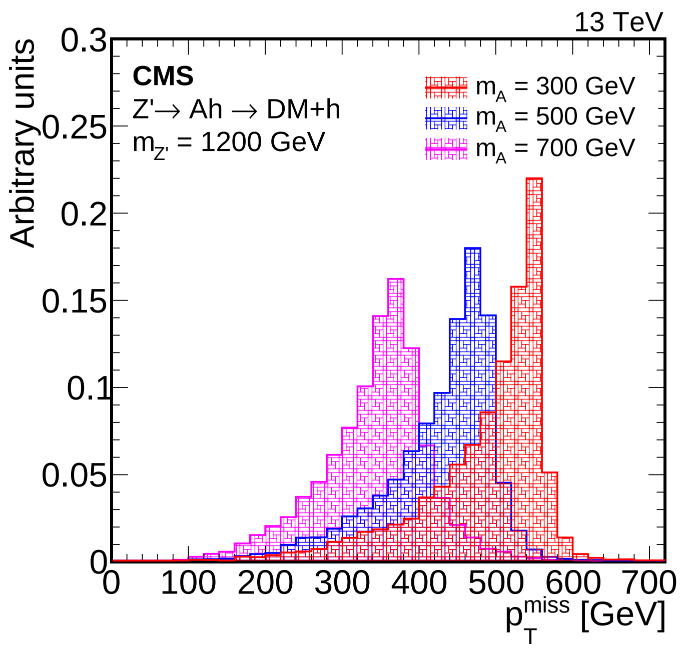

Figure 6.2: Shows the distribution of $\mathrm{P_T^{miss}}$ at generator level for $\mathrm{Z' \to A\ h \to DM + h}$ with $\mathrm{m_A} = 300$, 500, and 700 GeV with $m_{Z'} = 1200$ GeV. All other parameters of the model are fixed, as mentioned in the text.

the p_T of the A decreases as m_A increases. Therefore, the $\mathrm{P_T^{miss}}$ spectrum softens with increasing m_A. A comparison of the $\mathrm{P_T^{miss}}$ distributions for three values of m_A is shown in the Figure 6.2. The signal cross section is calculated for two assumptions on $g_{Z'}$: (i) a fixed value of $g_{Z'}= 0.8$, as considered in Ref. [**98**] and recommended in Ref. [**100**], and (ii) using the maximum value from electroweak global fits and constraints from dijet searches:

$$\mathrm{g_{Z'}} = 0.03\,\frac{\mathrm{g_W}}{\cos\theta_\mathrm{W}\sin^2\beta}\,\frac{\sqrt{\mathrm{m_{g_{Z'}}^2 - m_Z^2}}}{\mathrm{m_Z}}, \tag{6.1}$$

yielding $g_{Z'}$=0.485 for $m_{Z'}$=1 TeV, and $g_{Z'}$=0.974 for $m_{Z'}$=2 TeV. It can be seen from Eq. 6.1 that $g_{Z'} = 0.8$ is the maximum allowed value of $g_{Z'}$ for $\tan\beta = 1$ and $m_{Z'}$=1.7 TeV (the best reach of LHC as estimated by Ref. [**96**]). Note that this analysis does not consider the contribution of another decay that gives a similar mono-h signature: $Z' \to Zh$ where $Z \to \nu\overline{\nu}$.

The ratio of branching fractions, $\mathcal{B}(Z' \to Zh, Z \to \nu\overline{\nu})/\mathcal{B}(Z' \to Ah, A \to \chi\overline{\chi})$, is a function of $\tan\beta$ and $m_{Z'}$ and does not depend on $g_{Z'}$ since the value of $g_{Z'}$ cancels in the ratio.

The $H \to b\bar{b}$ decay mode has the largest branching fraction (≈58%) of all, but suffers from relatively poor mass resolution of about 10%, and while the $H \rightarrow \gamma\gamma$ branching fraction is small (≈0.2%), the channel benefits from the high precision in reconstructed diphoton mass, with a resolution of about 1–2%. In the $H \rightarrow b\bar{b}$ channel, the fact that the p_T of the h should increase with $m_{Z'}$ and decrease with m_A is exploited. The minimum separation in the pseudorapidity and azimuth (η, ϕ) plane between the decay products of h scales as m_h/p_{T}^h, where p_{T}^h is the transverse momentum of the h boson. The allowed mass ranges of $m_{Z'}$ and m_A imply a very wide range of values for p_{T}^h and consequently a wide range in the separation of the decay products. Analysis in this channel is therefore divided into two regimes: (i) a resolved regime where the h decays to two distinct reconstructed b jets, and (ii) a Lorentz-boosted regime where the h is reconstructed as a single fat jet. For each mass point, the analysis with best sensitivity for the expected limit is used as the final result. The signal extraction is performed through a simultaneous fit to the signal- and background-enriched control regions.

The search in the $H \rightarrow \gamma\gamma$ channel is performed by seeking an excess of events over the SM prediction in the diphoton mass spectrum, after requiring a large $\mathrm{P}_{\mathrm{T}}^{\mathrm{miss}}$. Control samples in data are used to estimate the reducible background, which mainly consists of diphoton SM production. A counting approach is used to estimate the potential signal.

6.2 Data and simulated samples

The analysis is performed with the proton-proton collision data at the centre of mass energy ($\sqrt{s}$) of 13 TeV collected by the CMS experiment at the LHC during the year 2015, corresponding to an integrated luminosity of 2.3 fb^{-1}.

The MadGraph5_amc@nlo v2.3.0 generator [**104**] is used to generate the mono-h signal at leading order (LO) as predicted by the Z'-2HDM model. In the MadGraph5_amc@nlo generation, a vector particle Z' that decays to a SM-like Higgs boson h with mass 125 GeV is produced resonantly together with a heavy pseudoscalar particle A that decays into a pair of DM particles. The decay of the SM-like Higgs boson is handled by PYTHIA 8.205 [**105**].

The associated production of a SM Higgs boson and a Z boson (Zh) is a small but irreducible background for both decay channels. The Vh (Zh and Wh) processes are simulated using POWHEG v2.0 [**106**, **107**] and MadGraph5_amc@nlo for $q\bar{q}$

and gluon-gluon fusion, respectively. In the $H \to \gamma\gamma$ channel, additional resonant but reducible backgrounds are considered. These backgrounds include the SM Higgs boson, produced through gluon fusion (ggh), through vector boson fusion (VBF), and in association with top quarks ($t\bar{t}h$). All of these resonant backgrounds are modeled at next-to-leading order (NLO) in simulation. The VBF Higgs boson samples are generated using POWHEG [**108**], while the ggh and $t\bar{t}h$ samples are generated with MadGraph5_amc@nlo.

The dominant background processes for the $H \to b\bar{b}$ decay channel are events with top quarks and W/Z bosons produced in association with jets. The $t\bar{t}h$ events, produced via the strong interaction, and electroweak production of single top quarks in the t- and tW-channels are generated at NLO with POWHEG [**109**, **110**, **111**, **112**, **113**]. The s-channel process of single top quark production is generated with MadGraph5_amc@nlo. Differential measurements of top quark pair production show that the measured p_T spectrum of top quarks is softer than the one produced in simulation. Scale factors to correct for this effect are derived from previous CMS measurements [**114**, **115**]. The sum of top quark pair events and single top quark events is referred to as "Top quark background". The W and Z boson production in association with jets is simulated at LO with MadGraph5_amc@nlo. Up to four additional partons in the matrix element calculations are included. The MLM matching scheme [**116**] is used as an interface to the parton shower generated with PYTHIA. The cross sections for W+jets and Z+jets processes are normalized to the next-to-next-to-leading order cross section, computed using FEWZ v3.1 [**117**]. Moreover, to improve the description of the distribution of high p_T W+jets and Z+jets processes, events are reweighted using the generated p_T of the vector boson to account for NLO quantum chromodynamics (QCD) and electroweak (EW) contributions [**118**, **119**, **120**]. The small background from diboson (WW, WZ, and ZZ) processes, labeled as VV, is simulated with PYTHIA.

For the $H \to \gamma\gamma$ decay channel, several non-resonant background sources can mimic the signal when an event has mis-measured $\mathrm{P}_\mathrm{T}^\mathrm{miss}$ and two photons with an invariant mass close to the mass of the SM-like Higgs boson. These sources include contributions from dijet and multijet events, EW processes such as t, $t\bar{t}h$, Z, ZZ, or W bosons produced in association with one or two photons, $\gamma\gamma$, γ+jet, and Drell–Yan (DY) production in association with jets, where the Z boson decays to pairs of electrons and neutrinos. These backgrounds are generated with MadGraph5_amc@nlo, with the exception of the ZZ sample, which is generated with POWHEG [**121**]. These non-resonant background samples are not used for the background estimation, but are used to optimize the selection.

All simulated samples use the NNPDF 3.0 PDF sets [**122**]. The parton showering and hadronization are performed with PYTHIA using the CUETP8M1 tune [**123**, **124**]. For the $H \rightarrow b\bar{b}$ decay channel, to perform systematic studies in the boosted regime, an additional signal sample is generated with MadGraph5_amc@nlo, parton-showered and hadronized by HERWIG++ v2.7.1 [**125**] using the UE-EE-5C tune [**126**, **127**]. The samples are processed through a GEANT4-based [**128**] simulation of the CMS detector. All samples include the simulation of "pileup" arising from additional inelastic proton-proton interactions in the same or neighboring bunch crossings. An average of approximately ten pileup interactions per bunch crossing is included in the simulation with a separation between bunches of 25 ns. The simulated pileup distribution is reweighted to match the corresponding observed distribution in the analyzed data.

6.3 Event reconstruction

A global event reconstruction is performed using the particle-flow (PF) algorithm [**129**, **130**, **131**], which optimally combines the information from all the subdetectors and produces a list of stable particles, namely muons, electrons, photons, charged and neutral hadrons.

The reconstructed interaction vertex with the largest value of $\sum_i p_{\mathrm{T}i}^2$, where $p_{\mathrm{T}i}$ is the transverse momentum of the i^{th} track associated with the vertex, is selected as the primary event vertex. This vertex is used as the reference vertex for all objects reconstructed using the PF algorithm. The offline selection requires all events to have at least one primary vertex reconstructed within a 24 cm window along the z-axis around the mean interaction point, and a transverse distance from the mean interaction region less than 2 cm.

Jets are reconstructed from the PF candidates, after removing charged hadrons originating from pileup vertices, using the anti-K_T clustering algorithm [**132**] with distance parameters of 0.4 (AK4 jet) and 0.8 (AK8 jet), as implemented in the FAST-JET package [**133**]. In order to improve the discrimination of signal against multijet background, the pruning algorithm described in Ref., [**134**, **135**], which is designed to remove contributions from soft radiation and pileup, is applied to AK8 jets. The pruned jet mass ($m_{\mathrm{corrected}}^{\mathrm{pruned}}$) is defined as the invariant mass associated with the four-momentum of the pruned jet, after the application of the jet energy corrections [**136**]. Corrections to jet momenta are further propagated to the $\mathrm{P}_{\mathrm{T}}^{\mathrm{miss}}$ calculation [**137**]. In addition, tracks with $p_T > 1$ GeV, $|\eta| < 2.5$, and with longitudinal impact parameter $|d_Z| < 0.1\ cm$ from the primary vertex are used to reconstruct the track-based missing transverse momentum vector, $\vec{p}_{\mathrm{T,trk}}^{\mathrm{miss}}$.

The jets originating from the decay of b quarks are identified using the combined secondary vertex (CSV) algorithm [**138**, **139**], which uses PF jets as inputs. The algorithm combines the information from the primary vertex, track impact parameters, and secondary vertices within the jet using a neural network discriminator. The loose (medium) working point (WP) used in this analysis has a b jet selection efficiency of 83% (69%), a charm jet selection efficiency of 28% (20%), and a mistag rate for light-flavor jets of ≈10% (1%). The AK8 jets are split into two subjets using the soft-drop algorithm [**140**, **141**]. The CSV algorithm is tested and validated for AK4 and AK8 jets. The working points for the analyses of the resolved and boosted regimes were chosen by maximizing the expected significance. The loose WP of the subjet b tagging algorithm is used for the boosted regime, whereas the medium WP of the AK4 jet b tagging algorithm is used for the resolved regime, since the background is higher in this case.

Photons are reconstructed in the CMS detector from their energy deposits in the ECAL, which come from an electromagnetic shower involving several crystals. The energy is clustered at the ECAL level by building a cluster of clusters, called as supercluster (SC), which is extended in the ϕ direction because of the strong magnetic field inside the detector, which deflects the electron and positron produced if the photon converts in the tracker [**142**]. In order to achieve the best photon energy resolution, corrections are applied to remove channel-to-channel response variations and to recover energy losses due to incomplete containment of the shower or conversions, as detailed in Ref. [**143**]. Additional residual corrections are made to the measured energy scale of the photons in data (≤1%) and to the energy resolution in simulation (≤2%) based on a detailed study of the mass distribution of $Z \rightarrow e^+e^-$ events. The uncertainties in the measurements of the photon energy scale and resolution are taken as systematic uncertainties as described in the Section 6.5. This process is outlined for the 8 TeV data set in Ref. [**143**] values are adjusted for the 13 TeV data set.

Electron reconstruction requires the matching of a supercluster in the ECAL with a track in the silicon tracker. Identification criteria [**144**] based on the ECAL shower shape. Muons are reconstructed by combining two complementary algorithms [**145**]: one in which tracks in the silicon tracker are matched to a muon track segment, and another in which a global track fit is performed, seeded by the muon track segment. Further identification criteria are imposed on muon candidates to reduce the number of misidentified hadrons. Hadronically decaying τ leptons (τh) are reconstructed using the hadron-plus-strips (HPS) algorithm [**146**], which uses the charged-hadron and neutral-electromagnetic objects to reconstruct intermediate resonances into which the τ lepton decays.

6.4 Event selection and background estimation

This analysis searches for excesses over the background-only prediction in events with large $\mathrm{P_T^{miss}}$ and a system of two b-tagged jets or two photons that has a reconstructed invariant mass close to the mass of the SM-like Higgs boson h. In the $H \to b\bar{b}$ decay channel, the analysis relies on fitting the $\mathrm{P_T^{miss}}$ distribution simultaneously in the signal region (SR), defined after selecting a mass window around the Higgs boson mass, and in background-enriched control regions (CRs). For the $H \to b\bar{b}$ decay channel, a simple analysis is performed where the signal and resonant background contributions are estimated by counting the number of simulated events in the SR, while the non-resonant background is extrapolated from the data in a low-$\mathrm{P_T^{miss}}$ region. In the following sections, the event selection and analysis strategy are described in detail for the two channels separately.

6.4.1 $H \to b\bar{b}$

A search for DM produced in association with $H \to b\bar{b}$ is performed in a resolved regime, where events are required to have at least two AK4 jets, and in the Lorentz-boosted regime where one AK8 jet is required. In addition, $\mathrm{P_T^{miss}}$ is required to be large because it is a key signature of the signal events and it provides strong rejection against the large reducible backgrounds described in the Section 6.2.

6.4.1.1 Event selection

The trigger used in the selection of signal-like events requires $\mathrm{P_T^{miss}} > 90$ GeV and $\mathrm{H_T^{miss}} > 90$ GeV, where $\mathrm{H_T^{miss}}$ is defined as the magnitude of the vectorial sum of the p_T of all jets in the event with $p_\mathrm{T} > 20\ GeV$. An additional trigger with a $\mathrm{P_T^{miss}} > 170$ GeV requirement is used to achieve higher efficiency. In this way, events with either high $\mathrm{P_T^{miss}}$ or high $\mathrm{H_T^{miss}}$ will pass the trigger. For events passing the selection criteria that have $\mathrm{P_T^{miss}} > 170$ (200) GeV for the resolved (boosted) analysis, the trigger efficiency is found to be greater than 98%. The $\mathrm{P_T^{miss}}$ threshold for the analysis of the resolved regime is set slightly lower to enhance the signal efficiency in this region of phase space, where the $\mathrm{P_T^{miss}}$ distribution is softer.

Event filters are used to remove spurious high $\mathrm{P_T^{miss}}$ events caused by instrumental noise in the calorimeters, or beam halo muons. It has been verified that the efficiency of these filters for accepting signal events is very close to 100%. The main part of the event selection consists of Higgs boson tagging. This selection is different for the resolved and boosted analyses. In the resolved regime, events are required to have two AK4 jets with $p_T > 30$ GeV and $|\eta| < 2.4$. These two jets are used to reconstruct the Higgs boson candidate, which is required to have $p_T > 150$ GeV. Each of the two AK4 jets in the resolved regime is required to pass the b tagging selection, whereas in the boosted regime, the two subjets inside an AK8 jet must both pass the b tagging selection. In the boosted regime, the decay products from the Higgs boson are merged. Therefore, an AK8 jet with p_T greater than 200 GeV is used to reconstruct the Higgs boson. If more than one Higgs boson candidate is reconstructed, the ambiguity is resolved by selecting the candidate with the highest p_T. Backgrounds due to hadronic jets are further reduced by constraining the reconstructed Higgs boson candidate mass, $m_{\mathrm{b\bar{b}}}$, to be between 100 and 150 GeV. For the resolved regime, the Higgs boson candidate mass is reconstructed using two b-tagged AK4 jets. For the boosted regime, the corrected pruned mass of the AK8 jet with two b-tagged subjets is used as the Higgs boson candidate mass.

Multijet events can act as a source of background when the energy of one of the jets is mismeasured. Therefore, the absolute difference between the azimuthal angles of the vector $\vec{p}_\mathrm{T}^{\,\mathrm{miss}}$ and any other AK4 jet with $p_T > 30$ GeV is required to be greater than 0.4 radians. Multijet background is further reduced in the resolved analysis by requiring the azimuthal angle difference between the $\vec{p}_\mathrm{T}^{\,\mathrm{miss}}$ and $\vec{p}_\mathrm{T,trk}^{\,\mathrm{miss}}$ to be less than 0.7 radians.

Events are rejected if they have any isolated electron (muon) with $p_T > 10$ GeV and $|\eta| < 2.5$ (2.4) or any τh candidates with $p_T > 20$ GeV and $|\eta| < 2.3$ [**144**, **146**, **147**]. In addition, the events must not have any additional loose AK4 b-tagged jet or more than one additional AK4 jet with $p_T > 30$ GeV and $|\eta| < 4.5$. These vetoes considerably reduce the background from semileptonic top decay modes and leptonic decays of W+jets.

The product of the detector acceptance and selection efficiency varies from 1 to 29%, depending on the values of $m_{Z'}$ and m_A. The average $\mathrm{P_T^{miss}}$ increases with $m_{Z'}$ and decreases with m_A. The overall selection efficiency, shown in the Table 6.9, follows the same trend.

6.4.1.2 Data analysis strategy

Several CRs are used to correct the background normalizations with dedicated scale factors. For both resolved and boosted regimes, the selection criteria of these CRs are kept as close as possible to those of the SR, except for the inversion of the additional object vetoes (leptons, jets) and the Higgs boson mass window. This makes the CRs orthogonal to the SR.

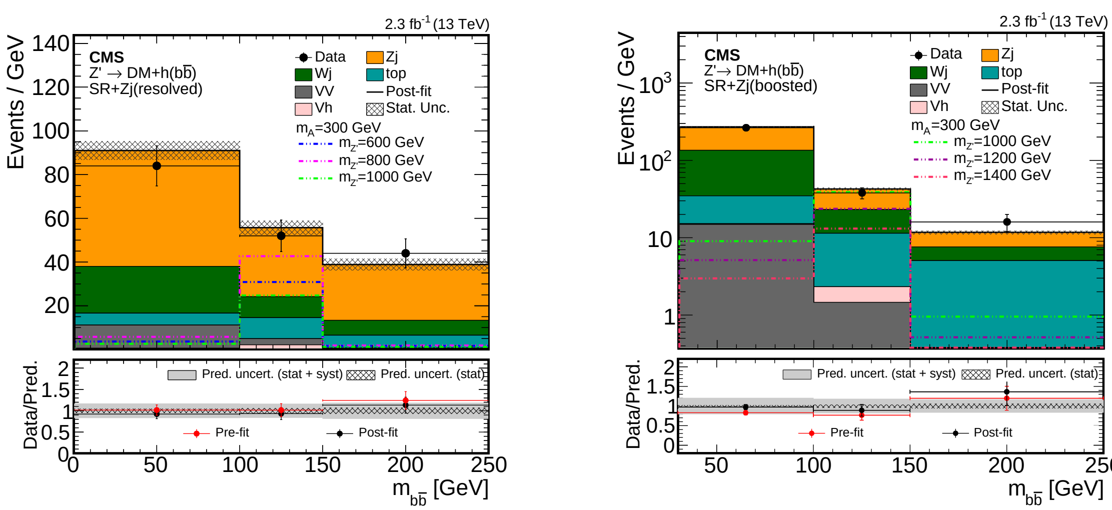

(a) (b)

Figure 6.3: Shows the post-fit distribution of the reconstructed Higgs boson candidate mass expected from SM backgrounds and observed in data for the resolved (a), and the boosted (b) regimes with three different $m_{Z'}$ signal points overlaid. Other parameters for this model are fixed to $m_\chi = 100$ GeV and $\tan\beta = g_\chi = 1$. The cross sections for the signal models are computed assuming $g_{Z'} = 0.8$. The bottom panels shows the data-to-simulation ratios for pre-fit (red markers) and post-fit (black markers) background predictions with a hatched band corresponding to the uncertainty due to the finite size of simulated samples and a gray band that represents the systematic uncertainty in the post-fit background prediction (see Section 6.5). The second bin represents the SR, while the events in the first and third bins are merged and represent the mass sidebands (Z($\to \nu\bar{\nu}$)+jets) CR.

For the resolved regime, three CRs are specified: Z($\rightarrow \nu\overline{\nu}$)+jets, top quark, and W+jets. The b tagging selection in all the CRs is the same as in the SR in order to minimize the b tagging systematic uncertainties when extrapolating the background scale factors measured in the CRs to the SR. The Z($\rightarrow \nu\overline{\nu}$)+jets CR is defined with the same selection as the SR, except for the inversion of the reconstructed Higgs boson mass requirement. The W+jets and top quark CRs are defined by removing the mass selection and requiring exactly one isolated electron (muon) with $p_T > 10$ GeV and $|\eta| < 2.5$ (2.4). Events with one additional AK4 jet are placed in the top quark CR, whereas events with no additional AK4 jets enter the W+jets CR.

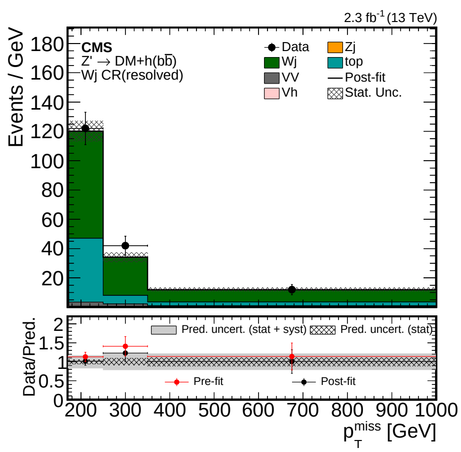

(a)

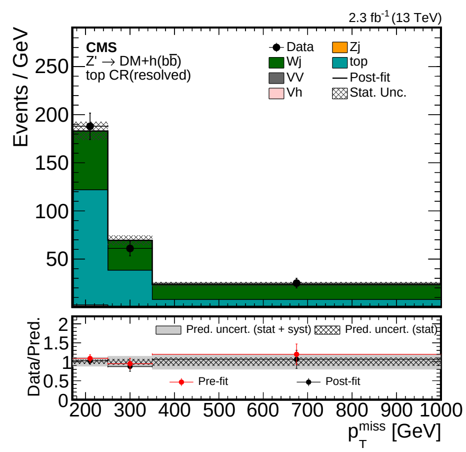

(b)

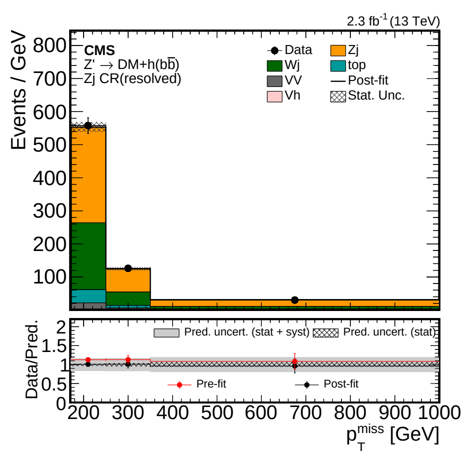

(c)

Figure 6.4: Shows the post-fit distribution of P_T^{miss} expected from SM backgrounds and observed in data for the W+jets (a), top quark (b), and Z($\rightarrow \nu\overline{\nu}$)+jets (c) CRs for the resolved regime.The bottom panels shows the Data-to-simulation ratios for pre-fit (red markers) and post-fit (black markers) background predictions with a hatched band corresponding to the uncertainty due to the finite size of simulated samples and a gray band that represents the systematic uncertainty in the post-fit background prediction (see Section 6.5). The last bin includes all events with $P_T^{miss} > 350$ GeV.

For the boosted regime, the Z($\rightarrow \nu\overline{\nu}$)+jets CR is defined by inverting the mass requirement for the AK8 jet. Owing to the low event count and very similar topology between the W+jets and top quark backgrounds it is difficult to construct two separate CRs for W+jets and top quark backgrounds. Hence, the single-lepton CR, a combination of mainly W+jets and top quark events, is defined using the same selection as that for the signal, but requiring exactly one isolated electron (muon) with $p_T > 10$ GeV and $|\eta| < 2.5$ (2.4) and removing the mass requirement.

Figure 6.3 shows the Higgs boson candidate mass for the resolved and boosted regimes. They correspond to the simultaneous fit of the $\mathrm{P_T^{miss}}$ distributions in the SR and background enriched CRs to extract the signal. Data-to-simulation ratios for pre-fit and post-fit background predictions are shown in the lower panels of all the Figures 6.3–6.6.

Figure 6.4 shows the comparison of data and simulation for the main observable, $\mathrm{P_T^{miss}}$, in the W+jets, top quark, and Z($\rightarrow \nu\overline{\nu}$)+jets CRs for the resolved regime. The comparison between data and simulated samples for the boosted regime is shown in the Figure 6.5 for the single-lepton CR and the Z($\rightarrow \nu\overline{\nu}$) mass sideband region.

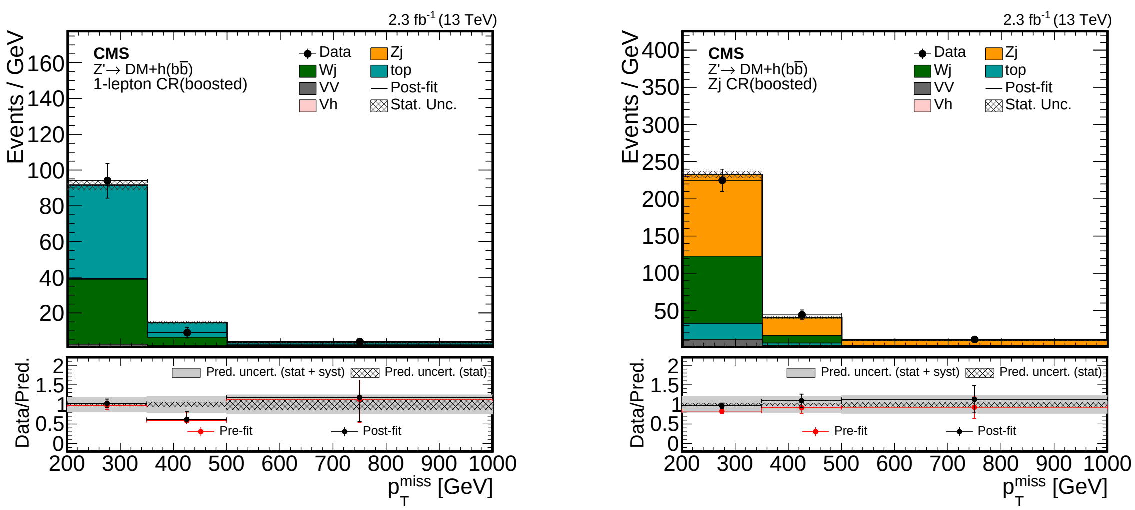

(a) (b)

Figure 6.5: Shows the post-fit distribution of $\mathrm{P_T^{miss}}$ expected from SM backgrounds and observed in data for the (a) single-lepton CR, and (b) Z($\rightarrow \nu\overline{\nu}$)+jets CRs for the boosted regime. The bottom panels show the data-to-simulation ratios for pre-fit (red markers) and post-fit (black markers) background predictions with a hatched band corresponding to the uncertainty due to the finite size of simulated samples and a gray band that represents the systematic uncertainty in the post-fit background prediction (see Section 6.5). The last bin includes all events with $\mathrm{P_T^{miss}} > 500$ GeV.

Figure 6.6 shows the $\mathrm{P_T^{miss}}$ distributions in three bins in the SR that are used for the final signal extraction. These three bins were chosen to optimize the expected limits. The selected signal and background events are compared to data and fit simultaneously in the SR and CRs in three P_T^{miss} bins, separately for the resolved and the boosted regimes.

The simultaneous fit of SR and background-enhanced CRs is performed correlating the scale factors and systematic uncertainties as described in the Section 6.5. The measured data-to-simulation post-fit scale factors are compatible with unity within the total combined statistical and systematic uncertainty. In particular, for the resolved regime, the scale factors for the backgrounds are 1.23 ± 0.17 for $Z(\rightarrow \nu\overline{\nu})$+jets, 1.33 ± 0.19 for W+jets, and 1.13 ± 0.17 for the top quark contributions.

For the boosted analysis, the scale factors are 0.77 ± 0.15 for $Z(\rightarrow \nu\overline{\nu})$+jets and 0.95 ± 0.19 for W+jets and top quark processes. Although the background scale factors do not show a common trend between the boosted and resolved analyses, it should be noted that the b-tagging requirement, selected phase space and other parameters are different in the two cases. Thus the two simultaneous fits are essentially independent, allowing the post-fit scale factors to move in either direction from unity.

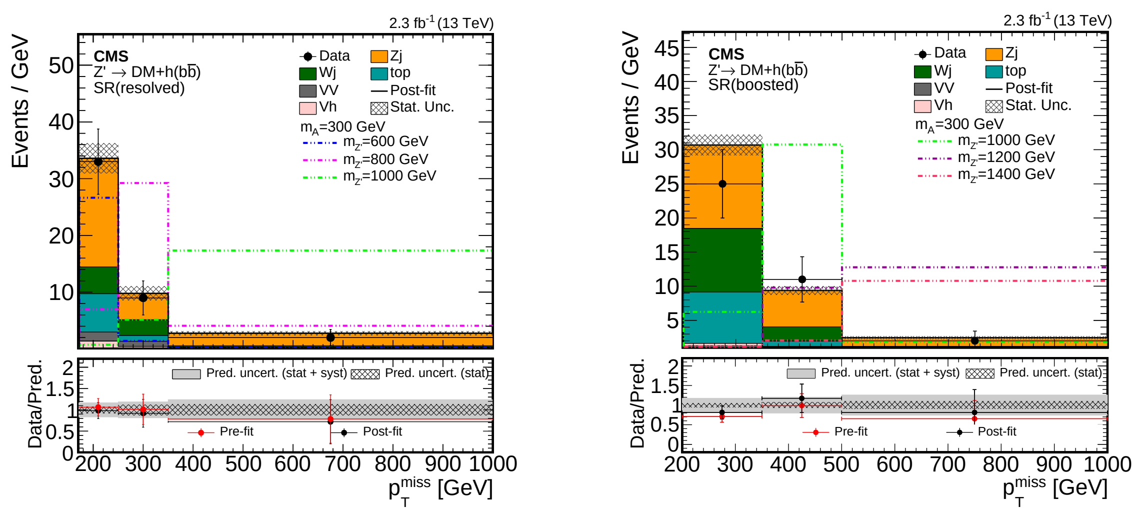

(a) (b)

Figure 6.6: Shows the post-fit distribution of P_T^{miss} expected from SM backgrounds and observed in data for the resolved (a), and the boosted (b) regimes in the signal region with three different $g_{Z'}$ signal points overlaid. Other parameters for this model are fixed to $m_\chi = 100$ GeV and $\tan\beta = g_\chi = 1$. The cross sections for the signal models are computed assuming $g_{Z'} = 0.8$. The bottom panels show the data-to-simulation ratios for pre-fit (red markers) and post-fit (black markers) background predictions with a hatched band corresponding to the uncertainty due to the finite size of simulated samples and a gray band that represents the systematic uncertainty in the post-fit background prediction (see Section 6.5). The last bin includes all events with $P_T^{miss} > 350$ (500) GeV for the resolved (boosted) regime.

6.4.2 $H \to \gamma\gamma$

The $H \to \gamma\gamma$ search is performed using a diphoton selection. A set of requirements is applied to ensure good-quality photon candidates. Additional kinematic requirements on the objects in the final state are applied to reduce the background. The diphoton invariant mass and $\mathrm{P_T^{miss}}$ are used as the discriminating variables to estimate the signal.

6.4.2.1 Event selection

Diphoton triggers with asymmetric transverse energy thresholds (30/18 GeV) are used to select events with the diphoton invariant mass above 95 GeV. The trigger selection uses a very loose photon identification based on the cluster shower shape and loose isolation requirements (both defined in detail in Ref. [**143**]), and a requirement that the ratio of hadronic-to-electromagnetic energy of the photon candidates is less than 0.1.

The main source of background for photons, which arises from jets with high electromagnetic energy content, is rejected by considering the ratio of energies deposited by the photon candidate in the hadron and electromagnetic calorimeters and the spread of the energy deposition in the η direction, as described in [**143**]. In addition, misidentified photons are rejected using the isolation variables $\mathrm{Iso_{Ch}}$, Iso_γ, and $\mathrm{Iso_{Neu}}$ calculated by summing the p_T of the charged hadrons, photons and neutral hadrons, respectively, in a cone of radius $\Delta R = 0.3$. In the photon identification, $\mathrm{Iso_{Neu}}$ and Iso_γ are corrected for the median transverse energy density (ρ) of the event to mitigate the effects of pileup [**148**].

The photons in the EB (i.e. the photons with $|\eta| \leq 1.44$) and photons in the EE ($1.566 \leq |\eta| \leq 2.5$) have different selection criteria, equivalent to those used in Ref. [**149**, **150**]. The working point chosen for this analysis corresponds to 90.4% (90.0%) photon ID efficiency in the EB (EE), while the misidentification rate in the EB (EE) is 16.2% (18.7%) for objects with p_T>20 GeV.

A high-quality interaction vertex, defined as the reconstructed vertex with the largest number of charged tracks, is associated to the two photons in the event. The efficiency of selecting the correct vertex for all generated mass points, defined as the fraction of signal events with well reconstructed vertices that have a z position within 1cm of the generator-level vertex, is approximately 78%.

The optimal signal selection is chosen by studying the discriminating power of variables such as the $p_T/m_{\gamma\gamma}$ of each photon, $\mathrm{P_T^{miss}}$, and the p_T of the diphoton system ($p_{\mathrm{T}\gamma\gamma}$). A selection on p_T that scales with $m_{\gamma\gamma}$ is chosen such that it does not distort the $m_{\gamma\gamma}$ spectrum shape. The $p_{\mathrm{T}\gamma\gamma}$ variable, included because it has a better resolution than $\mathrm{P_T^{miss}}$, has a distribution of values that are on average larger for signal than for background events, given that the Higgs boson is expected to be back-to-back in the transverse plane with the $\vec{p}_{\mathrm{T}}^{\,\mathrm{miss}}$.

In addition, two geometrical requirements are applied to enhance the signal over background discrimination and to veto background events with mismeasured $\mathrm{P_T^{miss}}$:

- the azimuthal separation between the $\vec{p}_{\mathrm{T}}^{\,\mathrm{miss}}$ and the Higgs boson direction (reconstructed from the two photons) $|\Delta\phi(\gamma\gamma, \vec{p}_{\mathrm{T}}^{\,\mathrm{miss}})|$ must be greater than 2.1 radians.

- the minimum azimuthal angle difference between the $\vec{p}_{\mathrm{T}}^{\,\mathrm{miss}}$ and the jet direction in the event $min(|\Delta\phi(\mathrm{jet}, \vec{p}_{\mathrm{T}}^{\,\mathrm{miss}})|)$ must be greater than 0.5 radians. The jet direction is derived by considering all the jets reconstructed from the clustering of PF candidates by means of the anti-k_t algorithm [**132**] with a distance parameter of 0.4. Jets are considered if they have a p_T above 50 GeV in the $|\eta|$ range below 4.7 and satisfy a loose set of identification criteria designed to reject spurious detector and reconstruction effects.

The set of selection criteria that maximizes the expected significance for each Z' mass point is studied. The optimized selection for the $m_{Z'} = 600$ GeV and $m_A = 300$ GeV sample maintains a large efficiency for the other signal mass points, while the backgrounds remain small. Therefore a common set of criteria is used for all signal masses with $m_{Z'}$ between 600 and 2500 GeV and m_A between 300 and 800 GeV. The chosen kinematic selections include $p_{\mathrm{T}1}/m_{\gamma\gamma} > 0.5$, $p_{\mathrm{T}2}/m_{\gamma\gamma} > 0.25$, $p_{\mathrm{T}\gamma\gamma} > 90$ GeV, $\mathrm{P_T^{miss}} > 105$ GeV. Events are vetoed if they have any muons or more than one electron present. This allows the analysis to be sensitive to events where an electron originating from conversion of the photon before reaching the ECAL is identified outside the photon supercluster. Standard lepton identification requirements are used [**144**, **147**]. This requirement is 100% efficient for the signal and reduces significantly the EW background contributions.

The SR of this analysis is defined as the region with $120 < m_{\gamma\gamma} < 130$ GeV and $\mathrm{P_T^{miss}}$ above 105 GeV. The distribution of $m_{\gamma\gamma}$ for the selected events before the $\mathrm{P_T^{miss}}$

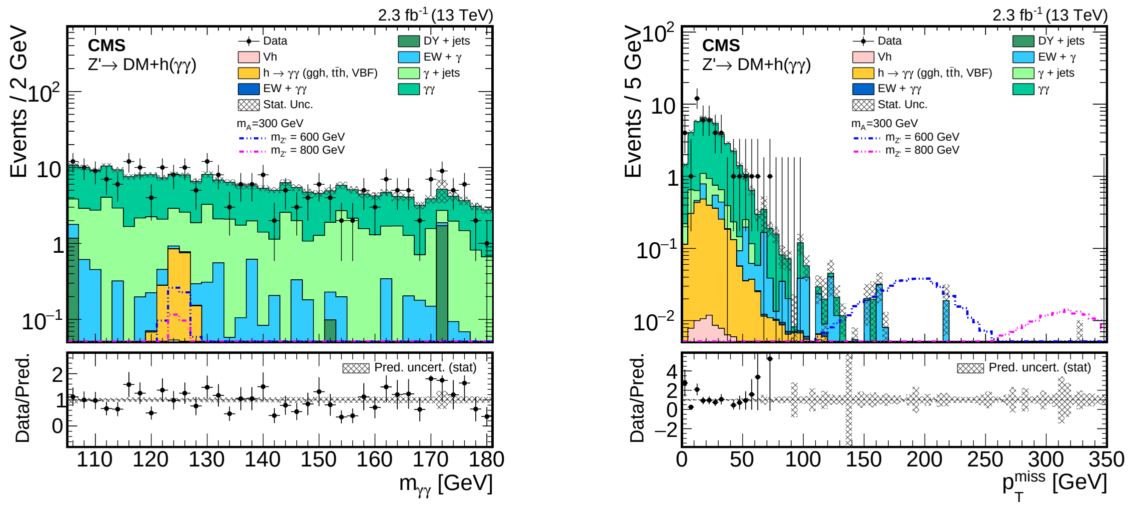

(a) (b)

Figure 6.7: Shows the (a) distribution of $m_{\gamma\gamma}$ in events passing all selection criteria except the $m_{\gamma\gamma}$ and requirement, and (b) expected and observed distribution of $\mathrm{P_T^{miss}}$ for events passing all selection criteria including 120 GeV$< m_{\gamma\gamma} <$ 130 GeV except $\mathrm{P_T^{miss}}$ requirement. Two different $m_{Z'}$ signal points are overlaid. Other parameters for this model are fixed to $m_\chi = 100$ GeV and $\tan\beta = g_\chi = 1$. The cross sections for the signal models are computed assuming $g_{Z'} = 0.8$. For both plots, the total simulated background is normalized to the total number of events in data. The bottom panels show the data-to-simulation ratios for background predictions with a hatched band corresponding to the uncertainty due to the finite size of simulated samples.

requirement is shown in the Figure 6.7 for the full mass range considered in this analysis: $105 < m_{\gamma\gamma} < 180$ GeV. Also, shown is the $\mathrm{P_T^{miss}}$ distribution of the selected events after the $m_{\gamma\gamma}$ SR selection. It can be seen that after applying the requirement that $m_{\gamma\gamma}$ has to be close to the Higgs boson mass, the SM background contribution in the high-$\mathrm{P_T^{miss}}$ region is close to zero and the DM signal is well separated from the background distribution.

6.4.2.2 Background estimation

The final state with a $\gamma\gamma$ pair and large $\mathrm{P_T^{miss}}$ has two classes of background: resonant and non-resonant. The contributions from each class are treated differently.

Resonant backgrounds arise from decays of the SM Higgs boson to two photons. They appear as an additional peak under the expected signal peak and are evaluated with the MC simulation by counting the number of expected events from all SM Higgs production modes in the SR.

The contribution of the non-resonant backgrounds ($N_{\mathrm{SB}}^{\mathrm{bkg}}$) in the sideband (SB) region, mostly multijets and EW processes with mismeasured large $\mathrm{P_T^{miss}}$ and misidentified photons, is evaluated from the data by counting the number of events in the $m_{\gamma\gamma}$ sidebands $105 < m_{\gamma\gamma} < 120$ GeV and $130 < m_{\gamma\gamma} < 180$ GeV, with $\mathrm{P_T^{miss}} > 105$ GeV in both cases [150]. Then $N_{\mathrm{SB}}^{\mathrm{bkg}}$ is scaled by a transfer factor α to take into account the relative fraction between the number of events in the $m_{\gamma\gamma}$ SR and SB region.

The expected number of non-resonant background events in the SR is given by:

$$N_{\mathrm{SR}}^{\mathrm{bkg}} = \alpha N_{\mathrm{SB}}^{\mathrm{bkg}}. \tag{6.2}$$

The derivation of α relies on the knowledge of the background shape $f_{\mathrm{bkg}}(m_{\gamma\gamma})$ as follows:

$$\alpha = \frac{\int_{\mathrm{SR}} f_{\mathrm{bkg}}(m_{\gamma\gamma}) dm_{\gamma\gamma}}{\int_{\mathrm{SB}} f_{\mathrm{bkg}}(m_{\gamma\gamma}) dm_{\gamma\gamma}}, \tag{6.3}$$

and is evaluated by performing a fit to the $m_{\gamma\gamma}$ distribution in a CR of the data. In this analysis, the low-$\mathrm{P}_{\mathrm{T}}^{\mathrm{miss}}$ CR, with $\mathrm{P}_{\mathrm{T}}^{\mathrm{miss}} < 105$ GeV, is used. The fit to data in the low-$\mathrm{P}_{\mathrm{T}}^{\mathrm{miss}}$ region used to calculate α is shown in the Figure 6.8. In this case the negligible contribution of the resonant SM Higgs boson processes is not considered. The data are fit with a background-only model using an analytic power law function:

$$f(x) = ax^{-b} \tag{6.4}$$

where the parameter a, the normalization, and b are free parameters, defined as positive. The fit is performed with an unbinned maximum likelihood technique. The function defined in the Equation (6.4) was chosen after examining several models and performing a bias study using non-resonant background MC to evaluate any possible background mismodeling, following the procedure described in Ref. [151]. It has been verified that the fitted parameters of the power law function are compatible within the uncertainties with both data and simulation.

To derive a robust estimate of α, several fits to both data and simulated background events are performed using different analytic functions and looking at different CRs of $\mathrm{P}_{\mathrm{T}}^{\mathrm{miss}}$. Within the uncertainties, α is independent of the $\mathrm{P}_{\mathrm{T}}^{\mathrm{miss}}$ CR used and is consistent between data and simulation. The fitted shape of the low-$\mathrm{P}_{\mathrm{T}}^{\mathrm{miss}}$ CR in data is taken as the nominal background shape. This yields $\alpha = 0.190 \pm 0.035$ (stat). Alternative analytic functions, as well as alternative $\mathrm{P}_{\mathrm{T}}^{\mathrm{miss}}$ CRs in both data and simulation are considered in order to estimate the systematic uncertainty in this parameter, as described in the Section 6.5.

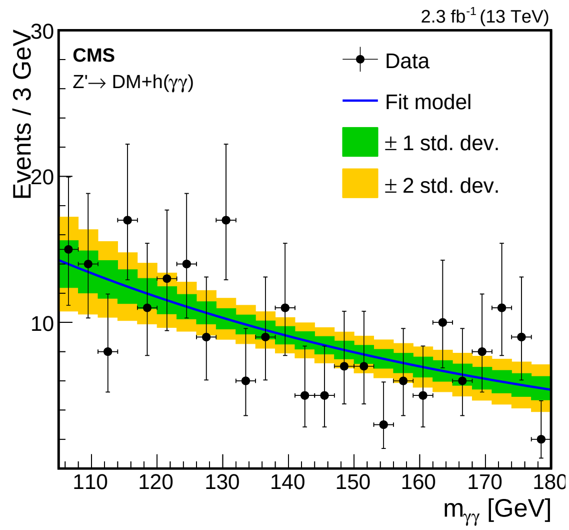

Figure 6.8: Fit to the diphoton invariant mass distribution in the low-$\mathrm{P_T^{miss}}$ CR in data used to evaluate α. The function used is a power law with one free parameter. The uncertainties in the background shapes associated with the statistical uncertainties of the fit are shown by the one and two standard deviation bands.

6.5 Systematic uncertainties

The systematic uncertainties common to the two Higgs boson decay channels are as follows.

An uncertainty of 2.7% is used for the normalization of simulated samples in order to reflect the uncertainty in the integrated luminosity measurement in 2015 [**152**]. In the $H \to b\bar{b}$ analysis an uncertainty of 2% is estimated in the signal yield for $\mathrm{P_T^{miss}}$ above 170 GeV by varying the parameters describing the trigger turn-on. For the $H \to \gamma\gamma$ analysis the trigger uncertainty (approximately 1%) is extracted from $Z \to e^+e^-$ events using the tag-and-probe technique [**153**]. The following uncertainties in clustered and unclustered calorimetric energy affect the $\mathrm{P_T^{miss}}$ shapes and the normalization of the signal and background yield predictions: the JES for each jet is varied within one standard deviation as a function of p_T and η, and the efficiency of the event selection is recomputed to assess the variation on the normalization and $\mathrm{P_T^{miss}}$ shape for signal and backgrounds; the signal acceptance and efficiency are recomputed after smearing the energy of each jet to correct for the difference in jet energy resolution between the data and simulation ($\approx$5%); the systematic uncertainties in the calibration of unclustered energy in the calorimeter are propagated as normalization and shape uncertainties in the $\mathrm{P_T^{miss}}$ calculation. The total effect of the systematic uncertainty in the signal yield, considering all of these variations on P_T^{miss} is approximately 3% for the $H \to b\bar{b}$ analysis and less than 1% for the $H \to \gamma\gamma$ analysis. Among the three sources, the JES is the one that most affects the signal yield.

The following systematic uncertainties only affect the $H \to b\bar{b}$ decay channel: The b tagging scale factors are applied consistently to jets in signal and background events. An average systematic uncertainty of 6% per b jet, 12% per c jet, and 15% per light quark or gluon jet is used to account for the normalization uncertainty [**138**]. The pruned mass distribution of the AK8 jet is not perfectly reproduced by simulation. Therefore, a control region, with a large number of events enriched in boosted hadronically decaying W bosons reconstructed as AK8 jets, is used to measure the systematic uncertainty due to this effect, giving an estimated value of 5%. Moreover, different hadronization algorithms (PYTHIA and HERWIG++) give slightly different shapes for the pruned mass distribution. Therefore, an additional uncertainty of 10% is assigned to account for the difference between simulations. For the boosted regime, the same background normalization scale factor is used for W+jets and top quark backgrounds. The uncertainty in the relative normalization of these two processes is 30%. An uncertainty of 2% is measured by varying the lepton efficiency scale factors within one standard deviation and recomputing the signal selection efficiency.

For W+jets, Z($\to \nu\overline{\nu}$)+jets and top quark backgrounds, variations in the renormalization and factorization scales directly affect the normalization and shape of the P_T^{miss} distribution. A variation of approximately 5% is found for the yields of these backgrounds in the signal region. The uncertainty in the signal acceptance and P_T^{miss} shape due to the choice of PDFs is measured following the method described by the PDF4LHC group [**154**]. A variation of approximately 3% is found in the signal yields. The effect of electroweak corrections as described in the Section 6.2 is studied by recomputing the normalization and shapes for the W+jets and Z($\to \nu\overline{\nu}$)+jets backgrounds, by alternately removing the corrections or doubling them. An uncertainty of 20% is assumed for the single top quark , SM Higgs boson, and diboson production rates. Uncertainties due to the finite size of the signal and background simulated samples are included in the normalization and shape, such that each bin of the final fitted distributions is affected independently.

In summary, for $H \to b\bar{b}$, the overall uncertainties related to background determination methods, simulation, and theory inputs are estimated to be 10% in the background contributions in the SR. The impact of the uncertainty in the major background contributions (W+jets, Z($\rightarrow \nu\overline{\nu}$)+jets and top quarks) in the SR is reduced by constraining the normalizations of these processes in data with the simultaneous fit of P_T^{miss} shapes in the SR and CRs. The major sources of systematic uncertainties that affect the fit are JES uncertainties, b tagging uncertainties, and the statistical uncertainty in the simulated Z($\rightarrow \nu\overline{\nu}$)+jets and W+jets background samples. The effect of the remaining uncertainties on the final fit is ≈1%.

The following systematic uncertainties affect only the $H \rightarrow \gamma\gamma$ analysis:

As shown in the Equation (6.2), the predicted number of non-resonant background events in the SR is evaluated from the number of observed events in the $m_{\gamma\gamma}$ sidebands in the high-P_T^{miss} region (N_{SB}^{bkg}) multiplied by a transfer factor α obtained by fitting the $m_{\gamma\gamma}$ distribution in the low-P_T^{miss}control region. Therefore two different systematic uncertainties are assigned to this procedure, one for N_{SB}^{bkg} and one for α.

The first systematic uncertainty takes into account the fact that N_{SB}^{bkg} is statistically limited. Secondly, a 20% systematic uncertainty is assigned to reflect the imperfect knowledge of the background $m_{\gamma\gamma}$ shape in the low-P_T^{miss} region, hence on the knowledge of the α factor. This uncertainty is obtained by performing the fit to the $m_{\gamma\gamma}$ distribution using several analytic functions, using data rather than using simulated events, and using other P_T^{miss} CRs.

An observed peak above the diphoton continuum in the $m_{\gamma\gamma}$ distribution around the SM Higgs boson mass would have a SM $H \rightarrow \gamma\gamma$ contribution. In order to extract the DM signal, the resonant background contribution has to be evaluated and subtracted. The SM Higgs boson contribution is affected by both theoretical and experimental systematic uncertainties. For each SM Higgs boson production mechanism (ggh, VBF, $t\bar{t}$h, Vh), the uncertainties on the PDFs and α_s, provided in Ref. [**155**], are addressed using the procedure from the PDF4LHC group [**154**]. The size of the systematic uncertainty is computed for each process and category separately by checking the effect of each weight on the final event yield. An additional uncertainty on the $H \rightarrow \gamma\gamma$ branching fraction of 5% is included following Ref. [**155**]. A 1% photon energy scale uncertainty is assigned. This number takes into account the knowledge of the energy scale at the Z boson peak and of its extrapolation to higher masses. The uncertainty on the photon resolution correction factors is evaluated by raising and lowering the estimated additional Gaussian smearing measured at the Z boson peak by 0.5% in quadrature. The photon identification uncertainty is taken as an uncertainty in the data-to-simulation scale factors, which can be as large as 2%, depending on the p_T and the η of the photon. The $H \to \gamma\gamma$ decay channel results are only marginally affected by systematic uncertainties as statistical uncertainties dominate the analysis.

6.6 Results

For the event selection described in the Section 6.4, the predicted signal acceptances multiplied by the efficiencies ($A\epsilon$) are listed in the Table 6.9 for the two decay channels.

Table 6.10 shows, for the $H \to b\bar{b}$ channel, the SR post-fit yields for each background and signal mass point along with the sum of the statistical and systematic uncertainties for the resolved and boosted regimes. The total background uncertainty is approximately 10% and mainly driven by the systematic uncertainty.

For the $H \to \gamma\gamma$ channel, when applying the event selection to the data, two events are observed in the $m_{\gamma\gamma}$ sidebands and are used to evaluate the magnitude of the non-resonant background as described in the Section 6.4.2.2.

m_A [GeV]	300	400	500	600	700	800
$m_{Z'}$ [GeV]	$h \to b\bar{b}$					
600	0.058 ± 0.003	0.013 ± 0.003	—	—	—	—
800	0.132 ± 0.003	0.117 ± 0.003	0.083 ± 0.003	0.040 ± 0.003	—	—
1000	0.245 ± 0.004	0.218 ± 0.003	0.167 ± 0.002	0.123 ± 0.003	0.181 ± 0.003	0.066± 0.003
1200	0.282 ± 0.003	0.272 ± 0.004	0.262 ± 0.003	0.238 ± 0.004	0.195 ± 0.003	0.126± 0.003
1400	0.286 ± 0.003	0.287 ± 0.003	0.283 ± 0.003	0.279 ± 0.003	0.285 ± 0.003	0.249± 0.003
1700	0.280 ± 0.003	0.284 ± 0.003	0.283 ± 0.003	0.284 ± 0.003	0.285 ± 0.004	0.284± 0.003
2000	0.269 ± 0.005	0.271 ± 0.003	0.275 ± 0.003	0.273 ± 0.003	0.276 ± 0.003	0.279± 0.004
2500	0.248 ± 0.003	0.246 ± 0.003	0.250 ± 0.004	0.251 ± 0.003	0.255 ± 0.003	0.256± 0.003
$m_{Z'}$ [GeV]	$h \to \gamma\gamma$					
600	0.317 ± 0.004	0.212 ± 0.003	—	—	—	—
800	0.399 ± 0.004	0.386 ± 0.003	0.348 ± 0.003	0.280 ± 0.003	—	—
1000	0.444 ± 0.004	0.437 ± 0.003	0.422 ± 0.003	0.402 ± 0.003	0.373 ± 0.003	0.330 ± 0.003
1200	0.474 ± 0.004	0.468 ± 0.003	0.461 ± 0.003	0.454 ± 0.003	0.438 ± 0.003	0.417 ± 0.003
1400	0.492 ± 0.004	0.493 ± 0.003	0.485 ± 0.003	0.481 ± 0.003	0.472 ± 0.003	0.465 ± 0.003
1700	0.493 ± 0.004	0.499 ± 0.003	0.504 ± 0.003	0.503 ± 0.003	0.499 ± 0.003	0.498 ± 0.003
2000	0.351 ± 0.004	0.373 ± 0.003	0.394 ± 0.003	0.421 ± 0.003	0.453 ± 0.003	0.488 ± 0.003
2500	0.213 ± 0.004	0.217 ± 0.003	0.227 ± 0.003	0.236 ± 0.003	0.254 ± 0.003	0.268 ± 0.003

Figure 6.9: The product of acceptance and efficiency (with statistical uncertainty) for signal in the SR, after full event selection for the $H \to b\bar{b}$ (upper) and the $H \to \gamma\gamma$ (lower) decay channels. The systematic uncertainty for $H \to b\bar{b}$ ($H \to \gamma\gamma$) is approximately 10% (5%). For $H \to b\bar{b}$, the value shown here is either for the resolved regime or for the boosted regime, depending on which is used for the calculation of the limit on σ ($Z' \to Ah \to \chi\bar{\chi}h$), as shown in the Figure 6.12 (a).

This yields an expected number of 0.38 ± 0.27 (stat) non-resonant background events in the SR. Expected resonant background contributions are taken from the simulation as detailed in Section 6.4.2.2 and are 0.057 ± 0.006 (stat) events considering both the Vh production (dominant) and the gluon fusion mode. Zero events are observed in the SR in the data.

$h \to b\bar{b}$ analysis	Number of events (in 2.3 fb^{-1})	
Process	Resolved	Boosted
$Z(\to \nu\bar{\nu})$+jets	29.6 ± 4.9	19.3 ± 2.0
top quark	7.3 ± 2.1	8.2 ± 2.3
W+jets	9.1 ± 2.2	10.7 ± 2.6
Diboson	2.7 ± 0.7	1.5 ± 0.5
Vh	2.0 ± 0.2	0.8 ± 0.2
Multijet	0.010 ± 0.002	0.02 ± 0.01
Total background	50.7 ± 5.4	40.5 ± 4.3
Data	44	38
$m_{Z'}$ [GeV]		
600	29.0 ± 3.5	—
800	40.4 ± 3.8	—
1000	23.3 ± 2.5	—
1200	—	23.6 ± 2.5
1400	—	13.1 ± 1.5
1700	—	5.6 ± 0.7
2000	—	2.3 ± 0.3
2500	—	0.24 ± 0.03

Figure 6.10: Post-fit background event yields and observed numbers of events in data for 2.3 fb^{-1} in both the resolved and the boosted regimes for the $H \to b\bar{b}$ analysis. The expected numbers of signal events for $m_{\mathrm{A}} = 300$ GeV, scaled to the nominal cross section with $g'_Z = 0.8$, are also reported. The statistical and systematic uncertainties are shown separately in that order.

Since no excess of events has been observed over the SM background expectation in the signal region, the results of this search are interpreted in terms of an upper limit on the production of DM candidates in association with a Higgs boson in the process $Z' \to Ah \to \chi\bar{\chi}h$. The upper limits are computed at 95% confidence level (CL) using a modified frequentist method (CL_s) [**155**, **156**, **157**] computed with an asymptotic approximation [**158**]. A profile likelihood ratio is used as the test statistic in which systematic uncertainties are modeled as nuisance parameters. These limits are obtained as a function of m'_Z and m_A for both Higgs boson decay channels and for the combination of the two. The two decay channels are combined using the branching ratios predicted by the SM. In the combination of the two analyses, all signal and P_T^{miss}-related systematic uncertainties as well as the systematic uncertainty in the integrated luminosity are assumed to be fully correlated.

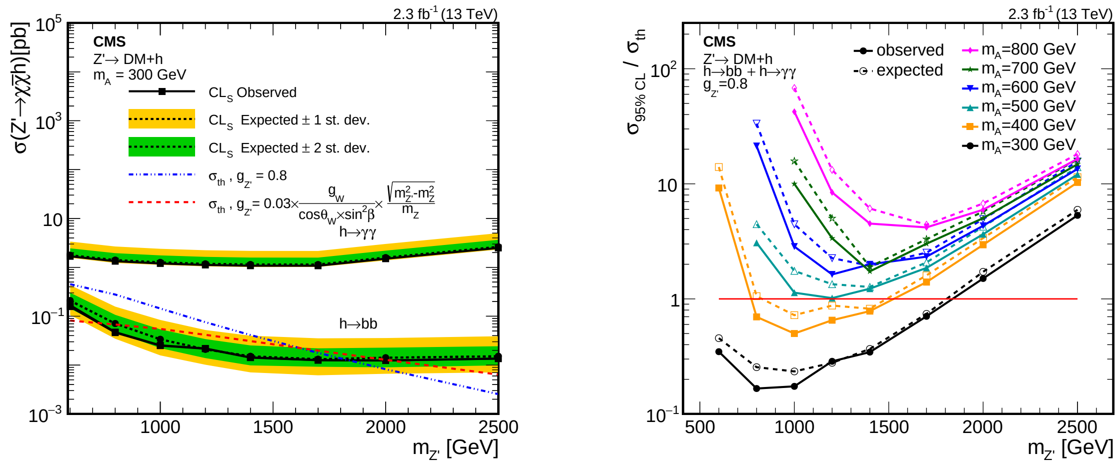

(a) (b)

Figure 6.11: Shows the (a) expected and observed 95% CL limits on dark matter production cross sections for $H \to b\bar{b}$ and $H \to \gamma\gamma$ for $m_A = 300$ GeV. The exclusion region is shown for two g'_Z values. The dark green and light yellow bands show the 68% and 95% uncertainties on the expected limit, and (b) expected and observed 95% CL limits on the signal strength for $m_A = 300$–800 GeV are shown. Other parameters for this model are fixed to $m_\chi = 100$ GeV and $\tan\beta = g_\chi = 1$. The theoretical cross section ($\sigma_{\rm th}$) used for the right-hand plot is calculated using $g'_Z = 0.8$.

Figure 6.11 (a) shows the 95% CL expected and observed limits on the dark matter production cross section $\sigma(Z' \to Ah \to \chi\bar{\chi}h)$, for $H \to b\bar{b}$ and $H \to \gamma\gamma$ for $m_A = 300$ GeV. These results, obtained with $m_\chi = 100$ GeV, can be considered valid for any dark matter particle mass below 100 GeV since the branching fraction for decays of A to DM particles, $\mathcal{B}(A \to \chi\bar{\chi})$, decreases as m_χ increases. As shown in the Figure 6.11, for the phase space parameters considered for this model (g_χ and $\tan\beta$ equal to unity), results of the combined analysis are mainly driven by the $H \to b\bar{b}$ channel. The combination with the $H \to \gamma\gamma$ channel provides a 2-4% improvement in terms of constraints on the model for the low Z' mass values. Future iterations of this search will explore additional phase space regions of the Z'-2HDM model, i.e. larger values of $\tan\beta$, where the $H \to \gamma\gamma$ channel becomes more sensitive than $H \to b\bar{b}$.

Figures 6.11 (b) and 6.12 show the 95% CL expected and observed upper limits on the signal strength $\sigma_{95\%\mathrm{CL}}(Z' \to Ah \to \chi\bar{\chi}h)/\sigma_{\mathrm{theory}}(Z' \to Ah \to \chi\bar{\chi}h)$.

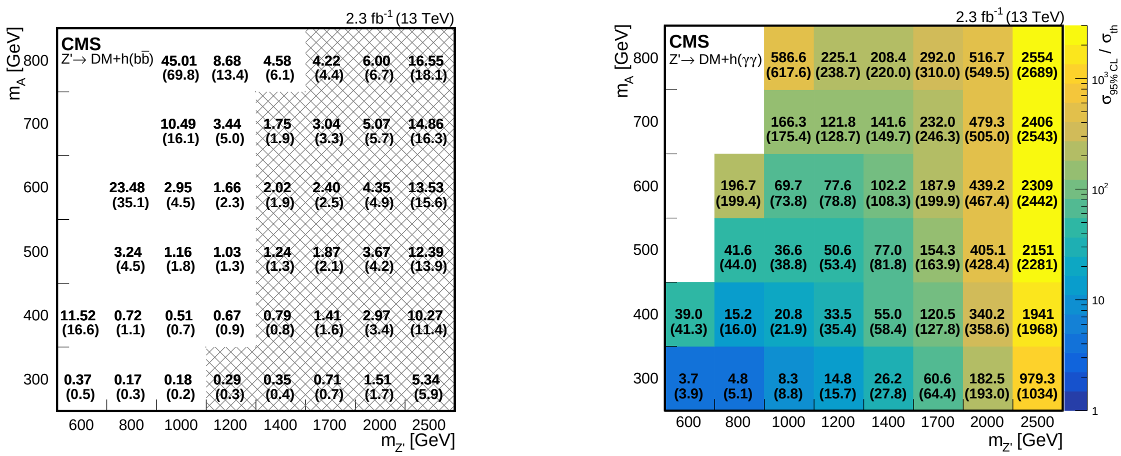

(a) (b)

Figure 6.12: (The observed (expected) 95% CL limits on the signal strength (as shown in the Figure 6.11 (b)), separately for the $H \to b\bar{b}$ (a), and $H \to \gamma\gamma$ (b) decay channels, and for m_A = 300-800 GeV and m'_Z = 600-2500 GeV. Other parameters for this model are fixed to $m_\chi = 100$ GeV and $\tan\beta = g_\chi = 1$. The theoretical cross sections are calculated using $g_{Z'} = 0.8$. For $H \to b\bar{b}$, the results for the resolved analysis are shown over a white background, whereas the boosted analysis results are shown over a hatched background

For $m_A = 300$ GeV, the Z' mass range from 600 to 1780 GeV is expected to be excluded with a 95% CL when the signal model cross section is calculated using $g'_Z = 0.8$, while the observed data, for $m_A = 300$ GeV, exclude the Z' mass range from 600 to 1860 GeV. When the signal model cross section is calculated using the constrained g'_Z, the expected exclusion range is 830 to 1890 GeV, and the observed exclusion range is 770 to 2040 GeV. Figure 6.12 shows the expected and observed upper limits on the signal strength for the $H \to b\bar{b}$ and $H \to \gamma\gamma$ decay channels.

Figure 6.13 shows the upper limits on the signal strength combining the results from both the $H \to b\bar{b}$ and $H \to \gamma\gamma$ decay channels.

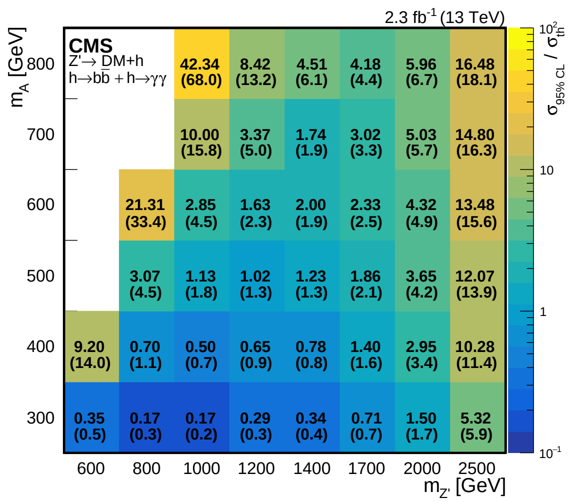

Figure 6.13: The observed (expected) 95% CL limits on the signal strength (as in the Figure 6.11 (b)) for the combination of $H \to \gamma\gamma$ and $H \to b\bar{b}$ decay channels, and for m_A = 300–800 GeV and m'_Z = 600–2500 GeV. Other parameters for this model are fixed to $m_\chi = 100$ GeV and $\tan\beta = g_\chi = 1$. The theoretical cross sections times branching fractions are calculated using $g_{Z'} = 0.8$.

7

Conclusions

> *"The most successful men in the end are those whose success in the result of steady accretion."*
>
> – Alexander Graham Bell

To improve the detection efficiency of the muons in the forward region of the CMS, the upgrade project includes the new layer of triple-GEM detector (known as GE1/1) has been approved in 2010. To understand the detector operation and installation in CMS a small scale test (known as slice test) was performed in 2016 under which 5 super-chambers were installed. Two different prototypes short (106.1 cm × 23.1 cm × 42.0 cm) and long (120.6 cm × 23.1 cm × 44.6 cm) has been installed after performing a precise QCs[1] procedure which ensure the best performance of the world largest triple-GEM detector. We have played a significant role in defining and performing the QCs on these prototyping detectors before the installation in CMS. After the successful installation and performance of the chambers in CMS, the large scale production of a total 144 trapezoidal shape triple-GEM detector was started at various production sites over the globe. We have developed the assembly and testing laboratory at DU and delivered 16 detectors from India. The installation and commissioning of these chambers is ongoing and will be operational after LS2. Along with this, two more upgrades knows as GE2/1 and ME0 with triple-GEM detector in the forward region of CMS has been approved, the installation of GE2/1 chambers is scheduled in 2022 and for ME0 chambers in between 2022 and 2024. A

[1] QCs has been divided into three major parts: First is the inspection of the material and characterization of the GEM foils at CERN, second is the assembly and testing of the triple-GEM detector at different production sites, and at last installation of electronics & cosmic test at CERN.

complete GE2/1 chamber (stack) of 8 modules has been built and passed all the QCs. On chamber electronics prototyping and testing for GE2/1 modules is finished and complete chamber is under testing. For the ME0, the chamber prototype mechanical design as well as on-chamber electronic design has been completed.

GEM foils were produced for the first time in India under the TOT agreement between Micropack Pvt. Ltd. and CERN. Micropack started the preparations for the GEM foil production in India. The first few attempts saw many deviations from the required quality. With further improvements in etching technology and several rounds of iterations, Micropack finally produced a batch of foils which appeared fine from visual inspection and preliminary checks. However, before these foils could be declared fit for applications and technology as reliable, we had to perform the desired quality assessment and characterization for these foils. For this purpose, we performed optical measurement to check the reliability and usability of the foils. Optical tests reveal that the holes are quite uniform with inner and outer diameters of 49.9 ± 1.6 μm and 70.01 ± 2.02 μm respectively. Here, the quoted errors are the Gaussian one sigma uncertainty on diameter distributions. The measured optical properties of Micropack foils were found to reflect the desired parameters and are at par with the double mask foils produced at CERN.

Micropack successfully built the small-area GEM foils. The foils were tested for their detector performance and compared with the one produced at CERN, which shows similar response. We received the first batch of four GEM foils having an active area of 10 cm $\times$ 10 cm. All of them were accepted after the optical inspection and we used three foils to build a GEM detector prototype with 3/1/2/1 (mm) gap configuration. However, before these foils can be utilized for various applications, it is important to characterize detector(s) assembled from them for advanced properties. We have tested these foils for their short term stability and the rate capability. The polarization and rate capability of detectors obtained using commercially manufactured foils in India is similar to the detectors built with CERN made foils. Therefore, these foils can be used for various purposes and the technology can be exploited in interdisciplinary applications such as medical, cultural heritage studies, muography, etc.

With the successful production of 10 cm $\times$ 10 cm double-mask GEM foils, Micropack has already extended their infrastructure to handle single-mask technology so that larger foils can be produced in order to ease the commercialization of large area GEM foils. A triple-GEM detector was built using the first batch of 30 cm $\times$ 30 cm single mask GEM foils manufactured by Micropack Pvt. Ltd. The detector has been tested for various basic and advance studies which are imperative to understand the quality of the foils as well as detector. Our studies shows no non-linearity in the gain, shows good spectrum using both the sources (X-ray and ^{109}Cd) and the rate handling capacity is found to be very good with lower discharge probability. These results are found to be in conformity when compared with the CERN foils produced using single mask technique. We conclude that the Micropack foils meets the high scientific standards and can be used for various applications, including the upgrade of the CMS Muon system, which is one of the primary goals of these efforts.

Furthermore, a commissioning and installation procedure of SRS (utilizing analog front-end chip APV25) has been documented by the DU group. Using the same setup a technique has been developed to detect the bending in the RO board as well as the induction gap uniformity in the MPGD detectors. An outstanding feature of this technique is that it can be used under the operation of the high voltage which means that this technique can be used at any stage of the QA/QC procedure. Also, it can be used for the quality assurance of the readout boards manufactured by the industries to detect possible defects during production. This technique can be used for any gaseous detector properly couple a plane to any readout.

At last, a search has been performed for dark matter produced in association with a Higgs boson. The analysis is based on 2.3 fb^{-1} of proton-proton collision data collected by the CMS experiment at $\sqrt{s} = 13$ TeV. This analysis focuses on a Z'-2HDM model in which the Z' decays to a light SM-like scalar Higgs boson and a pseudoscalar boson A, that in turn decays to two dark matter candidates. Two distinct channels are studied, where the Higgs boson decays to two b quarks or two photons. No significant deviation is observed from the standard model background. With optimized selections, limits on the signal cross section $\sigma(Z' \to Ah \to \chi\bar{\chi}h)$ are calculated for various values of m'_Z and m_A assuming g_χ and $\tan\beta$ equal to one. The limits are valid for any dark matter particle mass below 100 GeV. For $m_A = 300$ GeV, the observed data exclude the Z' mass range of 600 to 1860 GeV for $g'_Z = 0.8$, and the range 770 to 2040 GeV for the constrained value of g'_Z. This is the first result on a search for dark matter produced in association with a Higgs boson at $\sqrt{s} = 13$ TeV that combines results from the $H \to b\bar{b}$ and $H \to \gamma\gamma$ channels.

Appendix A

Triple-GEM detector assembly procedure

A.1 Preparation of the readout board

Preliminary Note : In this section some of the assembly steps were performed in a clean room for the purpose of improving the quality of the pictures. It was done in a very conscientious way and the work was immediately followed by a special cleaning. However the forthcoming steps are likely to produce dust and hence must be performed outside the clean room to prevent contamination.

A.1.1 Materials and tooling

The preparation of the GE1/1-X & GE2/1 readout board includes the mounting of the brass inserts in the lateral flanges, the threading of the gas holes and the glueing of the gas connectors. The following list describes all the components that are required for the preparation of the board. All these components are provided with the shipment box:

1. One readout board.

2. Two gas connectors Parker Legris PN:3299 03 09.

3. 11 for M1/M5, 8 for M2/M6, 10 for M3/M7 & 17 for M4/M8 Brass inserts Titanox PN: M0002292.

(a) GE1/1 Readout board. **(b)** GE2/1 Readout board.

(c) Gas connectors. **(d)** Brass inserts.

Figure A.1: List of components required for the readout board preparation.

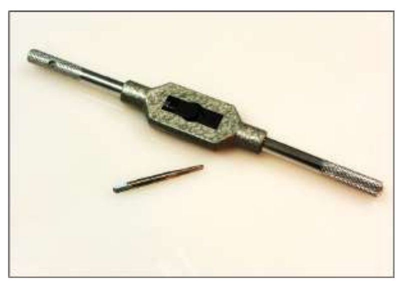

(a) Clamping hand. **(b)** Tap wrench.

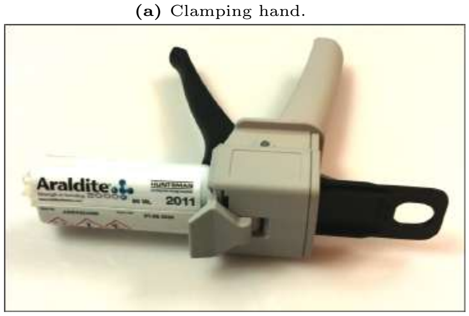

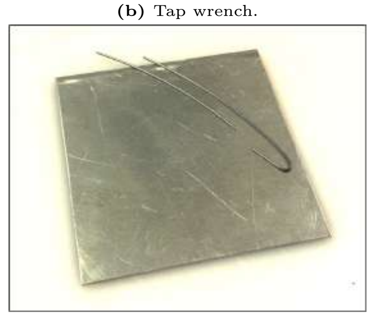

(c) Araldite 20 11. **(d)** Metallic support.

Figure A.2: List of components required for the readout board preparation.

The components are shown on Fig. A.1.

The tools required for proper assembly are listed below, and shown on Fig. A.2.

1. One clamping hand with flat head.
2. A tap wrench with M3 to 0.5 mm hand tap.
3. Two-part epoxy glue Araldite 20 11 with glue gun.
4. A small metallic support.
5. Pure ethanol and clean pieces of tissue.
6. A vacuum cleaner.

A.1.2 Step-by-step procedure

::Mounting of the brass inserts::

Step 1: Place the readout board on the working table with the strips facing up. It is recommended to use a soft material or a sheet of foam in between to avoid scratching the Panasonic connectors when working on the board (Fig. A.3).

Figure A.3: Preparing the working table and the board.

Step 2: Place each brass insert in the dedicated housing in the flanges, with the threaded side sitting inside of the holes (Fig. A.4 left).

Step 3: Use the clamping hand to press the insert against of the holes until it gets fixed in it (Fig. A.4 right).

Step 4: Finally, use your finger to make sure the heads of the inserts fit flush with the surface of the board.

Figure A.4: Clamping of the brass inserts.

::Glueing of the gas connectors::

Step 1: Flip the readout board upside down so that the Panasonic connectors face up (Fig. A.5 left).

Step 2: Insert the 3 mm tap in the hole dedicated to the gas connector. Keep the tool vertical while slowly screwing it by hand to create the thread pattern in the material (Fig. A.5 right).

Figure A.5: Clamping of the brass inserts.

Step 3: After screwing all the way through the hole, gently unscrew the tap to take it out (Fig. A.6).

Figure A.6: Making the thread in the gas in/outlets (1).

Step 4: Remove the resulting dust with a vacuum cleaner and clean both sides of the board around the hole with a clean tissue paper and ethanol (Fig. A.7).

Figure A.7: Cleaning of the gas in/outlets.

Step 5: Use again the ethanol to clean up the small metallic support where you will mix the glue (Fig. A.8).

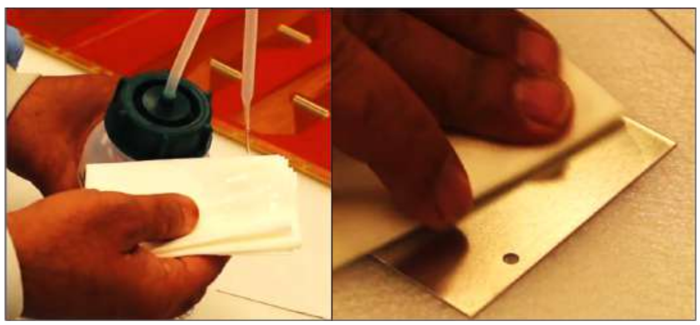

Figure A.8: Preparing the metallic support for the glue.

Step 6: Pour the two-part epoxy glue onto the support and vigorously mix it with a clean metallic stick until you obtain an opaque and uniform paste (Fig. A.9).

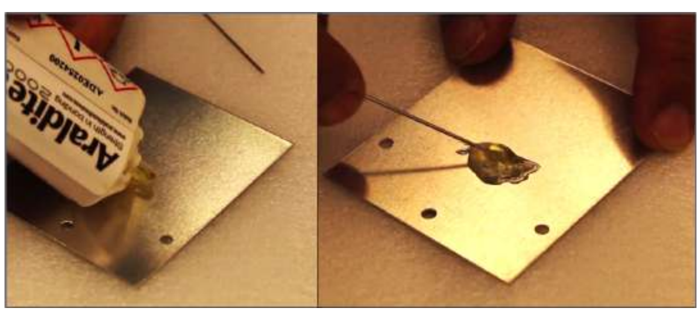

Figure A.9: Mixing the epoxy glue.

Step 7: Before applying the glue, remove the teflon washer from the gas plugs. This washer is a white circular piece sitting under the body of the connector (Fig. A.10).

Figure A.10: Removing the O-ring front he gas connector.

Step 8: Then use the metallic stick to apply a thin ring of glue between the body and the threaded part of the connector (Fig. A.11).

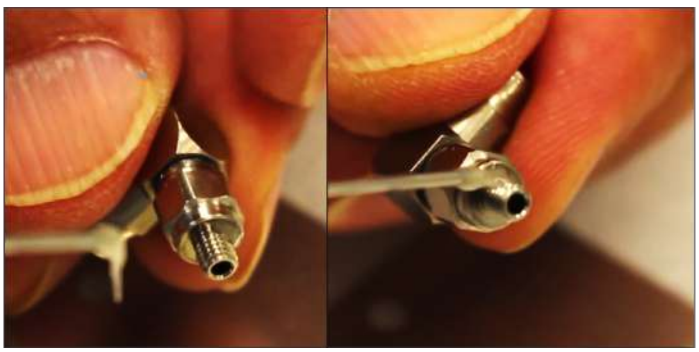

Figure A.11: Applying glue to the gas connector.

Step 9: Gently screw the connector on the board until the base of the connector's body touches the readout board (Fig. A.12 left). Make sure that the glue forms a nice and smooth ring all around the base of the connector (Fig. A.12 right).

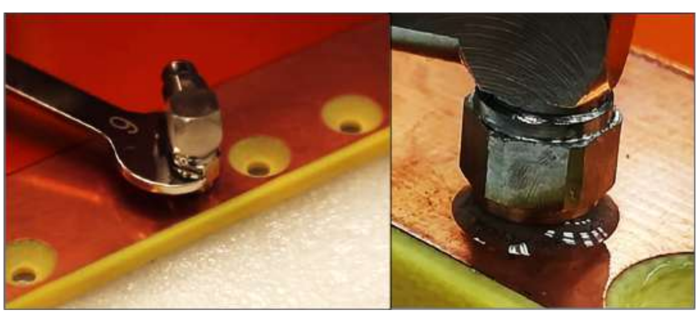

Figure A.12: Fixing the gas connector onto the board.

A.1.3 Comments and recommendations

The use of soft material between the table and the readout board is strongly recommended to prevent the damage of the fragile Panasonic connectors while clamping the brass inserts.

You should never touch the readout strips with bare fingers under the penalty of triggering copper oxidation that may affect later the operation of the detector.

A.2 Preparation of the drift board

Preliminary Note : In this section some of the assembly steps were performed in a clean room for the purpose of improving the quality of the pictures. It was done in a very conscientious way and the work was immediately followed by a special cleaning. However the forthcoming steps are likely to produce dust and hence must be performed outside the clean room to prevent contamination.

A.2.1 Materials and tooling

The preparation of the GE1/1-X drift board includes the mounting of the pull-outs, the soldering of the HV pins, the soldering of the SMD components and the cleaning of the board. The following list describes all the components that are required for the preparation of the board (Fig. A.13). All these components are provided with the shipment box:

1. One drift board.
2. 58 (short) or 62 (long) for GE1/1, 42(46) for M1(M5), 49(54) for M2(M6), 62(61) for M3(M7), 70(68) for M4/M8 stainless steel pull-outs.
3. 116 (short) or 124 (long) for GE1/1, 84(92) for M1(M5), 98(108) for M2(M6), 124(122) for M3(M7), 140(136) for M4(M8) screws M3x6 Bossard PN: 3183904.
4. 116 (short) or 124 (long) for GE1/1, 84(92) for M1(M5), 98(108) for M2(M6), 124(122) for M3(M7), 140(136) for M4(M8) nylon washers Bossard PN: 3139487.
5. HV contact pins (four FK_480, four FK_381 and four FK_519).

6. SMD components (one 10 MΩ resistor, one 100 kΩ resistor and one 330 pF capacitor).

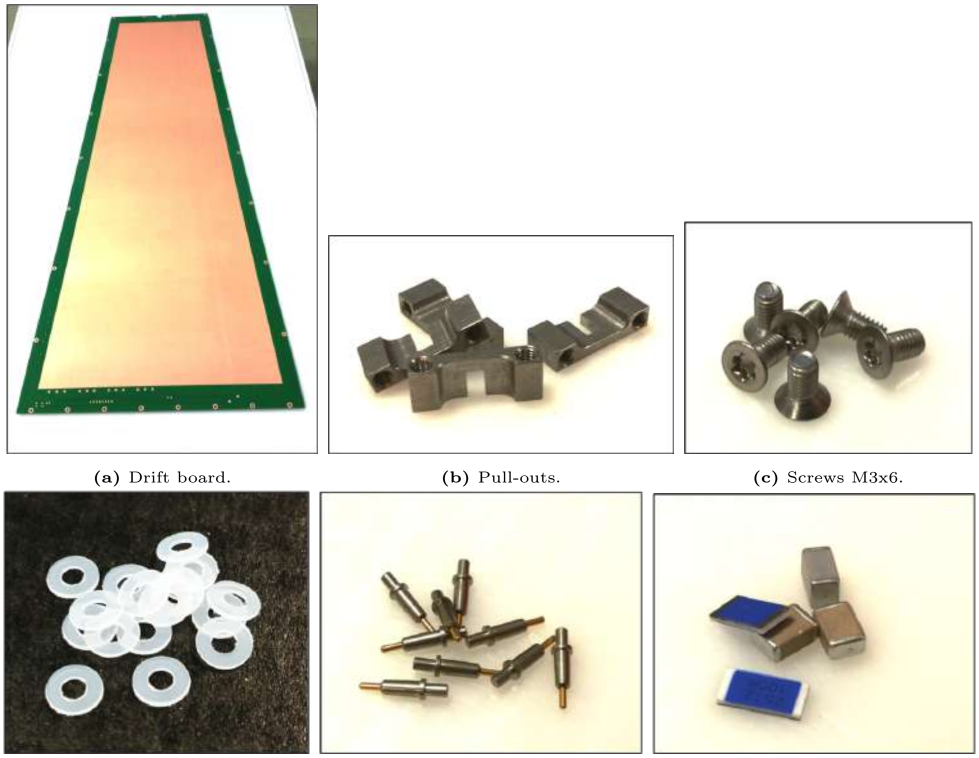

(a) Drift board. **(b)** Pull-outs. **(c)** Screws M3x6.

(d) Nylon washers. **(e)** HV contact pins. **(f)** SMD components.

Figure A.13: List of components required for the drift board preparation.

The tools required for a proper assembly are listed below and are shown on Fig. A.14.

1. A manual torque screw driver with a working range up to 1.2 Nm.

2. A pair of fine tweezers.

3. A soldering station with regular soldering tips and SMD tips.

4. Pure ethanol, acetone and clean pieces of tissue.

5. A metallic tub to collect excess ethanol.

(a) Torque screw driver. (b) Tweezers. (c) Soldering tips.

Figure A.14: List of components required for the drift board preparation.

A.2.2 Step-by-step procedure

::Mounting of the pull-outs::

Step 1: Place the pull-outs on the dedicated hole of the drift board (Fig. A.15 left). The active area of the board should face up.

Step 2: Attach the pull-outs with the screws and the nylon washers. When both screws are in place, tighten it with the torque screw driver at 1.2 Nm (Fig. A.15 right).

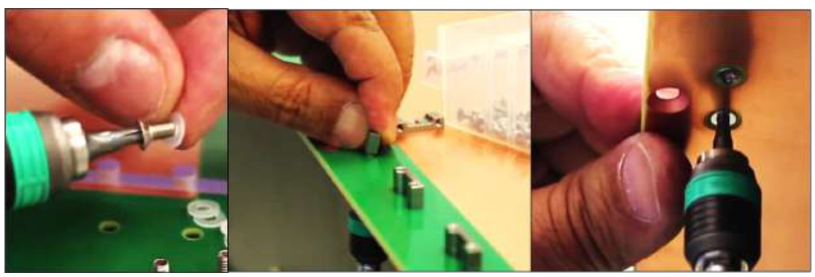

Figure A.15: Mounting the pull-outs on the drift board.

Step 3: Proceed like this all around the perimeter of the board, except on the large base of the trapezoid. This area must remain clear before soldering the HV components (Fig. A.16).

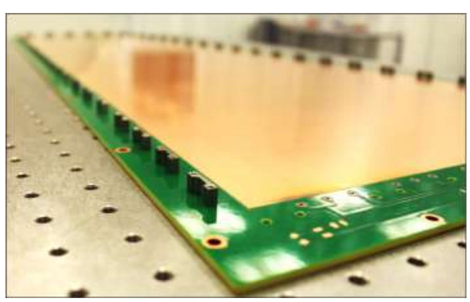

Figure A.16: Drift board after mounting the pull-outs.

::Soldering of the HV components::

Step 1: Clean the HV circuit with a clean piece of tissue ethanol (Fig. A.17).

Figure A.17: Cleaning of the HV circuit.

Step 2: The schematics in Fig. A.18 & Fig. A.19 shows the location of the HV pins in GE1/1 & GE2/1 drift board: the 6.1 mm pins FK-480 should go in the GEM 1 pads, the 8 mm FK-381 should go on the GEM 2 pads and the 9.28 mm FK-519 should go on the GEM 3 pads.

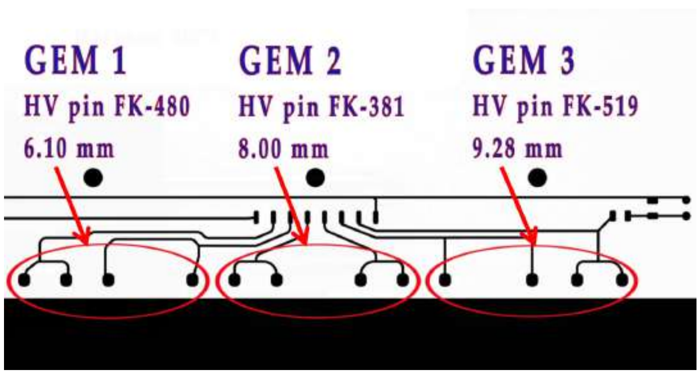

Figure A.18: Positioning of the HV pins on the GE1/1 drift board.

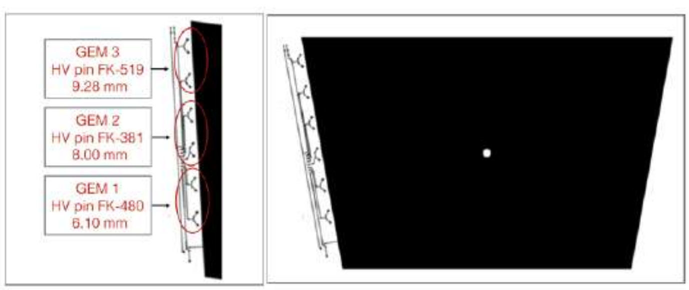

Figure A.19: Positioning of the HV pins on the GE2/1 drift board.

Step 3: Gently place the HV pins in the dedicated housing, making sure that the pins are vertically aligned within the holes (Fig. A.20 left).

Step 4: Apply the soldering tin all around the base of the pins while heating the pads with the iron (Fig. A.20 right). Keep the temperature below 350 °C to avoid melting the glue that keeps the copper pads attached to the PCB.

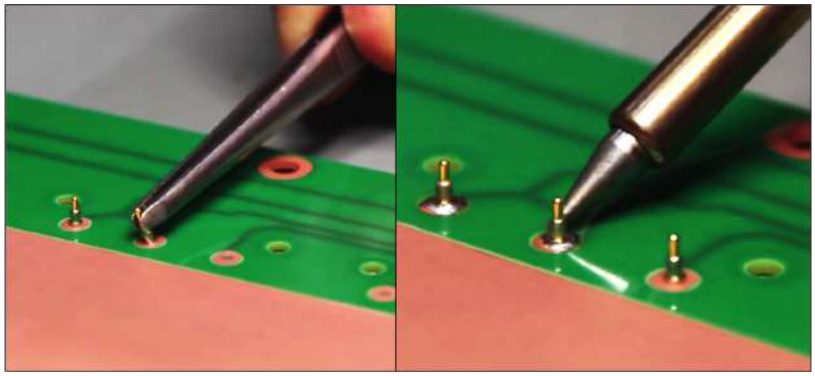

Figure A.20: Soldering of the HV pins.

Step 5: Similarly, clean the pads for the SMD components with tissue using ethanol (Fig. A.21 left).

Step 6: Apply a small amount of soldering tin to "wet" the pads before mounting the SMD components (Fig. A.21 right).

Figure A.21: Preparation of the SMD pads.

Step 7: The location of each components for GE1/1 & GE2/1 is shown on Fig. A.22 & Fig. A.23

Step 8: To mount a given SMD component, hold it with the soldering tweezers and place it on the pad. Then maintain it in position with another tool while removing

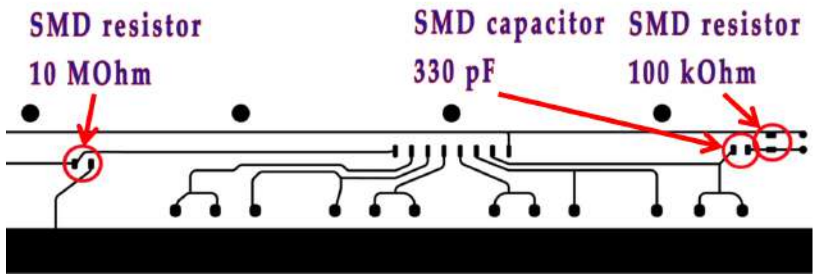

Figure A.22: Positioning of the SMD components on the GE1/1 drift board.

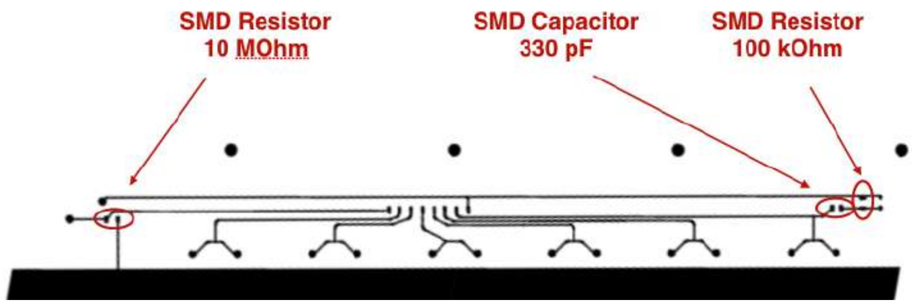

Figure A.23: Positioning of the SMD components on the GE2/1 drift board.

carefully the soldering iron. Keep the component in place until the tin is fully solidified (Fig. A.24).

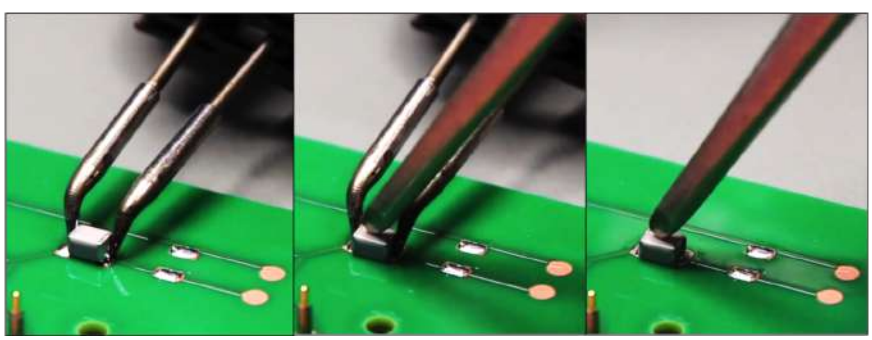

Figure A.24: Soldering of the SMD components.

::Cleaning of the drift board::

Step 1: Place the board in vertical position in the tub, the large base facing down. Tilt the tub to ensure that the acetone will flow before drying and leave contaminants on the edge of the PCB. (Fig. A.25).

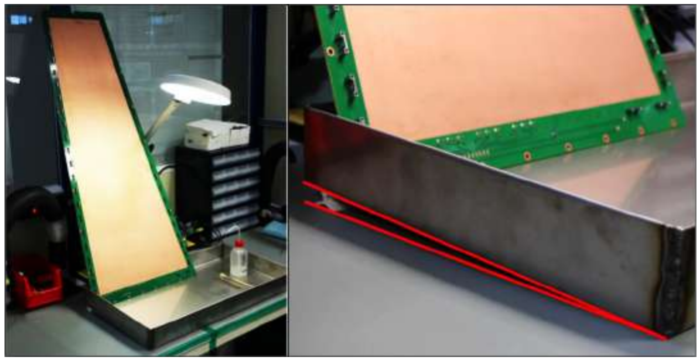

Figure A.25: Preparation for cleaning.

Step 2: Generously pour acetone just above the HV circuit while brushing all the soldering points. Repeat this step several times to ensure that all contaminants are removed (Fig. A.26).

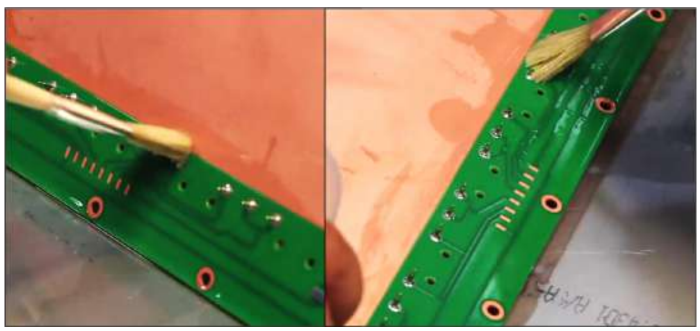

Figure A.26: Cleaning of the HV circuit.

Step 3: Clean the rest of the drift board with a clean piece of tissue using ethanol, insisting on the areas surrounding the pull-outs. Repeat this step until all stains and contaminants disappear (Fig. A.27).

Figure A.27: Cleaning of the active area.

::Mounting of the last pull-outs::

Step 1: Mount the remaining pull-outs in front of the HV circuit as indicated previously (Fig. A.28).

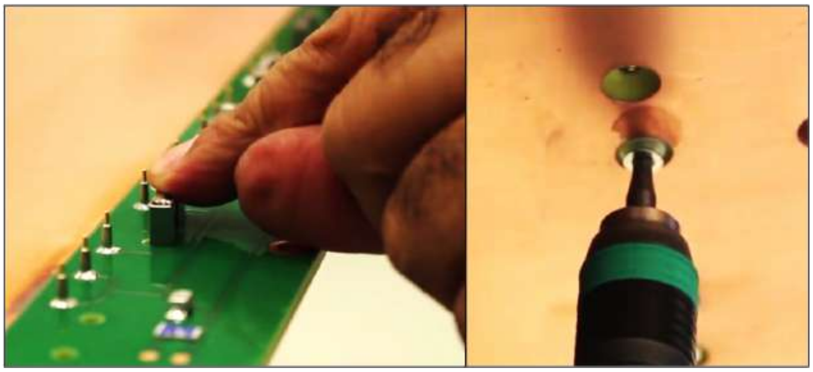

Figure A.28: Mounting of the remaining pull-outs.

Step 2: Proceed like this all along the large base of the board (Fig. A.29). The drift board is now ready for the assembly.

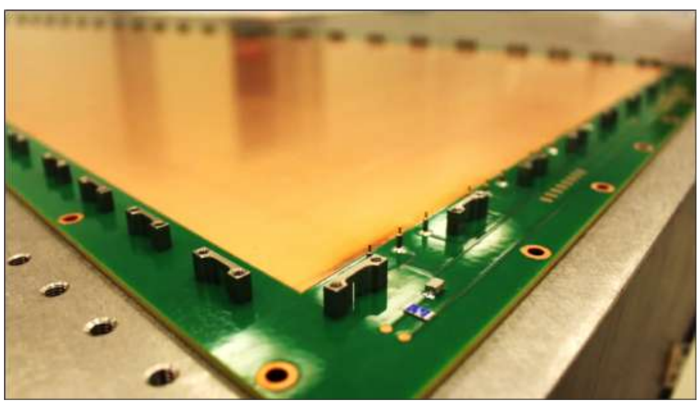

Figure A.29: Final state of the drift board.

A.2.3 Comments and recommendations

We recommended to first pair the M3 screws and the nylon washers before starting mounting the pull-outs. This will facilitate the work and limit the risk of damaging the PCB when pushing the screw inside the holes. One way to do so is shown on Fig. A.30.

When mounting the pull-outs, it is strongly suggested to use a guiding rail (Fig. A.31) to help in aligning the pull-outs with the perimeter of the trapezoid. With

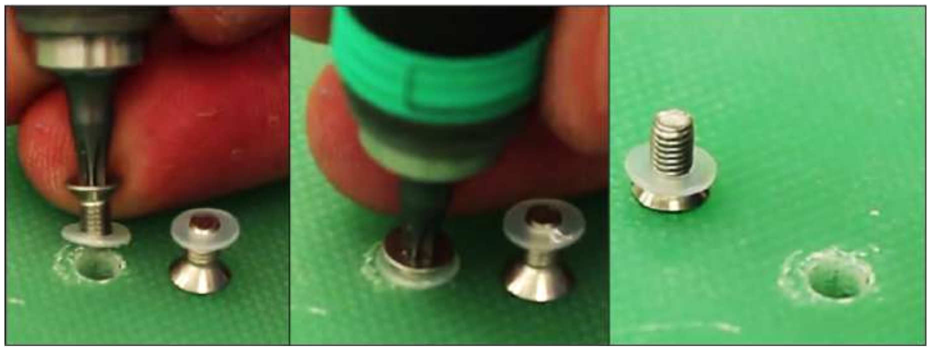

Figure A.30: Example of guiding rail to mount the pull-outs.

misaligned pull-outs, it will be impossible to close the chamber with the readout board.

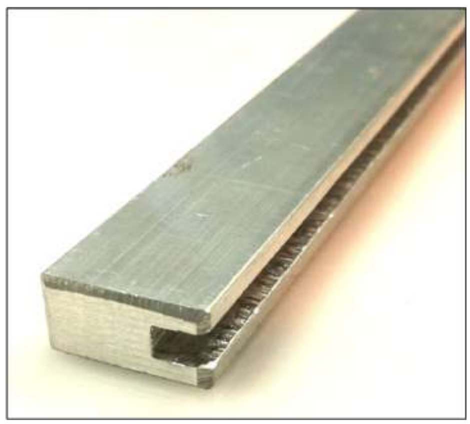

Figure A.31: Example of guiding rail to mount the pull-outs.

One should make sure the screws are perfectly concentric with the screw holes of the pull-outs. If not, it will create leak points that might be difficult to identify before closing the chamber. More critical, the friction between the screw and the pull-out may create metallic dust that can seriously harm the detector.

When soldering the SMD components, the temperature of the soldering iron should stay below 350 °C. Above this temperature, the component that maintains the copper trace and the epoxy plate together may melt, leaving the copper detached from the board.

One should never touch the active area of the drift with bare fingers under the penalty of triggering copper oxidation that may later affect the operation of the detector.

A.3 Preparation of the internal and external frames

A.3.1 Materials and tooling

The preparation of the GE1/1-X frames includes the insertion of the brass inserts in the internal frames and the mounting of the VITON O-ring on the external frame. The following list describes all the components that are required for the preparation of the frames (Fig. A.32). All these components are provided with the shipment box:

(a) Internal frames. **(b)** Brass inserts.

(c) External frame. **(d)** O-ring.

Figure A.32: List of components required for the frames preparation.

1. All 6 for M1/M5, 8 for M2/M6, 8 for M3/M7, 8 for M4/M8 3 mm thick internal frames (drift gap).

2. 222 for GE1/1-X, 120(132) for M1(M5), 139(154) for M2(M6), 178(175) for M3(M7), 139(196) for M4(M8) brass inserts Kerb Konus PN : 852 000 020800.

3. One external frame.

4. Two Viton O-rings.

The tools required for a proper assembly are listed below and are shown on Fig. A.33.

1. FR4 baseplate with a M4 hole (provided with the GE1/1 kit).

2. A mallet or a hammer with soft head.

(a) Frame baseplate. **(b)** Mallet.

Figure A.33: List of components required for the frame prepartion.

A.3.2 Step-by-step procedure

::Preparation of the internal frames::

Step 1: To remove the frames from their support, hold them in place with one hand while gently removing the tape (Fig. A.34). Proceed with great care, the frames are very thin and can be easily damaged when pulling the tape off.

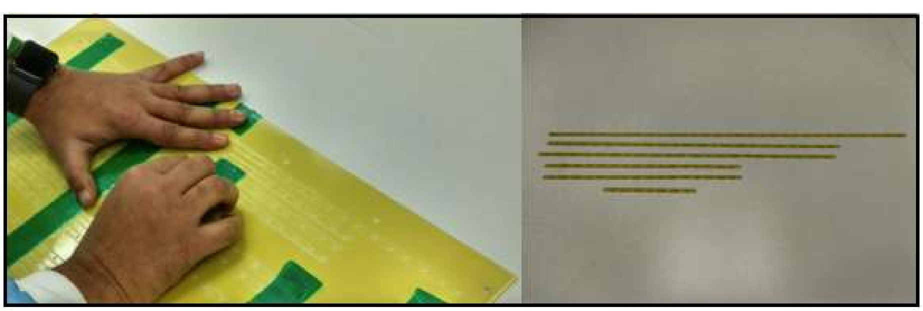

Figure A.34: Removing the internal frames.

Step 2: Attach the FR4 baseplate onto the table. Then place the piece of internal frame on top, the chamfer side facing up. Align the hole of the frame with the hole of the baseplate (Fig. A.35).

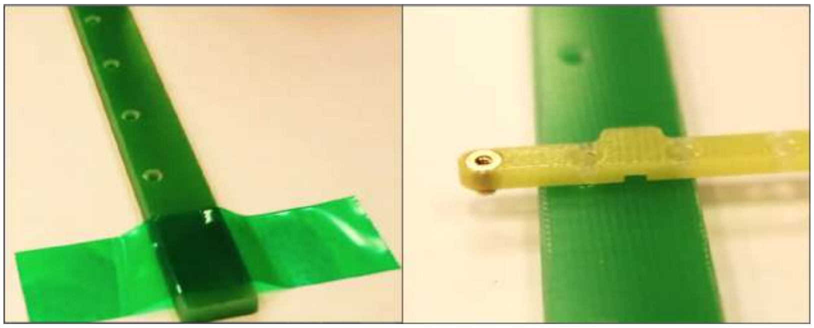

Figure A.35: Preparation of the baseplate.

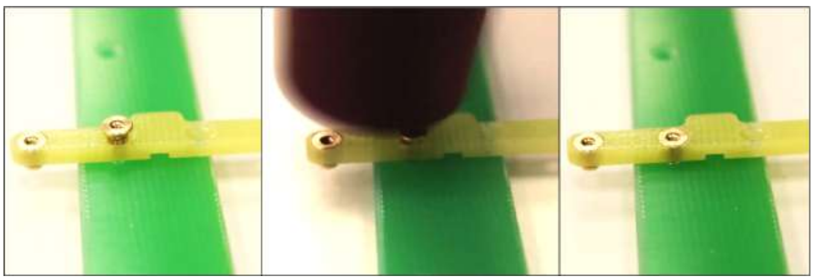

Figure A.36: Insertion of the brass inserts.

Step 3: Insert the brass piece into the hole and gently hammer it with the mallet until it is fully inserted (Fig. A.36).

Step 4: Follow the same procedure for the entire frame, and for all the other pieces of 3 mm frames. Check with the finger that the heads of the inserts fit flush with the surface of the frame (Fig. A.37).

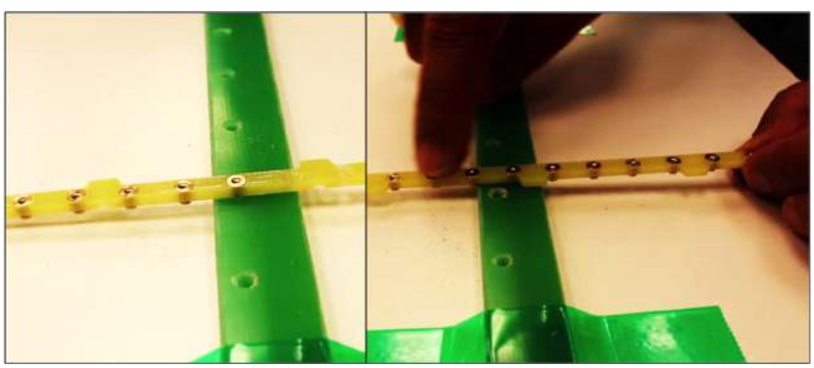

Figure A.37: Checking the flatness of the frame.

::Preparation of the external frames::

Step 1: Place the VITON O-ring in the dedicated groove of the external frame. Gently pull the O-ring at the four corners at the same time so that it fits the trapezoidal shape of the groove (Fig. A.38).

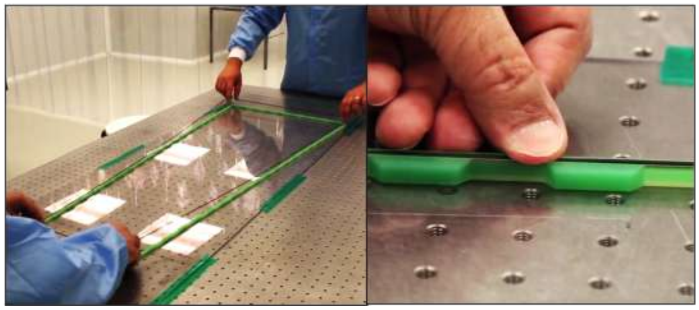

Figure A.38: Placing the VITON O-ring (1).

Step 2: Then gently press the O-ring with your finger to insert it in the trench. Check by eye and with your finger that the O-ring is placed properly and slightly exceeding the frame's housing (Fig. A.39).

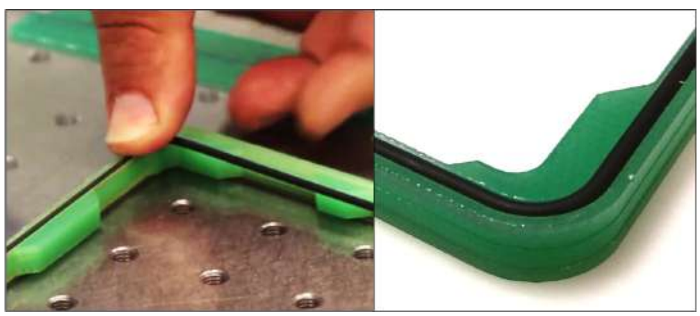

Figure A.39: Placing the VITON O-ring (2).

A.3.3 Comments and recommendations

When placing the VITON O-ring in the external frame, make sure you share the stress uniformly all around the trapezoid. If not, some parts of the O-ring may be too compact, which can later deform the PCB when closing the chamber, or create leak points.

A.4 Assembly of the GEM stack

A.4.1 Materials and tooling

The assembly of the GE1/1-X stack includes the preparation of the components, the cleaning and test of the GEM foils and the mounting of the stack. The following list describes all the components that are required for the assembly of the GEM stack (Fig. A.40). All these components are provided with the shipment box:

1. Three GEM foils.
2. All internal frames depending upon the module, including the 3mm ones equipped with brass inserts.
3. 222 screws for GE1/1, 120(132) for M1(M5), 139(154) for M2(M6), 178(175) for M3(M7), 139(196) for M4(M8); M2 x 6/X6 Bossard PN: 3183884
4. 58 (short) or 62 (long) for GE1/1, 42(46) for M1(M5), 49(54) for M2(M6), 62(61) for M3(M7), 70(68) for M4/M8 M2.5 Bossard PN : 3146251
5. 20 for GE1/1, 12(12) for M1(M5), 16(16) for 16(16), 16(16) for M3(M7), 16(16) for M4/M8 guiding pins Bossard PN : 1255568
6. 20 for GE1/1, 12(12) for M1(M5), 16(16) for 16(16), 16(16) for M3(M7), 16(16) for M4/M8 screws M2 x 12 Bossard PN : 1420607 with metallic nuts and washers.

(a) GEM foil.

(b) Prepared internal frame.

(c) Screws M2x6.

(d) Nuts M2,5.

(e) Guiding pins.

(f) Screws M2x6 long.

(g) T-Nuts M2,5.

Figure A.40: List of components required for the assembly of the GEM stack.

The tools required for a proper assembly are listed below and are shown on Fig. A.41.

(a) Assembly baseplate. **(b)** Plexiglas cover. **(c)** HV insulation meter. **(d)** Dust roller. **(e)** High voltage clip. **(f)** Polyamide tape. **(g)** Sharp blade. **(h)** Screw driver X6.

Figure A.41: List of components required for the assembly of the GEM stack.

1. One assembly baseplate depending upon the module.

2. One Plexiglas cover again depending upon the module and type of baseplate used.

3. A Giga-ohm insulation meter (a.k.a. Megger).

4. One silicon static roller and its sticky mat.

5. A pair of HV clips.
6. Polyamide green tape.
7. One or more sharp blades
8. One or more screw drivers X6.
9. Pure ethanol and clean pieces of tissue.

A.4.2 Step-by-step procedure

::Preparation of the GEM foils::

Step 1: Place all the GEM foils (together with their frames) in vertical position against the wall (Fig. A.42).

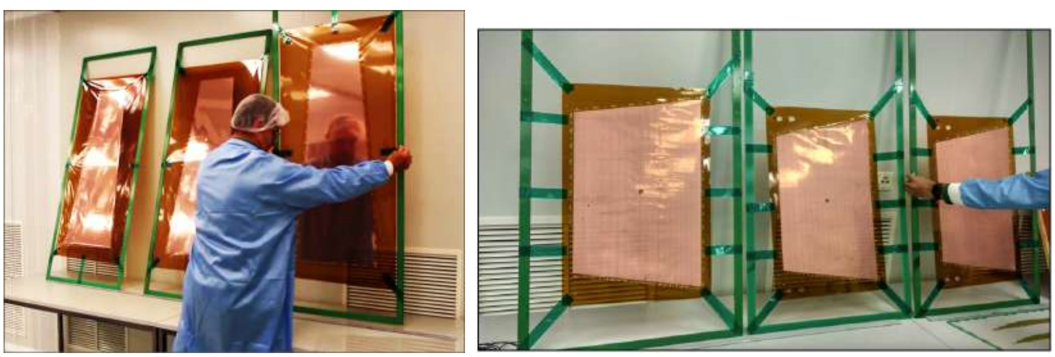

Figure A.42: Setting up the GEM foils in vertical position.

Step 2: Use the static roller to remove the possible dust from the foils. Gently press the roller onto the foil, including the active area and the excess Kapton areas on the sides (Fig. A.43).

Step 3: Flip the frame and continue the cleaning on the other side of the GEM foil (Fig. A.44). Regularly clean the roller with the sticky mat and proceed the same way for all the foils.

Figure A.43: Cleaning of the first side with the static roller.

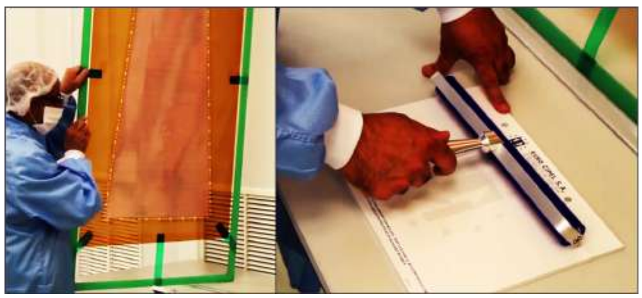

Figure A.44: Cleaning of the second side with the static roller.

Step 4: In order to test the GEM foils, place the HV clip so that the HV pins are in contact with of the top and bottom part of the foil (Fig. A.45). At this point, all of the HV pads are still connected to the active area of the foil. The location of these pads is shown on Fig. A.46.

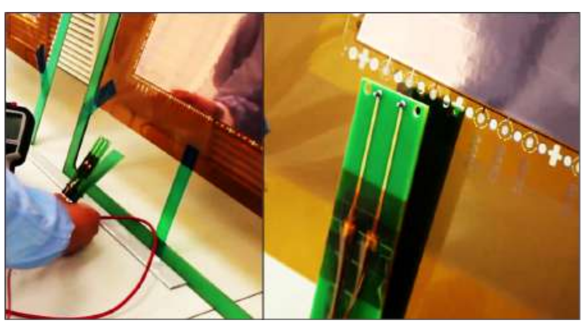

Figure A.45: Mounting of the HV clip on the foil.

Step 5: Set the insulation meter to 550 V and apply the voltage for several minutes, the resistance of the foils should reach 20 GΩ after few seconds with relative humidity lower than 40 % . (Fig. A.47). After the test is done, discharge the GEM foil.

Figure A.46: Location of the HV pads.

Figure A.47: Testing the GEM foil.

Step 6: The next step consists of cutting the spare HV pads to define the position of the foil in the detector. Fig. A.49, Fig. A.50 and Fig. A.51 indicate which pads should be removed in GEM1, GEM2 and GEM3 respectively.

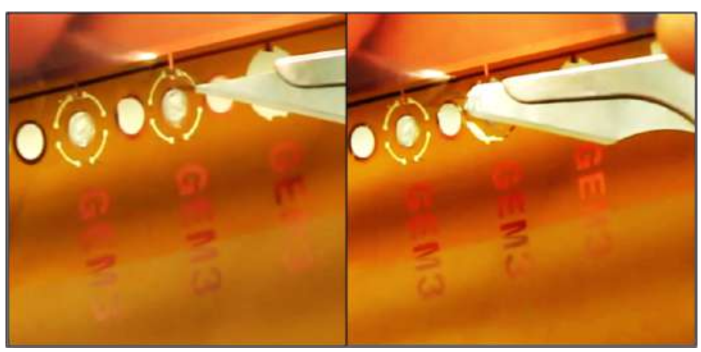

Figure A.48: Cutting off the spare HV pads.

Step 7: To remove the pads, use a very sharp blade and chop the uncut portions along the pre-cut circle (Fig. A.48). Carefully work in a comfortable position to avoid scratching the active area of the foils, which is only few millimeters away from the pads. Make sure the chopped-off pads do not remain attached to the foil due to electro-static forces.

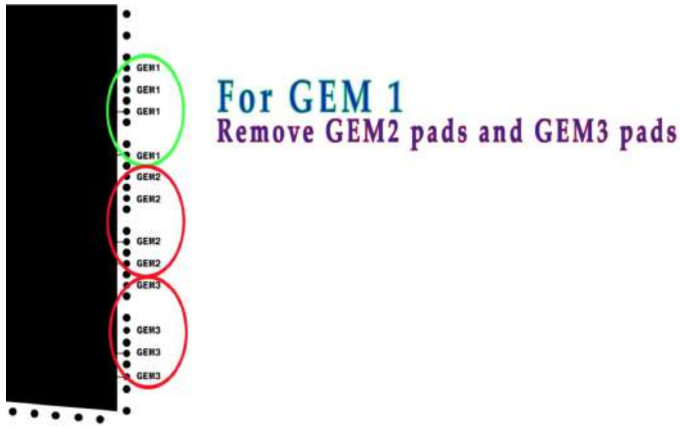

Figure A.49: Removing HV pads for GEM1.

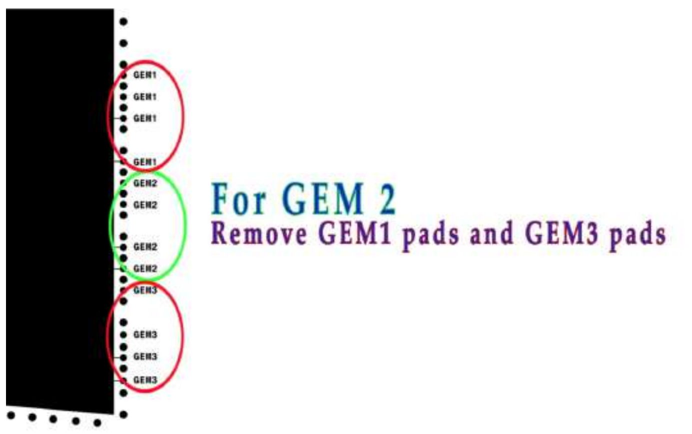

Figure A.50: Removing HV pads for GEM2.

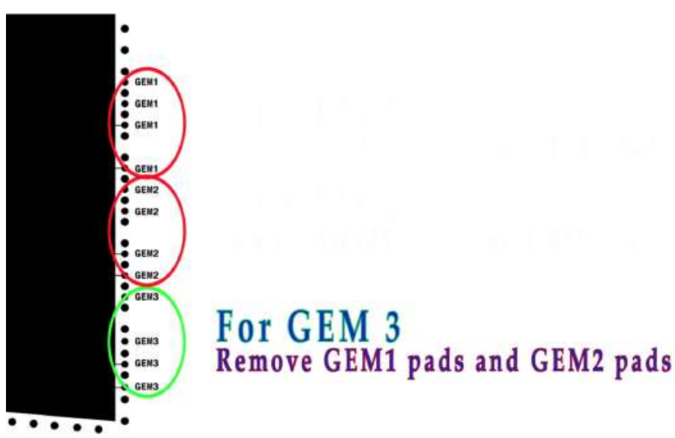

Figure A.51: Removing HV pads for GEM3.

::Mounting of the GEM stack::

Step 1: Place the Plexiglas baseplate on the assembly table and fix it with tape (Fig. A.52).

Figure A.52: Preparing the assembly baseplte.

Step 2: Clean the entire surface of the baseplate with a clean piece of tissue using ethanol (Fig. A.53).

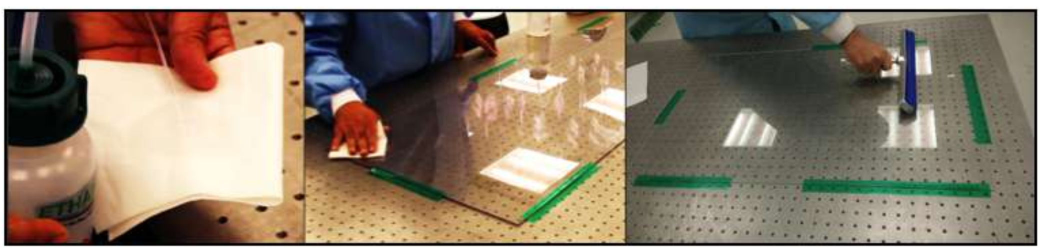

Figure A.53: Cleaning of the assembly baseplate.

Step 3: Put the guiding pins in place all around the trapezoid. Place pins in all the single holes, and in one of the grouped holes (Fig. A.54).

Figure A.54: Insertion of the guiding pins.

Step 4: Use the static roller to clean the 3 mm internal frames. Flip the frames upside down and repeat the process (Fig. A.55). This set of frames, equipped with the brass inserts, will form the drift gap.

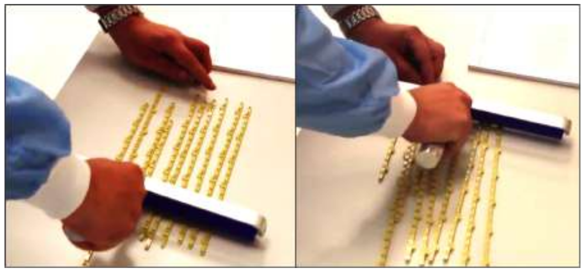

Figure A.55: Cleaning of the 3mm internal frames.

Step 5: Place the internal frame on the baseplate. The orientation and the location of each piece of frame is defined by matching the shape of the grouped holes present on the frame and on the baseplate.(Fig. A.56). The flanges should always face the inside of the trapezoid.

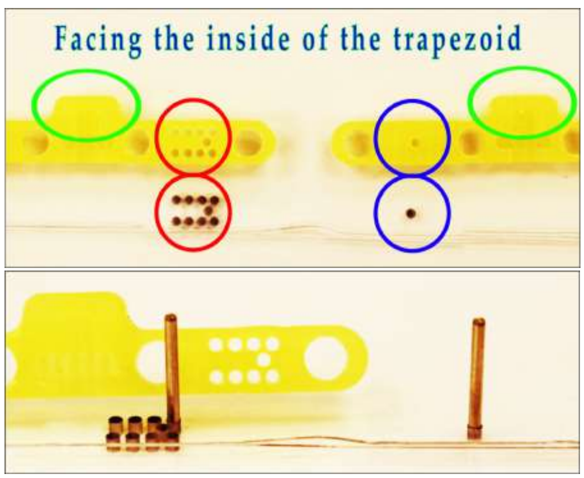

Figure A.56: Positioning of the internal frames.

Step 6: Put the frames in position all around the trapezoid using the guiding pins (Fig. A.57).

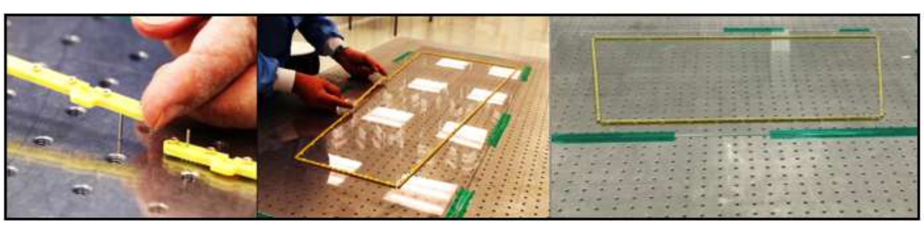

Figure A.57: Mounting of the 3 mm internal frames.

Step 7: Place the GEM1 on top of the 3 mm frames using the guiding pins for a proper positioning (Fig. A.58). Make sure the foil is well aligned to prevent scratching of the active area with the guiding pins.

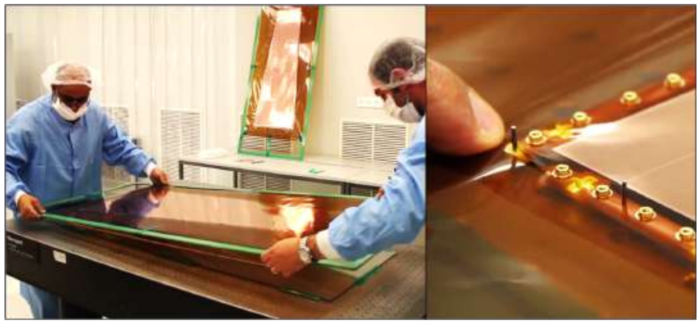

Figure A.58: Placing GEM1.

Step 8: When the foil is in place, detach the frame from it by cutting the tape with a sharp blade and remove the frame (Fig. A.59).

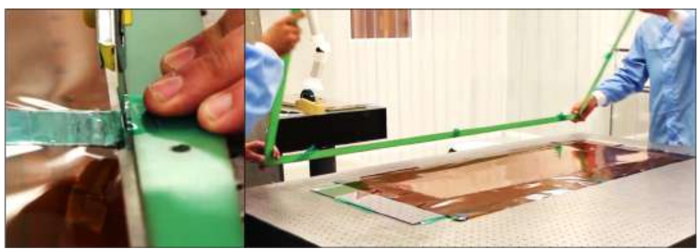

Figure A.59: Detaching the foil from its frame.

Step 9: In order to pre-stretch the foil, attach the tape on the Kapton area, on both large and small bases of the trapezoid, and then gently pull it towards you before fixing the tape on the table (Fig. A.60). Do not exaggerate the stretching strength under the penalty of deforming the GEM foil.

Figure A.60: Pre-stretching of GE1/1 foil (1).

Figure A.61: Pre-stretching of foil.

Step 10: Always proceed with two persons working in the opposite directions (Fig. A.61).

Step 11: The location of the stretching points and the order is shown on Fig. A.62.

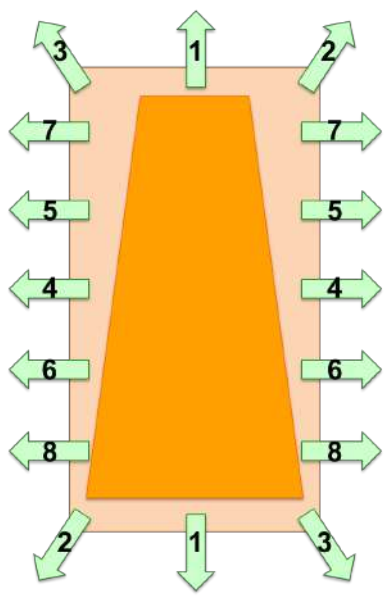

Figure A.62: Overview of the stretching points for GE1/1.

Step 12: Use the insulation meter to measure the impedance of the GEM foil. Connect the pins of the Megger to the pads corresponding to GEM1 top and GEM1 bottom, as indicated in Fig. A.63.

Figure A.63: Connecting the insulation meter to the GEM1 pads.

Step 13: Apply 550 V between the two electrodes during few minutes and check that the resistance reaches at least 20 GΩ after few seconds (Fig. A.64). After the test is done, discharge the GEM foil.

Figure A.64: Electrical test of GEM1.

Step 14: Clean the set of 1 mm thick internal frames which will form the first transfer gap (Fig. A.65). These frames have the cross-shape holes to accommodate the metallic nuts for the final stretching.

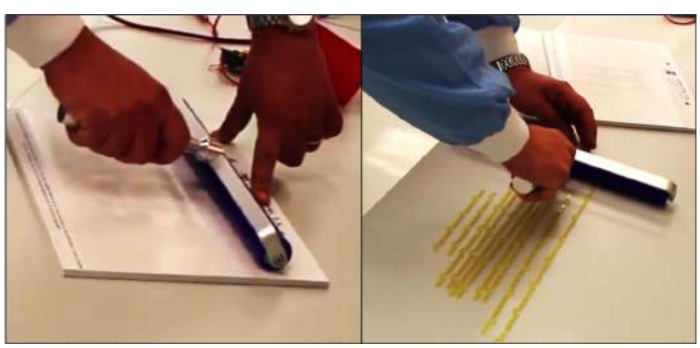

Figure A.65: Cleaning of the 1 mm internal frames.

Step 15: Place the frames on the stack using the guiding pins. Match the shape of the grouped holes to proper position and orientate the frames (Fig. A.66).

Figure A.66: Mounting the 1 mm internal frames.

Step 16: Before mounting the frame on the large base of the trapezoid, test again the GEM foil at 550V with the insulation meter. After the test is passed, discharge the foil and put the last piece of frame in place (Fig. A.67).

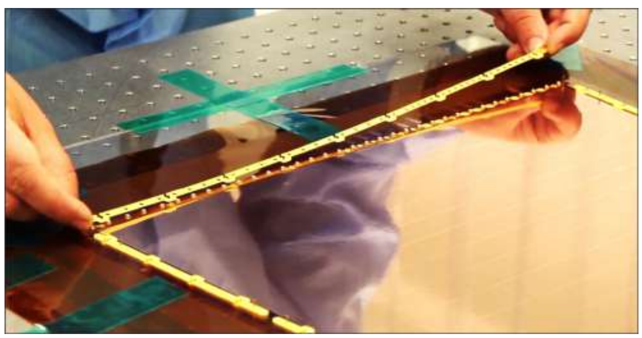

Figure A.67: Placing the last internal frame after testing.

Step 17: Take the second GEM foil and place it onto the stack using the guiding pins for the alignment (Fig. A.68).

Figure A.68: Placing GEM2.

Step 18: Detach the foil from its frame by cutting the piece of tape (Fig. A.69).

Figure A.69: Detaching the GEM frame.

Step 19: Use the green tape to pre-stretch the foil in opposite directions, starting from the large and the small bases of the trapezoid. (Fig. A.70). Continue stretching all around the stack until the foil becomes mirror flat.

Figure A.70: Pre-stretching GEM2.

Step 20: In GE2/1 assembly before placing the 2mm frame insert the T-shape nuts in the dedicated housing but for GE1/1 first place the 2mm frame and then nuts. Clean the set of 2 mm thick frames and place it on the stack to make the second transfer gap (Fig. A.71).

Figure A.71: Cleaning and positioning of the 2 mm internal frames.

Step 21: At this point you can insert the M2.5 metallic nuts in the dedicated housing of the internal frames. Take the time to double check that all frames are equipped with the nuts and that the nuts are fully inserted in the stack (Fig. A.72).

Figure A.72: Placing the metallic nuts in the internal frame.

Step 22: Before mounting the last piece on the large base of the trapezoid, check the impedance of the second foil by applying 550V (Fig. A.73). After the test is performed, discharge the foil, place the last piece of internal frame and insert the remaining nuts.

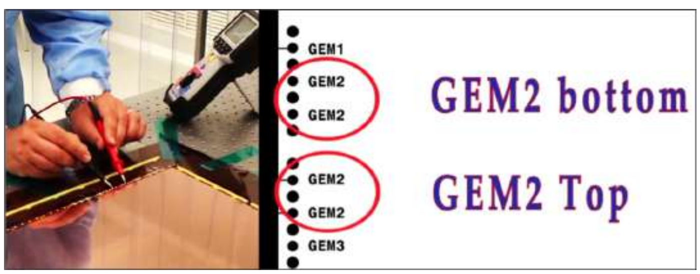

Figure A.73: Testing GEM2.

Step 23: Take the third GEM foil and place it on top of the stack (Fig. A.74).

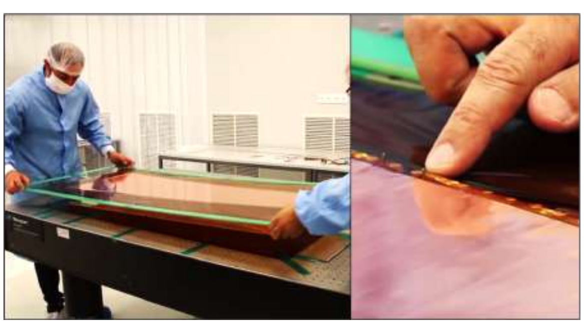

Figure A.74: Placing GEM3.

Step 24: After careful alignment, remove the tape that holds the foil and its frame together (Fig. A.75).

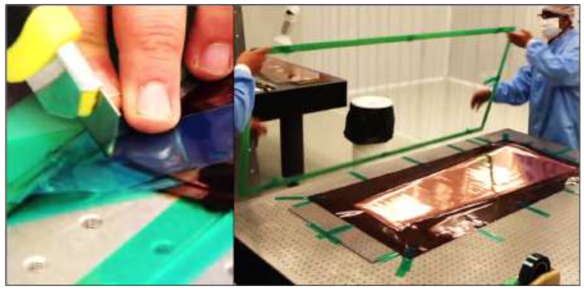

Figure A.75: Detaching GEM3.

Step 25: Perform the manual stretching of the last foil following the previous instructions (Fig. A.76).

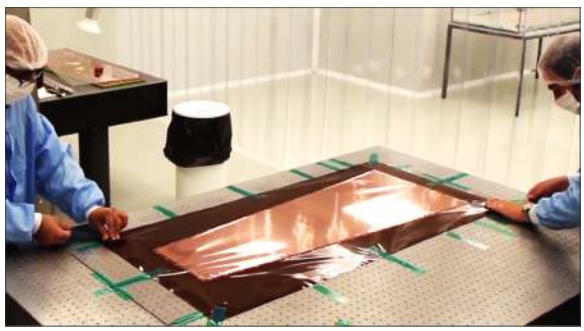

Figure A.76: Pre-stretching GEM3.

Step 26: Clean the last set of 1 mm internal frames and place them on the stack so as to form the induction gap (Fig. A.77).

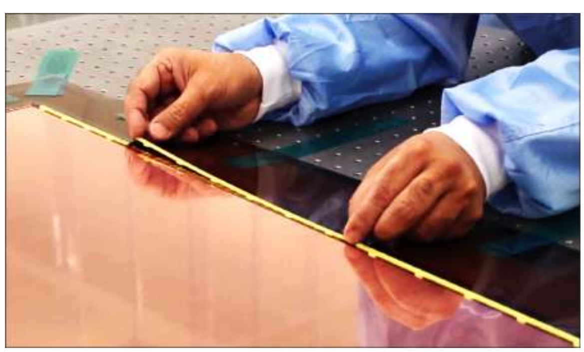

Figure A.77: Placing the 1mm internal frames.

Step 27: Before covering the large base, test the last foil by applying 550 V on the pads shown on Fig. A.78.

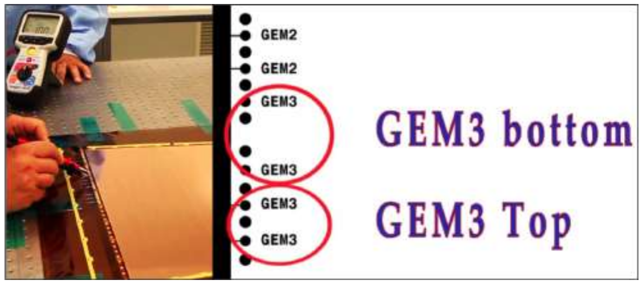

Figure A.78: Testing GEM3.

::Protecting the GEM stack::

Step 1: First use the static roller to clean the table and the entire surface of the Plexiglas cover (Fig. A.79).

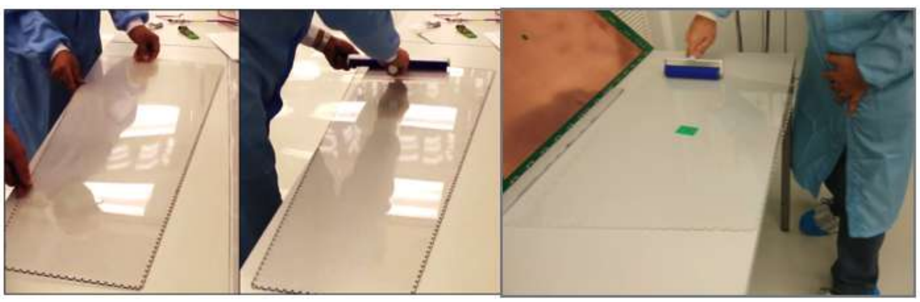

Figure A.79: Cleaning the Plexiglas cover (1).

Step 2: Clean the cover with a clean piece of tissue using ethanol (Fig. A.80).

Figure A.80: Cleaning the Plexiglas cover (2).

Step 3: Flip the cover upside down and repeat step 2 (Fig. A.81).

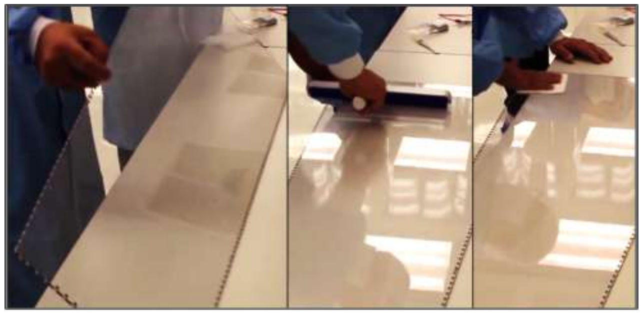

Figure A.81: Cleaning the Plexiglas cover (3).

Step 4: When the Plexiglas cover is perfectly clean, carefully place it on top of the GEM stack, using the guiding pins for proper positioning. (Fig. A.82).

Figure A.82: Placing the Plexiglas cover.

Step 5: Use the long M2 screws and washers in order to attach the Plexiglas cover to the stack. Insert the screws into the holes to catch the brass insert fixed in the 3 mm internal frames (Fig. A.83). Put these screws on the edges of each piece of internal frame and in the corners of the trapezoid.

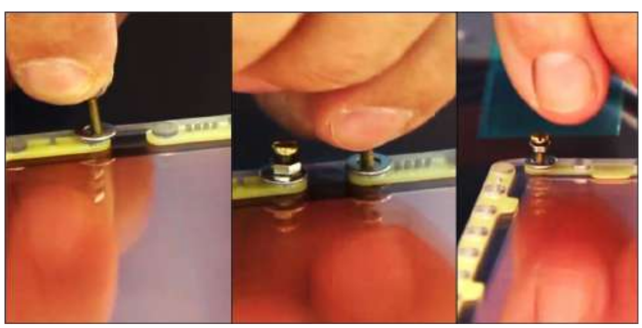

Figure A.83: Attaching the cover to the GEM stack.

Step 6: In order to hold the layers of internal frames together, place the M2x6mm screws provided with the GE1/1 kit in the dedicated holes of the Plexiglas cover (Fig. A.84). Tighten these screws with a manual X6 screwdriver without stressing too much against the thin pieces of frame.

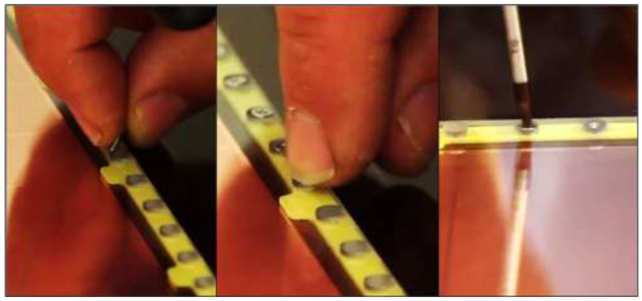

Figure A.84: Closing the internal frame (1).

Step 7: Follow the same procedure all around the GEM stack. All the holes should be equipped with M2x6 screws except on the edges of the frames where the longer screws are already fixed (Fig. A.85).

Figure A.85: Closing the internal frame (2).

A.4.3 Comments and recommendations

For this step it is strongly suggested have a fourth (spare) GEM foil available, dry and tested. In case a problem which may happen during the assembly, this additional foil can be used as an immediate replacement without leaving the stack opened in air for a longer period.

We recommend to reinforce the Plexiglas cover with a cross-shape stiffener, as shown on Fig. A.41 (b). In this way it will be easier to manipulate it and appose it on the GEM stack. Similarity, we recommend to modify the assembly baseplate and to equip it with HV pins to allow the electrical test of all the GEM foils during the assembly. Without these modifications it won't be possible to test the GEMs lying below the topmost foil.

A.5 Closing of the chamber

A.5.1 Materials and tooling

The closing of the GE1/1-X chamber includes the final preparation of the GEM stack, the stretching of the foils and the final electrical test after closure. The following list describes all the components that are required (Fig. A.86). All these components are provided with the shipment box:

(a) The GEM stack already assembled.

(b) One drift board equipped with pull-outs and SMD components.

(c) One readout board equipped with brass inserts.

(d) 58 (short) or 62 (long) GE1/1, 42(46) for M1(M5), 49(54) for M2(M6), 62(61) for M3(M7), 70(68) for M4/M8 screws M2,5x8 Bossard PN: 3136081

(e) 116 (short) or 124 (long) GE1/1, 84(92) for M1(M5), 98(108) for M2(M6), 124(122) for M3(M7), 140(136) for M4(M8) screws M3x6 Bossard PN: 3183904.

(f) 116 (short) or 124 (long) GE1/1, 84(92) for M1(M5), 98(108) for M2(M6), 124(122) for M3(M7), 140(136) for M4(M8) nylon washers Bossard PN: 3139487.

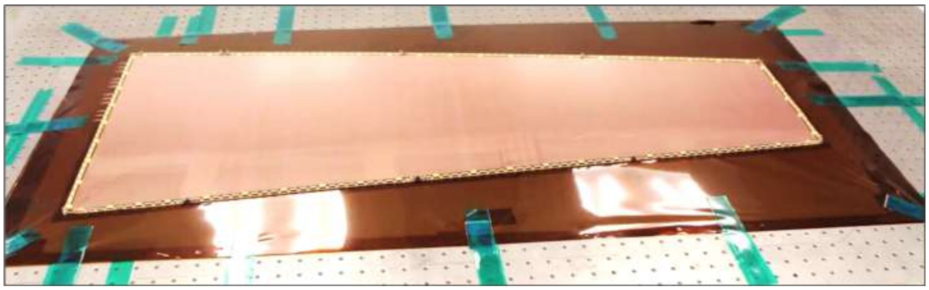

(a) Assembled GEM stack.

(b) Prepared drift board.

(c) Prepared readout board.

(d) Stretching screws M2,5.

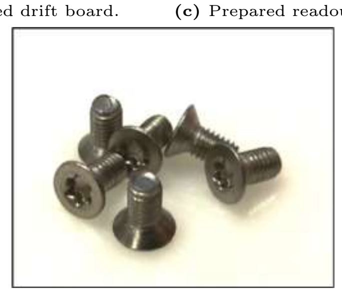

(e) Screws M3x6.

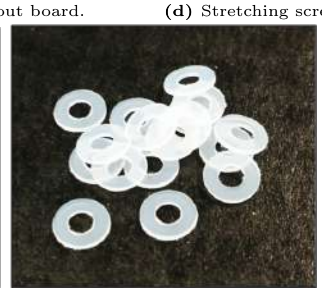

(f) Nylon washers.

Figure A.86: List of components required for the closing of the chamber.

The tools required for a proper assembly are listed below and are shown on Fig. A.87.

(a) One GE1/1 assembly jig (baseplate and aluminum bars).

(b) A Giga-ohm insulation meter (a.k.a. Megger).

(c) One silicon static roller and its sticky mat.

(d) A Panasonic-to-Lemo adapter board.

(e) One or more sharp blades.

(f) One electronic torque screw driver with a working range between 5 and 20 cNm.

(g) One or more manual torque screw driver with a working range up to 1.2 Nm.

(h) A pair of tweezers.

(i) Pure ethanol and clean pieces of tissue.

(j) A vacuum cleaner with HEPA filter.

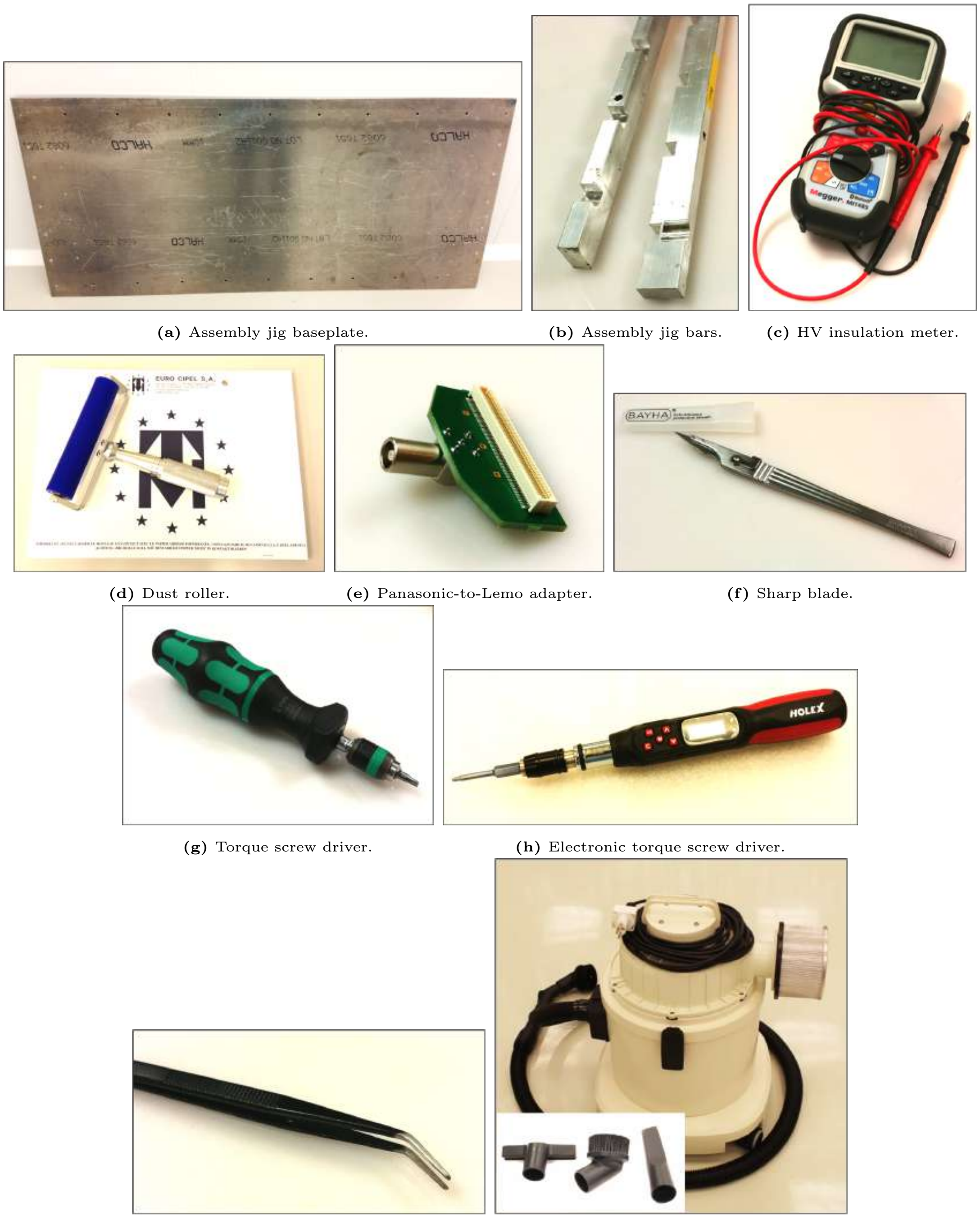

(a) Assembly jig baseplate. **(b)** Assembly jig bars. **(c)** HV insulation meter.

(d) Dust roller. **(e)** Panasonic-to-Lemo adapter. **(f)** Sharp blade.

(g) Torque screw driver. **(h)** Electronic torque screw driver.

(i) Tweezers. **(j)** HEPA vacuum cleaner.

Figure A.87: List of components required for the closing of the chamber.

A.5.2 Step-by-step procedure

::Finalizing the GEM stack::

Step 1: Clean the GEM stack with the vacuum cleaner, focusing on the edges of the internal frame and in the holes of the Plexiglas cover (Fig. A.88).

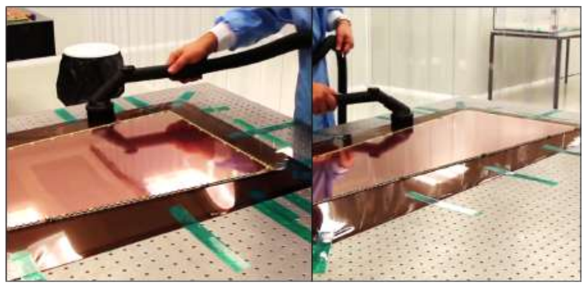

Figure A.88: Cleaning the GEM stack with the vacuum cleaner.

Step 2: Use a sharp blade to remove the excess Kapton foil. Start in the corners where the foil is partially pre-cut, and continue carefully all around the trapezoid (Fig. A.89). Use the Plexiglas cover as a stencil when cutting along the frames.

Figure A.89: Cutting the excess Kapton foil.

Step 3: Gently remove the excess Kapton making sure not to detach the baseplate from the assembly table (Fig. A.90).

Step 4: Finally, check the quality of the cut around the stack and adjust if necessary (Fig. A.91 left). The remaining piece of Kapton that exceeds the frame stack should not be longer than a fraction of millimeter. Use the vacuum cleaner to remove the possible shavings left after cutting (Fig. A.91 right).

Figure A.90: Removing the excess Kapton foil

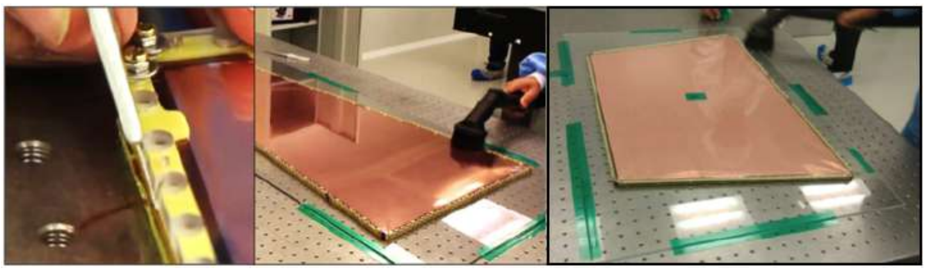

Figure A.91: Adjusting the cut and cleaning the stack.

Step 5: Clean the board with the vacuum cleaner, focusing on the pull-out and the electrical circuit and then use the static roller to clean the active area (Fig. A.92).

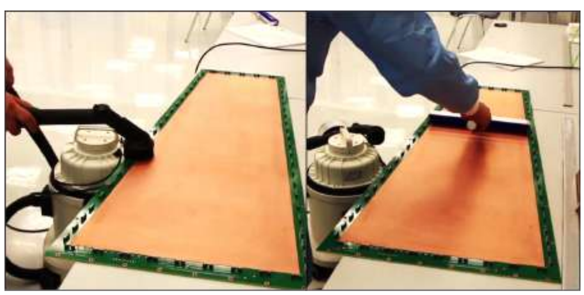

Figure A.92: Cleaning of the drift board.

Step 6: Without touching the active area, place the drift board just next to the GEM stack (Fig. A.93).

Step 7: Dissociate the stack from the Plexiglas base plate by gently pulling it upward (Fig. A.94 left). Make sure not to touch the bottom of GEM3 with your fingers or with the guiding pins that may remain attached to the baseplate. Then place the stack on the drift board in the area delimited by the pull-outs (Fig. A.94 right).

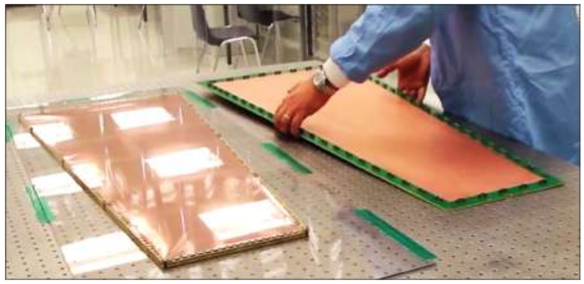

Figure A.93: Preparing the transfer of the GEM stack.

Figure A.94: Transferring the GEM stack to the drift board.

Step 8: Use tweezers to remove the guiding pins left in the frame stack (Fig. A.95).

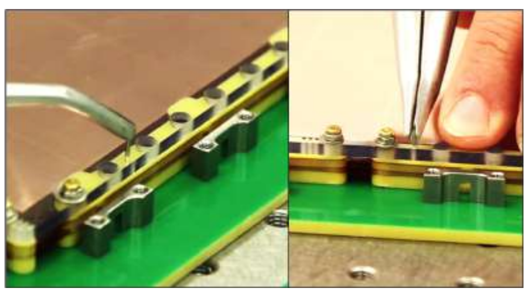

Figure A.95: Removing the guiding pins (1).

Step 9: Rub your finger along the frame to make sure all the pins were removed before moving to the next step (Fig. A.96).

Step 10: Move the chamber to the assembly jig, where the stretching will be performed (Fig. A.97).

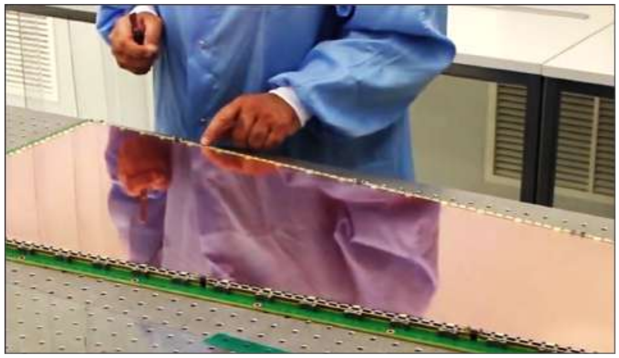

Figure A.96: Removing the guiding pins (2).

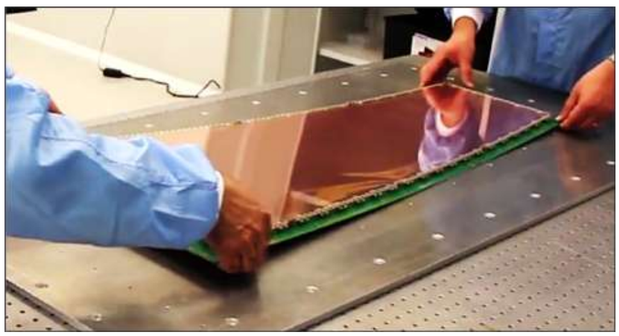

Figure A.97: Moving to the stretching table.

Step 11: Clamp the drift board to the assembly table with the aluminum bars, the chamfers should be oriented towards the inner side of the trapezoid (Fig. A.98).

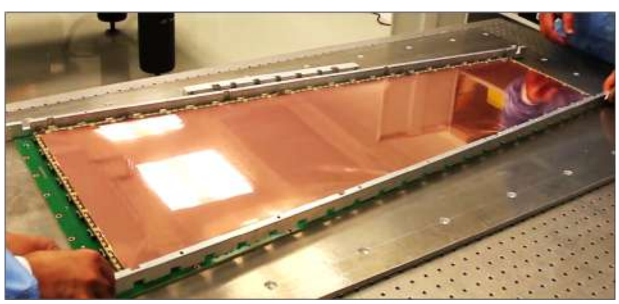

Figure A.98: Fixing the assembly jig (1).

Step 12: Screw the aluminum bars to the assembly jig (Fig. A.99). Apply sufficient strength to ensure the system will maintain the flatness of the board while performing the stretching of the foils.

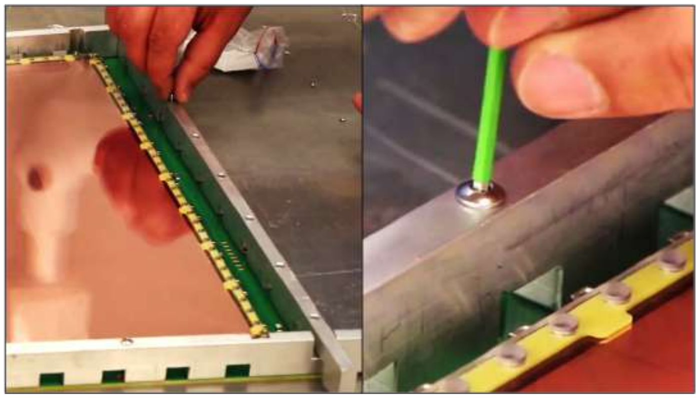

Figure A.99: Fixing the assembly jig (2).

Step 13: Remove the long M2 screws that hold the Plexiglas cover and the GEM stack together (Fig. A.100 left). Replace it with the final M2x6 mm screws as it was done for the other holes in the frame stack (Fig. A.100 right). You will need to keep the Plexiglas cover without screws in place to protect the foil. The internal frames will be free to move while stretching the foils.

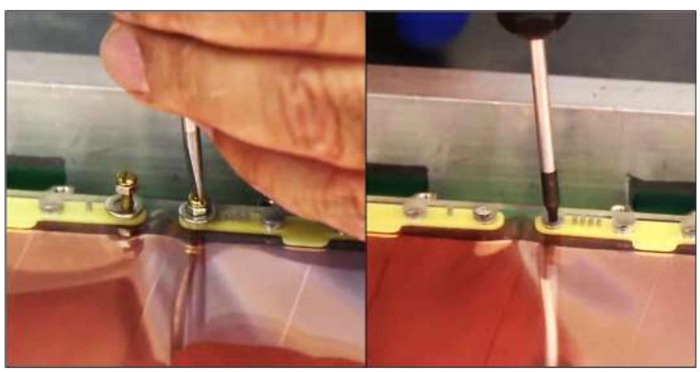

Figure A.100: Detaching the Plexiglas cover from the GEM stack.

::Stretching the GEM foils::

Step 1: The stretching of the GEM foil is described in Fig. A.101. It should be performed exactly in the same order to avoid creation of waves on the foils, especially between the different pieces of internal frames. Firstly, align the large and small bases of the GEM stack with their corresponding pull-outs on the drift board. Then stretch the opposite corners at the same time in order to remove the waves and to align all the lateral nuts with the lateral pull-outs, then continue with the lateral sides until all the screws are in place. Do not tighten the screws to the nominal value yet.

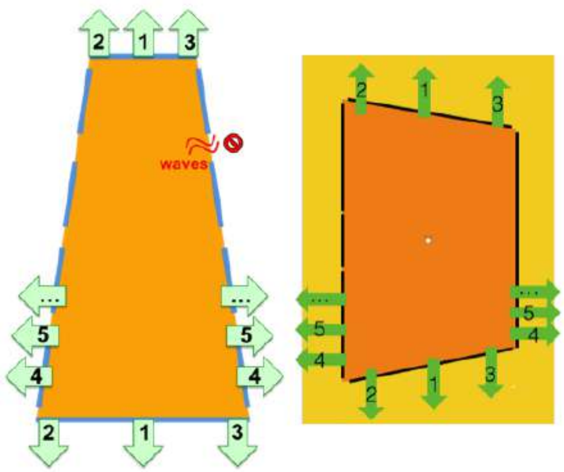

Figure A.101: description of the stretching procedure.

Step 2: Insert the M2.5x8 mm screws in the lateral holes of the aluminum bars, starting with the large and the small base of the trapezoid (Fig. A.102).

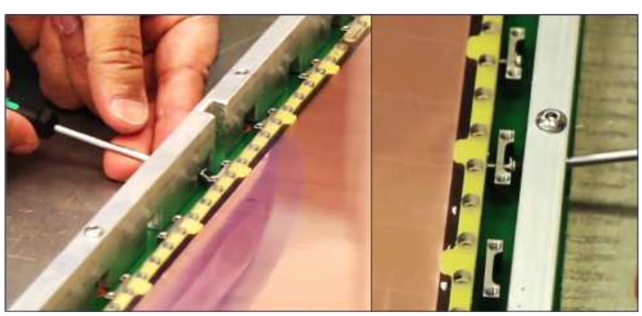

Figure A.102: Stretching of the foils (1).

Step 3: Continue with the lateral sides. Always proceed with two persons stretching in the opposite directions. (Fig. A.103).

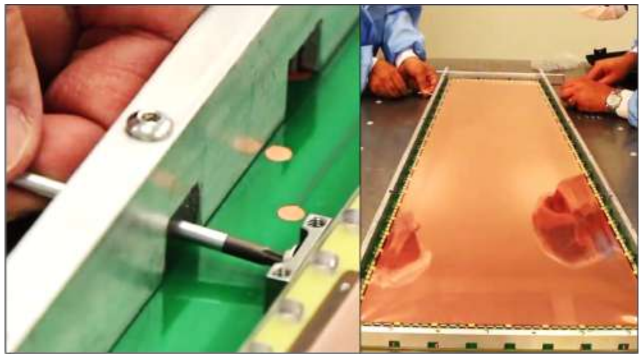

Figure A.103: Stretching of the foils (2).

Step 4: When all the screws are in place, remove the Plexiglas cover (Fig. A.104).

Figure A.104: Removing the plexiglass cover.

Step 5: Clean the top surface of the GEM stack with the static roller without applying too much force on the foils (Fig. A.105).

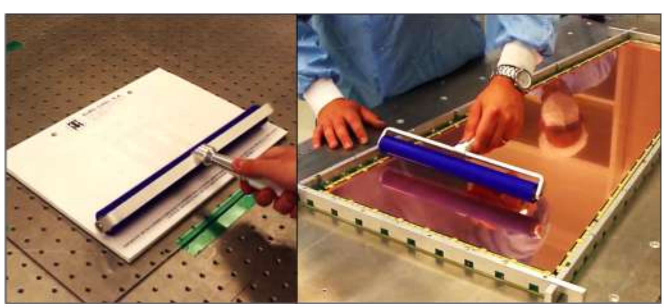

Figure A.105: Cleaning the top GEM foil.

Step 6: Test the three GEM foils one after the other at 550 V using the dedicated pads on the drift board (Fig. A.106). Discharge the foil after each test.

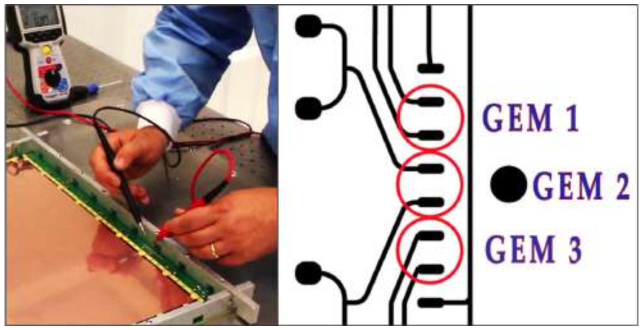

Figure A.106: Testing the GEM foils

Step 7: Similarly, Test the three first gaps one after the other at 550 V, using the dedicated pads on the drift board (Fig. A.107). Note that at this point the induction gap is not yet defined.

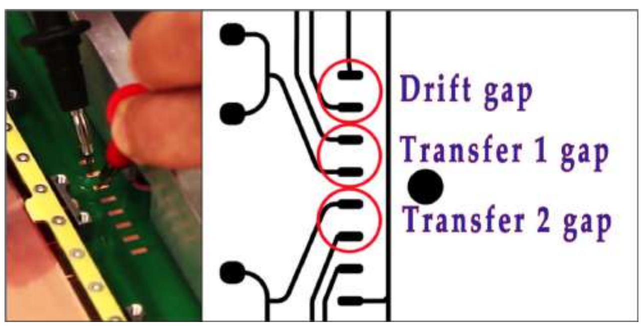

Figure A.107: Testing the gaps.

Step 8: In the case of GEM foils, the impedance should reach 20 GΩ after few seconds. The impedance of the gaps however should reach more than 100 GΩ immediately after applying the voltage (Fig. A.108).

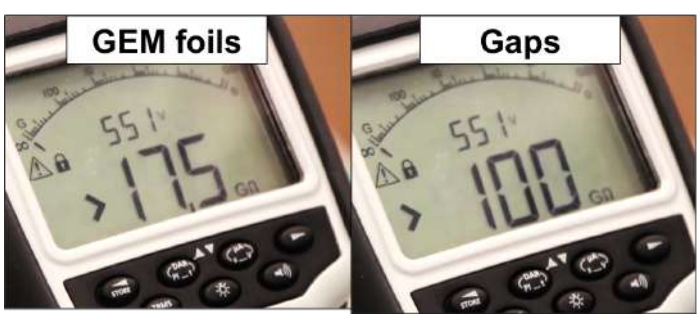

Figure A.108: Expected impedance of GEMs and gaps.

Step 9: After the test is complete, use the electronic screw driver to finalize the stretching of the foils (Fig. A.109). The nominal strength value on the side of the trapezoid is 9 cNm, while it can be slightly higher in the corners, up to 15 cNm.

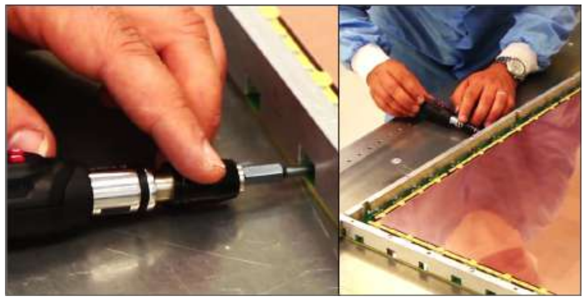

Figure A.109: Finalizing the stretching of the stack.

::Closing and electrical test::

Step 1: Place the external frame between the GEM stack and the aluminum bars (Fig. A.110). If the frame does not fit, simply unscrew the aluminum bars and adjust their position to accommodate the frame without stress. Then mount back the bars on the jig baseplate.

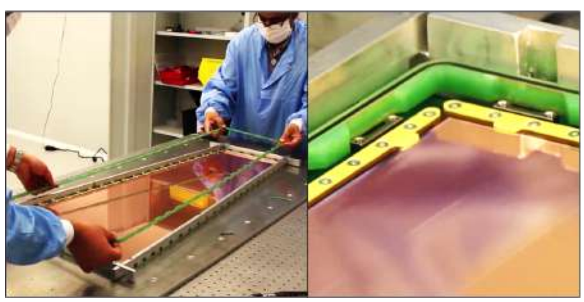

Figure A.110: Inserting the external frame.

Step 2: Use the vacuum cleaner on the side of the bars to suck up possible dust produced during the stretching and carefully vacuum the gap between the stack and the bars. Use the static roll to gently clean the top surface of the foil one more time (Fig.

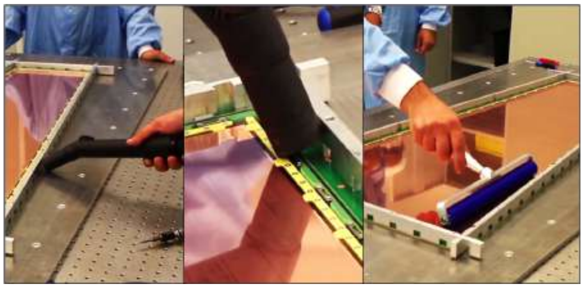

Figure A.111: Cleaninig the setup after stretching.

Step 3: Clean the active area of the readout board with the vacuum cleaner and with proper care so as not to scratch the copper traces. As for the drift, use the static roller to catch the possible dust left on the board (Fig. A.112).

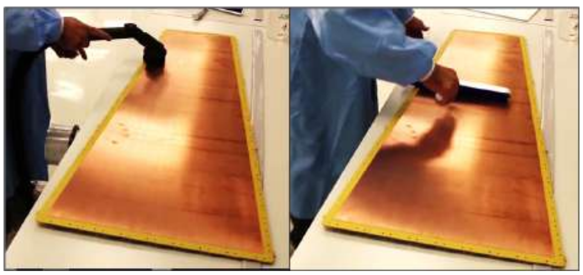

Figure A.112: Cleaning the readout board.

Step 4: Without touching the strips with fingers, place the readout board on top of the GEM stack (Fig. A.113).

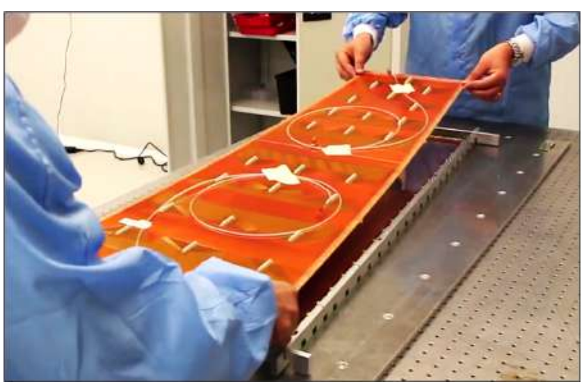

Figure A.113: Mouting the readout board on the stack.

Step 5: Place the polyamide washers in the conical holes and insert the M3 screws. As mentioned in the section "Preparation of the drift board", tighten the screws at 1.2 Nm using the manual torque screw driver (Fig. A.114).

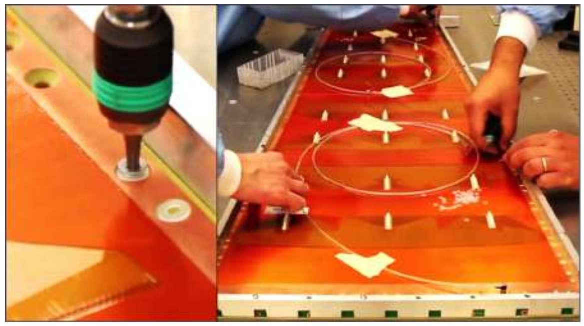

Figure A.114: Sealing the detector.

Step 6: When all the screws are in place, remove the aluminum bars to release the chamber.(Fig. A.115).

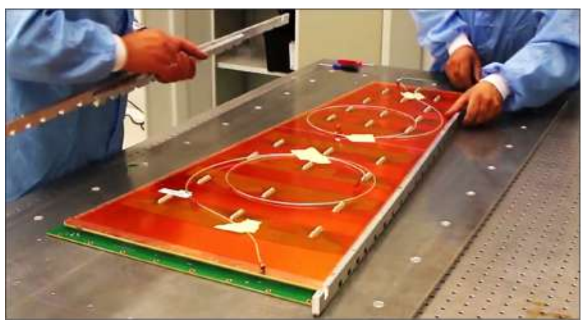

Figure A.115: Removing the assembly jig.

Step 7: Test again the GEM foils and the gaps at 550 V (Fig. A.116). Discharge the foils after each test.

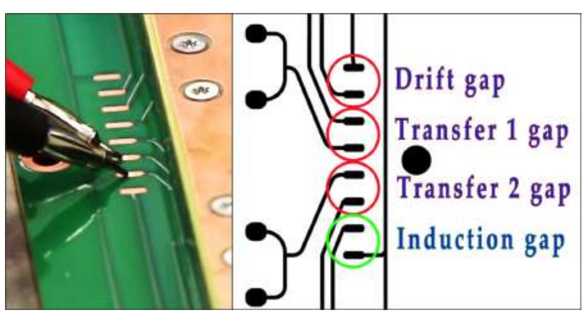

Figure A.116: Testing the GEM foils and the gaps.

Step 8: In this configuration, the induction gap can be tested as well. To do so, connect the Panasonic-to-Lemo adapter on one of the readout sectors (Fig. A.117 left).

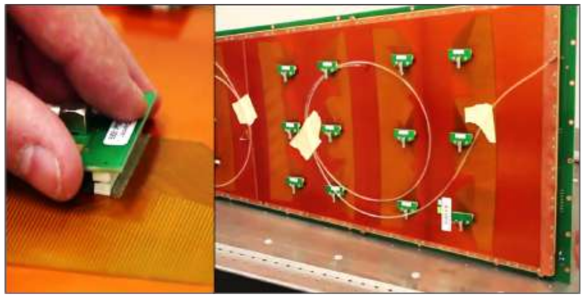

Figure A.117: Testing the induction gap (1).

Step 9: Holding the chamber in a vertical position, apply 550 V between the GEM3 bottom and the signal pad of the Panasonic-to-Lemo adapter. The location of the GEM3 bottom pad is shown on Fig. A.118 right. The impedance should immediately reach 100 GΩ.

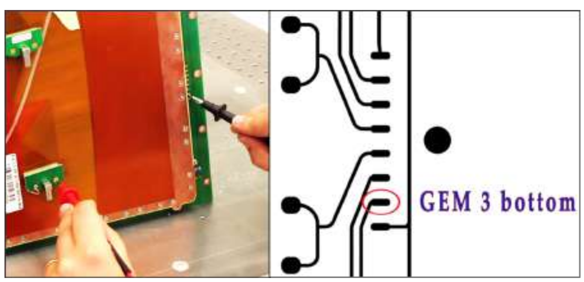

Figure A.118: Testing the induction gap (2).

Step 10: Follow the same procedure for all the readout sectors of the detectors (Fig. A.119).

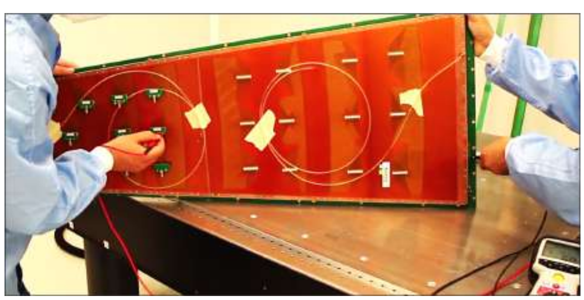

Figure A.119: Testing the induction gap (3).

Step 11: The GE1/1 chamber is now ready for the next quality controls (Fig. A.120).

Figure A.120: Chamber ready for QCs.

A.5.3 Comments and recommendations

When closing the readout board, one should make sure that the screws are perfectly concentric with the screw holes of the pull-outs. If not, it may create leak points that won't be identifiable before closing the chamber. More critical, the friction between the screw and the pull-out may create metallic dust that can seriously harm the detector.

As mentioned in the section "Preparation of the drift board", we recommended to first pair the M3 screws and the nylon washers before starting mounting the pull-outs. This will facilitate the work and limit the risk of damaging the PCB when pushing the screw inside the drift holes. One way to do so is shown on Fig. A.30.

All the steps following the removal of the Plexiglas cover should be performed with a great care since the GEM foils are directly exposed. In this case it is particularly important not to pass any object on top of the stack that can fall down and damage the GEMs (tools, screws etc ...). It is obviously mandatory to wear a mask and to limit the number of persons working around the setup.

One should never touch the active area of the drift or the readout boards with bare fingers under the penalty of triggering copper oxidation that may affect later the operation of the detector.

Stretching of GE2/1 foil stack

There are two methods two stretch the stack built using the GE2/1 size GEM foils:

(a) Hold the drift board using a small piece of PCB and screw on the assembly table having hole size of M6 as shown in Fig. A.121 & A.121 . But for stretching the stack of foils more than M2 or M6 need jig for that.

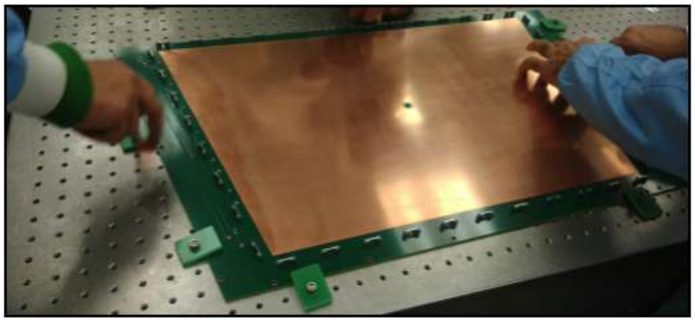

Figure A.121: Fixing drift without using the jig

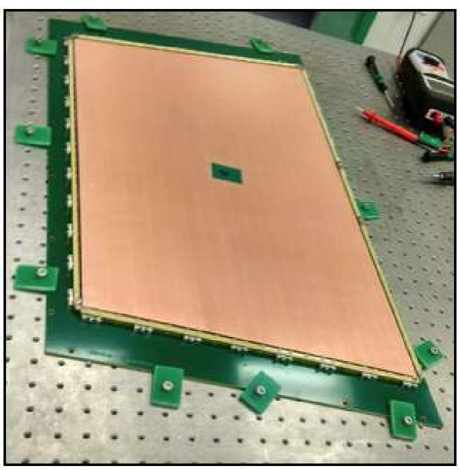

Figure A.122: Fixing drift without using the jig

(b) Second method of stretching the foils in stack is using the jig plate. Due to no available space on the wider base of the trapezoid in GE2/1 modules, it cannot be hold by the Aluminium bars. A new design is made to hold the drift PCB on the jig plate.

(c) After stretching of the foils place the FR4 pillar in the center of the stack as shown in Fig. A.123.

Figure A.123: Insertion of FR4 pillar.

Bibliography

[1] G. F. Knoll, Radiation Detection and Measurement, John Wiley & Sons, Inc., Hoboken, NJ, USA, third edition, 2000.

[2] J. Collot, Interaction of particles with matter (lecture i and ii), Euro- pean School of Instrumentation in Particle and Astroparticle Physics (ESIPAP), `http://lpsc.in2p3.fr/collot`.

[3] Particle Data Group, Passage of particles through matter, Technical report, 2011.

[4] Enrico Fermi, The ionization loss of energy in gases and in condensed materials, Technical report, Phys. Rev., 57 485, 1940.

[5] F. Sauli, Gaseous Radiation Detectors, Cambridge Univertsity Press, Cambridge, 2014.

[6] G. Charpak et al., The use of multiwire proportional counters to select and localize charge particles, NIM A 62 262, 1968.

[7] A. Breskin et al., Recent observations and measurements with high-accuracy drift chambers, NIM A 124 189, 1974.

[8] F. Sauli, A. Sharma, Micropattern Gaseous Detectors, Annual Review of Nuclear and Particle Science 49 341, 1999.

[9] A. Oed, Position-sensitive detector with microstrip anode for electron multiplication with gases, NIM A 263 351, 1988.

[10] F. Sauli, Development of high rate MSGCs: overview of results from RD-28, Nuclear Physics B Proceedings Supplements 61 236, 1998.

[11] F. Sauli, GEM: A new concept for electron amplification in gas detectors, NIM A 386 531, 1997.

[12] F. Sauli, Gas Electron Multiplier (GEM) Detectors: Principles of Operation and Applications, Comprehensive Biomedical Physics 8 367, 2014.

[13] S. Duarte Pinto, RD51, an R&D collaboration for Micropattern Gaseous Detectors, arXiv:0907.2673, 2009.

[14] G. Charpak et al., Micromegas, a multipurpose gaseous detector, NIM A 478, 2002.

[15] CMS Collaboration, The CMS Experiment at the CERN LHC, JINST 3 S08004, 2008.

[16] CMS detector, http://cms.web.cern.ch/news/cms-detector-design, 2011.

[17] J. A. Merlin, Study of long-term sustained operation of gaseous detectors for the high rate environment in CMS, Ph.D. thesis, CERN-THESIS-2016-041.

[18] CMS Collaboration, Performance and Future Upgrades of the CMS Drift Tube Muon Detector, CMS-CR-2017-414.

[19] Vorobiev, CMS Endcap Muon System Cathode Strip Chambers (CSC), `https://iopscience.iop.org/1742-6596/110/12/122022/media/22.pdf`.

[20] Giacomo Luca Bruno et al., The RPC detectors and the muon system for the CMS experiment at the LHC, CERN-THESIS-2001-081.

[21] CMS Collaboration, CMS Technical Design Report for the Muon Endcap GEM Upgrade, Technical Report CERN-LHCC-2015-012. CMS-TDR-013, CERN, 2015.

[22] CMS Collaboration, Technical proposal for the upgrade of the CMS detector through 2020, Technical Report CERN-LHCC-2011-006. LHCC-P-004, CERN, Geneva, 2011.

[23] G. Charpak, F. Sauli, The multistep avalanche chamber: A new high-rate, high-accuracy gaseous detector, Physics Letters B 78 523, 1978.

[24] S. Bachmann et al. Charge amplification and transfer processes in the gas electron multiplier. NIM A, 438 376, 1999.

[25] P. Thuiner, Ion space-charge effect in multi-GEM detectors: challenges and possible solutions for future applications, CERN-THESIS-2016-199.

[26] L. Benussi et al., properties of potential Eco-Friendly gas replacement for particle detectors in high-energy physics, cern-open-2015-004.

[27] Y. Assran, Transport Properties of operational gas mixtures used at LHC, arXiv:1110.6761.

[28] Federico Lucchetti, Study of a Triple GEM detector for the upgrade in the forward region of the CMS Muon System at the LHC, CERN-THESIS-2014-420.

[29] D. Abbaneo, Ashok Kumar, **M. Gola** et al., Layout and assembly technique of the GEM chambers for the upgrade of the CMS first muon endcap station, NIM A 918 67, 2019.

[30] A. Shah, A. Kumar, **M. Gola** et al., A Novel Assembly Procedure of GE1/1 Detectors for CMS High Luminosity Phase of the LHC, Spring. Proc. in Phy., 203 775, 2018.

[31] R. Rizwan, **Mohit Gola** et al., Design and Development of Gas Leakage Station for Gas Electron Multiplier (GEM) Chamber, Springer Proc.Phys. 203 889, 2018.

[32] M. Gola, Muon Chamber Endcap Upgrade of the CMS Experiment with Gas Electron Multiplier (GEM) Detectors and Their Performance, XXII DAE High Energy Physics Symposium, Springer Proceedings in Physics 203, 2018.

[33] G. Apollinari et al., High-Luminosity Large Hadron Collider (HL-LHC): Preliminary Design Report, CERN-2015-005.

[34] G. Apollinari et al., High-Luminosity Large Hadron Collider (HL-LHC), Technical Design Report V.0.1, CERN-2017-007-M.

[35] CMS Collaboration, The Phase-2 Upgrade of the CMS Muon Detectors, CERN-LHCC-2017-012; CMS-TDR-016-2017.

[36] COMPAS Collaboration, The COMPASS experiment at CERN, NIM A 577 455, 2007.

[37] TOTEM Collaboration, The TOTEM experiment at the CERN Large Hadron Collider, JINST 3 S08007, 2008.

[38] A. Cardini, B. Bencivenni, and P. De Simone, The Operational Experience of the Triple-GEM Detectors of the LHCb Muon System: Summary of 2 Years of Data Taking,. IEEE Nucl. Sci. Symp. Med. Imag. Conf. Rec. 759, 2012.

[39] A. Mohammad et al, Design of the Read Out Boards for the GE21 upgrade of the CMS experiment at the LHC facility, DAE Symp.Nucl.Phys. 63 1068, 2018.

[40] F.Sauli, Gas detectors: Recent developments and future perspectives, NIM A 419, 1998.

[41] M. Bucciantonio and F. Sauli, Proton computed tomography, Mod. Phys. Lett. A, 30 1540024, 2015.

[42] Md. Naimuddin et al., Development of a proton Computed Tomography detector system, JINST 11 C02012, 2016.

[43] Wang R., et al, A practical method to determine the spatial resolution of GEM detector, NIM A 701, 2013.

[44] Alice Alfonsi, Time resolution of a Triple-GEM detector for future upgrade of the CMS muon system, INFN-17-09/LNF(Thesis).

[45] P. Everaerts, Rate capability and ion feedback in GEM-detectors, Master thesis, Universiteit Gent, Ghent, (BE), 2006.

[46] A. Bondar et al., Study of ion feedback in multi-GEM structures, NIM A 496 2, 2003.

[47] Gnanvo K et al., Large size GEM for Super Bigbite Spectrometer (SBS) polarimeter for hall A 12 GeV program at JLAB, NIM A 782, 2015.

[48] A. K. Dubey et al., First signals from indigenously produced GEM foils, DAE-BRNS Symp. on Nucl. Phys. 61, 2016.

[49] M. Hoch, GEM - A novel gaseous particle detector, CERN-THESIS-2005-037.

[50] S. Duarte Pinto et al., A method of manufacturing a gas electron multiplier, Patent Wipo WO/2009127220.

[51] M. Posik et al., Optical and electrical performance of commercially manufactured large GEM foils, NIM A 802 10, 2015.

[52] U. Becker et al., Test and evaluation of new GEMs with an automatic scanner, NIM A 556, 2006.

[53] `http://hdl.handle.net/1721.1/32905`.

[54] `https://root.cern.ch`.

[55] F. Simon, et al., Development of Tracking Detectors With Industrially Produced GEM Foils, IEEE Trans. Nucl. Sci. NS 54 2646, 2007.

[56] ALICE collaboration, TDR for the Upgrade of the ALICE TPC, CERN/LHCC, 2014.

[57] M. Ball et al., Quality assurance of GEM foils for the upgrade of the ALICE TPC, JINST 12 C01081, 2017.

[58] L. F. Cruz et al., Assembly, functionality and performance of a Triple GEM Chamber Prototype, Nuclear and Particle Physics Proceedings, 267 427, 2015.

[59] G. Saviano et al., Properties of potential eco-friendly gas replacements for particle detectors in high energy physics, JINST 13 03 P03012, 2018.

[60] A. Buzulutskov et al., GEM operation in pure noble gases and the avalanche confinement, NIM A 433, 1999.

[61] O. Ahin et al., High-precision gas gain and energy transfer measurements in Ar/CO2 mixtures, NIM A 768 104, 2014.

[62] A. Marinov, Feasibility Study of a GEM Based Muon System for the CMS Detector at the Large Hadron Collider, Ph.D. thesis, Universiteit Gent, 2013.

[63] S. Bachmann et al., Discharge mechanisms and their prevention in the gas electron multiplier (GEM), NIM A 479 294, 2002.

[64] Keithley Instruments Inc., Model 6517B Electrometer Reference Manual, 6517B-901-01 Rev. B, Cleveland, 2009.

[65] S. Malhotra et al., Various Studies with Gas Electron Multiplier (GEM) Detectors, XXII DAE High Energy Physics Symposium, Springer Proceedings in Physics 203, 2018.

[66] M. V. Nemallapudi, Gain of a Single Gas Electron Multiplier, Theses and Dissertations. 533, `http://scholarworks.uark.edu/etd/533`.

[67] Sung Yong Ha et al., Energy Resolution of a Single GEM Detector, Journal of the Korean Physical Society, 55, 6 2366, 2009.

[68] A. Shah, **M. Gola** et al., Development, characterization and qualification of first GEM foils produced in India, NIM A 892 10, 2018.

[69] O. Bouianov, Foil geometry effects on GEM characteristics, NIM A 458 698, 2001.

[70] E. Erdal, Characterization of a glass GEM for sealed detectors application and reduction of charging-up effects, CERN-STUDENTS-Note-2014-034, 2014.

[71] R. Bellazzini et al., The WELL detector, ELSEVIER, 423 1 125, 1999.

[72] B. Azmoun et al., A Study of Gain Stability and Charging Effects in GEM Foils, IEEE Nuclear Science Symposium Conference Record, 2006.

[73] J. K. Quamara et al., The Photoinduced Polarization in Kapton-H Film, Appl. Phys. A 35 267, 1984.

[74] `https://amptek.com/products/mini-x-ray-tube`.

[75] M. Villa et al., Progress on large area GEMs, NIM A 628 182, 2011.

[76] YOU wen hao et al., A Large-area GEM Detector Using an improved Self-stretch Technique; arXiv:1405.1872.

[77] Lea Hallermann, Analysis of GEM Properties and Development of a GEM Support Structure for the ILD Time Projection Chamber, desy-thesis-2010-015.

[78] Gabriele Croci et al., Study of relevant parameters of GEM-based detectors, PhD thesis, Milan U., Milano, 2007.

[79] M. Gola et al., Stability test performed on the triple GEM detector built using commercially manufactured GEM foils in India; JINST 14, 2019.

[80] D. Abbaneo, **M. Gola**, A. Kumar et al., Performance of GE1/1 chambers for the CMS Muon Endcap Upgrade, arXiv:1903.02186, NIM A 972, 2020.

[81] S. Bachmann et al., Performance of GEM detectors in high intensity particle beams, NIM A 470 548, 2001.

[82] H. Raether, Electron avalanche and breakdown in gases, CERN CDS 191 1964.

[83] P. Gasik, Discharge probability studies with multi-GEM detectors for the ALICE TPC Upgrade, arXiv: 1807.02979v1.

[84] M. Alfonsi et al., The LHCb Triple-GEM Detector for the Inner Region of the First Station of the Muon System: Construction and Module-0 Performance, IEEE 0-7803-8701-5 2004.

[85] S Martoiu, H Muller, A Tarazon and J Toledo, Development of the scalable readout system for micro-pattern gas detectors and other applications, JINST 8, 2013.

[86] Sorin Martoiu, Hans Muller, J. Toledo, Front-end electronics for the Scalable Readout System of RD51, DOI:10.1109/NSSMIC.2011.6154414.

[87] M. Raymond et al., 2000 The APV25 0.25 μm CMOS readout chip for the CMS tracker, IEEE Nucl. Sci. Symp. Conf. Rec. 2 9/113.

[88] A. Bressan et al., Two-dimensional readout of GEM detectors, NIM A 425 254, 1999.

[89] A.Bondar et al., Performance of the triple-GEM detector with optimized 2-D readout in high intensity hadron beam", arXiv 0110054.

[90] G. Bertone et al., Particle dark matter: evidence, candidates and constraints, Phys. Rept. 405 279, 2005.

[91] ATLAS Collaboration, Observation of a new particle in the search for the Standard Model Higgs boson with the ATLAS detector at the LHC, Phys. Lett. B 716 1, 2012.

[92] CMS Collaboration, Observation of a new boson at a mass of 125 GeV with the CMS experiment at the LHC, Phys. Lett. B 716 30, 2012.

[93] CMS Collaboration, Observation of a new boson with mass near 125 GeV in pp collisions at $\sqrt{s} = 7$ and 8 TeV, JHEP 06 081, 2013.

[94] A. A. Petrov and W. Shepherd, Searching for dark matter at LHC with mono-Higgs production, Phys. Lett. B 730 178, 2014.

[95] L. Carpenter et al., Mono-Higgs-boson: A new collider probe of dark matter, Phys. Rev. D 89 075017, 2014.

[96] A. Berlin et al., Mono-Higgs detection of dark matter at the LHC, JHEP 06 078, 2014.

[97] ATLAS Collaboration, Search for dark matter produced in association with a Higgs boson decaying to two bottom quarks in pp collisions at $\sqrt{s} = 8$ TeV with the ATLAS detector, Phys. Rev. D 93 47, 2016.

[98] ATLAS Collaboration, Search for dark matter in association with a Higgs boson decaying to b-quarks in p p collisions at $\sqrt{s} = 13$ TeV with the ATLAS detector, Phys. Lett. B 765 11, 2017.

[99] ATLAS Collaboration, Search for dark matter in events with missing transverse momentum and a Higgs boson decaying to two photons in pp collisions at $\sqrt{s} = 8$ TeV with the ATLAS detector, Phys. Rev. Lett. 115 131801, 2015.

[100] D. Abercrombie et al., Dark matter benchmark models for early LHC Run-2 searches: report of the ATLAS/CMS dark matter forum, arXiv:1507.00966, 2015.

[101] T. D. Lee, A theory of spontaneous T violation, Phys. Rev. D 8 1226, 1973.

[102] G. C. Branco et al., Theory and phenomenology of two-Higgs-doublet models, Phys. Rept. 516 1, 2012.

[103] N. Craig et al., Searching for signs of the second Higgs doublet, arXiv:1305.2424, 2013.

[104] J. Alwall et al., The automated computation of tree-level and next-to-leading order differential cross sections, and their matching to parton shower simulations, JHEP 07 079, 2014.

[105] T. Sjostrandetal., An introduction to PYTHIA8.2, Comput. Phys. Commun. 191 159, 2015.

[106] C. Oleari, The POWHEG-BOX, Nucl. Phys. Proc. Suppl. 205 36, 2010.

[107] G. Luisoni, et al., $HW^{\pm}/HZ + 0$ and 1 jet at NLO with the POWHEG BOX interfaced to GoSam and their merging within MiNLO, JHEP 10 083, 2013.

[108] P. Nason and C. Oleari, NLO Higgs boson production via vector-boson fusion matched with shower in POWHEG, JHEP 02 037, 2010.

[109] P. Nason, A new method for combining NLO QCD with shower Monte Carlo algorithms, JHEP 11 040, 2004.

[110] S. Frixione et al., Matching NLO QCD computations with parton shower simulations: the POWHEG method, JHEP 11 070, 2007.

[111] S. Alioli, et al., A general framework for implementing NLO calculations in shower Monte Carlo programs: the POWHEG BOX, JHEP 06 043, 2010.

[112] S. Frixione, et al., A positive-weight next-to-leading-order Monte Carlo for heavy flavour hadroproduction, JHEP 09 126, 2007.

[113] E. Re, Single-top Wt-channel production matched with parton showers using the POWHEG method, Eur. Phys. J. C 71 1547, 2011.

[114] CMS Collaboration, Measurement of differential top-quark-pair production cross sections in the pp collision $\sqrt{s} = 7$ TeV, Eur. Phys. J. C 73 3, 2013.

[115] CMS Collaboration, Measurement of the differential cross section for top quark pair production in pp collisions at $\sqrt{s} = 8$ TeV, Eur. Phys. J. C 75 11, 2015.

[116] M. L. Mangano et al., Matching matrix elements and shower evolution for top-quark production in hadronic collisions, JHEP 01 013, 2007.

[117] Y. Li and F. Petriello, Combining QCD and electroweak corrections to dilepton production in FEWZ, Phys. Rev. D 86 094034, 2012.

[118] J. H. Kuhn et al., Electroweak corrections to hadronic photon production at large transverse momenta, JHEP 03 059, 2006.

[119] S. Kallweit et al., NLO electroweak automation and precise predictions for W+multijet production at the LHC, JHEP 04 012, 2015.

[120] S. Kallweit et al., NLO QCD+EW predictions for V+jets including off-shell vector-boson decays and multijet merging, JHEP 04 021, 2016.

[121] P. Nason and G. Zanderighi, W^+W^-, WZ and ZZ production in the POWHEG-BOX-V2, Eur. Phys. J. C 74 2702, 2014.

[122] NNPDF Collaboration, Parton distributions for the LHC Run II, JHEP 04 040, 2015.

[123] P. Skands, S. Carrazza, and J. Rojo, Tuning PYTHIA 8.1: the Monash 2013 tune, Eur. Phys. J. C 74 3024, 2014.

[124] CMS Collaboration, Event generator tunes obtained from underlying event and multiparton scattering measurements, Eur. Phys. J. C 76 3, 2016.

[125] M. Bahr et al., Herwig++ physics and manual, Eur. Phys. J. C 58 639, 2008.

[126] S. Gieseke, C. Rohr, and A. Siodmok, Colour reconnections in Herwig++, Eur. Phys. J. C 72 2225, 2012.

[127] M. H. Seymour and A. Siodmok, Constraining MPI models using σeff and recent Tevatron and LHC underlying event data, JHEP 10 113, 2013.

[128] GEANT4 Collaboration, GEANT4–a simulation toolkit, NIM A 506 250, 2003.

[129] CMS Collaboration, Particle-flow event reconstruction in CMS and performance for jets, taus, and p_T^{miss}, CMS Physics Analysis Summary CMS-PAS-PFT-09-001, CERN, 2009.

[130] CMS Collaboration, Commissioning of the particle-flow event reconstruction with the first LHC collisions recorded in the CMS detector, CMS Physics Analysis Summary CMS-PAS-PFT-10-001, 2010.

[131] CMS Collaboration, Particle-flow reconstruction and global event description with the CMS detector, arXiv:1706.04965, 2017.

[132] M. Cacciari, G. P. Salam, and G. Soyez, The anti-k_t jet clustering algorithm, JHEP 04 063, 2008.

[133] M. Cacciari, G. P. Salam and G. Soyez, FastJet user manual, Eur. Phys. J. C 72 012, 2012.

[134] S. D. Ellis, C. K. Vermilion, and J. R. Walsh, Techniques for improved heavy particle searches with jet substructure, Phys. Rev. D 80 051501, 2009.

[135] S. D. Ellis, C. K. Vermilion, and J. R. Walsh, Recombination algorithms and jet substructure: pruning as a tool for heavy particle searches, Phys. Rev. D 81 094023, 2010.

[136] CMS Collaboration, Jet energy scale and resolution in the CMS experiment in pp collisions at 8 TeV, arXiv:1607.03663, 2016.

[137] CMS Collaboration, Performance of missing energy reconstruction in 13 TeV pp collision data using the CMS detector, CMS Physics Analysis Summary CMS-PAS-JME-16-004, 2016.

[138] CMS Collaboration, Identification of b quark jets at the CMS experiment in the LHC Run 2, CMS Physics Analysis Summary CMS-PAS-BTV-15-001, 2016.

[139] CMS Collaboration, Identification of b-quark jets with the CMS experiment, JINST 8 P04013, 2013.

[140] M. Dasgupta, A. Fregoso, S. Marzani, and G. P. Salam, Towards an understanding of jet substructure, JHEP 09 029, 2013.

[141] A. J. Larkoski, S. Marzani, G. Soyez, and J. Thaler, Soft drop, JHEP 05 146, 2014.

[142] CMS Collaboration, CMS physics technical design report, volume II: physics performance, J. Phys. G 34 995, 2007.

[143] CMS Collaboration, Performance of photon reconstruction and identification with the CMS detector in proton-proton collision $\sqrt{s} = 8$ TeV, JINST 10 P08010, 2015.

[144] CMS Collaboration, Performance of electron reconstruction and selection with the CMS detector in proton-proton collision $\sqrt{s} = 8$ TeV, JINST 10 P06005, 2015.

[145] CMS Collaboration, Performance of CMS muon reconstruction in pp collision events at $\sqrt{s} = 7$ TeV, JINST 7 P10002, 2012.

[146] CMS Collaboration, Reconstruction and identification of τ lepton decays to hadrons and v_τ at CMS, JINST 11 01, 2016.

[147] CMS Collaboration, The performance of the CMS muon detector in proton-proton collisions at $\sqrt{s} = 7$ TeV at the LHC, JINST 8 P11002, 2013.

[148] M. Cacciari and G. P. Salam, Pileup subtraction using jet areas, Phys. Lett. B 659 119, 2008.

[149] CMS Collaboration, Measurement of differential cross sections for Higgs boson production in the diphoton decay channel in pp collisions at $\sqrt{s} = 8$ TeV, 76 13, 2016.

[150] CMS Collaboration, Observation of the diphoton decay of the Higgs boson and measurement of its properties, Eur. Phys. J. C 74 3076, 2014.

[151] CMS Collaboration, Search for resonant production of high-mass photon pairs in proton-proton collisions at $\sqrt{s} = 8$ & 13 TeV, Phys. Rev. Lett. 117 051802, 2016.

[152] CMS Collaboration, CMS luminosity measurement for the 2015 data taking period, CMS Physics Analysis Summary CMS-PAS-LUM-15-001, 2016.

[153] CMS Collaboration, Measurements of inclusive W and Z cross sections in pp collisions at $\sqrt{s} = 7$ TeV, JHEP 01 080, 2011.

[154] J. Butterworth et al., PDF4LHC recommendations for LHC Run II, J. Phys. G 43 023001, 2016.

[155] LHC Higgs Cross Section Working Group Collaboration, Handbook of LHC Higgs cross sections: 3. Higgs properties: report of the LHC Higgs cross section working group, Technical Report CERN-2013-004, Geneva, 2013.

[156] A. L. Read, Presentation of search results: the CLs technique, J. Phys. G 28 2693, 2002.

[157] T. Junk, Confidence level computation for combining searches with small statistics, NIM A 434 435, 1999.

[158] G. Cowan, K. Cranmer, E. Gross, and O. Vitells, Asymptotic formulae for likelihood-based tests of new physics, Eur. Phys. J. C 71 1554, 2011.